



UNIVERSITY OF CALABRIA

Department of Pharmacy and Health and Nutritional Sciences

Ph.D. in Translational Medicine

Cycle
XXXIII

**ADVANCED FUNCTIONALIZED MATERIALS FOR
MULTIPURPOSE APPLICATIONS**

**Scientific-Disciplinary Sector:
CHIM/02 Physical Chemistry**

Coordinator: Prof. Sebastiano Andò

Supervisor: Prof. Fiore P. Nicoletta

Ph.D. Candidate: Elvira Pantuso

A handwritten signature in black ink, reading "Elvira Pantuso".

TABLE OF CONTENTS

Preface		1
PART I		
Chapter 1	Light-Responsive Polymer Membranes (Review)	5
Chapter 2	Polymer Membranes Dispersed Liquid Crystal (PMDLC): a new electro-optical device	66
PART II		
Chapter 3	Chemical Vapor Deposition of photocatalyst nanoparticles on PVDF membranes for Advanced Oxidation Processes	77
Chapter 4	WO ₃ /buckypaper membranes for Advanced Oxidation Processes	93
Chapter 5	Electrocoagulation and Electroresponsive membranes	112
PART III		
Chapter 6	Silica sputtered PVDF membrane for the crystallization of Lysozyme	133
Chapter 7	Hybrid hydrogels for the crystallization and the controlled release of lysozyme	138
Chapter 8	The impact of polyelectrolytes on the crystallization of lysozyme crystals	155
PART IV		
Chapter 9	On the aggregation and nucleation mechanism of the monoclonal antibody ANTI-CD20 near liquid-liquid phase separation (LLPS)	186

PREFACE

The works presented in this Ph.D. thesis are the result of the activity research carried out in the laboratory of Applied Physical Chemistry of the Department of Pharmacy, Health and Nutritional Sciences (University of Calabria) and embrace different topics ranging from the development of innovative techniques of polymer materials functionalization to the study of chemical physical parameters to understand the aggregation mechanism of a complex biomacromolecule.

The first part of the thesis reviewed different functionalization methods able to realize stimuli-responsive polymer membranes with the ability to tune opportunely their physicochemical properties including electrical dipole moment, molecular volume, and exposed chemical group, under the application of light as external stimulus, paying particular attention to chemical groups and responsive mechanisms. Light can induce different and interesting physicochemical property changes, which can affect the performance of a great variety of devices. In fact, thanks to a reversible isomerization of a light-sensitive chemical groups or molecules, such as light-switchable chromophores incorporated in the structure of the polymer or immobilized onto the membrane surface, it is possible to reach a photocontrol of the final performance of the membrane.

Some of the light-switchable chromophores, mostly used to prepare light-responsive polymer membranes include azobenzene, spiropyran, and their derivatives able to undergo a reversible isomerization from the more stable trans form to the cis form upon light irradiation. Photochromic molecules have been applied in liquid crystal compounds and polymers in order to obtain photochromic liquid crystals having photoresponsive ability. Recently, the employment of polymer networks used to stabilize liquid crystals has become an attractive field of research thanks to the ability of polymer dispersed liquid crystals (PDLCs) to become transparent or opaque according to the liquid crystal orientation upon application of an external field.

In this context, an innovative electro-optical responsive device, formed by a porous polymer membrane imbued with liquid crystal, Polymer Membranes Dispersed Liquid Crystal (PMDLC) was presented. Polymer membranes sputtered with a thin layer of conductive indium tin oxide (ITO) act as polymer network hosting liquid crystals for the electric modulation of scattering properties. PMDLC represent an alternative, cheap and flexible to PDLC devices, thanks to the reduced amount of used liquid crystal, the absence of rigid conductive substrate and the fast response times. Thanks to the orientation of liquid crystals present in the polymer matrix, these materials can be characterized by an opaque OFF state or a transparent ON state in response to electric field as external stimulus.

In the second part of the thesis many strategies of functionalization were explored to improve the performance of existing materials making them suitable for potential applications such as Advanced Oxidation Process (AOP) or Electrocoagulation process (EC). Both processes are widely used in pharmaceutical field for the removal of emerging organic contaminants such pharmaceuticals from wastewater. However, these processes generally represent a preliminary or intermediate step during the large-scale industrial treatment of wastewater and the combination of membrane separation and AOP

or EC could become an advantageous and emerging technology for the complete removal of pollutants since each technique complements the advantages of the other.

The third part of the thesis is focused on the study on the impact different functionalized surfaces proposed as suitable substrate for the crystallization of the protein lysozyme used as model at lower supersaturation conditions. The combined effect of surface porosity at nano- and micro-meter length-scale and surface chemistry of a polymeric porous membranes supporting a thin layer of hydrophilic silica on the heterogeneous nucleation of crystals was investigated. The surface functionalization by physical vapor deposition (PVD) offers the possibility to combine the ability of silica nanoparticles to favor interactions protein-surface, keeping unchanged the porous structure of polymeric membranes able to promote the crystallization processes.

The protein crystallization process was also studied on the surface of a novel multifunctional hybrid alginate hydrogel functionalized with caffeic acid and graphene oxide with the double aim of obtaining a mitigation against the oxidative damage induced by X-rays and to modulate the release of lysozyme as an antibacterial agent for biomedical applications. This system aims to overcome a great challenge in both drug delivery and discovery, since the possibility to reduce oxidative damages is a key property for any material designed for interactions with living tissues, as well as in the X-ray crystallography, where the oxidation of protein sample in the crystallization droplet can lead to the failure of the crystallization process.

Besides, the impact of two types of polyelectrolytes having opposite charge, poly(acrylic acid) and polydiallyldimethyl ammonium chloride, on the crystallization of lysozyme was investigated functionalizing surfaces by simple coating and by Layer-by-Layer deposition method. Non-specific attractive and local interactions between the protein and the polyelectrolyte may promote the molecular collisions leading to the formation of the protein crystal nuclei in short time.

Finally, in the fourth part of the thesis, the study of crystallization is extended to a more complex biomacromolecule, the full-length monoclonal antibody Anti-CD20, a therapeutic protein extensively used for treatment of chronic lymphocytic leukaemia and non-Hodgkin's lymphoma.

Physico-chemical parameters like the osmotic second virial coefficient (B_{22}) and the melting temperature (T_m) are measured by correspondingly Static Light Scattering and Dynamic Light Scattering in order to investigate the aggregation mechanism and the colloidal stability of this protein in PEG400/ Na_2SO_4 / H_2O solution near liquid-liquid phase separation conditions. The relationships between the crystallization propensity of Anti-CD20 in the Na_2SO_4 /PEG400 solvent system of different compositions and these measurable parameters allow to understand the aggregation mechanism governing the nucleation-crystallization of this complex biomacromolecule. In fact, since the crystallization of mAb is not a trivial process, a thorough understanding of the intimate mechanism underlying protein behavior in the crystallization solution needs to be investigated taking account of the role of the solvent and the environmental conditions such pH, ionic strength and temperature.

PART I

INTRODUCTION

Functionalization is an effective way of adding properties to a material to achieve specific goals such as inducing a desired response, inhibiting a potentially adverse reaction or improving the interactions with the surrounding environment. Functionalized surfaces can be developed to address needs for biological, medical, commercial and industrial applications. Infact, several functionalized surfaces find numerous practical applications in various branches of industry and everyday life. A few examples include antimicrobial materials to prevent bacterial adhesion and infections, ¹ conductive devices able to control the transmittance of light when an external stimulus is applied, ^{2,3} biosensors based on the immobilization of enzymes, antibodies and other type of cells, ⁴⁻⁶ self-cleaning materials applied in energy and environmental areas ⁷.

Membranes are selective barriers able to separate components with different sizes or physical/chemical properties. The efficiency of a membrane separation process depends on the performance of used membrane and thus on its properties. In particular, the most important property of a membrane includes selectivity, which is the ability to separate solutes rejecting the unwanted compound and letting the desired one pass through. Generally, the membrane selectivity depends on the affinity between the substances and membrane surface. Hence the importance of modifying membrane surface to improve its properties making it suitable for the process in which it will be used.

Functionalization has been widely applied to polymeric membranes in many fields and has progressed rapidly in recent years. Membrane surface has been engineered to modify its chemistry and topography in order to achieve a final product characterized by innovative properties. The modified membranes have been widely used in various applications, such as in separation processes, catalysis, biomaterials and “smart” membranes. Membranes able to change their physicochemical properties to respond to environmental stimuli are called intelligent or smart membranes and are attracting ever-increasing interests in numerous fields ranging from controlled release to separations. Several functional groups incorporated in the membrane structure or grafted on its surface could change the membrane properties on demand. Stimuli such as light, temperature, pH, electric and magnetic fields, ionic strength, humidity cause the transition of a property at the microscopic level which led to macroscopic and, often, reversible changes in membrane performance in terms of separation, flux, fouling potential, and permselectivity. ⁸ Today the applications of stimuli-responsive membranes are numerous and the research aims at designing and developing new and innovative potential applications where membranes are key components of complex technical systems such as sensors, separation processes, and drug delivery devices. The use of stimuli-responsive polymers grafted on the membrane surface or into its porous structure, represents a common method to add responsiveness to the membrane. In such a way, it is possible to modify transport properties (e.g. permselectivity and hydrophilicity) enabling a fouling mitigation and tunable self-cleaning membrane surfaces without the use of physical/chemical cleaning methods required for membranes under normal operating conditions.⁸

REFERENCES

- [1] M.G. Katsikogianni, D.J. Wood, Y.F. Missirlis, in *Handbook of Bioceramics and Biocomposites*, (Eds: I. Antoniac), Springer, Cham. **2015**.
- [2] G. De Filpo, K. Armentano, E. Pantuso, A. Mashin, G. Chidichimo, F.P. Nicoletta. *Liq. Cryst.* **2019**, *46*, 1.
- [3] E. Pantuso, G. De Filpo, F.P. Nicoletta. *Adv. Opt. Mater.* **2019**, *7*, 1900252.
- [4] M.E. Marques, A.A.P. Mansur, H.S. Mansur. *Appl. Surf. Sci.* **2013**, *275*, 347.
- [5] B. Della Ventura, M. Banchelli, R. Funari, A. Illiano, M. De Angelis, P. Taroni, A. Amoresano, P. Matteini, R. Velotta, *Analyst* **2019**, *144*, 6871.
- [6] J. Arreola, J. Oberländer, M. Mätzkow, M. Keusgen, M.J. Schöning, *Electrochim. Acta* **2017**, *241*, 237.
- [7] S. Banerjee, D.D. Dionysiou, S.C. Pillai, *Appl. Catal. B- Environ.* **2015**, *176-177*, 396.
- [8] P. Formoso, E. Pantuso, G. De Filpo, F.P. Nicoletta, *Membranes* **2017**, *7*, 39.

CHAPTER 1

1. LIGHT-RESPONSIVE POLYMER MEMBRANES (REVIEW)

Published as: E. Pantuso, G. De Filpo, F.P. Nicoletta, Light-Responsive Polymer Membranes. *Advanced Optical Materials* **2019**, 7, 1900252. <https://doi.org/10.1002/adom.201900252>

1.1 SUMMARY

Stimuli-responsive polymer membranes have gained particular attention for the ability to tune opportunely their physicochemical properties under the application of an external stimulus. Heat, pH value, ionic strength, pressure, humidity, electric and magnetic fields, antigen/antibody interactions, chemical reactions, and light can be used as triggers for specific responses in polymer membranes. In particular, light is a fascinating stimulus, as it is a green energy, which can be modulated in a precise and convenient way. In addition, it allows remote and contactless interactions without changing the original chemical environment. This review reports recent progresses in light-responsive polymer membranes with particular attention to chemical groups and responsive mechanisms.

1.2 INTRODUCTION

Responsive membranes represent a new class of advanced membranes that are able to respond to one or more external stimuli and allow the control of membrane performance and functions.¹ Stimuli such as heat, electric and magnetic fields, humidity, light, and presence of specific ions cause the transition of a property at the microscopic level in responsive sites, which led to macroscopic and, often, reversible changes in membrane performance.² The responsive sites are coated as thin films onto the membrane, but can cover or fill the functionalized pore walls in the case of porous membranes. According to the induced property change, Darvishmanesh et al. categorized stimuli as:²⁻⁴

1. direct, if the membrane responsive sites respond to a specific cue (pH, ionic strength, biological cues);
2. indirect, if the changes in membrane performance are due to temperature or ultrasounds;
3. field induced, if the property transition is caused by light or an external electric or magnetic field.

The most common direct stimuli-responsive membranes are prepared with polymers bearing pH-responsive chemical groups such as pyridine and carboxyl groups. At low pH the acid-swellable groups (such as pyridine) are protonated and give rise to large charge repulsions between polymer chains, which cause the membrane swelling. Alkali-swellable groups such as carboxyl groups, on the contrary, experience an increase in charge density and a polymer swelling at high pH values.⁵ Typical polymers used in the manufacturing of direct stimuli-responsive membranes are poly(methacrylic acid), poly(acrylic acid), poly(4-vinylpyridine), and poly(N,N-dimethylaminoethyl methacrylate). Indirect stimuli-responsive membranes are generally prepared with polymers such as poly(N-isopropylacrylamide), poly(2-dimethylamino-ethyl methacrylate), or

poly(N,N'-diethyl acrylamide). These polymers show a critical solution temperature (CST), above which they undergo a phase transition from a soluble hydrophilic swollen state to an insoluble hydrophobic shrunk state (lower critical solution temperature or LCST). Polymers with an upper critical solution temperature, on the contrary, undergo a phase transition from an insoluble state to a soluble state if temperature is higher than CST.^{6,7}

High performance magnetic-responsive membranes are generally filled with magnetic-active nanoparticles of metals, metal oxides, or ferromagnetic materials. Their main application is the active delivery and release of drugs loaded in small polymer drug delivery systems such as liposomes, niosomes, and vesicles.^{8,9} Electroactive membranes can be obtained by addition of electroactive materials such as carbon nanostructures (nanoparticles, nanotubes, graphene nanosheets) or by using conductive polymers (e.g., polypyrrole, polythiophene, polyaniline). It is important to note that an electric field can increase the temperature through Joule-heating and confer thermoresponsive properties to an electroactive membrane.¹⁰

Electroactivity can be also obtained by casting or grafting of conductive polymer thin films on the membrane surfaces or by self-assembling of monolayers by physical and chemical vapor deposition, layer-by-layer assembly, and spin coating.¹⁰

Light-responsive chemical groups such as azobenzenes, spiropyrans, diarylethenes, and semiconductor nanoparticles can be physically blended or chemically bound within the membrane bulk structure or immobilized by coating or grafting onto the membrane surface and/or pores. Different light wavelength ranges (UV, Vis, NIR, and IR) can be used to trigger structural transformations according to the specific functional groups to be activated.³ Specific wavelengths can cause conformational changes of the particular light-responsive groups³ and/or heating of the surrounding environment leading to changes in macroscopic properties.⁴ This paper reports recent progresses and a guide to the relevant literature in light responsive polymer membranes with particular attention to photoswitching properties of the involved chemical groups and responsive mechanisms, which can change the membrane properties on demand. Readers interested to smart membrane technologies actuated by multistimuli can refer to excellent papers and reviews present in literature.¹¹⁻¹⁴

1.3 PHOTOSWITCHING MECHANISMS AND COMPOUNDS

1.3.1 POLYMER MEMBRANES AND LIGHT

A precise definition of the term membrane is rather difficult. A membrane is “a nonselective barrier that separates and contacts two adjacent phases” allowing the exchange of matter, energy, and, more in general, information between the two phases.¹⁵ A membrane can be solid or liquid, homogeneous or heterogeneous, with a symmetric or asymmetric structure, with selective or nonselective properties, and made with organic, inorganic, or biological materials.¹⁶ Accordingly to the constituent material, membranes can be categorized as liquid, metal, glass, ceramic, and polymer membranes. Polymers are characterized by peculiar properties such as high values of porosity, specific surface area, large permeability, and low density.¹⁷ In addition, polymers show chemical versatility and easy processability. Light represents an appealing stimulus that can alter the dimensional or structural composition of materials according to a contactless way and with no change in the

surrounding environment.¹⁸ Light also offers excellent spatial and temporal control over the energy input required for tuning material properties.¹⁹ In addition, compared to other external stimuli such as heat, pressure, pH, electric and magnetic fields,^{20–23} light is a fascinating stimulus, as it is a green energy, as its intensity, wavelength, and polarization direction can be modulated in a precise and convenient way. Color, alignment, wettability, charge, roughness, shape, ion binding, and permeability are some material surface/bulk properties that can be locally addressed and changed by light.^{24–26} The irradiation of a photoresponsive group generally causes a molecular rearrangement with a consequent modification of the electronic levels and light absorption allowing the visual observation of photoswitching.

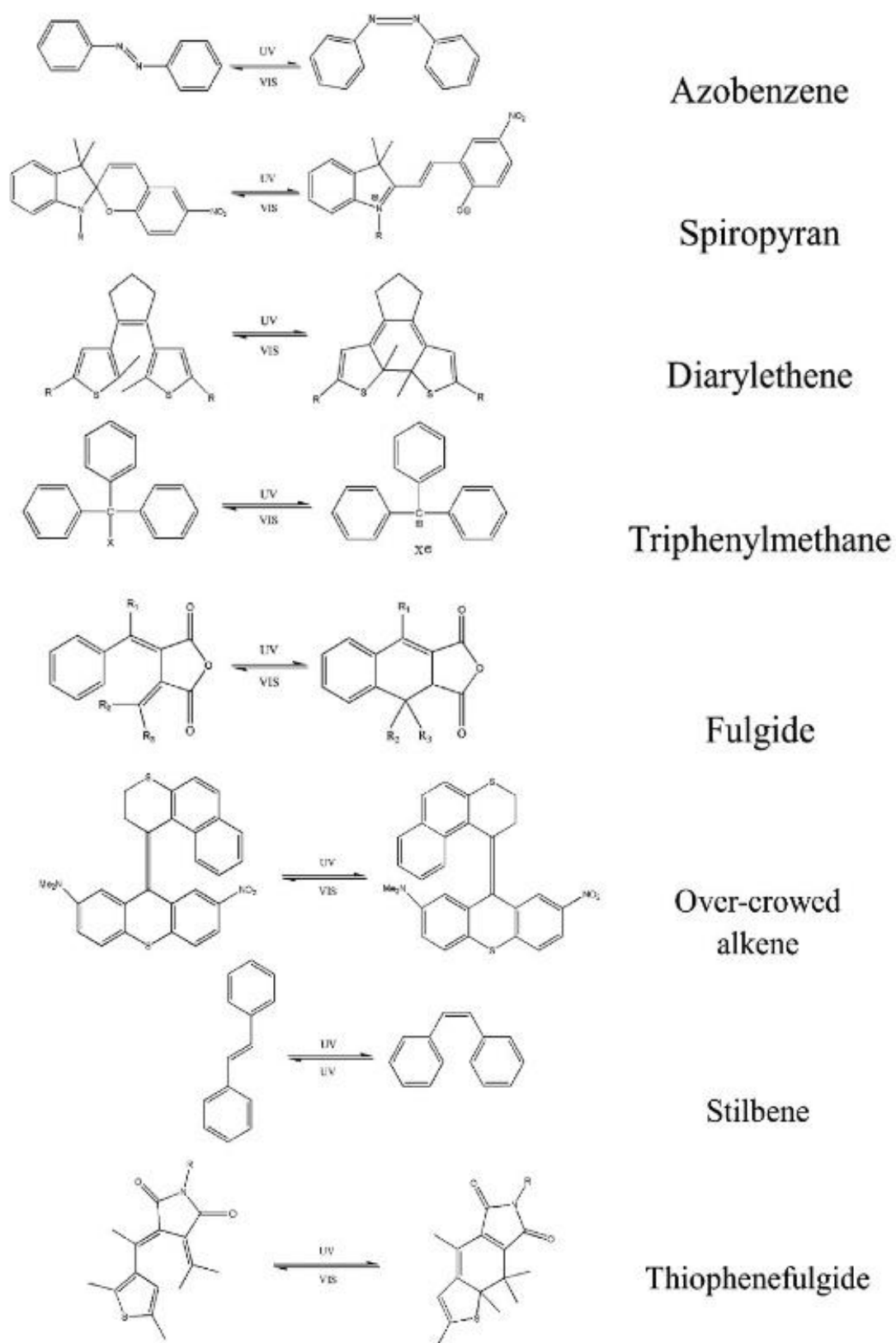
1.3.2 PHOTOSWITCHABLE CHEMICAL GROUPS

In order to make a polymer photoresponsive, a light-sensitive chemical group or molecule must be incorporated in its structure by entrapment, cross-linking, or insertion in the side chain or as a part of the main chain.²⁷

The light-induced changes in polymers are often based on a reversible isomerization upon exposure to UV or Visible (Vis) light of the chromophoric groups. The light-switchable chromophores, mostly used in light-induced changes in polymer matrices, are listed in Scheme 1. Azobenzene (Azo) and spiropyran (SP) derivatives represent undoubtedly the most commonly used chromophoric groups. Azo-derivatives can undergo a reversible isomerization from the more stable trans form to the cis form upon UV irradiation.

Heat and Vis irradiation allow the reverse reaction from cis to trans isomer, as shown in Scheme 1. The transition from the rod-shaped trans to the bent-shaped cis isomer decreases the Azo molecular length from 9.9 to 5.5 Å and increases its dipole moment from 0.5 D to 3.1 D. The different molecular geometry of the two isomers affects their electrical properties and allows the photocontrol of some properties including size, shape, wettability, swelling, solubility, adsorption, enzyme activity, sol–gel transition, permeability, and ion binding. Upon UV irradiation, SP groups can isomerize by a ring opening-reaction (Scheme 1), which leads to the reversible switching between the colorless hydrophobic ring-closed spiropyran form and the colored hydrophilic ring-opened merocyanine (MC) form. The dipole moment of SP molecule strongly changes by the formation of the zwitterionic MC structure from 4.3 D to 17.7 D.²⁸ The photoconversion from the SP to the MC form can be triggered by UV irradiation (typically at 365 nm), while SP form can be usually recovered by Vis light. The MC isomer can bind ions with a consequent color shift that allows its use as reversible chemosensor.²⁹ Photochemical induced cycloaddition reactions provide the possibility to reversibly create and break bonds between molecules.³⁰ However, reversible cycloaddition reactions in polymers are limited to a few molecules including thymine, coumarin, stilbene, and cinnamic acid for [2 + 2] cycloadditions and anthracene for [4 + 4] cycloaddition.³¹ The coumarin derivatives are known to undergo photodimerization reactions, which lead to the formation of cyclobutane rings through [2 + 2] cycloaddition, when they are irradiated with UV light with a wavelength greater than 350 nm.

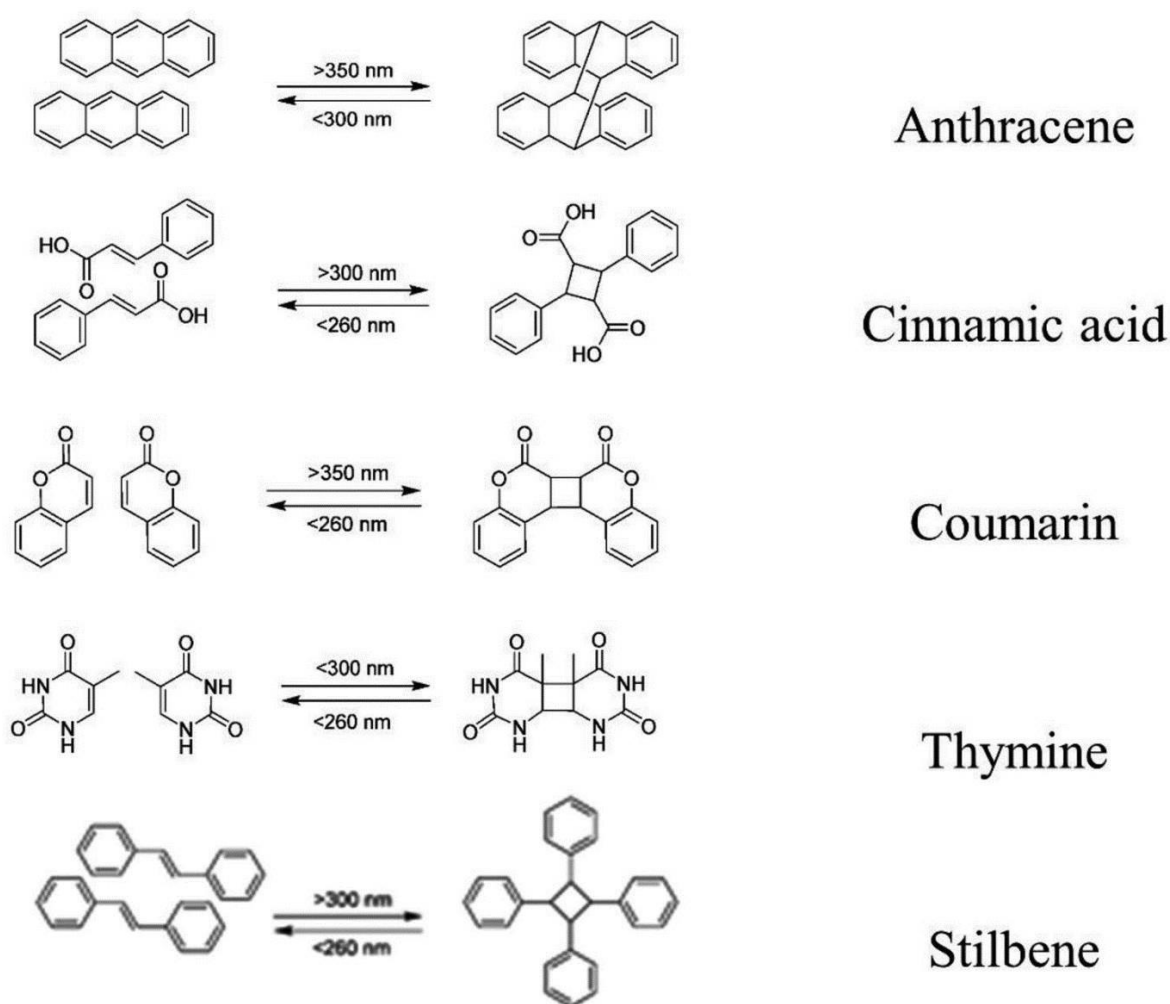
The reverse reaction is gained by irradiation with UV light at a wavelength shorter than 260 nm.³² Nevertheless, the risk of polymer damage is high, as the reverse reactions typically require high energy photons. Thus, an exciting challenge in photochemistry research is the development of catalyst-free (reversible) cycloaddition reactions driven by Vis light.³³



Scheme 1. Some light-switchable chromophores.

Typical molecules able to give reversible cycloaddition reactions are reported in Scheme 2. Schemes 1 and 2 show several light-switchable chromophores and reversible cycloaddition reactions, respectively. Despite some similarities in the previously reported molecular reactions, it is almost impossible to compare these

commonly used families of molecules in terms of their physicochemical properties such as volume change, responsive behavior (both switch and decay times), and sensitiveness, as they are characterized by different modes of action. In addition, photochemical reactions are dependent on several parameters including the nature of the molecule or polymer backbone to which the chromophore is bound, UV–Vis light intensity and frequency, exposure times, desired amount of change (e.g., percentage of variation in transmittance, release, or bending), effective free volume, environmental conditions (temperature, solvent polarity, viscosity, pH, solution, or solid state), and sample thickness. Consequently, there is no optimal photoresponsive molecule that can be used in any application.³⁴



Scheme 2. Typical moieties capable to give reversible cycloaddition reactions by UV irradiation. Reproduced with permission.³⁰ Copyright 2013, Royal Society of Chemistry.

1.3.3 PHOTOCROMIC LIQUID CRYSTALS AND PHOTOALIGNING AZO-COMPOUND DYES (PAADS)

Photochromic molecules have been applied in liquid crystal (LC) compounds and polymers to add photoresponsiveness to LC self-organization.^{35–37} Photochromic LCs are generally obtained by physical addition of small amounts of photochromic molecules or by incorporation of photochromic groups in polymer structures.³⁸ Upon light irradiation photoresponsive liquid crystalline materials can:

1. maintain their original phase;
2. transform into another LC phase;
3. undergo photoalignment or photoorientation;
4. modulate their properties such as pitch and polarization;
5. show photomechanical properties.

Photochromic LCs can undergo reversible phase transitions by light irradiation. Generally, the phase transition is due to the different compatibility of the two photoisomers within the LC matrix, which consequently decreases or increases the local order degree with a change in the phase transition temperature.³⁹

In the case of Azo-compounds, the local order change is due to the variation in the geometric size and shape of trans (long rod-shaped molecules) and cis (short bent-shaped molecules) isomers. Reversible photodisalignment or photoalignment of liquid crystals can be obtained by UV or Vis irradiation of a homeotropic photochromic layer, as shown in Figure 1.⁴⁰

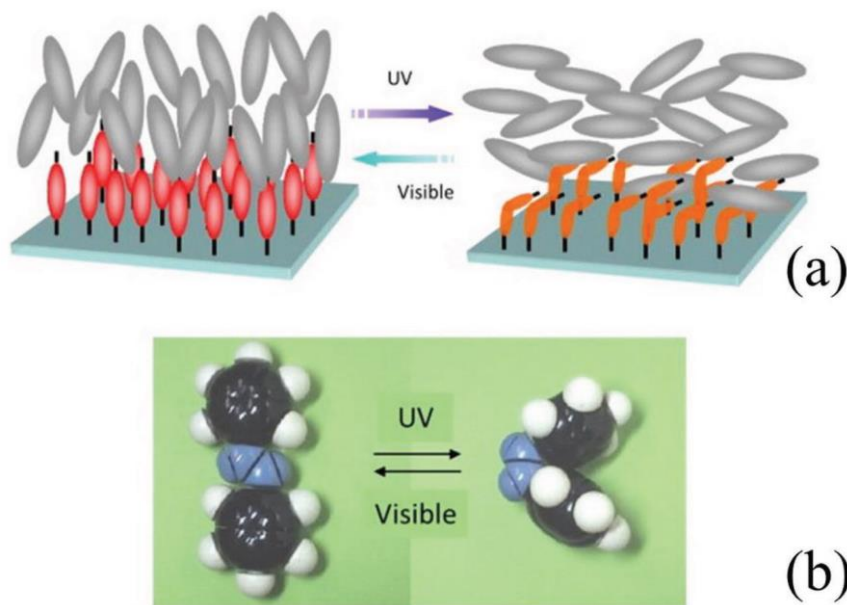


Figure 1. a) Reversible photoreorientation of a LC cell between homeotropic and random planar states upon irradiation with UV and Vis light. b) Molecular structure of azobenzene isomers. Reproduced with permission.⁴⁰ Copyright 2013, Elsevier.

One important and simple application of Azo-compounds in the last 30 years has been their use as thin films to photoalign LC.^{41,42} The PAAD have been found to be effective in the alignment and formation of high resolution patterns in LC, enabling their use as grating polarizers and spiral phase wave-plates.⁴³

The main advantages of PAADs are their extended absorption range (up to 4000 nm), the low exposure energy, and the possibility to be easily deposited over large areas.⁴⁴ The UV light causes the isomerization of photochromic layer and the LC transition from a homeotropic to a random planar state.

Common chiral LC phases, such as cholesteric LCs, blue phases, and chiral smectic C phases, display quite fascinating optical and electro-optical phenomena, including the lightdriven pitch modulation and photoinduced phase transitions by isomerization of light-responsive molecules. In addition, PAAD layers can

be used to make all-optically controlled LC modulators and phase shifters. In their work, Perivolari et al.⁴⁵ reported an optically controlled half-wave plate based on a commercially available photoaligning Azo-dye (PAAD-22D) and a twisted nematic liquid crystal cell. The irradiation of PAAD-22D layer (casted on one cell substrate) with a Vis light caused its isomerization from the trans to cis state and the switching between two perpendicular alignment states in the cell surface, resulting in a controllable polarization. In fact, the PAAD-LC cell switched from the initial planar to a final twisted state, obtaining a rewritable LC device driven only by visible light without the use of electric fields. The device controlled in an efficient way both the light transmission and polarization with a high recovery (90%) of the transmitted intensity after many twist and untwist cycles. Thanks to their reduced thickness (a few hundred nanometers) PAAD layers can be attractive to form surface relief gratings after irradiation by two interfering laser beams.⁴² Mavrona et al. studied the optical properties and photoinduced response of three different photoaligning Azo-dyes (PAAD-22D, PAAD-22E, and PAAD-22N).⁴⁶ Dyes were casted as thin films (thickness between 15 and 150 nm) by spin-coating on indium tin oxide coated glasses by dissolving PAADs in methanol. Results showed that the films were characterized by high refractive indices (between 1.6 and 1.8) and a significant photoinduced birefringence. Birefringent phase gratings were recorded with Vis light and diffraction efficiency measurements were used to monitor their temporal evolution. The time constants to record the photoinduced diffraction gratings were 5, 4, and 120 s for PAAD-22D, PAAD-22E, and PAAD-22N, respectively. The PAAD-22N films showed the highest diffraction efficiency ($\eta_{22N} \approx 3 \times 10^{-5} > \eta_{22D} = \eta_{22E} \approx 10^{-6}$). The photoinduced gratings in such thin films were found to be associated to the refractive index change rather than to the formation of a surface relief. More robust photoresponsive coatings can be synthesized from organic azobenzene dyes and polyhedral oligomeric silsesquioxanes (Azo-POSSs). Tkachenko et al. described the synthesis of a new series of branched Azo-POSS structures with different flexible spacers between the inorganic POSS cores.⁴⁷ These new hybrid materials were able to form thin and smooth films characterized by enhanced thermal, mechanical, and optical properties. In fact, thin films (≈ 60 nm) of all Azo-POSS had low refractive indices (≈ 1.46) and smooth morphologies were found by atomic force microscopy investigations in Azo-POSS films with Azo-dyes having side isolation groups into the POSS core. Morphology smoothness was possible thanks to the suppression of the crystallization and aggregation of azobenzene chromophores. Moreover, such molecules had a significant decrease in the trans–cis photoisomerization rate as the isolation groups effectively prevented the chromophores aggregation and allowed faster photoisomerization processes.^{48,49} The light absorption by a dichroic dye is dependent on its polarization, being maximum or minimum if light is polarized parallel or perpendicular to the principal axis of dyes. When dichroic dyes are dispersed in LC, the dye molecules align parallel to LC director and the light absorption can be modulated by the LC director reorientation. In addition, a loss in the local order can be obtained by the trans–cis photoisomerization of Azo-chiral dopants that induce the transition from the chiral to the achiral structure.

Wang et al. dispersed a dichroic dye in a mixture of an Azochiral dopant and a nematic LC in order to achieve three stable states (focal conic, fingerprint, and homeotropic) with different optical transmittance characteristics (opaque, attenuated, and transparent, respectively), as shown in Figure 2.⁵⁰ Switching among the three different states could be obtained by applying light with a wavelength of 408 or 532 nm. An easy

switching, acceptable contrast ratio, and low power consumption were the main advantages of such device. The initial LC cell was in a focal conic state. Irradiation with a low intensity (10 mW cm^{-2}) 408 nm laser light switched cell first in a fingerprint state and then in a homeotropic texture state when the following condition was fulfilled

$$P > 2d \frac{k_{22}}{k_{33}} \quad (1)$$

where P is the cholesteric pitch, d the cell thickness, k_{22} and k_{33} the twist and bend LC constants, respectively.

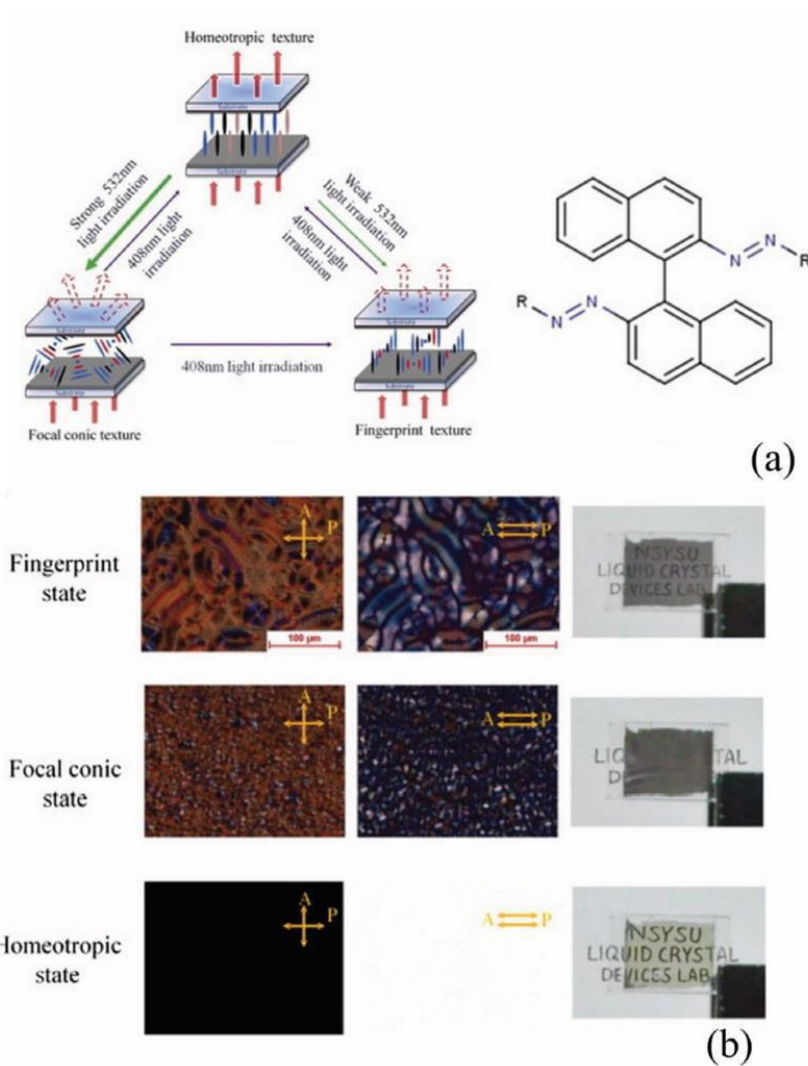


Figure 2. a) Optical switching in a tristable CLC device. b) Textures and optical transmittances in the three states. Reproduced with permission.⁵⁰ Copyright 2014, Elsevier.

The homeotropic texture relaxed back to the focal conic texture within a few hours after the 408 nm light turning off. The dye back-isomerization process to the focal conic state could be accelerated by cell irradiation with a 532 nm laser light intensity larger than 200 mW cm^{-2} . For lower intensities of 532 nm light the homeotropic texture relaxed back to the fingerprint texture. In the focal conic state, incident light was absorbed

by dichroic dye and scattered by randomly oriented cholesteric liquid crystal (CLC), while in the fingerprint state LC molecules did not scatter light as CLC helical axes were perpendicular to the incident light. In the homeotropic state both dye and LC molecules were parallel to incident light leading to a maximum transmittance value as scattering and absorption were strongly reduced.⁵⁰

1.3.4 PHOTORESPONSIVE WINDOWS

The employment of polymer networks to stabilize LCs has recently become an attractive field of research.⁵¹ Two different types of LC/polymer dispersions can be produced according to the polymer concentration. In polymer dispersed liquid crystals (PDLCs) the polymer concentration is kept in the range 20–80%. LC can form micrometer-sized droplets randomly dispersed in the polymer matrix (Swiss cheese morphology) or is dispersed in the voids and crevices of a polymer ball morphology. The refractive index mismatching or matching between LC and polymer matrix confer to PDLCs an opaque or transparent appearance due to incident light scattering. Upon application of an external field, the liquid-crystal phase reorients and film becomes transparent or opaque according to the initial LC orientation and dielectric anisotropy (direct or reverse mode PDLCs, respectively).^{52–54} In polymer stabilized liquid crystal texture polymer concentration is maintained below 10% in order to stabilize the LC (generally cholesteric) textures.⁵⁵ Yeon et al. realized a light shutter, formed by a dye-doped CLC layer and a PDLC film for simultaneous control of haze and transmittance.⁵⁶ In the opaque state it provided black color by the dye-doped CLC and hid the objects by using the PDLC film properties. By switching the light shutter placed at the back of the see-through device, it was possible to choose between the see-through mode and the high-visibility mode. In addition to the control of haze and transmittance, photochromic PDLCs can confer to smart windows self-adjusting photocontrol and color aesthetic added values.^{57,58} Debije and co-workers designed smart windows consisting of LC-based luminescent solar concentrators,⁵⁹ able to absorb sunlight and emit downshifted light. The emitted light could escape from the lightguide edges, where the attached photovoltaic cells converted the collected light into electricity. These devices were proposed as an alternative green source of electricity.⁶⁰

1.4 LIGHT-DRIVEN FUNCTIONS

1.4.1 LIGHT-DRIVEN WETTABILITY

“Wettability is the ability of a liquid to maintain contact with a solid surface, and it is controlled by a balance between the intermolecular interactions of adhesive type (liquid to surface) and cohesive type (liquid to liquid).”⁶¹ Lotus leaves, butterfly wings, gecko feet, rose surfaces, and fish scales are some beautiful examples of controlled wettability in nature,^{62,63} which inspired researchers to design new photoresponsive materials (such as inorganic materials, small organic molecules, and photoactive polymers) able to control their wettability.^{64–68} These changes are often based on the reversible isomerization of Azo or SP groups upon exposure to UV or Vis light.^{69,26} Pei et al. investigated the structure and wettability properties of photoactive Azo monolayers casted on silicon surfaces.⁷⁰ The reversible water contact angle (CA) changes are due to the photoisomerization process, which changes the dipole moment of Azo moieties during UV or Vis irradiation. Consequently, the CAs decrease due to the higher dipole moment of the azobenzene cis-

isomers,⁷¹ while wettability recovers its initial value after Vis irradiation. The photoisomerization of Azo-compounds present on surfaces,⁷² the shuttling of cyclodextrin rings,⁷³ or the release of hydrophilic guests⁷⁴ can hide or expose the hydrophobic/hydrophilic groups, resulting in the surface wettability variations.

Cyclodextrins (CDs) have been used as host molecules because of their characteristic structure with a hydrophilic exterior surface and a hydrophobic interior cavity, able to accommodate a wide range of molecules as guests.^{75,76} Azo groups do not possess photocleavage properties, but in combination with α -cyclodextrines (α -CD) may form photodissociating supramolecular complexes upon irradiation with light at 365 nm. Upon irradiation at 460 nm the Azo groups photoisomerize back to the trans species and the Azo/ α -CD complexes form again.⁷⁷ A successful example of tunable surfaces with a supramolecular Azo/ α -CD host–guest system was presented by Wan et al., who fabricated a kind of molecular shuttles on gold with reversible changes in CA of nearly 50°. The as-prepared monolayer was hydrophilic thanks to presence of CD molecules on the surface, but after UV light irradiation, the CD sliding down along the alkyl chain made the surface hydrophobic, as shown in Figure 3.⁷³ Chen et al. controlled the surface wettability of gold substrates designing a tripodal stator to fix an overcrowded alkene group, which upon irradiation exposed or hid a hydrophobic fluorinated chain. As the -CF₃ groups faced outside the surface wettability change between 60° ± 1° and 82° ± 1°.⁷⁸

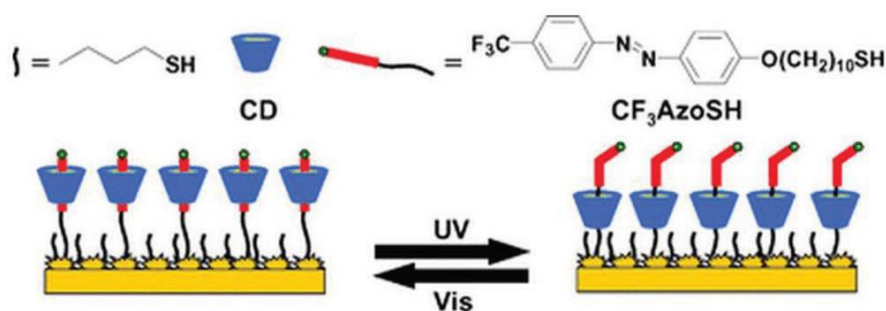


Figure 3. Photoreversible azobenzene shuttles. Reproduced with permission.⁷³ Copyright 2008, Royal Society of Chemistry.

Moreover, the wettability of Azo and SP layers can be influenced by the surface roughness and presence of aligned functional groups.^{79,80} Surface coatings with a SP-containing polymer showed large reversible and reproducible changes in wettability with difference in water CA values up to 30° (from 48° to 78°) over ten cycles.⁸¹ After 12 h in dark conditions, SP molecules recovered the pristine hydrophobic state. The reversible wettability of photoresponsive SP-containing surfaces could be enhanced by increasing the substrate roughness.⁸² Vis light responsive materials have received increasing attention in recent years since high energy UV light hinders some biomedical applications of photosensitive molecules due to their possible photodegradation.⁸³ The group of Read de Alaniz^{84,85} designed and synthesized a new class of visible light activated molecules, named donor–acceptor Stenhouse adducts (DASA). They have a unique combination of physical and chemical properties with excellent fatigue resistance and large polarity changes. The photoswitching mechanism of DASAs is based on the structural change from a conjugated, colored, opened chain, hydrophobic triene form to a zwitterionic cyclopentenone, colorless, hydrophilic form upon irradiation

with Vis light.⁸⁶⁻⁸⁸ Singh et al. grafted responsive DASAs on an amino functionalized polycarbonate film surface using a photoresponsive triene derivative of Maldrum's acid.⁸⁹ Furthermore, Balamurugan and Lee reported the synthesis of an acrylate-based polymer bearing some DASA groups as probe for the selective and real-time photodetection of diethyl cyanophosphate both in solution and vapor phase.⁹⁰ Another interesting application was proposed by Sinawang et al., who reported the synthesis of a polystyrene-based, photoresponsive polymer with DASA pendants.⁸³ Under Vis light, DASA films displayed good photolithographic performance with welldefined patterns.

1.4.2 LIGHT-DRIVEN ROUGHNESS

The surface roughness is "the local deviation of a surface from a perfectly flat plan" and can affect the properties and performance of surfaces.^{18,91,92} The surface of lotus flower leaves is kept clean by the presence of nanoscaled architectures superimposed on microscaled papillae which gives repellency toward dust particles and water.^{93,94} Such self-cleaning effects inspired researchers in the fabrication of super-hydrophobic surfaces by choosing appropriate chemicals and structures. The actual challenge is to make these surface structures switchable, i.e., able to be turned ON and OFF on demand by an external and remote trigger such as light. Different surface relief patterns were realized by introducing Azo moieties in polymers. The switching of the CA between different wetting regimes was possible by using surfaces with a nanoscale roughness and a coverage with azobenzene functional groups.^{95,96}

Yadavalli and Santer demonstrated the possibility to switch reversibly the topography of Azo-containing polymers in situ by changing the irradiation conditions.⁹⁷ The reorientation of Azo molecules along a direction perpendicular to that of the light polarization caused modifications in the orientation of polymer backbones to which the Azo moieties were attached. Macroscopic surface deformations appeared due to the strong mechanical coupling between the photoactive molecules and the polymer matrix.^{98,99}

Lomadze et al.¹⁰⁰ reported on Azo groups covalently bound to poly(methacrylic acid) brushes polymer chains, able to move freely along the light intensity gradient and create different topographies in response to light. Thus, relief gratings were obtained after photoisomerization of Azo groups with interference patterns, as shown in Figure 4. The height of the grating was controlled by irradiation time. Sample irradiation for shorter times gave patterns that could be erased by solvents, while permanent patterns were obtained with longer irradiation times because of the photochemical scission of covalent bonds and degrafting of polymer chains.

Zettsu et al. reported on liquid crystalline linear polymer systems that can generate surface relief gratings.¹⁰¹ Kopyshev et al.¹⁰² investigated in real time the lightinduced reversible changes in thickness and roughness of poly(methacrylic acid) brushes loaded with a cationic surfactant containing an Azo group in its hydrophobic tail. Under UV light irradiation ($\lambda = 365$ nm) the brush complex shrank inducing the decrease of polymer film thickness and the consequent increase of the surface roughness (see Figure 5), because the cis-azobenzene unit requires more free volume than its trans counterpart. Polymer brushes recovered their initial state under blue

light irradiation ($\lambda = 460$ nm). The contraction and expansion processes were reversible over repeated irradiation cycles and characterized by switching times lower than a few seconds.

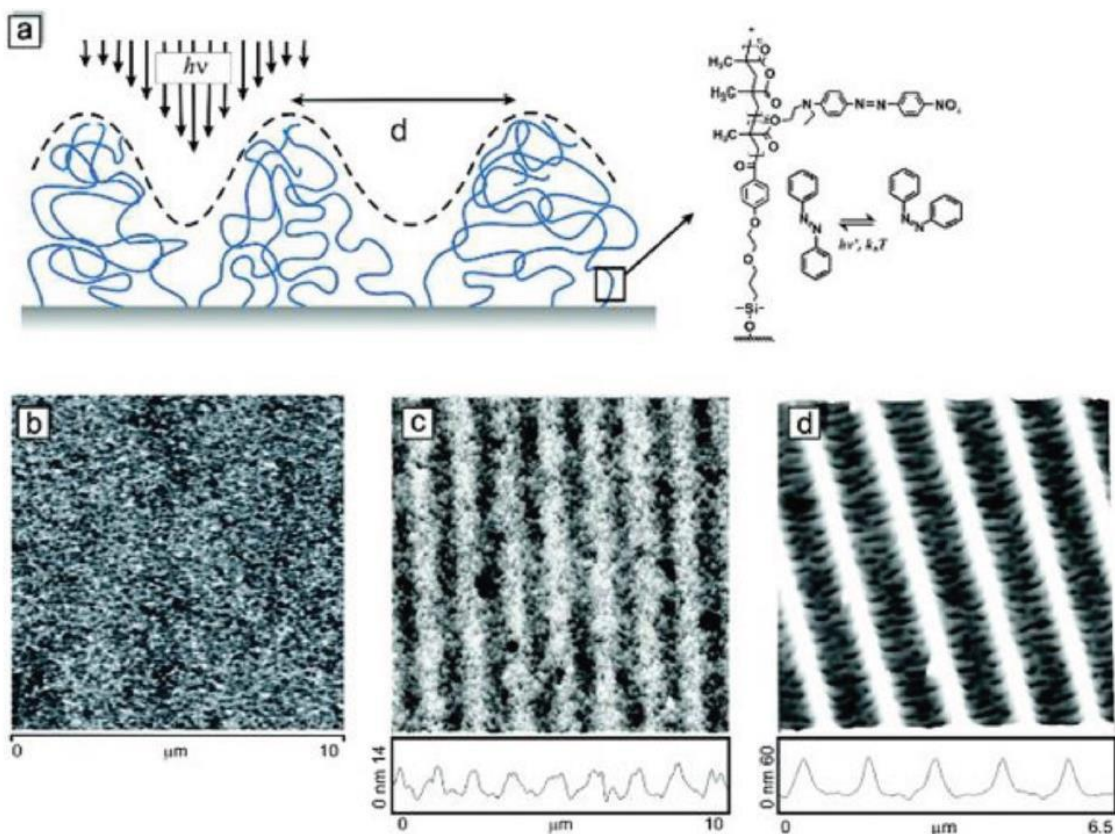


Figure 4. a) Generation of photosensitive azo-poly(methacrylic acid) brushes. b) Initial polymer layer. c,d) Brushes after 10 and 30 min of UV irradiation. Reproduced with permission.¹⁰⁰ Copyright 2011, American Chemical Society.

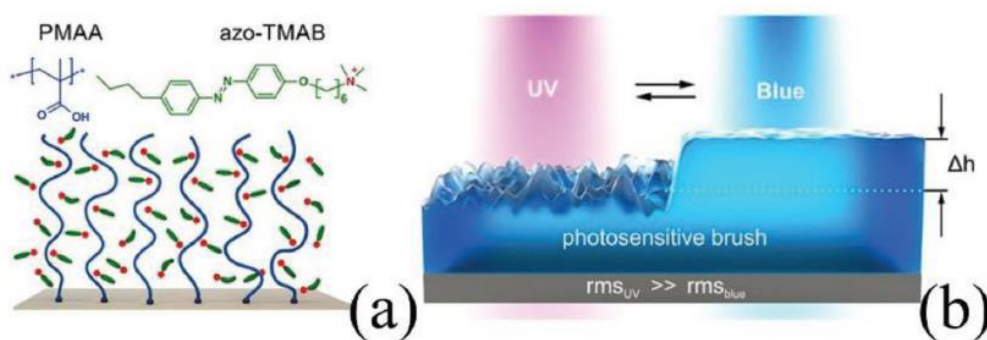


Figure 5. a) Chemical structure of polyelectrolyte brushes and cationic surfactants containing Azo groups. b) Representation of the thickness and roughness switching under UV or Vis irradiation. Reproduced with permission.¹⁰² Copyright 2016, American Chemical Society.

1.4.2.1 LIGHT-DRIVEN ROUGHNESS BY LC NETWORKS

Liquid crystal networks (LCN) consist of reactive LC photochromic monomer mixtures acting as cross-linkers and deformation triggers. The elasticity, anisotropy, stimuli-responsiveness, and molecular cooperation of LCN allow to build interesting photoresponsive surfaces.^{103–106} Generally, monomer mixtures are in situ photopolymerized after having gained a preferential alignment. UV exposure of prealigned Azo-containing

LCN changes the local molecular order and creates localized topographies without the need of complex optical setups. Several studies of Liu et al. demonstrated that the network free volume responsible for the topography formation was enhanced by the presence of Azo mesogen cross-linkers.^{107–109} They obtained permanent topography changes in Azo-LCN by adding chain transfer agents to the mixture components. By contrast, reversible surface topographies could be fabricated with normal polymerization conditions (i.e., in absence of chain transfer agents) under continuous or sequential illumination. In addition, the same authors reported on the photoformation of fingerprint textures in flat CLN coatings aligned parallel to the substrates, as shown in Figure 6. When the CLN coating was actuated by light, 3D fingerprint structures appeared as helices formed protrusions where molecules were aligned parallel to the surface, while surfaces withdrew where their orientation was perpendicular. Fingerprint-shaped protrusions disappeared when light was switched off.¹¹⁰ Zhan et al.¹¹¹ made photoresponsive azotolane-CLNs with different surface topographies, including sub-micropillars and sub-microcones arrays by using colloidal lithography techniques. These two surfaces exhibited super-hydrophobicity (CA, larger than 141°) and completely different water wettability mimicking rose petal and lotus leaf behavior, respectively (see Figure 7). The sub-micropillar arrayed film behaved as a rose petal (with a large water adhesion and a sliding angle, SA, greater than 90°), while the sub-microcone arrayed film behaved as a lotus leaf (with a large water repellence and a SA $\approx 3.1^\circ$) thanks to its hierarchical, dual-length scale morphology. Both microarrayed films showed reversible CA switching in the super-hydrophobic region under alternating irradiation with blue and green light.

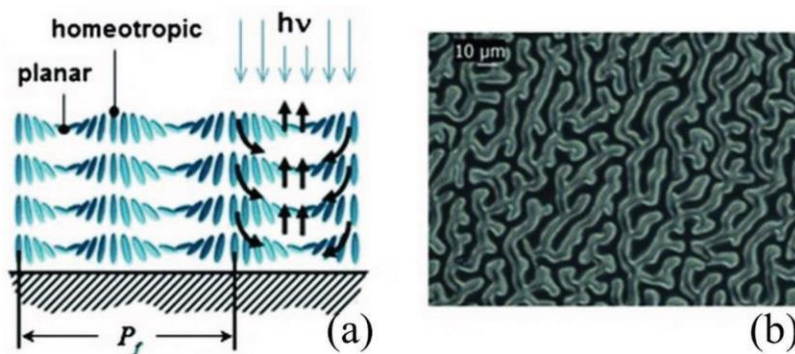


Figure 6. a) Schematic representation of fingerprints dynamics. b) Polarized optical microscopy images of a fingerprint texture as observed between crossed polarizers. Bright regions correspond to planar and black areas to homeotropic orientation. Reproduced with permission.¹¹⁰ Copyright 2014, Wiley-VCH.

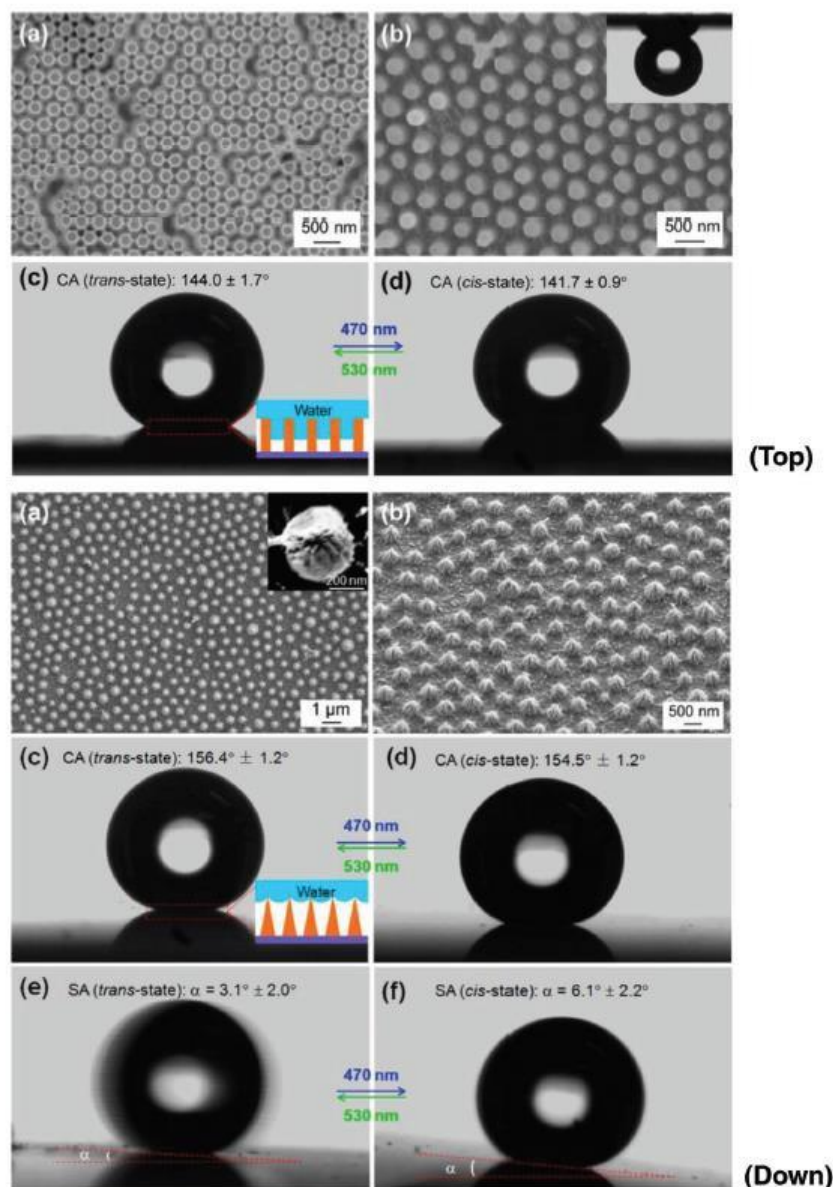


Figure 7. (Top) SEM images of a) the top view and b) at a tilt angle view of sub-micropillar arrayed film. c,d) Contacting behavior of a 5 μL water droplet on the sub-micropillar arrayed film in trans state (CA = 144.0°) and cis-state (CA = 141.7°), respectively. (Down) SEM images of a) the top view and b) at a tilt angle view of sub-microcone arrayed film. c,d) Contacting behavior of a 5 μL water droplet on the sub-microcone arrayed film in trans state (CA = 156.4°) and cis-state (CA = 154.5°), respectively. e,f) Sliding angles in the trans and cis states. The alternating irradiation time for blue light (470 nm, 120 mW cm^{-2}) and green light (530 nm, 30 mW cm^{-2}) was 120 s in both cases. Reproduced with permission.¹¹¹ Copyright 2015, American Chemical Society.

1.4.2.2 LIGHT-DRIVEN ROUGHNESS BY SKIN BILAYERS

Reversible light-responsive patterns were created by using surface wrinkles of a stiff skin bound to an elastomeric substrate. A reversible variation of wettability was observed as a consequence of the dramatic changes in surface roughness.^{112,113} Near-infrared (NIR) wavelengths represent an efficient approach to tune spatially and temporally the surface features with the advantages of ultrafast response, controllable operability, and region selectivity.¹¹⁴ Li et al.¹¹⁵ obtained novel NIR-light-responsive dynamic wrinkle patterns by using a

bilayer system formed by a substrate of polydimethylsiloxane (PDMS) elastomer doped with single-walled carbon nanotubes (CNTs) and a top stiff layer of functional polymers. Upon exposure to NIR-radiation, photoswitchable wrinkle patterns formed as a consequence of the high photon-to-thermal energy conversion by CNTs, which caused the expansion of the elastic CNT-PDMS substrate. Reversible transitions from the wrinkled state to the wrinkle-free state were obtained by turning ON or OFF NIR light (see Figure 8). These NIR-responsive dynamical wrinkles could be used to prepare dynamic light gratings, no-ink displays, and NIR-controlled electronics. The NIR-driven wrinkling strategy could be exploited by the introduction of other NIR-responsive materials into the elastic substrate (e.g., graphene, metal nanoparticles, organic dyes, and conjugated polymers) and the use of more versatile elastic substrates such as liquid crystalline elastomers.^{116,117}

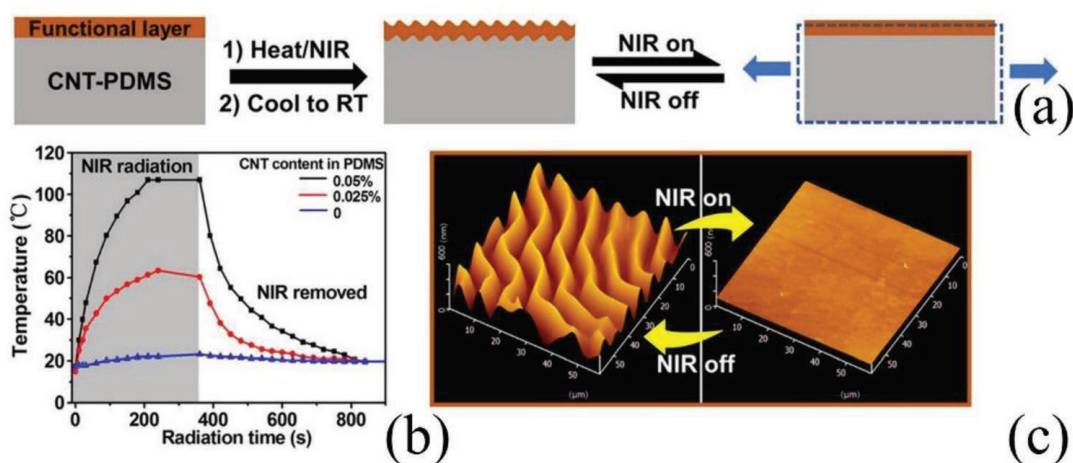


Figure 8. a) Fabrication process of NIR-driven dynamic wrinkles. b) Temperature variation in CNT-PDMS substrate during NIR ON or OFF switch. c) Atomic force microscopy images to test reversibility of NIR-driven wrinkles. NIR intensity was $\approx 1.5 \text{ W cm}^{-2}$. Reproduced with permission.¹¹⁵ Copyright 2018, American Association for the Advancement of Science.

1.4.3 LIGHT-DRIVEN ACTUATION

A light-driven actuator is a device component that under the application of a light signal responds by converting the stimulus energy into motion. Therefore, light-responsive polymer films can find application as actuators of the electromagnetic radiation energy.

The simplest light-responsive actuator is a bilayer formed by a light-responsive polymer casted as an active layer on a passive layer¹¹⁸ or added by postpolymerization modification of polymers.¹¹⁹

In this frame a film of the light-responsive polymer, poly[di(ethylene glycol)methyl ether methacrylate-co-4-(4-methoxy-phenylazo) acrylate], was physically adsorbed onto the surface of a polypropylene fabric, acting as passive layer.¹²⁰ The functional polymer composite promptly responded to UV stimuli and showed reversible shape (bending) transitions, due to the volume constrictions in the active layer. Similarly, Kim et al. synthesized polynorbornenes with Azo-based dendron side chains, which upon irradiation with UV light expanded and bent away from the light source.¹²¹

1.4.3.1 LIQUID CRYSTALLINE ACTUATORS

Even if cumbersome synthetic routes are required, the majority of light-responsive actuators consists of liquid-crystalline Azo moieties aligned along one direction in flexible matrices.^{122,123} The development of light-driven liquid crystalline materials has exploited in the last years by the design and synthesis of new molecules and the study of particular photoinduced phenomena and properties such as phase transitions, alignment, orientation, polarization, pitch modulation, and deformation. Ultraviolet, visible, and infrared light can drive these materials, which are often the result of a fascinating combination of photochromism, liquid crystallinity, experimental techniques, and fabrication additives.

Liu et al. prepared light-responsive films and fibers with reactive linear liquid crystal polymers bearing Azo, which curled toward the incident light direction (at 405 or 445 nm) and reverted to their initial state through heating or light irradiation at 530 nm.¹²⁴

Gelebart et al.¹²⁵ reported on a rewritable polymer film that could generate various shapes upon Vis light irradiation.

The LCN film contained a pH- and light-responsive azomerocyanine dye that could be locally converted into the hydroxyazopyridinium form by an acid treatment. The order reduction in the LCN imparted by photoisomerization and photothermal effects led to anisotropic shape changes. The use of azobenzenes to achieve light-induced surface topographies has some limits such as reduced polymer lifetime due to the characteristic UV absorption of Azo groups and the undesired yellow-color of coatings. It has been shown that it is possible to design opportunely linear Azo polymers to overcome these drawbacks.¹²⁶ Nevertheless, an ambitious goal is to synthesize light trigger molecules,¹²⁷ which can respond to natural light sources.

Kumar et al.¹²⁸ incorporated a photopolymerizable orthofluoroazobenzene into a nematic polymer network to develop a Vis light responsive soft actuator based on LCN. The resulting film displayed an autonomous oscillation upon exposure to sunlight or the combined light of blue and green light emitting diodes (LEDs), as shown in Figure 9.

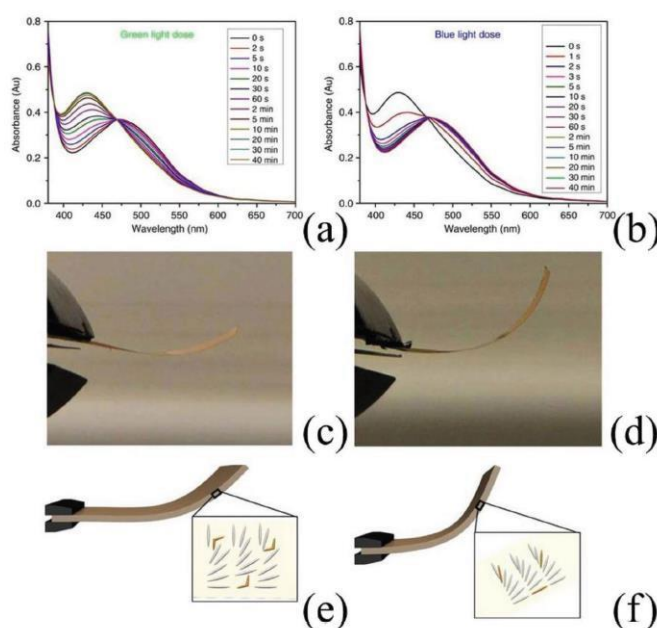


Figure 9. a,b) UV–Vis absorption spectra of the planar aligned polymer film as a function of illumination time after exposure to light of 530 and 405 nm, respectively. c,d) Splay-oriented film after illumination by light wavelengths of 530

and 405 nm, respectively. e,f) Representations of the film molecular order, after exposure to light of 530 and 405 nm, showing the mesogen (grey) and Azo molecules (orange), respectively. Reproduced under the terms of a CC-BY license.¹²⁸ Copyright 2016, The authors, published by Springer Nature.

Moreover, these polymers are attractive as self-propelling actuators for self-cleaning coatings and surfaces powered by sunlight, being able to prevent adhesion of particles and (bio) chemicals in outdoor applications. Ikeda's group¹²⁹⁻¹³⁴ fabricated LC polymer films using mono- and di-acrylates containing Azo groups, able to fold along the same direction of a linearly polarized light. The authors evidenced that the bending intensity and rate were dependent on the polymer cross-linking degree and initial alignment of the Azo groups. In fact, Azo-monodomains folded only when the light polarization was parallel to the alignment direction of mesogenic azo-groups, while in polydomains the folding took place along all the light polarization directions (see Figure 10).

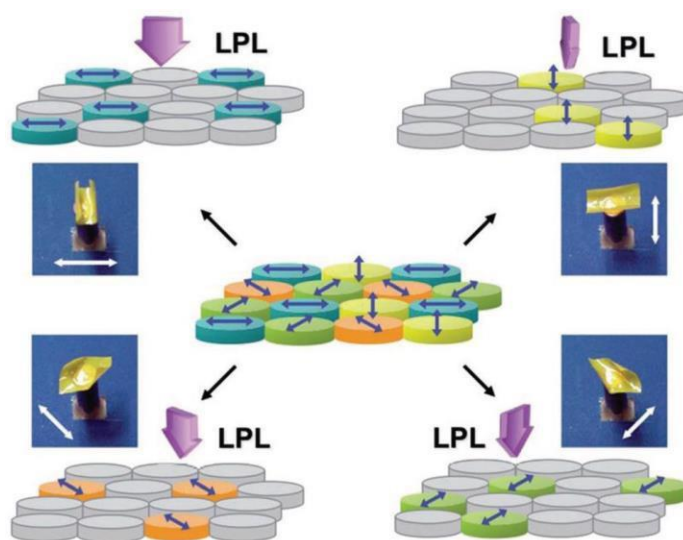


Figure 10. Precisely direction-controlled bending of polydomain films induced by linearly polarized light (LPL). Reproduced with permission.¹³⁴ Copyright 2011, Elsevier.

This entailed a contraction of the film surface with homogeneous orientation and an expansion of the film with homeotropic orientation.

The light-induced folding was explained considering the large absorption extinction coefficient and the reduction of the long range orientational order of the azobenzene chromophores in the upper surface of irradiated film, which caused a volume contraction on the film surface (see Figure 11).¹³⁰

LC polymers can respond to light through the reversible change in their order parameter, which can induce mechanical deformations.¹³⁵ Polymer films with hierarchical order in 3D can give rise to more complex and macroscopic deformations through the use of patterned alignment layers in combinations with polymerizable LC. They have been proposed as components for light-driven belts, cones, and oscillators.^{131,136,137}

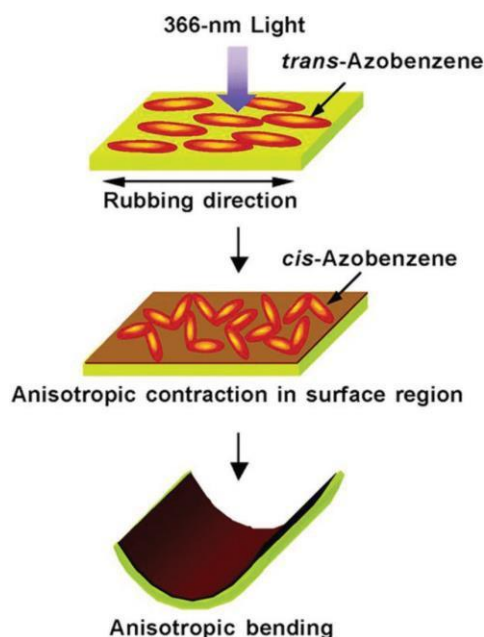


Figure 11. Anisotropic volume contraction in the surface region and consequent anisotropic bending. Reproduced with permission.¹³⁰ Copyright 2004, American Chemical Society.

1.4.4 SHAPE MEMORY POLYMERS

Shape memory polymers are a particular class of shape-shifting polymers, able to temporarily fix and later recover on demand some programmed shapes.^{138,139} A plastic polymer is a permanently reshaping polymer without macroscopic melting.¹⁴⁰ Plasticity may be triggered by heat or light exposure.^{141,142} Liu et al.¹⁴³ proposed a simple strategy for the self-folding of 2D polystyrene sheets into 3D objects using light. They could temporally and spatially control the sequence of shape transformation to generate multiple and complex shapes from the same starting material. The surface of polymer sheets was printed with ink, which discriminately absorbed light. Hinges of different colors printed onto the same sheet fold sequentially depending on the used light wavelength, as shown in Figure 12.

The absorbed light gradually heated the underlying polymer and caused the strain relief inducing folding. Another example of polymer light responsive shape shifting was presented by Iamsaard et al.¹⁴⁴ They designed spring-like materials combining the asymmetric deformation of thin films of LC polymer networks with a differential stiffness that ran through the film thickness. The UV induced structural changes at a molecular level converted into large-amplitude shape variation as a function of cutting directions, as shown in Figure 13. The springs returned to their initial shape in ambient light conditions. Irradiation with Vis light accelerated the shape recovery.

Nanomotors and micromotors are small-scale devices, able to respond to specific stimuli with particular mechanical movement(s) such as rolling, rotation, contraction, shuttling, or a more general collective behavior.¹⁴⁵ UV or Vis radiation is the most appealing fuel for small scale-motors being light a renewable contactless green energy source. The usefulness of wettability control has been demonstrated in the macroscopic transport of a liquid across a surface. The remote control of wettability could provide a gentle and cheap alternative to expensive microscopic pumps and strong electric fields in lab-on-a-chip applications.¹⁴⁶

Ichimura et al. were able to induce reversible motion of an olive oil droplet with a diameter of several millimeters by UV radiation.¹⁴⁷ They coated with an Azo-terminated calix[4]resorcinarenes monolayer the inner surface of a glass tube and observed light-driven droplet migration upon asymmetric irradiation. As the olive oil interacts more favorably with the fully extended trans alkyl chains of calix[4]arene molecules, the formation of more trans-calix[4]arene on one side rather than on the other side caused the movement of the droplet away from the cis-rich regions. When the olive oil was replaced with a liquid crystal, the choice of the direction and intensity of the light gradient allowed the control of the motion direction.¹⁴⁸

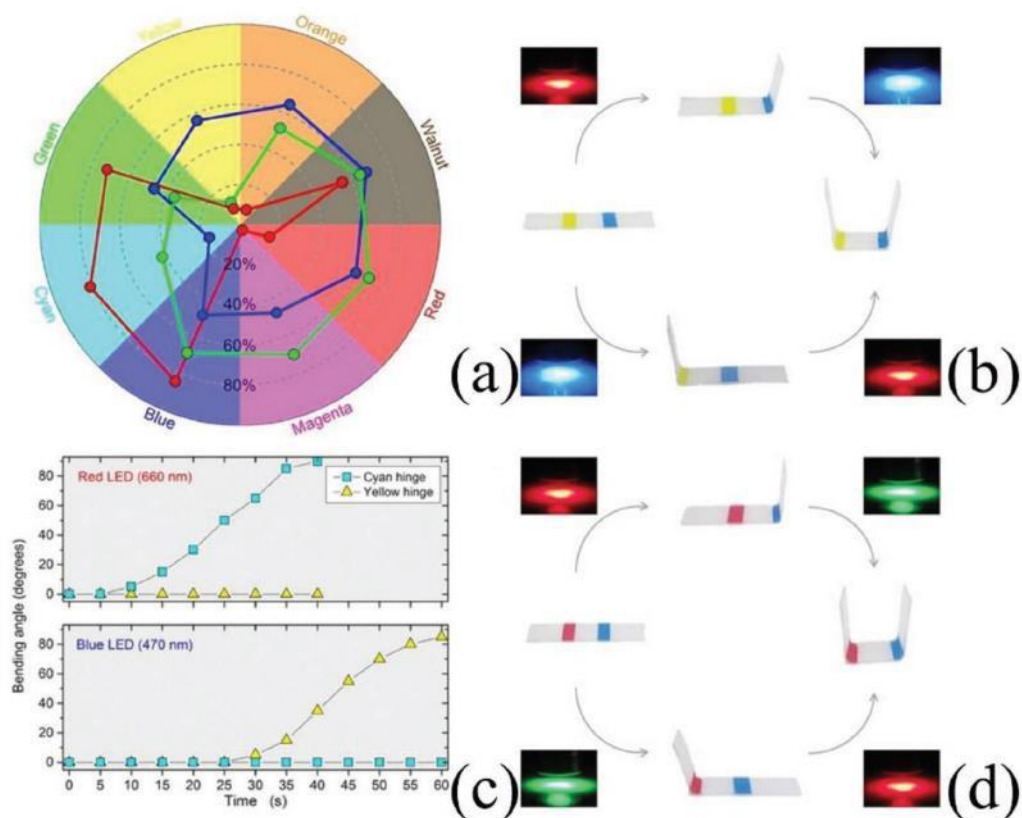


Figure 12. a) Radar plot for used ink colors. b,d) Controlled folding of polystyrene sheets by using different hinges in response to different color LEDs. c) Bending angle as a function of LED exposure time for yellow and cyan hinges under the exposure of red and blue LEDs. Reproduced with permission.¹⁴³ Copyright 2017, American Association for the Advancement of Science.

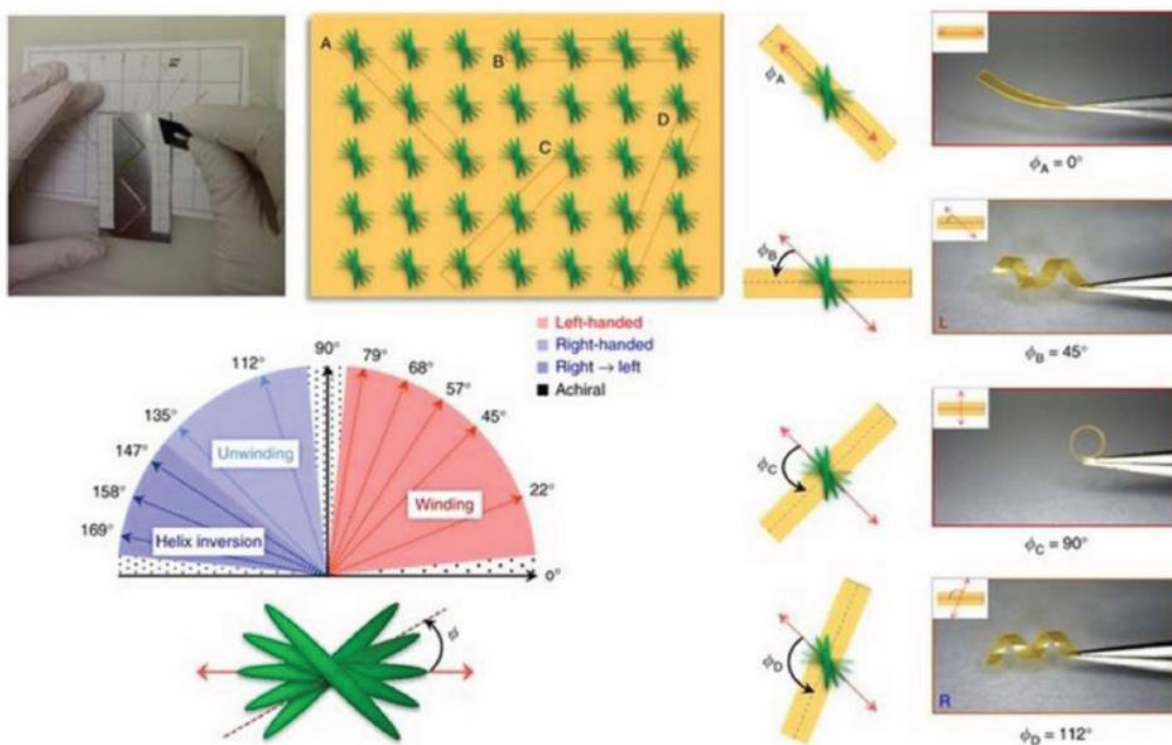


Figure 13. Polymer spring shapes as a function of the cutting angle ϕ . Reproduced with permission.¹⁴⁴ Copyright 2016, Springer Nature.

1.4.5 PHOTORESPONSIVE HYDROGELS

In recent years, microfluidic devices have been the subject of intense research activity as they can allow complex measurements through miniaturized processes.[149,150] Photosensitive hydrogels can be composed by either photoactive chains[151] or thermosensitive hydrogels mixed with dyes, acting as photothermal converters.¹⁵² If photosensitive gels exhibit a LCST phase transition, the irradiated area shrinks after having reached the LCST and results in dampening of heat generation. When the cooling, due to the surrounding environment, overcomes the light heating, the shrunken hydrogel starts to reswell once it has reached a temperature below the LCST, resulting in the increase of heat generation, which will promote an autonomous oscillation.

Narita and co-workers investigated photoresponsive behavior of thermosensitive hydrogels with LCST and containing carbon black. Both experimental results and numerical simulations confirmed that photosensitive gels with hysteresis can selfoscillate under stationary light.¹⁵³

Sugiura et al. developed spirobenzopyran-functionalized poly(N-isopropylacrylamide) (pNIPAAm) gels allowing for realtime pathway opening and enhanced flow photocontrol.¹⁵⁴

Delaney et al.¹⁵⁵ showed that hydrogels allow the flow rate control in microfluidic channels. Valve structures were created using photoresponsive SP-functionalized pNIPAAm hydrogels photopolymerized around pillar structures within the channels. The set up was highly stable over several hours of constant operation with no drift in the flow rate.

Similarly, Coleman et al.¹⁵⁶ were able to regulate the flow rate of a pNIPAAm valve by irradiation with a pulsating LED light, which kept the valve state intermediate between a fully opened and a closed state. The flow rate depended on the ON/OFF frequency and pulse duration of LED source.

However, one should consider that hydrogel-based valves have three main limitations:

1. hydrogels are soft materials with limited values of pressure they can withstand;
2. valve materials are in direct contact with fluid medium and could absorb or release components present in the fluid, during swelling or shrinking steps;
3. hydrogels are generally limited to water-based media.

In this regard, tremendous improvements have been reported by reducing the valve operation time, decoupling the valve from the analytical fluid placing a flexible protective membrane between the valve and sample, and using an external reservoir for the valve hydration, thus solving the contamination issue.¹⁵⁷

Among the various methods used to move the fluid through the channel,^{158–160} systems able to mimic peristaltic motion in response to light have aroused much interest.^{161,162} This movement has been recently studied by Francis et al.¹⁶³ who placed onto a ratcheted surface a bipedal hydrogel walker, based on pNIPAAm-co-acrylated spiropyran-co-acrylic acid p(NIPAAmco-SP-co-AA) able to shrink and swell in aqueous environments, when exposed to light. The actuation of the bipedal gel produced a walking motion in a unidirectional fashion (see Figure 14).

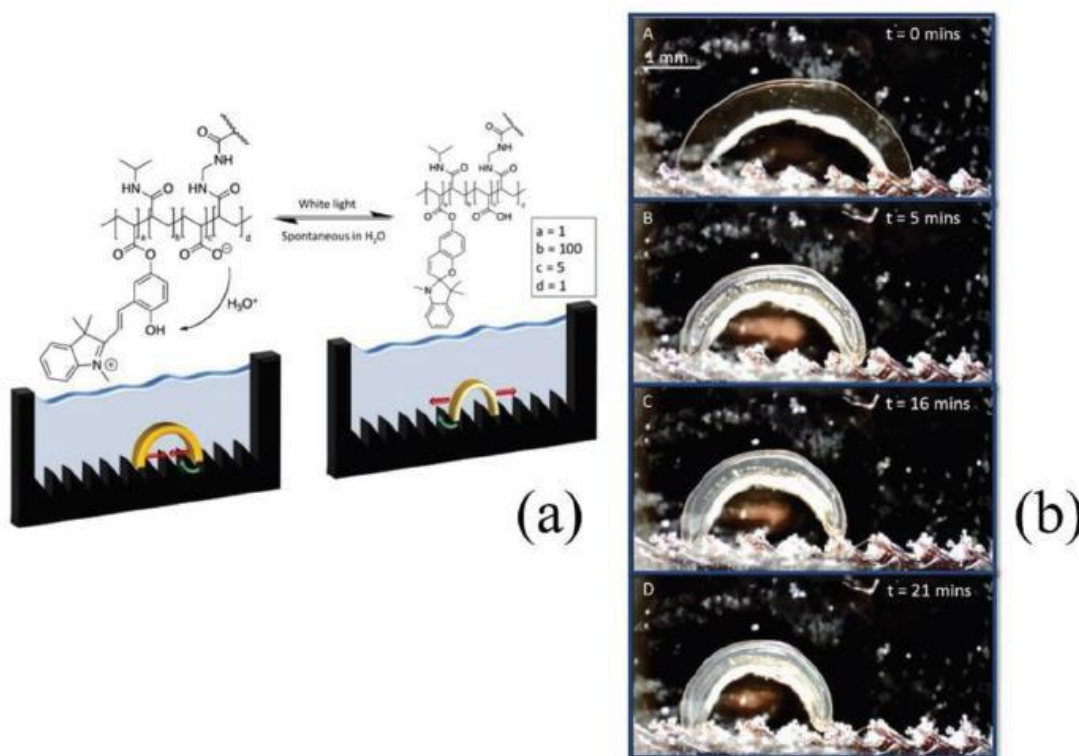


Figure 14. a) p(NIPAAm-co-SP-co-AA) photoswitchable mechanism. b) Snapshots showing the behavior of a hydrogel walker. Reproduced with permission.¹⁶³ Copyright 2017, Elsevier.

1.4.6 PHOTOTHERMAL EFFECTS

Interesting photoresponsive materials can be obtained from polymer/carbon nanocomposites.¹⁶⁴ The inclusion of carbon nanoparticles, nanotubes, and nanosheets in polymer membranes allows a high localized photothermal effect, due to the optical absorption by carbon atoms and fast thermal energy dissipation in the polymer film.^{165,166} These polymer/carbon nanocomposites can be used as optomechanically deformable materials.^{167–169} Pimentel-Domínguez et al.¹⁷⁰ studied the photothermal response of polydimethylsiloxane/carbon nanoparticle films (PDMS/CNP) as a function of several parameters including the concentration of carbon nanostructures, polymer material, membrane geometry, and dimensions. The change in heat generation and membrane conduction was evaluated for the application of these films as microfluidic devices and thermal-responsive coatings. In particular, the authors investigated boiling flows in microchannels as prototypes of efficient cooling systems to be applied in microelectronics.¹⁷¹ Experimentally, they produced two-phase flows in microchannels by evaporating water inside a glass capillary coated with PDMS/CNP, which was heated with a laser light (see Figure 15). Different flow regimes were produced, including the optimal bubbly flow regime, by adjusting the flow rate inside the capillary and the laser optical power. In fact, the bubbly flow represents the optimal compromise between a good heat removal and a satisfactory flow. Photothermal effects of PDMS/CNP coatings were tested on optical fiber Bragg grating (FBG),¹⁷² in order to realize optically tunable fibers as alternative to devices activated by electrooptic effects. The irradiation of PDMS/CNP coatings with a uniform 975 nm IR laser shifted the reflection peak of the FBG spectrum of ≈ 0.170 nm (equivalent to a local increase in temperature of about 16.8 °C) for the maximum used power. Finally, thin layers of CNP were embedded immediately underneath the polymer surface and allowed for etching the PDMS surface with improved resolution.

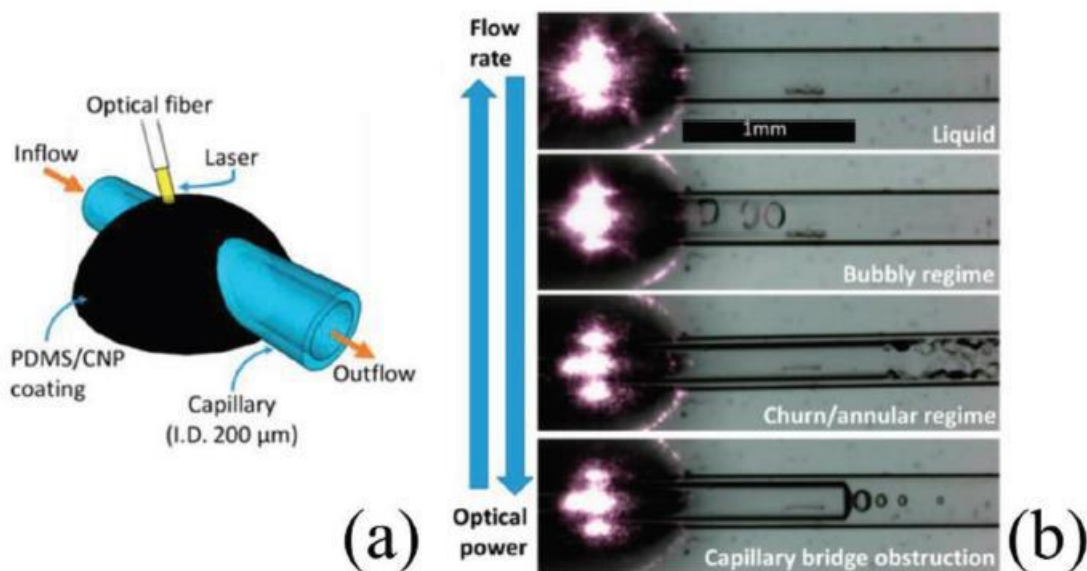


Figure 15. a) PDMS/CNP coatings for boiling flows. b) Different flows obtained by adjusting the flow rate and optical power. Reproduced under the terms of a CC-BY license.¹⁷⁰ Copyright 2016, Multidisciplinary Digital Publishing Institute (MDPI).

1.5 LIGHT ADAPTIVE GATES

Gating is the ability of smart nanochannels to open and close in response to external stimuli in a similar way to biological ion channels. Selective and programmable mass transfer (including ions, liquids, and gases) represents an important way to create several customized nanovalves, which have potential for applications as drug delivery, signal transduction, optical switches, and nanofluidic systems.¹⁷³ Blockage, surface charge distribution, wettability, and geometry are some properties of the inner surface that can control gating.

The selection of materials and fabrication technologies to prepare synthetic nanochannels is influenced by their specific application requirements. Two different approaches can be used to design smart photoresponsive nanochannels: the direct fabrication with functional materials or the functionalization of the inner surfaces or pore orifices of channels.¹⁷⁴ Photosensitive nanochannels have been successfully developed by using several photoresponsive molecules such as spiropyrans, azobenzenes, and porphyrins.^{175–179} The photoinduced variation of diameter, wettability, and surface charge in nanochannels can effectively control the transport of ions and molecules across the membrane nanochannels.^{180,181}

Upon irradiation, the chromophores can switch either between the trans and cis isomers (stilbenes, azobenzenes, and hemithioindigos) or interconvert between closed and opened forms (diarylethenes, spiropyrans, and fulgides) and the resulting geometry change can control mass and ion transport.¹⁷³

1.5.1 PHOTORESPONSIVE POLYMER NANOCHANNELS

Block copolymers with microphase separated structures are interesting molecular systems for the fabrication of heterogeneous and homogeneous light-responsive nanochannels. Soberats et al. photocontrolled the conductivity in ion channels by azobenzene liquid crystalline moieties irradiated with linear polarized light.¹⁸² The authors achieved a photocontrollable 2D ion-transporting membrane by homeotropic orientation of the ionic layers in a smectic LC imidazoliumbased material, bearing azobenzene groups. The as-obtained film was characterized by anisotropic ion transport along the directions perpendicular to the smectic layers and reversibly changed its alignment and transport direction upon irradiation with linearly polarized light, as shown in Figure 16. Membranes with nanochannels can find applications in water or gas purification as their high porosity, narrow pore diameter distribution, and tunable physicochemical properties guarantee high permeability and selectivity.^{183,184} In addition, the photoresponsive gas permeability by photochromic modified membranes shows potential use as nanovalves in microreactors for light-controllable addition of reactants and removal of products. Weh et al.¹⁸⁵ described the photoswitchable gas permeation through zeolite-hosted Azo-modified membranes. The change in gas permeation through these host–guest composite membranes depended on the irradiation wavelength, membrane quality, and amount of adsorbed azobenzene. Gas permeation was higher when Azo was in the trans-form and, consequently, decreased under photoirradiation. The original permeability could be reproduced under dark conditions. Similarly, mesoporous silica glasses modified with photochromic spironaphthoxazine suppressed the gas permeation of gaseous N₂ and CO₂ after photoisomerization to the merocyanine form.¹⁸⁶

In the work of Fujiwara and Imura,¹⁸⁷ the Azo substituents were grafted to an anodized alumina membrane to achieve a photoresponsive nanoporous system able to regulate the permeation of water under the simultaneous

UV and Vis irradiation (from 300 to 600 nm) for 10 min. Water did not permeate if the membrane was irradiated only with UV (around 350 nm) or Vis (around 440 nm) light. Furthermore, this membrane allowed the purification of feed water, because dyes, proteins, and salts dispersed in the feed were not involved in the photoinduced permeation. Less than 0.01% of salt content permeated through the membrane if a 3.5% NaCl solution was used as model seawater, confirming the great potential of such devices to seawater desalination and water purification by solar energy.^{188,189}

The pore hydrophilicity plays a key role in the transport of ion water solutions across microchannels.^{175,190} Vlassiok et al.¹⁸¹ and Kumeria et al.¹⁹¹ confirmed that smart nanoporous membranes provide the possibility to control on demand the molecular transport and separation selectivity for various advanced applications.¹⁹² Multiresponsive nanochannels, mimicking the functions of biological ion channels, play an important role in life sciences for their real-world applications as molecular filters, biosensors, and nanofluidic devices. Zhang et al.¹⁹³ modified with spiropyrans single nanochannels, which behaved as light-gated and pH-controlled nanofluidic diode systems, with current rectification features. They produced a single conical nanochannel with a base side of ≈ 350 nm and tip side ≈ 12 nm in the middle of a 12 μm thick poly(ethylene terephthalate) membrane functionalized with spiropyrans. Under UV light irradiation (365 nm) and at pH 7, the gate was in an opened state and the current flowed from the tip to the base, analogously to a diode. In dark conditions, the nanochannel switched into a closed state (due to change of configuration) and behaved as a resistance. At pH 3, the situation (and the diode) was reversed. The neutral SP form was hydrophobic and the channel was in the closed state, while the MC ring-opened form was in a hydrophilic state after irradiation with UV light.

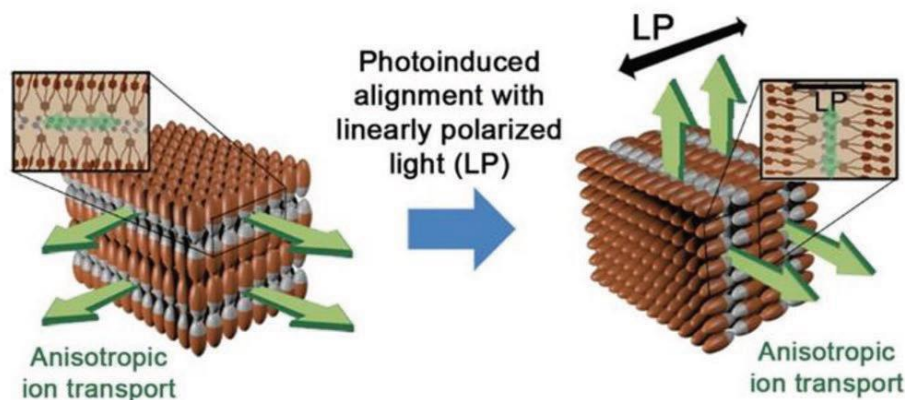


Figure 16. Photoinduced reorientation of smectic layers and resulting anisotropic ion transportation change. Reproduced with permission.¹⁸² Copyright 2014, American Chemical Society.

The channel was cation-selective at pH 7 because of the negatively charged form. On the contrary, at pH 3, the channel became anion-selective. Wen et al. functionalized the interior surface of a conical nanochannel with a malachite green derivative to create an efficient and reversible ionic gate activated by pH and light.¹⁹⁴ The single conical nanochannel was prepared in a 12 μm thick polyimide membrane. The nanochannel was in OFF state after modification with the malachite green derivative, which was neutral and hydrophobic. After pH lowering or UV irradiation, the nanochannel gate opened because the inner channel surface had become

positively charged due to hydroxide ions release. The OFF state was recovered by putting the positively charged system in an alkali environment or storing the system in dark conditions. Xiao et al. obtained a multiresponsive ionic gate incorporating 8-hydroxypyrene-1,3,6-trisulfonate on the inner surface of a track-etched single conical nanochannel.¹⁹⁵ pH and UV light could activate separately or cooperatively the gate. The inner surface of nanochannels was first grafted with ethylenediamine via a coupling reaction with 1-ethyl-3-(3-dimethylaminopropyl) carbodiimide and N-hydroxysuccinimide. Then, the 8-hydroxypyrene-1,3,6-trisulfonate was assembled onto the ethylenediamine-modified nanochannel by electrostatic interactions. UV irradiation or an increase of environmental pH transformed the surface charge of nanochannels from neutral to negative and the smart nanochannel switched from a nonselective state to cation-selective state. The channel could recover the nonselective state after pH lowering or UV switching off. The switchable changes could be maximized when UV and pH operated simultaneously.

1.5.2 PHOTOCLEAVABLE DEVICES

1.5.2.1 PHOTOACID GENERATORS (PAG)

PAG are commercially available molecules used in microelectronics, able to undergo photolysis by UV light and form an acidic moiety. Ikbal et al. used PAG to impart photoresponsiveness to surfaces. They exploited the ability of ferrocene and ferrocenyl derivatives to undergo chemical modifications in the presence of light and designed new PAGs based on 1-acetylferroceneoxime (1-acetylferroceneoxime-polycaprolactone), and demonstrated its controlled wettability. Before UV irradiation the surface showed a CA $\approx 145^\circ$ indicating that the surface was hydrophobic. UV light irradiation (≥ 365 nm) changed the surface wettability (CA $\approx 35^\circ$) and caused the polymer decomposition with the photogeneration of polar $-\text{CO}_2\text{H}$ groups.¹⁹

1.5.2.2 LAYER-BY-LAYER (LbL) FILMS

LbL technique is based on the electrostatic interactions between materials with opposite charges and can be obtained by dip-coating, spin-coating, spray-coating, and flow-based techniques.^{196,197} Dip-coating technique is carried out by immersing substrates alternately in different solutions containing positive (polycations) and negative species (polyanions). Uniform photoresponsive films can be obtained by multilayer films assembled using the above-described LbL techniques. Pennakalathil and Hong developed a double LbL film composed by a thin (1–5 layers) film of poly(acrylatemerocyanine) and poly(diallyldimethylammonium, which served as photodelamination substrate for a second thicker (several tens of layers) film.¹⁹⁸ Under white light irradiation in water, the photoconversion of negatively charged MC to the neutral SP form in the thinner LbL film caused the disassembly of the first layers and detachment of the second film. Following this idea, Campos et al. investigated the photoinduced disassembly using Vis light of a LbL film made with bilayers of poly(allylamine hydrochloride) and photochromic norbornene polymer bearing merocyanine side groups.¹⁹⁹ Such films were able to disassemble under photoirradiation with white light, due to the photoconversion of the MC molecules from their zwitterionic opened form to the neutral SP closed form. A 5 bilayers film with an initial thickness of 165 nm was disassembled to a thickness of 11 nm after white light irradiation for 22 h. Therefore, SP-functionalized polymers were suggested in the production of photoresponsive capsules for the photocontrolled release of therapeutics in targeted areas.

1.5.2.3 PHOTODIMERIZATION REACTIONS

Photodimerization is an interesting photoreversible reaction for its applications as photoresists, self-healing materials, nanocarriers, and responsive polymers.^{30,200} In addition, dimerizations can be considered green chemistry reactions because photons do not leave residues and reactions can take place at room temperature and even in the solid state.^{201–203} Photodimerization reactions have been applied for the fabrication of hydrogels, i.e., cross-linked polymer networks capable of absorbing high percentages of water and avoiding the dissolution of their hydrophilic chains.²⁰⁴ Chujo et al.²⁰⁵ studied the first hydrogel based on photodimerization reactions. In particular, they synthesized a polyoxazoline having both anthracene and disulphide groups by partial hydrolysis of poly(N-acetylenimine) with (9-anthracenyl) methyl hydrogen 3,3'-dithio-dipropionate in the presence of dicyclohexylcarbodiimide as condensing agent. If the polyoxazoline solution was irradiated ($\lambda > 300$ nm), the photosensitive groups dimerized cross-linking the polymer chains and leading to the formation of a gel, which was able to swell in water. The degree of swelling (up to 2000 %) was studied both as a function of the irradiation time and number of replacing anthracene groups. Gelation was reversible upon the reductive cleavage of disulfide cross-links. Zheng et al.²⁰⁶ reported the synthesis, photogelation, and photocleavage of a new photoswitchable hydrogel (i.e., a macromer or a hydrogel system able to undergo a fast photogelation or photocleavage in the absence of either initiators or catalysts). They synthesized nitrocinnamate modified poly(ethylene glycol), which was photogelated via [2 + 2] photodimerization of nitrocinnamate groups under UV light at wavelengths greater than 290 nm. The obtained cyclobutene ring could be cleaved upon irradiation with UV light of wavelength lower than 260 nm. Miyamoto et al. synthesized a hyaluronan derivative, linking cinnamic acid to the carboxyl moiety of hyaluronan by 3-aminopropanol.²⁰⁷ The hyaluronan derivatives were photocrosslinked via the photodimerization of the cinnamic acid leading to the formation of a water insoluble hyaluronate hydrogel. Gels showed good tissue compatibility and did not induce excessive inflammation at the injection sites. Gattàs-Asfura et al. reported the synthesis of gelatin having p-nitrocinnamate pendant groups.²⁰⁸ UV irradiation at a wavelength of 365 nm caused the formation of a gelatin hydrogel only in a few minutes. The hydrogel swelling degree was found to depend on gelatin concentration, solution ionic strength, and irradiation type. The photocleavage of the hydrogel network was obtained with UV light irradiation at 254 nm. Yang and Zeng synthesized a thymine-functionalized multiresponsive hydrogel based on polyacrylamide.²⁰⁹ Gelation and solubilization of polyacrylamide were obtained via the photodimerization and photocleavage of grafted thymines upon irradiation with 365 and 240 nm UV light. Moreover, polyacrylamide chains were able to form thymine–Hg²⁺–thymine complexes and, consequently, a hydrogel in the presence of mercury dications. The hydrogel dissolution was obtained via the complex dissociation. Recently cinnamoyl, coumarin, and anthracene photoresponsive moieties have been added as pendant groups in polymer chains to confer self-healing properties by reversible photodimerization reactions.^{210–212} Light irradiation can induce the self-healing of surface cracks if the photoreactive moieties form new chemical bonds via [2 + 2] cycloaddition.²¹³ Another application of photodimerization reactions is the synthesis of nanosized photocross-linked hydrogel particles (nanogels)²¹⁴ and the stabilization of micelles for their interesting applications as drug delivery systems. In an aqueous medium amphiphilic block copolymers, i.e., polymers with both hydrophilic and hydrophobic parts,

form supramolecular core/shell structures (micelles), where the hydrophobic and hydrophilic parts form the micellar core and shell, respectively.

Polymer cross-linking can stabilize the micelles and cycloaddition reactions representing the preferred method for the abovementioned green advantages.²¹⁵ Interesting photoresponsive molecules are anthracene and its derivatives, used in optoelectronics thanks to their high fluorescence quantum yields.²¹⁶ Anthracene is a polycyclic aromatic hydrocarbon, which undergoes photodimerization on exposure to light or heat.²¹⁷

In a recent study, Madhavan et al.¹⁹² prepared a block copolymer membrane by using poly(styrene-*b*-anthracene methyl methacrylate-*b*-methylmethacrylate), containing anthracene moiety as mid-block between poly(styrene) and poly(methyl methacrylate). The amphiphilic character of the block copolymer allowed the formation of both lamellar and ordered hexagonal aggregates in bulk solution under appropriate solvent compositions. After UV irradiation at 365 nm, the anthracene moieties underwent photochemical dimerization to give [4 + 4] cycloadducts, which allowed the photoorganization of bulk aggregates into surface layers of spherical and cylindrical aggregates. Surface layers could be photocleaved to original bulk solution upon exposure to UV light at 254 nm, as shown in Figure 17.

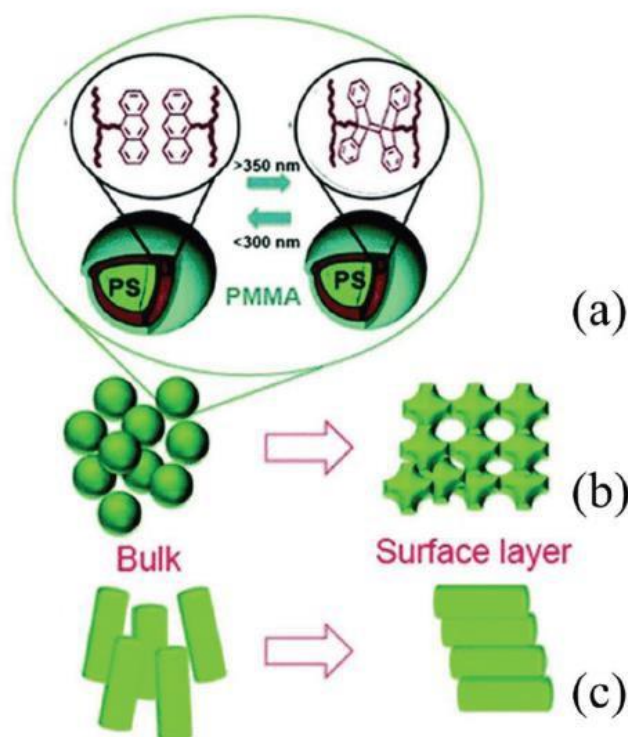


Figure 17. a) Self-assembly of poly(styrene-*b*-anthracene methyl methacrylate-*b*-methylmethacrylate) copolymers: anthracene block dimerization under irradiation. b,c) Organization from solution bulk to membrane surface as spherical and cylindrical micelles, respectively. Reproduced with permission.¹⁹² Copyright 2016, Royal Society of Chemistry.

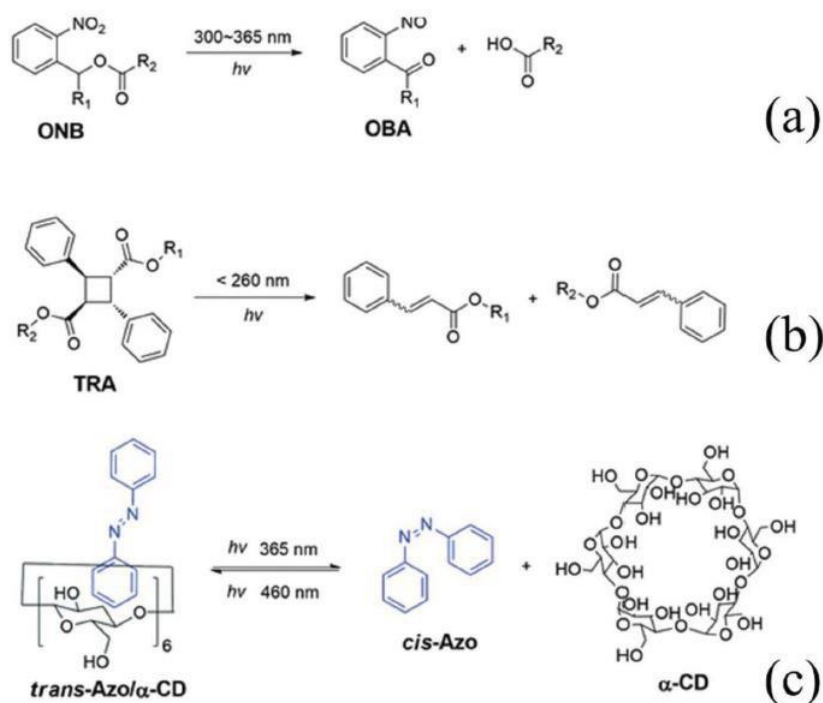
1.6 BIOLOGICAL APPLICATIONS

Light has been proposed to trigger phase transitions and control surface properties also in biological systems.^{218,219} The noninvasive feature and spatiotemporal control make photostimuli promising triggers in

biological applications including drug delivery, programmable matrices for controlled release, templates for cell micropatterning, cell manipulation, and programmable scaffolds for tissue engineering.^{220–224}

1.6.1 LIGHT-CONTROL OF BIOLOGICAL FUNCTIONS

The development of photoresponsive systems is very attractive in biotechnology, if one considers the possibility to reversibly control biological functions. LC polymer networks were used to tailor in a permanent way the topography and roughness of hybrid surfaces by using patterned masks and dosing UV intensity to study their influence on cell migration.^{105,109} Koçer et al. showed that the cell speed and migration patterns were strongly dependent both on the topography height and surface roughness. Such results open the research in the field of on demand reversible topographies to enhance the performance of biomaterials for regenerative medicine applications.²²⁵



Scheme 3. Irreversible and reversible photocleavable groups: a) o-nitrobenzyl (ONB) derivatives, b) truxillic acid (TRA) derivatives, and c) azobenzene (Azo) and α -cyclodextrin (α -CD) host-guest complexes. Reproduced with permission.²³⁷ Copyright 2013, Royal Society of Chemistry.

Shimoboji et al.²²⁶ proposed a technology for the photoswitching of enzyme activity. They designed a photoresponsive polymer incorporating two photoactive coelements into the polymer backbone, N,N-dimethyl acrylamide-co-4-phenylazophenyl acrylate and N,N-dimethyl acrylamide-co-N-4-phenylazophenyl acrylamide. The activity of N55C mutant of endoglucanase 12A could be modulated by $\approx 25\%$ by UV radiation in the coupled conditions. Interestingly, when the polymers were added to the enzyme solution as a physical mixture, no significant difference in activity was found. Different research groups^{227–230} showed that Azo derivatives can work as optical switches of regulatory molecules and biological fluorescence imaging agents.

Nicotinic acetylcholine receptor, endonuclease 12A, chymotrypsin, voltage-gated potassium channels, ionotropic glutamate receptors have been investigated for optical manipulation.^{231,232} Trauner's group obtained the control of K⁺ channels in nerve cells and realized the light control of ionotropic glutamate receptors (iGluR).^{233,234} In the latter work a light-gated iGluR used the maleimide-azobenzene-glutamic acid 9 as photochromic agonist. Only the cis isomer allowed the interaction between glutamic acid and receptor active site, opening the ion channels.

1.6.2 PHOTOCONTROLLED PROTEIN ADSORPTION AND CELL ADHESION

Photocleavable polymers are a particular class of polymers that contain metastable photochromic groups. Light irradiation can detach these groups with the resulting degradation of polymer structure.

The first synthesis of a polymer incorporating chromophoric groups in its chain was made by Barltrop et al. in 1966,²³⁵ who used o-nitrobenzyl groups (ONB) as photocleavable groups. The ONB group isomerizes from ONB into o-nitrosobenzaldehyde (OBA) form only in a few minutes upon UV exposure ($300 < \lambda < 365$ nm) as reported in Scheme 3.²³⁶ The photocleavage is irreversible.

Similar behavior is shown by truxillic acid derivatives, which undergo a photocleavage upon UV irradiation at wavelengths lower than 260 nm.²³⁷ Incorporation of photosensitive moieties in their backbones can confer photodegradability properties to polymers. In fact, bond cleavage of photosensitive functional groups can split the polymer chains in desired fragments if photosensitive moieties are opportunely placed in the polymer backbone (e.g., between different segments of a block copolymer, at the midpoint of a homopolymer chain, as part of the repeat units).²³⁷

Surface modification with photocleavable linkers, which connect functional polymer chains to the substrate, allows to control hydrophobicity, protein immobilization, and cell adhesion by light.²³⁸

Cell adhesion on aminobearing surfaces was controlled by reversible conjugation of polyethylene glycol via a photocleavable linker, 1-(5-methoxy-2-nitro-4-prop-2-ynyloxyphenyl)ethyl-N-succinimidyl carbonate.²³⁹ The photocleavable linkers had alkyne and succinimidyl carbonate at each end connected by photocleavable 2-nitrobenzyl ester. The molecules were conjugated between amines and azides. Therefore, the linkage could cleave upon near-UV light irradiation and affect dramatically protein adsorption and cell adhesion.

Physically cross-linked photolabile hydrogels have potential applications as a functional surface that can selectively release adherent abiotic or living species.²⁴⁰ Yamaguchi et al.²⁴¹ added an ONB linker between poly(ethylene glycol) (PEG) chains and oleyl groups to obtain a photoresponsive cell substrate. Under dark conditions oleyl groups bound to nonadherent cells via insertion into cell membranes. On the contrary, light irradiation promoted the photocleavage of ONB linkers and the cell detachment from substrates. By using opportune photomasks it was possible to create micropatterned cell populations as cells aggregated in masked areas and detached in irradiated ones, as shown in Figure 18.

Pendant ONB functional groups can confer to macromolecular chains photoresist characteristics for successive surface modification. In the work of Azzaroni's group,²⁴² photofunctional groups were able to modulate interfacial properties upon exposure to light. In particular, the surface of a silicon-glass wafer could be

selectively switched from a hydrophobic to a hydrophilic state by the UV photolysis of covalently coated poly(4,5-dimethoxy-2-nitrobenzyl methacrylate) brushes grafted onto glass surfaces.

Light can also activate surfaces containing chemical functionalities, cell binding domains, bioadhesive linkers, like arginine-glycine-aspartic acid (RGD), protected with a photocleavable group (cage).^{243–245} Light irradiation removes the cage (ONB group) and exposes the reactive groups present onto the surface inducing a controllable transition from substrates with cell antiadhesion properties to substrates with cell adhesion properties. In particular, cell adhesion was promoted by RGD adequately protected by ONB and its derivatives on the carboxylic acid side chain.^{246,247} After bond cleavage, RGD and other bioadhesive linkers could be exposed on the surfaces for the enhancement of cell adhesion.²⁴⁸ Similarly, bioadhesive poly-L-lysine concealed by nitrobenzyl cages did not allow cell adhesion, but after UV irradiation, the nitrobenzyl groups underwent bond cleavage allowing the exposure of RGD peptides and promoting cell adhesion as shown in Figure 19a.²⁴⁹ The photocontrollable cell detachment is also promising for cell diagnostic and tissue engineering. For instance, PEG molecules with 4-(hydroxymethyl)-3-nitrobenzoic acid (ONA) and RGD groups underwent bond cleavage and the RGD moieties with cells detached from the surface upon NIR irradiation, as shown in Figure 19b.²⁵⁰

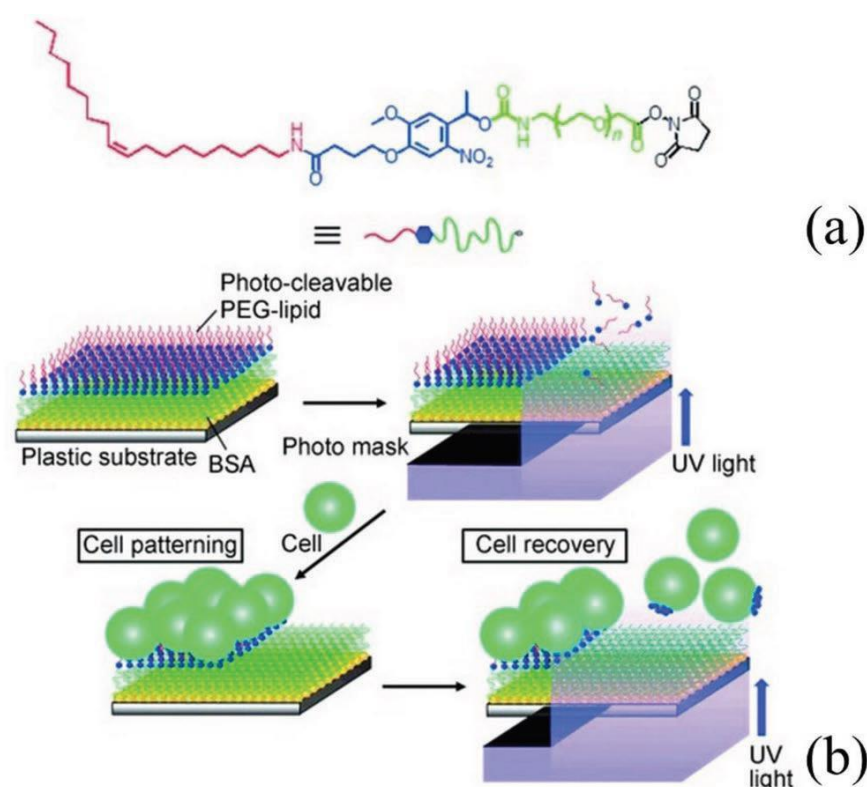


Figure 18. a) Chemical structure of (blue) ONB functional groups used as photolabile linkers between (green) maleimide-terminated PEG chains and (red) oleyl groups. b) Schematic illustration of cell pattern formation by selective removal of oleyl groups through light-induced scission of ONB linkers. Reproduced with permission.²⁴¹ Copyright 2012, Wiley-VCH.

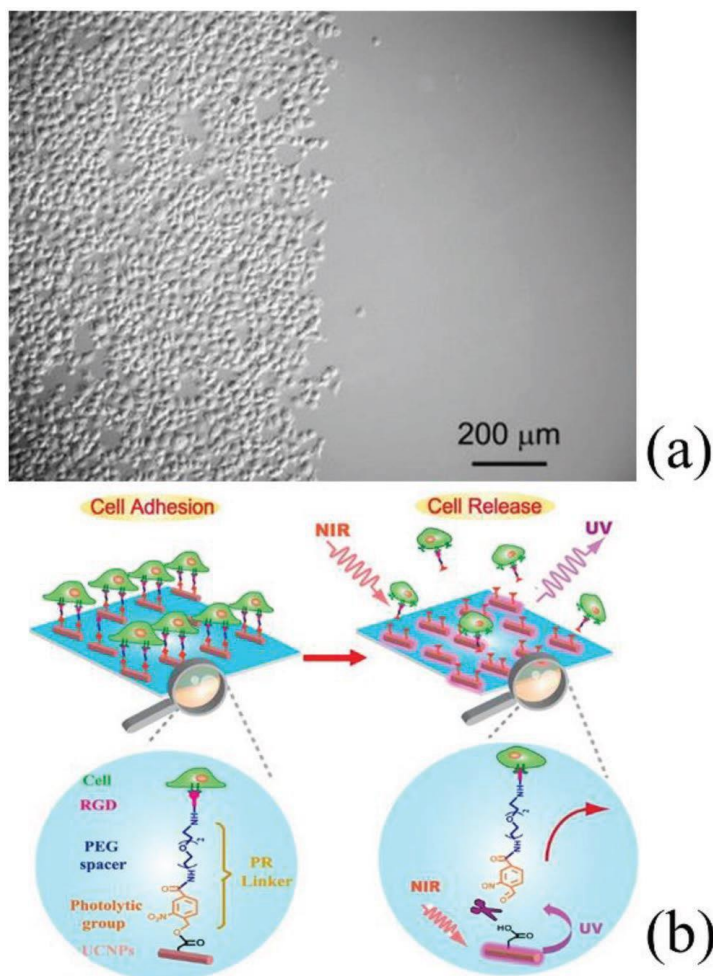


Figure 19. a) Photoresponsive surfaces from cell antiadhesion to cell adhesion. Reproduced with permission.²⁴⁹ Copyright 2008, Wiley-VCH. b) ONA-based polymers can control cell detachment. Reproduced with permission.²⁵⁰ Copyright 2014, American Chemical Society.

Photoresponsive surfaces including SP moieties, such as poly(nitrobenzospiropyran-co-methyl methacrylate) and poly(SP-co-NIPAAm), were used to control cell detachment by the wettability switch induced by UV light.²⁵¹

Higuchi et al. observed the photoinduced detachment of mesenchymal stem cells from dishes coated with a copolymer of nitrobenzospiropyran and methyl methacrylate upon UV irradiation. The hydrophilicity of the cell culture dishes was reversibly altered due to change of closed nonpolar SP into the polar zwitterionic MC isomer.²⁵² Surfaces grafted with cell recognition sites linked to photocleavable groups can control cell detachment and attachment from substrate. Wirkner et al. studied surfaces grafted with RGD peptides bearing a photocleavable group in order to phototrigger the cell release.²⁵³ Upon photocleavage, researchers observed the effective detachment of cells from the substrate. Inspired by biological systems, He et al. integrated an ONB protected acrylamide into a thermoresponsive polyacrylamide (pNIPAAm) in order to enable temperature- and light-responsive smart polymers.²⁵⁴ Upon UV irradiation, the hydrophobic ONB groups were cleaved with subsequent release of the caged NH groups and generation of more hydrogen bonds with water,

resulting in an increased LCST of pNIPAAm in water. Light-responsive biomaterials represent promising candidates for the controlled culture of stem cells.^{255–257} Stem cells can be easily detached from dishes with immobilized light-responsive polymers avoiding damaging methods such as the use of enzymes, thermal liftoff, and mechanical means.²⁵⁸ Auernheimer et al. investigated the possibility to photocontrol cell adhesion properties by changing the distance and orientation of the RGD peptide. They prepared a poly(methyl methacrylate) surface grafted with integrin binding domains of cyclic Arg-Gly-Asp-Phe-Lys (cRGDfK) peptides, which were bound to Azo molecules and joint segments.²⁵⁹ Upon UV light irradiation (wavelength 366 nm), they observed the detachment of mouse fibroblasts. Micropatterned surfaces modified with RGD peptideconjugated Azo can reversibly regulate the cell adhesion and detachment. The application of UV light (15 W@365 nm) for 10 min allowed the release of RGD peptide-conjugated Azo from the α -cyclodextrin substrate and cells detachment from the micropatterned surface.²⁶⁰

1.6.3 LIGHT-RESPONSIVE POLYMER MEMBRANES AS DRUG DELIVERY SYSTEMS

One future perspective in the field of medical materials is the employing of adaptive materials able to simultaneously monitor the physiological parameters and deliver drugs on-demand.²⁶¹ One example is the development of smart transdermal delivery systems that can overcome undesired peaks in drug concentration.^{262,263} In fact, photoresponsive drug delivery systems allow site-specific release and activation by controlling the light irradiation site, power, and duration.[264] Biocompatibility, biostability, and high oxygen permeability^{265–267} make poly(2-hydroxyethyl acrylate) and polydimethylsiloxane conetworks appealing as matrices for controlled drug release, contact lenses, cell culture surfaces, tissue engineering scaffolds, immunoisolation membranes, biomaterials, antifouling surfaces, sensors, nanoreactors, and functional transdermal delivery devices.^{268–271} Another great advantage is the control of the permeability resistance by adjusting the membrane composition and thickness. It is possible to give photoresponsiveness to these conetworks by the incorporation of photochromic dyes either by postmodification of preformed membranes or copolymerization. Schöller et al.²⁷² created photochromic membranes incorporating SP and spirooxazine derivatives into nonporous films of poly(2-hydroxyethyl acrylate) and polydimethylsiloxane. The authors studied in their permeability tests the transdermal delivery of caffeine, able to stimulate the respiratory system and reduce the risk of apnea in preterm neonates.²⁷³

Under UV irradiation the reversible heterolytic ring-opening reaction of dye molecules led to the polar MC form, while white light resulted in the back-isomerization to the SP form.²⁷⁴ MC form, being more hydrophilic than SP isomer, increased the permeability of caffeine through the membrane.^{275,276} Permeability properties were tested in vitro as a function of components ratio and film thickness using porcine ear skin in order to simulate the permeability of human preterm neonatal skin. The caffeine flux through conetworks increased or decreased of around +40% or –40% under UV or Vis light as compared to the drug flux through the porcine ear skin ($0.15 \text{ mm cm}^{-2} \text{ h}^{-1}$) in dark conditions. Qian et al. developed a hypoxia-responsive drug-delivery system based on 2-nitroimidazole-grafted conjugated polymer and poly(vinyl alcohol)-based surface coating, able to encapsulate doxorubicin, DOX. The conjugated polymer was able (under Vis or NIR radiation) to consume oxygen and produce radical oxygen scavengers, thus creating a hypoxic environment and inducing

tumor cell apoptosis and necrosis as well as vascular damage. As such, 2- nitroimidazole underwent a transformation to 2-aminoimidazole via single-electron reduction and triggered the nanocarrier dissociation and DOX release.²⁷⁷

LC polymers can be tailored with a desired uniform nanometer pore size, which favors molecular adsorption.^{278,279} In order to control the capture, transport, and release of chemical species in nanoporous materials by light, van Kuringen et al. reported on a free-standing photoresponsive nanoporous LC polymer film incorporating Azo cross-linkers (a mixture in the molar ratio 5: 95 of A6MA, a photoresponsive Azo diacrylate cross-linker, and 6OBA, a hydrogen-bonded dimer diacrylate) in a smectic hydrogenbonded polymer network.^{280,35} The polymer network was treated with an alkaline solution in order to break H bonds and create nanopores. After UV light exposure a decrease in the layer spacing of the smectic phase was observed, suggesting that the dimensions of cavities, hosting the Azo molecules, were lowered. In addition, light reduced the number of the binding sites due to the adsorption of cations as a consequence of light-induced change in the dipole moment of Azo cross-linkers. Nevertheless, the release of absorbed cations needed the pH lowering.

1.6.4 PHOTORESPONSIVE SILICA MATERIALS

Zeolites, AlPO₄, hexagonal mesoporous silica, Mobil Composition of Matter No. 41 (MCM-41), Santa Barbara Amorphous-15 (SBA-15), and porous glasses are some of the most common silica materials characterized by a uniform and ordered distribution of their pore size.[281] Porous silicas can be classified as microporous, mesoporous, and macroporous according to their pore size ρ ($\rho < 2$ nm, $2 < \rho < 50$ nm, and $\rho > 50$ nm, respectively).²⁸² In addition to their well-defined surface properties, mesoporous silica materials (MSMs) are extensively investigated because of their easy surface functionalization with different types of molecules (including stimuli-responsive, luminescent, and capping groups) and the possibility to control on demand their pore size.²⁸³ The large surface area and small volume make these materials suitable for a wide range of applications including separation,²⁸⁴ adsorption,²⁸⁵ catalysis,²⁸⁶ imaging,²⁸⁷ chemical sensing,²⁸⁸ medicine,²⁸⁹ energy storage,^{290,291} nanotechnology,²⁹² chromatography,²⁹³ photonic²⁹⁴ and electronic devices,²⁹⁵ and drug delivery.²⁹⁶

Moreover, the catalytic activity and adsorptive capacity of these solids can be enhanced by hosting large molecules into their cavities including heavy metal ions, biomolecules, and organic volatiles.²⁹⁷

The most common mesoporous silicas are MCM-41 and SBA-15, which belong to the families of mesoporous silicate and aluminosilicate materials, respectively. They are characterized by a 2D hexagonal arrays of uniform, cylindrical, and controllable mesopores.²⁸¹ Several methods have been proposed to synthesize these materials.^{281,298-302} The most common synthetic strategies use templating agents around which a framework of nanosized silica spheres is built up. Then, the template is removed by calcination, solvent evaporation, or washing. The molecular chain length of the templating agents (generally quaternary ammonium ions and triblock copolymers for MCM-41 and SBA-15, respectively) determines the pore size.³⁰³ Recently, functionalized SBA-15 mesoporous particles have been used as porous fillers to improve the performance of

various polymer membranes in terms of permeability, fouling resistance, and separation ability.^{304,305} Wang et al. investigated the properties of a polysulfone hybrid ultrafiltration membrane incorporating SBA-15 mesoporous silica functionalized with poly[poly(ethylene glycol) methyl ether methacrylate]. The water permeability and antifouling properties of such hybrid membranes were enhanced with respect to SBA-15-free membranes and the membrane selectivity was not altered.³⁰⁶

Applications of MSMs as smart sensors and gated switches³⁰⁷ use MCM-41 and SBA-15 particles functionalized with responsive polymer brushes, able to control the pore opening and closing in response to the surrounding physicochemical changes.

Li et al. realized a controllable ion transport system by grafting an Azo-diblock copolymer on the pore inner surface of SBA-15. The poly(2-(dimethylamino)ethyl methacrylate) (PDMAEMA) block conferred pH and thermal responsivity to the system, while the trans–cis photoisomerization of the terminal Azo-block controlled the brush opening and closing. The device was able to regulate the ion conductivity in response to pH, temperature change, or UV light exposure. More precisely, the coil–recoil response of PDMAEMA increased as a result of trans–cis photoisomerization. The gate-on state was achieved at high pH and temperatures above the lower critical solution temperature under UV light irradiation, while a gateoff state was possible upon exposure to Vis light.³⁰⁸ The biocompatibility of MSMs has been widely exploited in biotechnological and pharmaceutical applications, as high quantities of therapeutic agents can be loaded in MSM-based drug delivery systems.³⁰⁹ In order to combine together photothermal therapy and chemotherapy, Zhang et al. realized a NIR-responsive and photothermally triggered drug delivery system based on MSMs, DNA, and CuS, which allowed DOX release in response to temperature, NIR irradiation, and glutathione treatment.³¹⁰

He's group assembled reduced graphene oxide (RGO) with trimethoxy-(octadecyl)silane functionalized MCM-41 (MSNC18) to develop a novel NIR light-responsive intracellular drug delivery system for cancer therapy. In absence of NIR light the pores of MSN-C18 were closed by the capping of RGO sheets. The pore uncapping occurred upon exposure to NIR light, which caused the RGO abscission and the release of loaded DOX as shown in Figure 20a.³¹¹ A similar anticancer drug delivery nanocarrier based on a polymer-coated MSM, responsive to both Vis light and pH, was developed by Wang et al. MSMs were employed to load DOX, while perylene-functionalized poly(dimethylaminoethyl methacrylate) was electrostatically bound on the MSM surface to seal the pores. The synergic Vis light and acidic pH stimulation caused the polymer stretching, pore unsealing, and release of the loaded DOX, as shown in Figure 20b.³¹² Periodic mesoporous organosilicas (PMOs) represent another class of mesoporous silica material characterized by a periodically organized pore system and a very narrow pore radius distribution. Inside the pores, organic groups act as bridges between the Si centers ((R'O)₃Si–R–Si(OR')₃ (R' = CH₃ or C₂H₅, R bridging organic groups)).³⁰³ The organic functionalization of the inner surfaces of PMOs allows the tuning of the surface properties including hydrophilicity, mechanical or optical properties, surface reactivity, molecular binding, resistance from chemical attack, and molecular transport.³¹³ In particular, the pore tunability can be achieved by incorporating switchable photoactive bridging organic groups.³¹⁴ Inagaki's group obtained PMOs with enhanced light-harvesting properties by binding coumarin groups.³¹⁵ Grösch et al. employed biphenyl-bridged PMOs with

crystallike pore walls and two types of chromophores loaded into PMO pores to study the light-harvesting behavior of these systems by multistep fluorescence resonance energy transfer experiments.³¹⁶

1.6.5 PHOTOCROMIC LIPID BILAYERS

Biological membranes are bilayered structures formed by mixtures of lipids and proteins that separate cells from the surrounding environment. They act as selectively permeable barriers by protein-based ion channels that allow the passage of specific ions after appropriate stimulation. The incorporation of photoswitchable molecules in channel proteins can allow the control of channel function *in vivo*. Moreover, bilayer organization and membrane permeability can be controlled by the use of photoresponsive amphiphiles.

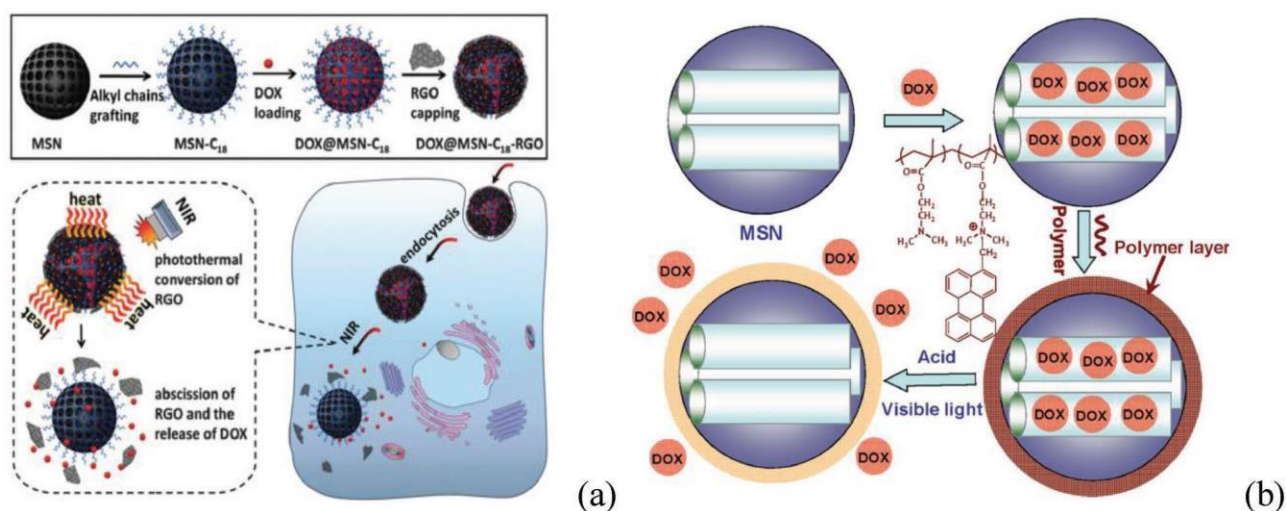


Figure 20. a) DOX@MSN-C18-RGO system as carrier for NIR photoresponsive drug delivery. Reproduced with permission.³¹¹ Copyright 2015, Royal Society of Chemistry. b) MSMs coated with PDMAEMA and loaded with DOX. Upon Vis light irradiation and acidic pH the nanopores were unsealed and DOX was released. Reproduced with permission.³¹² Copyright 2016, Wiley-VCH.

Szymanski et al.³¹⁷ used a photochromic molecule to confer light sensitivity to a mechanosensitive channel located in the cytoplasmic membrane of *Escherichia Coli*. These channels respond to tension changes in the lipid bilayer upon a sudden hypo-osmotic shock and function as safety valves to protect bacteria from lysing.³¹⁸ Channels can also gate upon an increase in the pore hydrophilicity. Small photocleavable molecules were bound to the channel pore restrictions. In dark conditions no current flow was observed through the protein channels, but, upon UV irradiation, the channel pores opened. Furthermore, Feringa's group rendered these channels pH responsive on demand using photolyzable groups that could be removed only by UV radiation. The same authors applied the reversible photoinduced change in the abovementioned mechanosensitive channels in order to control gating even in the absence of tension triggers.³¹⁹ Upon irradiation at 366 nm, photochemical ring-opening processes took place, resulting in channels characterized by higher wettability and increased flow toward water and ions. Exposure to Vis light (larger than 460 nm) resulted in the reverse ring-closing reaction, which restored the original closed state. An effective alternative to photomodulate the

transport through the lipid membrane is the use of stimuli-responsive bilayers, which can be obtained by three general strategies.³²⁰ In the first approach, photoswitchable copolymers are incorporated in the lipid bilayer,³²¹ while in the second strategy, light-responsive lipids are used as dopants in the membrane.³²² Alternatively, the bilayer can be constructed completely with photochromic lipids.³²³ The group of Tribet³²¹ incorporated photoswitchable Azo-bearing copolymers into lipid bilayers to realize lipid bilayers with photomodulated permeability.

1.7 MEMBRANE PROCESSES

1.7.1 TRANSPORT ACROSS POLYMER MEMBRANES

The performance of a membrane depends on several parameters including polymer crystallinity, porosity, wettability, surface roughness, and synthetic procedure (phase inversion, stretching, template leaching, sintering, track etching, polymerization).³²⁴ Polymerization is the conversion of reacting monomers into larger polymer molecules or 3D-cross-linked networks. Photopolymerization has been and is one of the most rapidly expanding processes for production of materials, due to the advantages related to the use of light rather than heat. In fact, light-driven monomer \rightarrow polymer conversion is a solvent-free, fast, spatial-controlled, low energy-input, versatile chemical reaction.³²⁵ The net movement of atoms, ions, or molecules from a region where they show a higher concentration to a region with a lower concentration determines their coefficient of diffusion. Flow across porous polymer membranes is mainly regulated by solution-diffusion and pore-flow mechanisms according to the membrane nature.³²⁶ Diffusion in dense (nonporous) membranes is due to the molecular permeation through transient thermally driven opening of free-volumes in the polymer chains, allowing the molecular jumps from a polymer cavity to another adjacent cavity. Koros and Fleming³²⁷ defined the diffusion coefficient, D_{dm} , in polymer dense membranes as

$$D_{dm} = \frac{fl^2}{6} \quad (2)$$

where l and f are the average jump length and frequency. Obviously, f is dependent on temperature (according to an Arrhenius-like relation) and molecular geometry (shape and size).³²⁸ The transport of molecules in porous membranes is due to the presence of their permanent pores. Diffusion in porous polymer membranes takes place when the potential energy of molecules within the pores is lower than their external potential energy external (membrane-suction action). The pore diameter, for which the difference between external and internal potential energy, ΔE , is zero, determines the minimum pore size, ρ_{min} , for molecular surface-diffusion, while the condition $\Delta E = RT$ defines the Knudsen diameter, ρ_K . Activated-, surface-, and Knudsen-diffusion mechanisms can account for the diffusion in polymer porous membranes according to their pore size ρ ($\rho < \rho_{min}$, $\rho_{min} < \rho < \rho_K$, $\rho > \rho_K$, respectively).³²⁹

Membranes allow the separation of mixture components because of their different transport rates (fluxes) across the membrane upon the application of a driving force (pressure, concentration, temperature, chemical

and electrical potential gradients).^{330–332} The flux of a molecular species M, J_M , is given by the following Equation

$$J_M = \frac{\Delta\mu A}{R} \quad (3)$$

where $\Delta\mu$ is the permeation driving force, A and R are the membrane effective area and resistance of component M, respectively. $\Delta\mu$, R, and A are usually constants in a given membrane process and in absence of fouling settlements, giving a constant value for J_M . The separation can be achieved by phase equilibrium mechanisms as in thermally driven processes or by sieving mechanisms as in pressure-driven processes.¹⁵ Porous polymer membranes consist of a solid porous matrix with interconnected voids and crevices with an average size ranging from sub-nanometer dimensions to several tens of micrometers. According to their pore size, which enables the different membrane processes (pervaporation, reverse osmosis, gas separation, nanofiltration, ultrafiltration, microfiltration, distillation) and component separation (gas, salts, sugars, proteins, bacteria, emulsions, colloids), porous membranes can be distinguished in nonporous ($\rho < 0.1$ nm), microporous ($0.1 < \rho < 2$ nm), mesoporous ($2 < \rho < 50$ nm), and microporous ($\rho > 50$ nm) membranes.¹⁵ Separation in sieving processes is strongly dependent on feed components and membrane pore sizes and applied stimuli.⁸

1.7.2 ADVANCED OXIDATION PROCESSES (AOP)

An AOP by membrane reactors is the exploit of the polymer membrane filtration to remove particulate matter and the chemical oxidation of dissolved organic compounds by hydroxyl radicals generated from different reactions (ozone, H_2O_2 , ultraviolet radiation, Fenton reaction, electrolysis, sonolysis, and photocatalysis) in a single reactor. The most common membrane reactors for AOP are ozone membrane reactors,³³³ electrochemically active filtration devices,³³⁴ and photocatalytic membrane reactors.³³⁵ In a photocatalytic membrane reactor, UV light activates the photocatalytic semiconductor suspended in the feed or entrapped onto membrane surface leading to the oxidation (i.e., degradation in H_2O and CO_2) of the dissolved or deposited organic compounds. Accordingly, it is possible to mitigate and control membrane fouling and enhance flux. Both suspension and entrapment of photocatalysts have some drawbacks. In particular, suspensions are affected by the problem of catalyst recovery, while reduced photoactivity and risk of polymer membrane damage could limit the photocatalyst entrapment onto the membranes.³³⁶

1.7.3 ANTIFOULING AND ANTIMICROBIAL MEMBRANES

Fouling is the detrimental time reduction of the flux through a membrane due to concentration polarization effects and the formation of cakes or gel layers by the accumulation and attachment of inorganic, organic, and biological constituents of the feed solution onto membrane surfaces.¹⁶ Fouling is dependent on several parameters including the particular membrane process, polymer material, feed flow, module design, particle size and concentration, ionic strength, pH, and surface interactions.³³⁷ Fouling is an irreversible process, which can scale from some minutes to several days. The best method for the prevention and control of membrane

fouling depends on the material and mechanisms causing the fouling.³³⁸ It is often a set of different methods such as feed pretreatments (prefiltration, chemical precipitation, chlorination, pH adjustment, and carbon adsorption), surface modification with hydrophilic or charged layers, hydrodynamic optimization of the membrane module, periodic membrane chemical cleaning and/or physical washing. More generally, the inhibition of foulants adsorption or settlement on a membrane surface can be obtained by any method able to weaken the attractive interactions between foulants and membrane surfaces.

The antimicrobial activity of a membrane module is defined as its capacity to prevent the development of microorganisms. Antimicrobial compounds as chlorine-based disinfectants are generally introduced in the feed effluent during the cleaning stages.³³⁹ Nevertheless, this approach suffers the disadvantage of the formation of undesired by-products, so the use of ozone and AOP is preferred even if they are more expensive. Membrane biofouling is probably the main drawback of polymer membrane processes, as it decreases transmembrane fluxes and permeates quality increasing production costs. In particular, drinkable water must be pathogen-free. Antimicrobial membranes used for water treatment have to show good antibacterial properties and low toxicity toward health and environment.³⁴⁰ Commonly used antimicrobial agents are quaternary ammonium compounds, silver and copper ions or metal oxide nanoparticles, carbon nanomaterials, UV light in cooperation with photoactive compounds (e.g., TiO₂).^{341–343}

1.7.4 SELF-CLEANING MEMBRANES

Self-cleaning membrane surfaces can be obtained by deposition of metals oxides such as TiO₂, ZnO, Fe₂O₃, CdS, and CuO, which under UV irradiation cause the chemical decomposition of organic contaminants and actuate the hydrophobic/hydrophilic transition making the surfaces easily washable.³⁴⁴

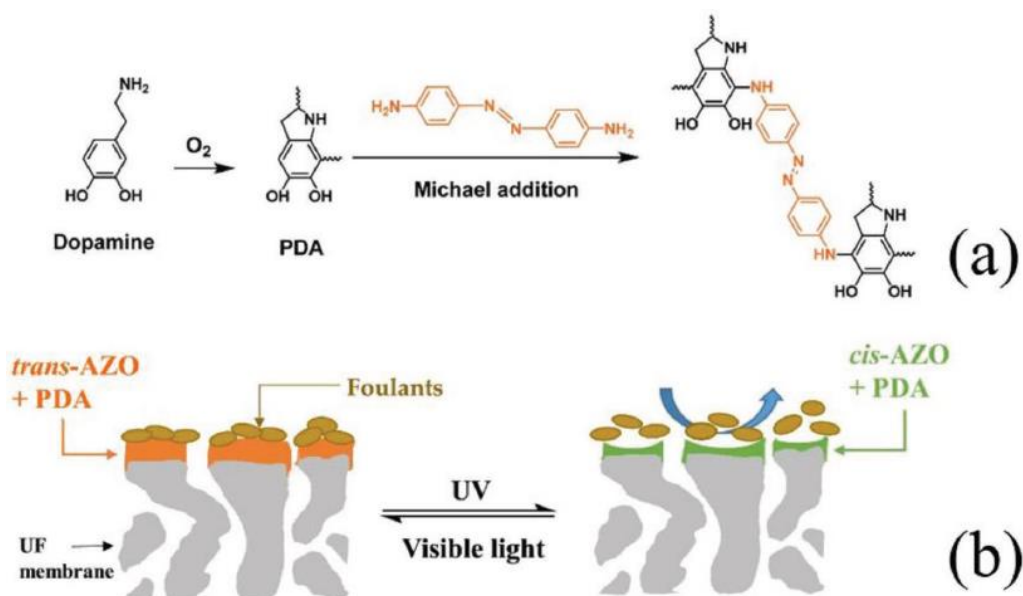


Figure 21. a) Scheme of PDA formation and reactions between 4,4'-azodianiline and PDA through Michael addition, leading to covalent linkages. b) Self-cleaning behavior of the photoresponsive membrane. Reproduced with permission.[357] Copyright 2018, Elsevier.

TiO₂ is undoubtedly the most used photocatalyst, thanks to its nontoxicity, large availability, chemical stability, recyclability, and biocompatibility.³⁴⁵ Recently, the degradation of Rhodamine B dye by poly(allyl amine hydrochloride) and poly(styrene sulfonate sodium salt) multilayers containing TiO₂ has been evaluated after 4 h of UV irradiation.³⁴⁶ Composite membranes, prepared from mixtures of CNTs and TiO₂/Al₂O₃, were proposed for pollutant degradation during water treatment. The achieved fluxes were three times higher and the removal rate of humic acid was 10% larger than values obtained from CNT-free membranes.³⁴⁷ This could be ascribed to the ability of CNTs to work as electrons acceptors, thereby suppressing the charges recombination under UV irradiation. Polyvinylidene fluoride (PVDF) membranes were loaded with different amounts of TiO₂ yielding antibacterial properties against *E. Coli*, photodegradation against Reactive Black 5 dye, and self-cleaning and antifouling characteristics against bovine serum albumin solutions.³⁴⁸ Fouled membranes need periodic cleaning procedures by back-flushing or using chemicals (e.g., bases, acids, biocides).³⁴⁹ However, such cleaning procedures interrupt the industrial production cycle and use strong chemicals, which can cause irreversible damages to the polymer membrane surfaces.³⁵⁰ Self-cleaning membranes possess a thin layer of “smart” materials able to respond to the environment changes, improve membrane surface properties, and mitigate fouling.^{2,351} In this approach, photoresponsive materials can be grafted or coated in order to provide switchable and antifouling properties using light as a noninvasive stimulus.³⁵² For example, the switchability of SP-based materials, which become zwitterionic and thus more hydrophilic under UV light, can be used to generate antifouling surfaces.^{353,354} The control of surface wettability and permeability by UV light can be gained if the membrane surfaces are modified with Azo-based derivatives.³⁵⁵ The main advantage of polymers incorporating Azo groups³⁵⁶ is the possibility to cast them on membrane surfaces as thin films without pore blockage and permeance decrease. Ramanan et al.³⁵⁷ demonstrated a facile one-step coating with 4,4'-azodianiline and polydopamine (PDA) on different commercial ultrafiltration membrane surfaces to achieve selfcleaning when membranes were exposed alternatively to UV and Vis light, as shown in Figure 21. In particular, azodianiline and PDA were casted on membranes, in order to allow the covalent grafting of the aminecontaining dye to the polymer membrane surface through Michael addition or Schiff base reactions without a dramatic blocking of the surface pores. In addition, azodianiline might also interact with PDA through π - π stacking and hydrogen bonding (noncovalent bonds).³⁵⁸⁻³⁶⁰ The PDA/Azo layer reversibly shrank and expanded under alternative exposure to the UV and Vis light, avoiding the foulant accumulation onto surfaces. Furthermore, the polymer stability under UV light was increased by the presence of PDA providing UV protection and free radical scavenging. The membrane permeance was measured using a dead-end filtration system, while the feed water was replenished to maintain the concentration of bovine serum albumin solution at 1 g L⁻¹. The fouling tests confirmed the film effectiveness in self-cleaning the membrane surface and increasing water permeance by almost 160% in UV irradiated membranes. Current methods for achieving antifouling properties in membranes coated with PDA require alkali conditions and relatively long reaction times. Baek et al.³⁶¹ obtained a PDA modification of a polyamide membrane in deionized water by UV irradiation for 30 min. The obtained membranes maintained

good salt rejection and water permeability and exhibited excellent antifouling properties toward alginate. Dübner et al.³⁵² demonstrated a new method for the fabrication of a pH- and light-responsive polypropylene membrane. pH-responsiveness was imparted via grafting of poly(methacrylic acid) (PMAA) brushes using a plasma-induced free-radical graft polymerization. Conversion into a light-responsive membrane was performed via a two-step postpolymerization modification, which allowed the covalent attachment of SP moieties to the grafted polymer brushes (PMAA-SP). A pH change or the application of a light stimulus successfully changed the wettability and permeability of both PMAA- and PMAA-SP-modified membranes. The brush swelling changed dramatically the flux properties of pH-switched PMAA-modified membranes, while the photoswitching of SP-modified membranes was highly influenced by hydrophilicity changes.

1.7.5 LIGHT RESPONSIVE POLYMER MEMBRANES FOR WATER PURIFICATION

One of the most important applications of stimuli-responsive polymer membranes is the removal of pollutants from feed streams and, in particular, of oil contaminants hampering the quality of water.

Accidental oil spills and industrial oily wastewater can generate high stable oil/water (nano)emulsions. Thin membranes with superwetting properties resulted as interesting filters for their low energy consumption, scalable productivity, high separation efficiency, good durability, and stability. Under UV irradiation for 3 h, thin film membranes made by TiO₂-coated single-walled carbon nanotubes^{362,363} gained reversible superhydrophilic and underwater oleophobic wettability properties³⁶⁴ as the surface CA changed from $\approx 82^\circ$ to $\approx 0^\circ$. The initial CA value was recovered after 7 days in the dark. The film was effective in separating oil/water mixtures with a high flux rate ($30\,000\text{ L m}^{-2}\text{ h}^{-1}\text{ bar}^{-1}$) and separation efficiency (99.99%), as shown in Figure 22. The UV irradiation granted antifouling and light-induced self-cleaning properties. These membranes could be efficiently used for the treatment of emulsified wastewater and purification of crude oil and fuel. Hu et al. developed a dual light- and temperature-responsive nanoporous membrane composed of PDA-coated single-walled CNTs modified with light-sensitive gold nanorods and temperature-sensitive poly(N-isopropylacrylamide-co-acrylamide).³⁶⁵ Similarly to the previous thin films, these membranes showed hydrophilic and underwater oleophobic wettabilities and were able to separate oil-in-water nanoemulsions with a high efficiency (99.99%) and flux (up to $35\,890\text{ L m}^{-2}\text{ h}^{-1}\text{ bar}^{-1}$). In addition, light irradiation allowed the modulation of the permeation flux and enhancement of the antifouling and recyclability properties, thanks to the incorporation of gold nanorods and copolymer.

Surface coating and grafting with nonpolar hydrophobic molecules, such as fluorinated and silicone-based photoresponsive polymers, represent the most commonly used chemical modifications to impart self-cleaning properties to polymer membranes.^{366,367} The zwitterionic hydrophilic MC isoform possesses excellent antifouling properties, i.e., high resistance to the adsorption of biomolecules present in the feed.^{368–370} Recently, Kaner et al.³⁵⁴ prepared thin film membranes with antifouling properties due to light induced changes in surface morphology at constant pore size and water permeability. The self-cleaning membranes were obtained by coating a porous PVDF membrane with a thin layer of comb-shaped graft copolymers at two side-chain lengths featuring polyacrylonitrile backbones and photoreactive SP methacrylate side chains. Upon UV irradiation photoresponsive groups isomerized from the hydrophobic SP state (that allow the adsorption of organic

solutes) to the zwitterionic, hydrophilic MC state. The changes in surface hydrophilicity caused morphology changes on the membrane surface, the release of adsorbed molecules, and the full recovery of the initial water flux after 2 h of irradiation at 254 nm. In addition, partial self-cleaning of a fouled membrane was detected upon back-isomerization to the hydrophobic SP isomer after Vis irradiation. This result can be considered the first report of a self-cleaning mechanism accompanied by a decrease in hydrophilicity. Photochromic molecules can be used to selectively bind metal ions. Photocontrolled metal ion detection using SP derivatives has been widely demonstrated.^{29,371} To realize the photodetection and binding of metal ions, several approaches have been reported in literature including coatings of microbeads and surfaces integrated into microcapillaries.^{372,373} Dunne et al.³⁷⁴ realized microcapillaries operating in a continuous flow regime, capable of light-regulated binding and qualitative detection of divalent metals. Specifically, microcapillaries were coated with SP polymer brushes using ring-opening metathesis polymerization and were able to self- indicate through a colorimetric response the flow system state (passive, active, metal-ion bound). In addition, an external light source allowed the control of both metal ion release and uptake.

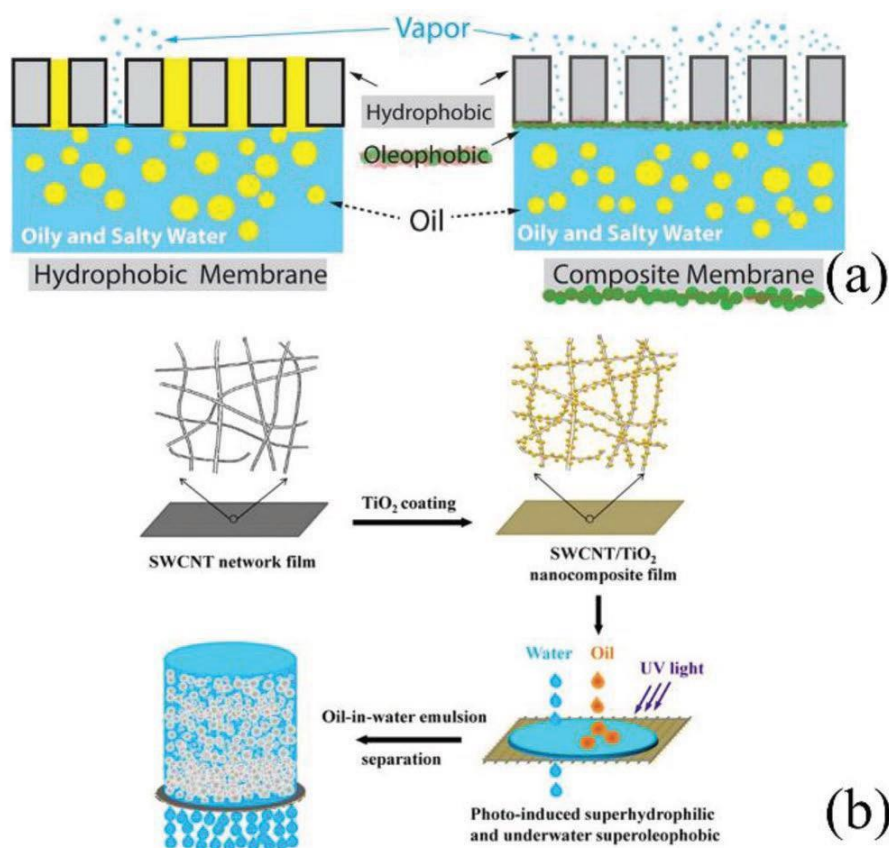


Figure 22. a) Differences between hydrophobic and underwater oleophobic membranes. Reproduced with permission.³⁶⁴ Copyright 2016, American Chemical Society. b) Separation of an oil-in-water emulsion by light responsive membranes made by TiO₂-coated single-walled carbon nanotubes. Reproduced with permission.³⁶² Copyright 2014, American Chemical Society.

UV light irradiation switched the SP polymer brushes from the passive state to the active MC isoform, which resulted able to bind several divalent ions such as Cd²⁺, Ni²⁺, Cu²⁺, Co²⁺, and Zn²⁺. Irradiation with white light

caused the recovery of the passive SP isoform and the release of the divalent ions from the microcapillary coating.

1.7.6 FLUX CONTROL

Pore size and flux through polymer porous membranes can be controlled by the conformational changes in light responsive polymer chains upon UV irradiation. Thus, many research groups have focused their investigations in developing on demand gated membranes containing light responsive molecules able to modulate pore size, surface hydrophilicity, channel charge, and polarity.^{375–377} Shi et al.³⁷⁸ prepared a photoresponsive polyethersulfone membrane based on the host–guest complex between Azo and β -cyclodextrin (β -CD). Poly(ethylene glycol) (PEG-2000 and PEG-6000) was used as a “bridge” between the Azo/ β -CD and polymer membrane to provide sufficient space for the photoisomerization and complex formation. Under irradiation at 450 nm, the formation of complexes between Azo and β -CD molecules closed the membrane pores and permeability for water and PEG solutions was low; under UV irradiation at 365 nm the complex collapse opened the membrane pores and permeability increased, as shown in Figure 23. The photoresponsivity increased with the amount of Azo and β -CD and did not show evident attenuation after 8 irradiation cycles.

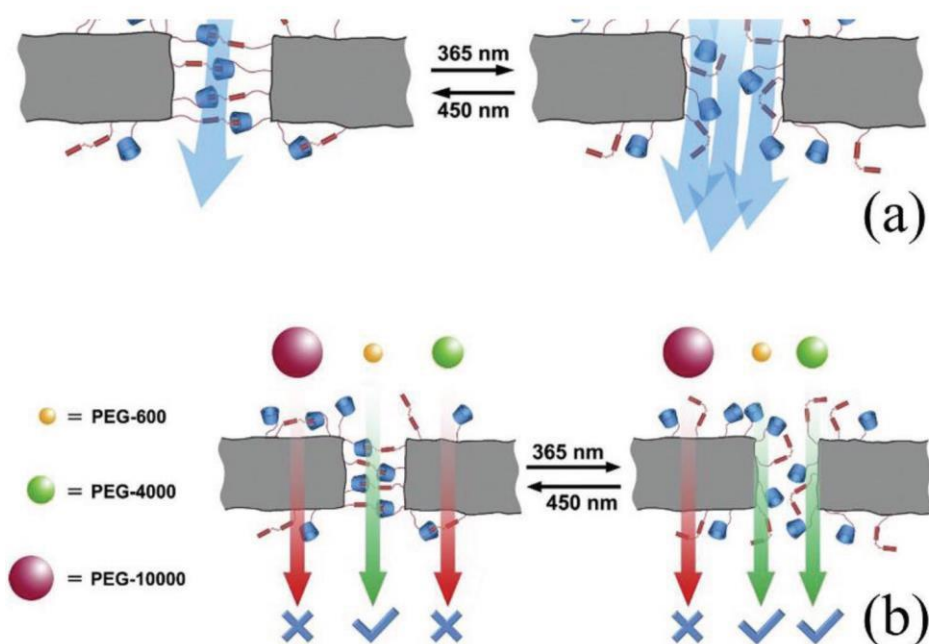


Figure 23. a) Polyethersulfone membranes with photoresponsive permeability. b) Selective permeation of PEG-600, PEG-4000, and PEG-10 000. Reproduced with permission.³⁷⁸ Copyright 2014, Elsevier.

1.8 CONCLUSION

In this paper, we reported recent progresses in light responsive polymer membranes with particular attention to photoswitching properties of the involved chemical groups and responsive mechanisms, which can change the membrane properties on demand. Light can induce very few physicochemical property changes, which can affect the performance of a great variety of devices. This progress report has focused its attention on some

important research applications driven by photoresponsive polymer membranes. The chemical groups commonly used to prepare light-responsive polymer membranes were reviewed in the first part of this progress report. Upon irradiation, the new isomer generally shows a different molecular geometry, which results in a variation of several physicochemical properties including electrical dipole moment, molecular volume, and exposed chemical groups. The change of such molecular properties is exploited in the manufacturing of polymer membranes able to photocontrol their wettability, swelling, adsorption, enzyme activity, cleaning, and permeability. Particular focus was given to some important applications of photoresponsive polymer membranes according to the used chromophoric groups. Photochromic liquid crystals and liquid crystalline polymer networks can reversibly change their mesomorphism, alignment, or pitch after UV or Vis light irradiation. Generally, it results in a macroscopic change of the optical states (opaque, intermediate, and transparent) of liquid crystal devices, polymer dispersed liquid crystals, and cholesteric cells.

Several applications related to photoreversible change of surface and pore-wettability in polymer membranes incorporating azobenzene and spiropyran groups have been reported. The change in the hydrophilic or hydrophobic behavior of polymer membranes allows the production of light adaptive nanochannels, gates, and valves for the mass transfer of ions, liquids, and gases.

Furthermore, photochromic molecules placed on the surface of polymer membranes can photocontrol the surface roughness and confer to the membranes superhydrophilic or superhydrophobic properties able to influence the cell migration on polymer membrane surfaces. Particular attention has been paid to light-driven actuators (i.e., devices able to convert the electromagnetic radiation energy into motion) such as photochromic bilayers, polymer films, liquid crystalline polymers, elastomers, hydrogels, and droplets flowing in microchannels. For instance, motion can be due to the reversible bending of photochromic polymer films related to the anisotropic volume contraction in the irradiated surface or the cyclic swelling and shrinking of photoresponsive and thermoresponsive hydrogels. The biological applications of photoresponsive polymer membranes in the present work include the progresses in the control of biological functions, protein adsorption, cell adhesion, and drug delivery by light. Finally, membrane processes were reviewed with a particular focus on the transport theory through porous polymer membranes, advanced oxidation processes able to confer antifouling, antimicrobial, and self-cleaning properties, and applications of light-responsive polymer membranes in water purification and flux control. There is no doubt that the development of light-responsive polymer membranes will offer numerous opportunities for designing advanced multifunctional surfaces and new high-performance devices in analogy to natural biological membranes, where multistimuli response mechanisms are present. Moreover, computational studies will undoubtedly provide a valuable guidance to find the optimal coupling between membrane physicochemical properties and photoresponsive groups to be used in advanced applications.

REFERENCES

- [1] D. Bhattacharyya, T. Schäfer, S. R. Wickramasinghe, D. S., *Responsive Membranes and Materials*, Chichester, West Sussex, UK **2013**.
- [2] S. Darvishmanesh, X. H. Qian, S. R. Wickramasinghe, *Curr. Opin. Chem. Eng.* **2015**, 8, 98.
- [3] K. Ishihara, N. Hamada, S. Kato, I. Shinohara, *J. Polym. Sci., Part A-1: Polym. Chem.* **1984**, 22, 121.
- [4] A. Gugliuzza, *Membranes* **2013**, 3, 151.
- [5] P. K. Bolla, V. A. Rodriguez, R. S. Kalhapure, C. S. Kolli, S. Andrews, J. Renukuntla, *J. Drug Delivery Sci. Technol.* **2018**, 46, 416.
- [6] Z. Liu, Y. Faraj, X.-J. Ju, W. Wang, R. Xie, L.-Y. Chu, *J. Polym. Sci., Part B: Polym. Phys.* **2018**, 56, 1306.
- [7] U. Kauscher, M. N. Holme, M. Björnmalm, M. M. Stevens, *Adv. Drug Delivery Rev.* **2019**, 138, 259.
- [8] J. Son, G. Yi, J. Yoo, C. Park, H. Koo, H. S. Choi, *Adv. Drug Delivery Rev.* **2019**, 138, 133.
- [9] M. K. Purkait, M. K. Sinha, P. Mondal, R. Singh, in *Stimuli Responsive Polymeric Membranes*, Vol. 25 (Eds: M. K. Purkait, M. K. Sinha, P. Mondal, R. Singh), Elsevier, Amsterdam, Netherlands **2018**.
- [10] P. Formoso, E. Pantuso, G. De Filipo, F. P. Nicoletta, *Membranes* **2017**, 7, 39.
- [11] J. J. t. Keating, J. Imbrogno, G. Belfort, *ACS Appl. Mater. Interfaces* **2016**, 8, 28383.
- [12] A. Khan, L. Wang, H. Yu, M. Haroon, R. S. Ullah, A. Nazir, T. Elshaarani, M. Usman, S. Fahad, F. Haq, *Appl. Organomet. Chem.* **2018**, 32, e4575.
- [13] Y. Li, Q. Li, in *Intelligent Stimuli-Responsive Materials: From Well-Defined Nanostructures to Applications* (Ed: Q. Li), Wiley-VCH, Weinheim, Germany **2013**, Chap. 1.
- [14] L. Qin, Y. Yu. in *Responsive Polymer Surfaces: Dynamics in Surface Topography* (Eds: D. Liu, D. J. Broer), Wiley-VCH, Weinheim, Germany **2017**, Chap. 1.
- [15] E. Drioli, L. Giorno, in *Encyclopedia of Membranes* (Eds: E. Drioli, L. Giorno), Springer-Verlag, Berlin/Heidelberg, Germany **2016**.
- [16] H. Strathmann, L. Giorno, E. Drioli, in *Comprehensive Membrane Science and Engineering* (Eds: E. Drioli, L. Giorno), Elsevier, Oxford, UK **2010**, p. 91.
- [17] H. P. C. van Kuringen, A. P. H. J. Schenning, *Hydrogen Bonded Supramolecular Materials*, Springer, Heidelberg, Berlin **2015**.
- [18] D. Liu, D. J. Broer, *Responsive Polymer Surfaces: Dynamics in Surface Topography*, Wiley-VCH, Weinheim, Germany **2017**.
- [19] M. Iqbal, R. Banerjee, S. Barman, S. Atta, D. Dhara, N. D. P. Singh, *J. Mater. Chem. C* **2014**, 2, 4622.
- [20] J. S. Leng, X. Lan, Y. J. Liu, S. Y. Du, *Prog. Mater. Sci.* **2011**, 56, 1077.
- [21] F. Ilievski, A. D. Mazzeo, R. E. Shepherd, X. Chen, G. M. Whitesides, *Angew. Chem., Int. Ed.* **2011**, 50, 1890.

- [22] J. S. Leng, W. M. Huang, X. Lan, Y. J. Liu, S. Y. Du, *Appl. Phys. Lett.* **2008**, *92*, 014104.
- [23] R. Mohr, K. Kratz, T. Weigel, M. Lucka-Gabor, M. Moneke, A. Lendlein, *Proc. Natl. Acad. Sci. USA* **2006**, *103*, 3540.
- [24] A. H. Gelebart, M. Mc Bride, A. P. H. J. Schenning, C. N. Bowman, D. J. Broer, *Adv. Funct. Mater.* **2016**, *26*, 5322.
- [25] J. E. Stumpel, D. J. Broer, A. P. H. J. Schenning, *Chem. Commun.* **2014**, *50*, 15839.
- [26] N. Wagner, P. Theato, *Polymer* **2014**, *55*, 3436.
- [27] F. P. Nicoletta, D. Cupelli, P. Formoso, G. De Filpo, V. Colella, A. Gugliuzza, *Membranes* **2012**, *2*, 134.
- [28] R. Klajn, *Chem. Soc. Rev.* **2014**, *43*, 148.
- [29] K. Fries, S. Samanta, S. Orski, J. Locklin, *Chem. Commun.* **2008**, 6288.
- [30] G. Kaur, P. Johnston, K. Saito, *Polym. Chem.* **2014**, *5*, 2171.
- [31] Y. Inaki, H. Hiratsuka, *J. Photopolym. Sci. Technol.* **2000**, *13*, 739.
- [32] Y. Kita, T. Uno, Y. Inaki, K. Takemoto, *J. Polym. Sci., Part A-1: Polym. Chem.* **1981**, *19*, 1733.
- [33] D. E. Marschner, H. Frisch, J. T. Offenloch, B. T. Tuten, C. R. Becer, A. Walther, A. S. Goldmann, P. Tzvetkova, C. Barner-Kowollik, *Macromolecules* **2018**, *51*, 3802.
- [34] K. Stranius, K. Börjesson, *Sci. Rep.* **2017**, *7*, 41145.
- [35] H. P. C. van Kuringen, J. W. A. Leijten, A. H. Gelebart, D. J. Mulder, G. Portale, D. J. Broer, A. P. H. J. Schenning, *Macromolecules* **2015**, *48*, 4073.
- [36] D. Cupelli, G. Filpo, G. Chidichimo, F. P. Nicoletta, *J. Appl. Phys.* **2006**, *100*, 024508.
- [37] D. Cupelli, F. P. Nicoletta, S. Manfredi, G. De Filpo, G. Chidichimo, *Sol. Energy Mater. Sol. Cells* **2009**, *93*, 329.
- [38] H. K. Bisoyi, Q. Li, *Chem. Rev.* **2016**, *116*, 15089.
- [39] H. K. Lee, A. Kanazawa, T. Shiono, T. Ikeda, T. Fujisawa, M. Aizawa, B. Lee, *J. Appl. Phys.* **1999**, *86*, 5927
- [40] T. Seki, S. Nagano, M. Hara, *Polymer* **2013**, *54*, 6053.
- [41] N. Tsutsumi, *Polym. Int.* **2017**, *66*, 167.
- [42] O. R. Bennani, T. A. Al-Hujran, J. M. Nunzi, R. G. Sabat, O. Lebel, *New J. Chem.* **2015**, *39*, 9162.
- [43] L. De Sio, D. E. Roberts, Z. Liao, S. Nersisyan, O. Uskova, L. Wickboldt, N. Tabiryan, D. M. Steeves, B. R. Kimball, *Opt. Express* **2016**, *24*, 18297.
- [44] A. Priimagi, A. Shevchenko, *J. Polym. Sci., Part B: Polym. Phys.* **2014**, *52*, 163.
- [45] E. Perivolari, J. R. Gill, N. Podoliak, V. Apostolopoulos, T. J. Sluckin, G. D'Alessandro, M. Kaczmarek, *J. Mol. Liq.* **2018**, *267*, 484.

- [46] E. Mavrona, S. Mailis, N. Podoliak, G. D'Alessandro, N. Tabiryan, M. Trapatseli, J. F. Blach, M. Kaczmarek, V. Apostolopoulos, *Opt.Mater. Express* **2018**, 8, 420.
- [47] I. M. Tkachenko, Y. L. Kobzar, V. F. Korolovych, A. V. Stryutsky, L. K. Matkovska, V. V. Shevchenko, V. V. Tsukruk, *J. Mater. Chem. C* **2018**, 6, 4065.
- [48] E. Lucenti, C. Botta, E. Cariati, S. Righetto, M. Scarpellini, E. Tordin, R. Ugo, *Dyes Pigm.* **2013**, 96, 748.
- [49] P. A. Ledin, M. Russell, J. A. Geldmeier, I. M. Tkachenko, M. A. Mahmoud, V. Shevchenko, M. A. El-Sayed, V. V. Tsukruk, *ACS Appl. Mater. Interfaces* **2015**, 7, 4902.
- [50] C. T. Wang, Y. C. Wu, T. H. Lin, *Dyes Pigm.* **2014**, 103, 21.
- [51] C. V. Rajaram, S. D. Huson, L. C. Chien, *Chem. Mater.* **1995**, 7, 2300.
- [52] M. Macchione, D. Cupelli, G. De Filpo, F. P. Nicoletta, G. Chidichimo, *Liq. Cryst.* **2000**, 27, 917.
- [53] M. Macchione, D. Cupelli, G. De Filpo, F. P. Nicoletta, G. Chidichimo, *Liq. Cryst.* **2000**, 27, 1337.
- [54] F. P. Nicoletta, G. De Filpo, D. Cupelli, M. Macchione, G. Chidichimo, *Appl. Phys. Lett.* **2001**, 79, 4325.
- [55] D. K. Yang, L. C. Chien, Y. K. Fung, in *Liquid Crystals in Complex Geometries Formed by Polymer and Porous Networks*, Vol. 9 (Eds: G. P. Crawford, S. Zumer), Taylor & Francis, London **1996**, Chap. 5.
- [56] J. Yeon, T. W. Koh, H. Cho, J. Chung, S. Yoo, J. B. Yoon, *Opt. Express* **2013**, 21, 10358.
- [57] D. Cupelli, F. P. Nicoletta, S. Manfredi, M. Vivacqua, P. Formoso, G. De Filpo, G. Chidichimo, *Sol. Energy Mater. Sol. Cells* **2009**, 93, 2008.
- [58] G. De Filpo, P. Formoso, S. Manfredi, A. I. Mashin, F. P. Nicoletta, *Liq. Cryst.* **2017**, 44, 1607.
- [59] J. A. H. P. Sol, G. H. Timmermans, A. J. van Breugel, A. P. H. J. Schenning, M. G. Debije, *Adv. Energy Mater.* **2018**, 8, 1702922.
- [60] B. McKenna, R. C. Evans, *Adv. Mater.* **2017**, 29, 1606491.
- [61] C. Serban, V. D. Moldoveanu, in *Selection of the HPLC Method in Chemical Analysis*, Elsevier, Amsterdam, Netherlands **2017**, Chap. 7.
- [62] L. Feng, S. H. Li, Y. S. Li, H. J. Li, L. J. Zhang, J. Zhai, Y. L. Song, B. Q. Liu, L. Jiang, D. B. Zhu, *Adv. Mater.* **2002**, 14, 1857.
- [63] K. S. Liu, D. L. Tian, L. Jiang, in *Modern Inorganic Synthetic Chemistry* (Eds: R. Xu, Y. Xu), Elsevier, Amsterdam, Netherlands **2017**, p. 687.
- [64] X. J. Feng, L. Jiang, *Adv. Mater.* **2006**, 18, 3063.
- [65] F. Xia, L. Feng, S. T. Wang, T. L. Sun, W. L. Song, W. H. Jiang, L. Jiang, *Adv. Mater.* **2006**, 18, 432.
- [66] L. Valentini, M. Cardinali, J. M. Kenny, M. Prato, O. Monticelli, *Eur. J. Inorg. Chem.* **2012**, 2012, 5282.
- [67] H. Amarné, C. Baik, S. K. Murphy, S. Wang, *Chem. - Eur. J.* **2010**, 16, 4750.
- [68] P. Formoso, R. Muzzalupo, L. Tavano, G. De Filpo, F. P. Nicoletta, *Mini-Rev. Med. Chem.* **2016**, 16, 668.
- [69] S. Moller, U. Pliquet, C. Hoffmann, *RSC Adv.* **2012**, 2, 4792.

- [70] X. Pei, A. Fernandes, B. Mathy, X. Laloyaux, B. Nysten, O. Riant, A. M. Jonas, *Langmuir* **2011**, *27*, 9403.
- [71] W. H. Jiang, G. J. Wang, Y. N. He, X. G. Wang, Y. L. An, Y. L. Song, L. Jiang, *Chem. Commun.* **2005**, *28*, 3550.
- [72] J. Zhang, H. Tian, in *Photochromic Materials Preparation, Properties and Applications* (Eds: H. Tian, J. Zhang), Wiley-VCH, Weinheim, Germany **2016**, Chap. 6.
- [73] P. B. Wan, Y. G. Jiang, Y. P. Wang, Z. Q. Wang, X. Zhang, *Chem. Commun.* **2008**, 5710.
- [74] X. Y. Zhang, H. Y. Zhao, D. M. Tian, H. T. Deng, H. B. Li, *Chem.- Eur. J.* **2014**, *20*, 9367.
- [75] Y. Liu, Y. Chen, *Acc. Chem. Res.* **2006**, *39*, 681.
- [76] S. Tamesue, Y. Takashima, H. Yamaguchi, S. Shinkai, A. Harada, *Angew. Chem., Int. Ed.* **2010**, *49*, 7461.
- [77] A. Harada, *Acc. Chem. Res.* **2001**, *34*, 456.
- [78] K. Y. Chen, O. Ivashenko, G. T. Carroll, J. Robertus, J. C. Kistemaker, G. London, W. R. Browne, P. Rudolf, B. L. Feringa, *J. Am. Chem. Soc.* **2014**, *136*, 3219.
- [79] Y. Zakrevskyy, M. Richter, S. Zakrevska, N. Lomadze, R. von Klitzing, S. Santer, *Adv. Funct. Mater.* **2012**, *22*, 5000.
- [80] M. Kettunen, R. J. Silvennoinen, N. Houbenov, A. Nykanen, J. Ruokolainen, J. Sainio, V. Pore, M. Kemell, M. Ankerfors, T. Lindstrom, M. Ritala, R. H. A. Ras, O. Ikkala, *Adv. Funct. Mater.* **2011**, *21*, 510.
- [81] D. Kessler, F. D. Jochum, J. Choi, K. Char, P. Theato, *ACS Appl. Mater. Interfaces* **2011**, *3*, 124.
- [82] D. Wang, P. W. Jiao, J. M. Wang, Q. L. Zhang, L. Feng, Z. Z. Yang, *J. Appl. Polym. Sci.* **2012**, *125*, 870.
- [83] G. Sinawang, B. Wu, J. L. Wang, S. Li, Y. N. He, *Macromol. Chem. Phys.* **2016**, *217*, 2409.
- [84] S. Helmy, S. Oh, F. A. Leibfarth, C. J. Hawker, J. Read de Alaniz, *J. Org. Chem.* **2014**, *79*, 11316.
- [85] S. Helmy, F. A. Leibfarth, S. Oh, J. E. Poelma, C. J. Hawker, J. Read de Alaniz, *J. Am. Chem. Soc.* **2014**, *136*, 8169.
- [86] Y. He, Y. Zhu, Z. Chen, W. He, X. Wang, *Chem. Commun.* **2013**, *49*, 5556.
- [87] M. M. Lerch, S. J. Wezenberg, W. Szymanski, B. L. Feringa, *J. Am. Chem. Soc.* **2016**, *138*, 6344.
- [88] A. D. Laurent, M. Medved, D. Jacquemin, *ChemPhysChem* **2016**, *17*, 1846.
- [89] S. Singh, K. Friedel, M. Himmerlich, Y. Lei, G. Schlingloff, A. Schober, *ACS Macro Lett.* **2015**, *4*, 1273.
- [90] A. Balamurugan, H. I. Lee, *Macromolecules* **2016**, *49*, 2568.
- [91] M. Macchione, G. De Filpo, F. P. Nicoletta, G. Chidichimo, *Chem. Mater.* **2004**, *16*, 1400.
- [92] A. Lafuma, D. Quere, *Nat. Mater.* **2003**, *2*, 457.
- [93] K. Koch, B. Bhushan, W. Barthlott, *Soft Matter* **2008**, *4*, 1943.

- [94] K.-S. Liu, D. L. Tian, L. Jiang, in *Modern Inorganic Synthetic Chemistry* (Eds: R. Xu, Y. Xu), Elsevier, Amsterdam, Netherlands **2017**.
- [95] C. Schuh, N. Lomadze, J. Ruhe, A. Kopyshv, S. Santer, *J. Phys. Chem. B* **2011**, *115*, 10431.
- [96] D. Y. Kim, S. K. Tripathy, L. Li, J. Kumar, *Appl. Phys. Lett.* **1995**, *66*, 1166.
- [97] N. S. Yadavalli, S. Santer, *J. Appl. Phys.* **2013**, *113*, 224304.
- [98] M. Saphiannikova, D. Neher, *J. Phys. Chem. B* **2005**, *109*, 19428.
- [99] V. Toshchevnikov, M. Saphiannikova, G. Heinrich, *J. Phys. Chem. B* **2009**, *113*, 5032.
- [100] N. Lomadze, A. Kopyshv, J. Ruhe, S. Santer, *Macromolecules* **2011**, *44*, 7372.
- [101] N. Zettsu, T. Ogasawara, N. Mizoshita, S. Nagano, T. Seki, *Adv. Mater.* **2008**, *20*, 516.
- [102] A. Kopyshv, C. J. Galvin, R. R. Patil, J. Genzer, N. Lomadze, D. Feldmann, J. Zakrevski, S. Santer, *ACS Appl. Mater. Interfaces* **2016**, *8*, 19175.
- [103] H. Finkelmann, *Angew. Chem., Int. Ed. Engl.* **1987**, *26*, 816.
- [104] E. K. Fleischmann, R. Zentel, *Angew. Chem., Int. Ed.* **2013**, *52*, 8810.
- [105] T. J. White, D. J. Broer, *Nat. Mater.* **2015**, *14*, 1087.
- [106] D. Cupelli, F. P. Nicoletta, G. De Filipo, P. Formoso, G. Chidichimo, *J. Polym. Sci., Part B: Polym. Phys.* **2011**, *49*, 257.
- [107] D. Q. Liu, C. W. M. Bastiaansen, J. M. J. den Toonder, D. J. Broer, *Macromolecules* **2012**, *45*, 8005.
- [108] D. Q. Liu, D. J. Broer, *Liq. Cryst. Rev.* **2013**, *1*, 20.
- [109] D. Liu, D. J. Broer, *Nat. Commun.* **2015**, *6*, 8334.
- [110] D. Liu, D. J. Broer, *Angew. Chem., Int. Ed.* **2014**, *53*, 4542.
- [111] Y. Zhan, J. Zhao, W. Liu, B. Yang, J. Wei, Y. Yu, *ACS Appl. Mater. Interfaces* **2015**, *7*, 25522.
- [112] H. Hou, J. Yin, X. Jiang, *Adv. Mater.* **2016**, *28*, 9126.
- [113] S. Zeng, R. Li, S. G. Freire, V. M. M. Garbellotto, E. Y. Huang, A. T. Smith, C. Hu, W. R. T. Tait, Z. Bian, G. Zheng, D. Zhang, L. Sun, *Adv. Mater.* **2017**, *29*, 1700828.
- [114] C. Liu, Y. Zhang, M. Liu, Z. Chen, Y. Lin, W. Li, F. Cao, Z. Liu, J. Ren, X. Qu, *Biomaterials* **2017**, *139*, 151.
- [115] F. Li, H. H. Hou, J. Yin, X. S. Jiang, *Sci. Adv.* **2018**, *4*, eaar5762.
- [116] C. S. Li, Y. Liu, C. W. Lo, H. R. Jiang, *Soft Matter* **2011**, *7*, 7511.
- [117] L. Q. Yang, K. Setyowati, A. Li, S. Q. Gong, J. Chen, *Adv. Mater.* **2008**, *20*, 2271.
- [118] H. Y. Wen, W. D. Zhang, Y. Y. Weng, Z. J. Hu, *RSC Adv.* **2014**, *4*, 11776.
- [119] H. Zhao, P. Theato, *Polym. Chem.* **2013**, *4*, 891.

- [120] J. J. Shang, S. J. Lin, P. Theato, *Polym. Chem.* **2018**, *9*, 3232.
- [121] D. Y. Kim, S. Shin, W. J. Yoon, Y. J. Choi, J. K. Hwang, J. S. Kim, C. R. Lee, T. L. Choi, K. U. Jeong, *Adv. Funct. Mater.* **2017**, *27*, 1606294.
- [122] Z. Liu, R. Tang, D. Xu, J. Liu, H. Yu, *Macromol. Rapid Commun.* **2015**, *36*, 1171.
- [123] D. Liu, D. J. Broer, *Langmuir* **2014**, *30*, 13499.
- [124] Y. Liu, W. Wu, J. Wei, Y. Yu, *ACS Appl. Mater. Interfaces* **2017**, *9*, 782.
- [125] A. H. Gelebart, D. J. Mulder, G. Vantomme, A. P. H. J. Schenning, D. J. Broer, *Angew. Chem., Int. Ed.* **2017**, *56*, 13436.
- [126] L. M. Goldenberg, L. Kulikovskiy, O. Kulikovskaya, J. Stumpe, *J. Mater. Chem.* **2009**, *19*, 8068.
- [127] D. Bleger, S. Hecht, *Angew. Chem., Int. Ed.* **2015**, *54*, 11338.
- [128] K. Kumar, C. Knie, D. Bleger, M. A. Peletier, H. Friedrich, S. Hecht, D. J. Broer, M. G. Debije, A. P. Schenning, *Nat. Commun.* **2016**, *7*, 11975.
- [129] Y. Yu, M. Nakano, T. Ikeda, *Nature* **2003**, *425*, 145.
- [130] Y. L. Yu, M. Nakano, A. Shishido, T. Shiono, T. Ikeda, *Chem. Mater.* **2004**, *16*, 1637.
- [131] M. Yamada, M. Kondo, J. Mamiya, Y. Yu, M. Kinoshita, C. J. Barrett, T. Ikeda, *Angew. Chem., Int. Ed.* **2008**, *47*, 4986.
- [132] A. Shimamura, A. Priimagi, J. Mamiya, T. Ikeda, Y. Yu, C. J. Barrett, A. Shishido, *ACS Appl. Mater. Interfaces* **2011**, *3*, 4190.
- [133] T. Ube, K. Kawasaki, T. Ikeda, *Adv. Mater.* **2016**, *28*, 8212.
- [134] T. Ikeda, T. Ube, *Mater. Today* **2011**, *14*, 480.
- [135] C. Ohm, M. Brehmer, R. Zentel, *Adv. Mater.* **2010**, *22*, 3366.
- [136] L. T. de Haan, C. Sanchez-Somolinos, C. M. Bastiaansen, A. P. Schenning, D. J. Broer, *Angew. Chem., Int. Ed.* **2012**, *51*, 12469.
- [137] S. Serak, N. Tabiryan, R. Vergara, T. J. White, R. A. Vaia, T. J. Bunning, *Soft Matter* **2010**, *6*, 779.
- [138] M. Behl, M. Y. Razzaq, A. Lendlein, *Adv. Mater.* **2010**, *22*, 3388.
- [139] O. S. Bushuyev, M. Aizawa, A. Shishido, C. J. Barrett, *Macromol. Rapid Commun.* **2018**, *39*, 700253.
- [140] P. Taynton, K. Yu, R. K. Shoemaker, Y. Jin, H. J. Qi, W. Zhang, *Adv. Mater.* **2014**, *26*, 3938.
- [141] Z. Pei, Y. Yang, Q. Chen, E. M. Terentjev, Y. Wei, Y. Ji, *Nat. Mater.* **2014**, *13*, 36.
- [142] C. J. Kloxin, T. F. Scott, H. Y. Park, C. N. Bowman, *Adv. Mater.* **2011**, *23*, 1977.
- [143] Y. Liu, B. Shaw, M. D. Dickey, J. Genzer, *Sci. Adv.* **2017**, *3*, e1602417.
- [144] S. Iamsaard, E. Villemin, F. Lancia, S. J. Asshoff, S. P. Fletcher, N. Katsonis, *Nat. Protoc.* **2016**, *11*, 1788.

- [145] M. Guix, C. C. Mayorga-Martinez, A. Merkoci, *Chem. Rev.* **2014**, *114*, 6285.
- [146] S. Erbas-Cakmak, D. A. Leigh, C. T. McTernan, A. L. Nussbaumer, *Chem. Rev.* **2015**, *115*, 10081.
- [147] K. Ichimura, S. K. Oh, M. Nakagawa, *Science* **2000**, *288*, 1624.
- [148] S.-K. Oh, M. Nakagawa, K. Ichimura, *J. Mater. Chem.* **2002**, *12*, 2262.
- [149] G. M. Whitesides, *Nature* **2006**, *442*, 368.
- [150] C. Y. Lee, C. L. Chang, Y. N. Wang, L. M. Fu, *Int. J. Mol. Sci.* **2011**, *12*, 3263.
- [151] Z. Qiu, H. Yu, J. Li, Y. Wang, Y. Zhang, *Chem. Commun.* **2009**, 3342.
- [152] D. Kim, H. S. Lee, J. Yoon, *RSC Adv.* **2014**, *4*, 25379.
- [153] S. Nakamura, S. Onimaru, Y. Oishi, T. Narita, *Polymer* **2017**, *116*, 534.
- [154] S. Sugiura, A. Szilagyi, K. Sumaru, K. Hattori, T. Takagi, G. Filipcsei, M. Zrinyi, T. Kanamori, *Lab Chip* **2009**, *9*, 196.
- [155] C. Delaney, P. McCluskey, S. Coleman, J. Whyte, N. Kent, D. Diamond, *Lab Chip* **2017**, *17*, 2013.
- [156] S. Coleman, J. ter Schiphorst, A. Ben Azouz, S. Bakker, A. P. H. J. Schenning, D. Diamond, *Sens. Actuators, B* **2017**, *245*, 81.
- [157] J. ter Schiphorst, J. Saez, D. Diamond, F. Benito-Lopez, A. P. H. J. Schenning, *Lab Chip* **2018**, *18*, 699.
- [158] L. Florea, K. Wagner, P. Wagner, G. G. Wallace, F. Benito-Lopez, D. L. Officer, D. Diamond, *Adv. Mater.* **2014**, *26*, 7339.
- [159] T. Wu, T. A. Nieminen, S. Mohanty, J. Miotke, R. L. Meyer, H. Rubinsztein-Dunlop, M. W. Berns, *Nat. Photonics* **2012**, *6*, 62.
- [160] Z. Walsh, S. Scarmagnani, F. Benito-Lopez, S. Abele, F. Q. Nie, C. Slater, R. Byrne, D. Diamond, B. Paull, M. Macka, *Sens. Actuators, B* **2010**, *148*, 569.
- [161] S. Maeda, Y. Hara, T. Sakai, R. Yoshida, S. Hashimoto, *Adv. Mater.* **2007**, *19*, 3480.
- [162] S. Maeda, Y. Hara, R. Yoshida, S. Hashimoto, *Int. J. Mol. Sci.* **2010**, *11*, 52.
- [163] W. Francis, A. Dunne, C. Delaney, L. Florea, D. Diamond, *Sens. Actuators, B* **2017**, *250*, 608.
- [164] G. De Filpo, S. Siprova, G. Chidichimo, A. I. Mashin, F. P. Nicoletta, D. Cupelli, *Liq. Cryst.* **2012**, *39*, 359.
- [165] J. R. Velez-Cordero, J. Hernandez-Cordero, *Int. J. Therm. Sci.* **2015**, *96*, 12.
- [166] E. Miyako, H. Nagata, K. Hirano, T. Hirotsu, *Lab Chip* **2009**, *9*, 788.
- [167] M. Hautefeuille, L. Cabriales, R. Pimentel-Dominguez, V. Velazquez, J. Hernandez-Cordero, L. Oropeza-Ramos, M. Rivera, M. P. Carreon-Castro, M. Grether, E. Lopez-Moreno, *Lab Chip* **2013**, *13*, 4848.
- [168] S. V. Ahir, E. M. Terentjev, *Nat. Mater.* **2005**, *4*, 491.

- [169] F. M. Sanchez-Arevalo, I. M. Garnica-Palafox, P. Jagdale, J. Hernandez-Cordero, S. E. Rodil, A. O. Okonkwo, F. C. R. Hernandez, A. Tagliaferro, *Opt. Mater. Express* **2015**, *5*, 1792.
- [170] R. Pimentel-Dominguez, A. M. Velazquez-Benitez, J. Rodrigo Velez-Cordero, M. Hautefeuille, F. Sanchez-Arevalo, J. Hernandez-Cordero, *Polymers* **2016**, *8*, 84.
- [171] S. Szczukiewicz, M. Magnini, J. R. Thome, *Int. J. Multiphase Flow* **2014**, *59*, 84.
- [172] A. M. Velazquez-Benitez, M. Reyes-Medrano, J. R. Velez-Cordero, J. Hernandez-Cordero, *J. Lightwave Technol.* **2015**, *33*, 176.
- [173] K. Xiao, X. Y. Kong, Z. Zhang, G. H. Xie, L. P. Wen, L. Jiang, *J. Photochem. Photobiol., C* **2016**, *26*, 31.
- [174] L. P. Wen, L. Jiang, *Natl. Sci. Rev.* **2014**, *1*, 144.
- [175] G. Mayer, A. Heckel, *Angew. Chem., Int. Ed.* **2006**, *45*, 4900.
- [176] S. Howorka, Z. Siwy, *Chem. Soc. Rev.* **2009**, *38*, 2360.
- [177] L. P. Wen, X. Hou, Y. Tian, J. Zhai, L. Jiang, *Adv. Funct. Mater.* **2010**, *20*, 2636.
- [178] L. P. Wen, Y. Tian, Y. L. Guo, J. Ma, W. D. Liu, L. Jiang, *Adv. Funct. Mater.* **2013**, *23*, 2887.
- [179] I. Vlassiuk, S. Smirnov, Z. Siwy, *Nano Lett.* **2008**, *8*, 1978.
- [180] N. G. Liu, D. R. Dunphy, P. Atanassov, S. D. Bunge, Z. Chen, G. P. Lopez, T. J. Boyle, C. J. Brinker, *Nano Lett.* **2004**, *4*, 551.
- [181] I. Vlassiuk, C. D. Park, S. A. Vail, D. Gust, S. Smirnov, *Nano Lett.* **2006**, *6*, 1013.
- [182] B. Soberats, E. Uchida, M. Yoshio, J. Kagimoto, H. Ohno, T. Kato, *J. Am. Chem. Soc.* **2014**, *136*, 9552.
- [183] W. A. Phillip, M. Amendt, B. O'Neill, L. Chen, M. A. Hillmyer, E. L. Cussler, *ACS Appl. Mater. Interfaces* **2009**, *1*, 472.
- [184] R. Raccis, A. Nikoubashman, M. Retsch, U. Jonas, K. Koynov, H. J. Butt, C. N. Likos, G. Fytas, *ACS Nano* **2011**, *5*, 4607.
- [185] K. Weh, M. Noack, K. Hoffmann, K. P. Schroder, J. Caro, *Microporous Mesoporous Mater.* **2002**, *54*, 15.
- [186] S. Yagi, N. Minami, J. Fujita, Y. Hyodo, H. Nakazumi, T. Yazawa, T. Kami, A. H. Ali, *Chem. Commun.* **2002**, *20*, 2444.
- [187] M. Fujiwara, T. Imura, *ACS Nano* **2015**, *9*, 5705.
- [188] A. Politano, P. Argurio, G. Di Profio, V. Sanna, A. Cupolillo, S. Chakraborty, H. A. Arafat, E. Curcio, *Adv. Mater.* **2017**, *29*, 1603504.
- [189] A. Politano, G. Di Profio, E. Fontananova, V. Sanna, A. Cupolillo, E. Curcio, *Desalination* **2019**, *451*, 192.
- [190] Z. Y. Meng, H. Bao, J. T. Wang, C. D. Jiang, M. H. Zhang, J. Zhai, L. Jiang, *Adv. Mater.* **2014**, *26*, 2329.

- [191] T. Kumeria, J. X. Yu, M. Alsawat, M. D. Kurkuri, A. Santos, A. D. Abell, D. Losic, *Adv. Mater.* **2015**, *27*, 3019.
- [192] P. Madhavan, B. Sutisna, R. Sougrat, S. P. Nunes, *RSC Adv.* **2016**, *6*, 75594.
- [193] M. H. Zhang, X. Hou, J. T. Wang, Y. Tian, X. Fan, J. Zhai, L. Jiang, *Adv. Mater.* **2012**, *24*, 2424.
- [194] L. P. Wen, Q. Liu, J. Ma, Y. Tian, C. H. Li, Z. S. Bo, L. Jiang, *Adv. Mater.* **2012**, *24*, 6193.
- [195] K. Xiao, G. H. Xie, P. Li, Q. Liu, G. L. Hou, Z. Zhang, J. Ma, Y. Tian, L. P. Wen, L. Jiang, *Adv. Mater.* **2014**, *26*, 6560.
- [196] K. Liang, G. K. Such, Z. Y. Zhu, Y. Yan, H. Lomas, F. Caruso, *Adv. Mater.* **2011**, *23*, H273.
- [197] M. Delcea, H. Mohwald, A. G. Skirtach, *Adv. Drug Delivery Rev.* **2011**, *63*, 730.
- [198] J. Pennakalathil, J. D. Hong, *ACS Nano* **2011**, *5*, 9232.
- [199] P. P. Campos, A. Dunne, C. Delaney, C. Moloney, S. E. Moulton, F. Benito-Lopez, M. Ferreira, D. Diamond, L. Florea, *Langmuir* **2018**, *34*, 4210.
- [200] P. Froimowicz, D. Klinger, K. Landfester, *Chem. - Eur. J.* **2011**, *17*, 12465.
- [201] P. T. Anastas, *Crit. Rev. Anal. Chem.* **1999**, *29*, 167.
- [202] P. Johnston, C. Braybrook, K. Saito, *Chem. Sci.* **2012**, *3*, 2301.
- [203] M. Sierant, P. Paluch, M. Florczak, A. Rozanski, B. Miksa, *Colloids Surf., B* **2013**, *111*, 571.
- [204] A. S. Hoffman, *Adv. Drug Delivery Rev.* **2002**, *54*, 3.
- [205] Y. Chujo, K. Sada, R. Nomura, A. Naka, T. Saegusa, *Macromolecules* **1993**, *26*, 5611.
- [206] Y. J. Zheng, F. M. Andreopoulos, M. Micic, Q. Huo, S. M. Pham, R. M. Leblanc, *Adv. Funct. Mater.* **2001**, *11*, 37.
- [207] K. Miyamoto, M. Sasaki, Y. Minamisawa, Y. Kurahashi, H. Kano, S. Ishikawa, *J. Biomed. Mater. Res.* **2004**, *70A*, 550.
- [208] K. M. Gattas-Asfura, E. Weisman, F. M. Andreopoulos, M. Micic, B. Muller, S. Sirpal, S. M. Pham, R. M. Leblanc, *Biomacromolecules* **2005**, *6*, 1503.
- [209] K. Yang, M. Zeng, *New J. Chem.* **2013**, *37*, 920.
- [210] J. Ling, M. Z. Rong, M. Q. Zhang, *J. Mater. Chem.* **2011**, *21*, 18373.
- [211] C. M. Chung, Y. S. Roh, S. Y. Cho, J. G. Kim, *Chem. Mater.* **2004**, *16*, 3982.
- [212] S. R. Trenor, A. R. Shultz, B. J. Love, T. E. Long, *Chem. Rev.* **2004**, *104*, 3059.
- [213] R. Seoane Rivero, P. Bilbao Solaguren, K. Gondra, L. Peponi, A. Marcos-Fernández, *eXPRESS Polym. Lett.* **2016**, *10*, 84.
- [214] Y. Sasaki, K. Akiyoshi, *Chem. Rec.* **2010**, *10*, 366.

- [215] G. Kaur, S. L. Y. Chang, T. D. M. Bell, M. T. W. Hearn, K. Saito, *J. Polym. Sci., Part A: Polym. Chem.* **2011**, *49*, 4121.
- [216] K. Nakabayashi, S. Inoue, Y. Abiko, H. Mori, *Macromolecules* **2013**, *46*, 4790.
- [217] J. You, Y. Kim, E. Kim, *Mol. Cryst. Liq. Cryst.* **2010**, *520*, 128/[404].
- [218] I. Tomatsu, K. Peng, A. Kros, *Adv. Drug Delivery Rev.* **2011**, *63*, 1257.
- [219] G. J. Wang, J. Zhang, *J. Photochem. Photobiol., C* **2012**, *13*, 299.
- [220] Y. W. Hao, J. X. Meng, S. T. Wang, *Chin. Chem. Lett.* **2017**, *28*, 2085.
- [221] A. M. Kloxin, M. W. Tibbitt, A. M. Kasko, J. A. Fairbairn, K. S. Anseth, *Adv. Mater.* **2010**, *22*, 61.
- [222] C. A. DeForest, K. S. Anseth, *Angew. Chem., Int. Ed.* **2012**, *51*, 1816.
- [223] B. L. Feringa, W. R. Browne, *Molecular Switches*, Wiley-VCH, Groningen, Netherlands **2011**.
- [224] F. Bonardi, G. London, N. Nouwen, B. Feringa, A. J. M. Driessen, *Angew. Chem., Int. Ed.* **2010**, *49*, 7234.
- [225] G. Kocer, J. Ter Schiphorst, M. Hendriks, H. G. Kassa, P. Leclere, A. Schenning, P. Jonkheijm, *Adv. Mater.* **2017**, *29*, 1606407.
- [226] T. Shimoboji, E. Larenas, T. Fowler, S. Kulkarni, A. S. Hoffman, P. S. Stayton, *Proc. Natl. Acad. Sci. USA* **2002**, *99*, 16592.
- [227] S. Basak, V. D. Punetha, G. Bisht, S. S. Bisht, N. G. Sahoo, J. W. Cho, *Polym. Rev.* **2015**, *55*, 163.
- [228] J. L. Rodriguez-Redondo, A. Sastre-Santos, F. Fernandez-Lazaro, D. Soares, G. C. Azzellini, B. Elliott, L. Echegoyen, *Chem. Commun.* **2006**, 1265.
- [229] R. Siewertsen, H. Neumann, B. Buchheim-Stehn, R. Herges, C. Nather, F. Renth, F. Temps, *J. Am. Chem. Soc.* **2009**, *131*, 15594.
- [230] J. Yoshino, N. Kano, T. Kawashima, *Chem. Commun.* **2007**, 559.
- [231] I. Tochitsky, M. R. Banghart, A. Mourot, J. Z. Yao, B. Gaub, R. H. Kramer, D. Trauner, *Nat. Chem.* **2012**, *4*, 105.
- [232] M. Banghart, K. Borges, E. Isacoff, D. Trauner, R. H. Kramer, *Nat. Neurosci.* **2004**, *7*, 1381.
- [233] M. Volgraf, P. Gorostiza, R. Numano, R. H. Kramer, E. Y. Isacoff, D. Trauner, *Nat. Chem. Biol.* **2006**, *2*, 47.
- [234] J. Broichhagen, D. Trauner, *Curr. Opin. Chem. Biol.* **2014**, *21*, 121.
- [235] J. A. Barltrop, P. J. Plant, P. Schofield, *Chem. Commun.* **1966**, 822.
- [236] C. P. Holmes, D. G. Jones, *J. Org. Chem.* **1995**, *60*, 2318.
- [237] Q. Yan, D. H. Han, Y. Zhao, *Polym. Chem.* **2013**, *4*, 5026.
- [238] S. Kaneko, K. Yamaguchi, J. Nakanishi, *Langmuir* **2013**, *29*, 7300.

- [239] S. Kaneko, H. Nakayama, Y. Yoshino, D. Fushimi, K. Yamaguchi, Y. Horiike, J. Nakanishi, *Phys. Chem. Chem. Phys.* **2011**, *13*, 4051.
- [240] C. C. Zhu, C. Ninh, C. J. Bettinger, *Biomacromolecules* **2014**, *15*, 3474.
- [241] S. Yamaguchi, S. Yamahira, K. Kikuchi, K. Sumaru, T. Kanamori, T. Nagamune, *Angew. Chem., Int. Ed.* **2012**, *51*, 128.
- [242] A. A. Brown, O. Azzaroni, W. T. S. Huck, *Langmuir* **2009**, *25*, 1744.
- [243] C. A. Goubko, A. Basak, S. Majumdar, H. Jarrell, N. H. Khieu, X. D. Cao, *J. Biomed. Mater. Res., Part A* **2013**, *101A*, 787.
- [244] J. X. Cui, V. San Miguel, A. del Campo, *Macromol. Rapid Commun.* **2013**, *34*, 310.
- [245] J. X. Cui, T. H. Nguyen, M. Ceolin, R. Berger, O. Azzaroni, A. del Campo, *Macromolecules* **2012**, *45*, 3213.
- [246] U. Hersel, C. Dahmen, H. Kessler, *Biomaterials* **2003**, *24*, 4385.
- [247] J. D. Humphries, A. Byron, M. J. Humphries, *J. Cell Sci.* **2006**, *119*, 3901.
- [248] J. Nakanishi, *Chem. - Asian J.* **2014**, *9*, 406.
- [249] Y. Ohmuro-Matsuyama, Y. Tatsu, *Angew. Chem., Int. Ed.* **2008**, *47*, 7527.
- [250] W. Li, J. S. Wang, J. S. Ren, X. G. Qu, *J. Am. Chem. Soc.* **2014**, *136*, 2248.
- [251] J. Edahiro, K. Sumaru, Y. Tada, K. Ohi, T. Takagi, M. Kameda, T. Shinbo, T. Kanamori, Y. Yoshimi, *Biomacromolecules* **2005**, *6*, 970.
- [252] A. Higuchi, A. Hamamura, Y. Shindo, H. Kitamura, B. O. Yoon, T. Mori, T. Uyama, A. Umezawa, *Biomacromolecules* **2004**, *5*, 1770.
- [253] M. Wirkner, J. M. Alonso, V. Maus, M. Salierno, T. T. Lee, A. J. Garcia, A. del Campo, *Adv. Mater.* **2011**, *23*, 3907.
- [254] L. R. He, S. Vibhagool, H. Zhao, V. Hoven, P. Theato, *Macromol. Chem. Phys.* **2018**, *219*, 1800104.
- [255] S. R. Braam, C. Denning, S. van den Brink, P. Kats, R. Hochstenbach, R. Passier, C. L. Mummery, *Nat. Methods* **2008**, *5*, 389.
- [256] K. Okita, T. Ichisaka, S. Yamanaka, *Nature* **2007**, *448*, 313.
- [257] A. Higuchi, Q. D. Ling, Y. Chang, S. T. Hsu, A. Umezawa, *Chem. Rev.* **2013**, *113*, 3297.
- [258] A. Higuchi, Q.-D. Ling, S. S. Kumar, Y. Chang, T.-C. Kao, M. A. Munusamy, A. A. Alarfaj, S.-T. Hsu, A. Umezawa, *Prog. Polym. Sci.* **2014**, *39*, 1585.
- [259] J. Auernheimer, C. Dahmen, U. Hersel, A. Bausch, H. Kessler, *J. Am. Chem. Soc.* **2005**, *127*, 16107.
- [260] Y. H. Gong, J. Yang, F. Y. Cao, J. Zhang, H. Cheng, R. X. Zhuo, X. Z. Zhang, *J. Mater. Chem. B* **2013**, *1*, 2013.

- [261] D. F. Stamatialis, B. J. Papenburg, M. Girones, S. Saiful, S. N. M. Bettahalli, S. Schmitmeier, M. Wessling, *J. Membr. Sci.* **2008**, *308*, 1.
- [262] K. A. Moga, L. R. Bickford, R. D. Geil, S. S. Dunn, A. A. Pandya, Y. P. Wang, J. H. Fain, C. F. Archuleta, A. T. O'Neill, J. M. DeSimone, *Adv. Mater.* **2013**, *25*, 5060.
- [263] L. Tavano, F. P. Nicoletta, N. Picci, R. Muzzalupo, *Colloids Surf., B* **2016**, *139*, 132.
- [264] Y. Zhou, H. Ye, Y. B. Chen, R. Y. Zhu, L. C. Yin, *Biomacromolecules* **2018**, *19*, 1840.
- [265] C. S. Patrickios, T. K. Georgiou, *Curr. Opin. Colloid Interface Sci.* **2003**, *8*, 76.
- [266] G. Erdodi, J. P. Kennedy, *Prog. Polym. Sci.* **2006**, *31*, 1.
- [267] L. Mespouille, J. L. Hedrick, P. Dubois, *Soft Matter* **2009**, *5*, 4878.
- [268] C. P. Lin, I. Gitsov, *Macromolecules* **2010**, *43*, 10017.
- [269] A. Haesslein, M. C. Hacker, H. Ueda, D. M. Ammon, R. N. Borazjani, J. F. Kunzler, J. C. Salamone, A. G. Mikos, *J. Biomater. Sci., Polym. Ed.* **2009**, *20*, 49.
- [270] Y. P. Wang, D. E. Betts, J. A. Finlay, L. Brewer, M. E. Callow, J. A. Callow, D. E. Wendt, J. M. DeSimone, *Macromolecules* **2011**, *44*, 878.
- [271] N. Bruns, J. C. Tiller, *Nano Lett.* **2005**, *5*, 45.
- [272] K. Scholler, S. Kupfer, L. Baumann, P. M. Hoyer, D. de Courten, R. M. Rossi, A. Vetushka, M. Wolf, N. Bruns, L. J. Scherer, *Adv. Funct. Mater.* **2014**, *24*, 5194.
- [273] B. Schmidt, P. J. Anderson, L. W. Doyle, D. Dewey, R. E. Grunau, E. V. Asztalos, P. G. Davis, W. Tin, D. Moddemann, A. Solimano, A. Ohlsson, K. J. Barrington, R. S. Roberts, C. A. P. C. Tri, *JAMA, J. Am. Med. Assoc.* **2012**, *307*, 275.
- [274] F. Ercole, T. P. Davis, R. A. Evans, *Polym. Chem.* **2010**, *1*, 37.
- [275] L. Baumann, D. de Courten, M. Wolf, R. M. Rossi, L. J. Scherer, *ACS Appl. Mater. Interfaces* **2013**, *5*, 5894.
- [276] L. Baumann, K. Scholler, D. de Courten, D. Marti, M. Frenz, M. Wolf, R. M. Rossi, L. J. Scherer, *RSC Adv.* **2013**, *3*, 23317.
- [277] C. G. Qian, J. C. Yu, Y. L. Chen, Q. Y. Hu, X. Z. Xiao, W. J. Sun, C. Wang, P. J. Feng, Q. D. Shen, Z. Gu, *Adv. Mater.* **2016**, *28*, 3313.
- [278] H. P. C. van Kuringen, G. M. Eikelboom, I. K. Shishmanova, D. J. Broer, A. P. H. J. Schenning, *Adv. Funct. Mater.* **2014**, *24*, 5045.
- [279] Y. Ishida, *Materials* **2011**, *4*, 183.
- [280] L. Zhai, *Chem. Soc. Rev.* **2013**, *42*, 7148.
- [281] W. M. Buda, S. Pasieczna, J. Ryczkowski, J. Goworek, *J. Phys. IV* **2005**, *129*, 207.
- [282] N. K. Mal, M. Fujiwara, Y. Tanaka, *Nature* **2003**, *421*, 350.

- [283] H. A. Meng, M. Liong, T. A. Xia, Z. X. Li, Z. X. Ji, J. I. Zink, A. E. Nel, *ACS Nano* **2010**, *4*, 4539.
- [284] Y. P. Liu, D. K. Shen, G. Chen, A. A. Elzatahry, M. Pal, H. W. Zhu, L. L. Wu, J. J. Lin, D. Al-Dahyan, W. Li, D. Y. Zhao, *Adv. Mater.* **2017**, *29*, 1702274.
- [285] A. A. Belogorlov, S. A. Bortnikova, P. G. Mingalev, *J. Surf. Invest.: X-Ray, Synchrotron Neutron Tech.* **2017**, *11*, 425.
- [286] Y. N. Palai, K. Anjali, A. Sakthivel, M. Ahmed, D. Sharma, S. K. Badamali, *Catal. Lett.* **2018**, *148*, 465.
- [287] Y. Chen, K. Ai, J. Liu, G. Sun, Q. Yin, L. Lu, *Biomaterials* **2015**, *60*, 111.
- [288] F. Sancenõn, L. Pascual, M. Oroval, E. Aznar, R. Martínez-Máñez, *ChemistryOpen* **2015**, *4*, 418.
- [289] N. Hosseinpour Moghadam, S. Salehzadeh, J. Rakhtshah, A. Hosseinpour Moghadam, H. Tanzadehpanah, M. Saidijam, *Int. J. Biol. Macromol.* **2019**, *125*, 931.
- [290] S. Soltani, U. Rashid, S. I. Al-Resayes, I. A. Nehdi, in *Clean Energy for Sustainable Development, Comparisons and Contrasts of New Approaches* (Eds: M. G. Rasul, A. K. Azad, S. C. Sharma), Academic Press, London, UK **2017**.
- [291] A. Eftekhari, *Microporous Mesoporous Mater.* **2017**, *243*, 355.
- [292] G. G. Walmsley, A. McArdle, R. Tevlin, A. Momeni, D. Atashroo, M. S. Hu, A. H. Feroze, V. W. Wong, P. H. Lorenz, M. T. Longaker, D. C. Wan, *Nanomedicine: Nanotechnol. Biol. Med.* **2015**, *11*, 1253.
- [293] S. Dahane, M. Martinez Galera, M. E. Marchionni, M. M. Socias Viciano, A. Derdour, M. D. Gil Garcia, *Talanta* **2016**, *152*, 378.
- [294] A. Vassilakopoulou, V. Georgakilas, N. Vainos, I. Koutselas, *J. Phys. Chem. Solids* **2017**, *103*, 190.
- [295] S. Choi, H. Lee, R. Ghaffari, T. Hyeon, D. H. Kim, *Adv. Mater.* **2016**, *28*, 4203.
- [296] D. Wang, J. Chen, L. Ren, Q. Li, D. Li, J. Yu, *Inorg. Chem. Front.* **2017**, *4*, 468.
- [297] J. S. Beck, J. C. Vartuli, W. J. Roth, M. E. Leonowicz, C. T. Kresge, K. D. Schmitt, C. T. W. Chu, D. H. Olson, E. W. Sheppard, S. B. McCullen, J. B. Higgins, J. L. Schlenker, *J. Am. Chem. Soc.* **1992**, *114*, 10834.
- [298] C. T. Kresge, M. E. Leonowicz, W. J. Roth, J. C. Vartuli, J. S. Beck, *Nature* **1992**, *359*, 710.
- [299] S. Samanta, S. Giri, P. U. Sastry, N. K. Mal, A. Manna, A. Bhaumik, *Ind. Eng. Chem. Res.* **2003**, *42*, 3012.
- [300] Y. Li, W. Zhang, L. Zhang, Q. Yang, Z. Wei, Z. Feng, C. Li, *J. Phys. Chem. B* **2004**, *108*, 9739.
- [301] A. Endo, Y. Inagi, S. Fujisaki, T. Yamamoto, T. Ohmori, M. Nakaiwa, K. Iwakabe, *AIChE J.* **2006**, *52*, 1275.
- [302] Y. Xu, S. Xu, T. Emmler, F. Roelofs, C. Boettcher, R. Haag, G. Buntkowsky, *Chem. - Eur. J.* **2008**, *14*, 3311.
- [303] O. B Pagar, H. S Nagare, Y. M Chine, R. R Autade, P. R Narode, V. Sanklecha, *Int. J. Pharm. Drug. Anal.* **2018**, *6*, 1.

- [304] J. W. Fan, D. D. Li, W. Teng, J. P. Yang, Y. Liu, L. L. Liu, A. A. Elzatahry, A. Alghamdi, Y. H. Deng, G. M. Li, W. X. Zhang, D. Y. Zhao, *J. Mater. Chem. A* **2016**, *4*, 3850.
- [305] A. Martín, J. M. Arsuaga, N. Roldán, A. Martínez, A. Sotto, *J. Membr. Sci.* **2016**, *520*, 8.
- [306] H. Wang, X. Lu, D. Lu, P. Wang, J. Ma, *J. Appl. Polym. Sci.* **2019**, *136*, 47353.
- [307] L. Chang, D. Gallego-Perez, C. L. Chiang, P. Bertani, T. Kuang, Y. Sheng, F. Chen, Z. Chen, J. Shi, H. Yang, X. Huang, V. Malkoc, W. Lu, L. J. Lee, *Small* **2016**, *12*, 5971.
- [308] W. Li, T. Kuang, X. Jiang, J. Yang, P. Fan, Z. Zhao, Z. Fei, M. Zhong, L. Chang, F. Chen, *Chem. Eng. J.* **2017**, *322*, 445.
- [309] Y. Chen, H. Chen, J. Shi, *Adv. Mater.* **2013**, *25*, 3144.
- [310] L. Zhang, Y. C. Li, Z. X. Jin, J. C. Yu, K. M. Chan, *Nanoscale* **2015**, *7*, 12614.
- [311] D. He, X. Li, X. He, K. Wang, J. Tang, X. Yang, X. He, X. Yang, Z. Zou, *J. Mater. Chem. B* **2015**, *3*, 5588.
- [312] G. Wang, J. Dong, T. Yuan, J. Zhang, L. Wang, H. Wang, *Macromol. Biosci.* **2016**, *16*, 990.
- [313] N. Mizoshita, T. Tani, S. Inagaki, *Chem. Soc. Rev.* **2011**, *40*, 789.
- [314] Y.-J. Li, L. Wang, B. Yan, *J. Mater. Chem.* **2011**, *21*, 1130.
- [315] S. Inagaki, O. Ohtani, Y. Goto, K. Okamoto, M. Ikai, K.-i. Yamanaka, T. Tani, T. Okada, *Angew. Chem., Int. Ed.* **2009**, *48*, 4042.
- [316] L. Grösch, Y. J. Lee, F. Hoffmann, M. Fröba, *Chem. - Eur. J.* **2015**, *21*, 331.
- [317] W. Szymanski, D. Yilmaz, A. Kocer, B. L. Feringa, *Acc. Chem. Res.* **2013**, *46*, 2910.
- [318] S. Sukharev, A. Anishkin, *Trends Neurosci.* **2004**, *27*, 345.
- [319] A. Kocer, M. Walko, W. Meijberg, B. L. Feringa, *Science* **2005**, *309*, 755.
- [320] D. Wandera, S. R. Wickramasinghe, S. M. Husson, *J. Membr. Sci.* **2010**, *357*, 6.
- [321] S. C. Sebai, D. Milioni, A. Walrant, I. D. Alves, S. Sagan, C. Huin, L. Auvray, D. Massotte, S. Cribier, C. Tribet, *Angew. Chem., Int. Ed.* **2012**, *51*, 2132.
- [322] R. M. Uda, E. Hiraishi, R. Ohnishi, Y. Nakahara, K. Kimura, *Langmuir* **2010**, *26*, 5444.
- [323] X. L. Liang, X. L. Yue, Z. F. Dai, J. Kikuchi, *Chem. Commun.* **2011**, *47*, 4751.
- [324] B. Lalia, V. Kochkodan, R. Hashaikeh, N. Hilal, *Desalination* **2013**, *326*, 77.
- [325] C. Decker, *Prog. Polym. Sci.* **1996**, *21*, 593.
- [326] A. B. Scranton, C. N. Bowman, R. W. Peiffer, in *Photopolymerization: Fundamentals and Applications*, ACS Symposium Series, Vol. 673, American Chemical Society, Washington, DC **1997**.
- [327] W. J. Koros, G. K. Fleming, *J. Membr. Sci.* **1993**, *83*, 1.

- [328] A. J. Burggraaf, in *Membrane Science and Technology*, Vol. 4 (Eds: A. J. Burggraaf, L. Cot), Elsevier, Amsterdam, Netherlands **1996**.
- [329] A. Thornton, J.M. Hill, A. Hill, in *Modelling Gas Separation in Porous Membranes* (Eds: Y. Yampolskii, B. Freeman), Wiley, Chichester, UK **2010**, Chap. 5.
- [330] G. Di Profio, M. Polino, F. P. Nicoletta, B. D. Belviso, R. Caliendo, E. Fontananova, G. De Filpo, E. Curcio, E. Drioli, *Adv. Funct. Mater.* **2014**, *24*, 1582.
- [331] S. M. Salehi, G. Di Profio, E. Fontananova, F. P. Nicoletta, E. Curcio, G. De Filpo, *J. Membr. Sci.* **2016**, *504*, 220.
- [332] E. Fontananova, V. Grosso, S. A. Aljlil, M. A. Bahattab, D. Vuono, F. P. Nicoletta, E. Curcio, E. Drioli, G. Di Profio, *J. Membr. Sci.* **2017**, *541*, 198.
- [333] S. Heng, K. L. Yeung, M. Djafer, J. C. Schrotter, *J. Membr. Sci.* **2007**, *289*, 67.
- [334] C. D. Vecitis, M. H. Schnoor, M. S. Rahaman, J. D. Schiffman, M. Elimelech, *Environ. Sci. Technol.* **2011**, *45*, 3672.
- [335] K. H. Choo, R. Tao, M. J. Kim, *J. Membr. Sci.* **2008**, *322*, 368.
- [336] S. Mozia, *Sep. Purif. Technol.* **2010**, *73*, 71.
- [337] S. Ognier, C. Wisniewski, A. Grasmick, *J. Membr. Sci.* **2004**, *229*, 171.
- [338] J. L. Nilsson, *J. Membr. Sci.* **1988**, *36*, 147.
- [339] A. Matin, Z. Khan, S. M. J. Zaidi, M. C. Boyce, *Desalination* **2011**, *281*, 1.
- [340] J. Song, H. Kong, J. Jang, *Colloids Surf., B* **2011**, *82*, 651.
- [341] I. Banerjee, R. C. Pangule, R. S. Kane, *Adv. Mater.* **2011**, *23*, 690.
- [342] G. De Filpo, A. M. Palermo, F. Rachiele, F. P. Nicoletta, *Int. Biodeterior. Biodegrad.* **2013**, *85*, 217.
- [343] G. De Filpo, A. M. Palermo, R. Tolmino, P. Formoso, F. P. Nicoletta, *Cellulose* **2016**, *23*, 3265.
- [344] G. De Filpo, E. Pantuso, K. Armentano, P. Formoso, G. Di Profio, T. Poerio, E. Fontananova, C. Meringolo, A. I. Mashin, F. P. Nicoletta, *Membranes* **2018**, *8*, 35.
- [345] G. De Filpo, A. M. Palermo, R. Munno, L. Molinaro, P. Formoso, F. P. Nicoletta, *Int. Biodeterior. Biodegrad.* **2015**, *103*, 51.
- [346] D. N. Priya, J. M. Modak, A. M. Raichur, *ACS Appl. Mater. Interfaces* **2009**, *1*, 2684.
- [347] H. Zhao, H. Li, H. Yu, H. Chang, X. Quan, S. Chen, *Sep. Purif. Technol.* **2013**, *116*, 360.
- [348] R. A. Damodar, S. J. You, H. H. Chou, *J. Hazard. Mater.* **2009**, *172*, 1321.
- [349] X. F. Shi, G. Tal, N. P. Hankins, V. Gitis, *J. Water Process Eng.* **2014**, *1*, 121.
- [350] S. F. E. Boerlage, M. D. Kennedy, M. P. Aniyee, E. M. Abogrean, D. E. Y. El-Hodali, Z. S. Tarawneh, J. C. Schippers, *Desalination* **2000**, *131*, 201.
- [351] Z. Liu, W. Wang, R. Xie, X. J. Ju, L. Y. Chu, *Chem. Soc. Rev.* **2016**, *45*, 460.

- [352] M. Dubner, M. E. Naoum, N. D. Spencer, C. Padeste, *ACS Omega* **2017**, *2*, 455.
- [353] A. C. Pauly, K. Scholler, L. Baumann, R. M. Rossi, K. Dustmann, U. Ziener, D. de Courten, M. Wolf, L. F. Boesel, L. J. Scherer, *Sci. Technol. Adv. Mater.* **2015**, *16*, 034604.
- [354] P. Kaner, X. Hu, S. W. Thomas 3rd, A. Asatekin, *ACS Appl. Mater. Interfaces* **2017**, *9*, 13619.
- [355] B. Tylkowski, S. Peris, M. Giamberini, R. Garcia-Valls, J. A. Reina, J. C. Ronda, *Langmuir* **2010**, *26*, 14821.
- [356] K. Weh, M. Noack, R. Ruhmann, K. Hoffmann, P. Toussaint, J. Caro, *Chem. Eng. Technol.* **1998**, *21*, 408.
- [357] S. N. Ramanan, N. Shahkaramipour, T. Tran, L. X. Zhu, S. R. Venna, C. K. Lim, A. Singh, P. N. Prasad, H. Q. Lin, *J. Membr. Sci.* **2018**, *554*, 164.
- [358] H. Lee, S. M. Dellatore, W. M. Miller, P. B. Messersmith, *Science* **2007**, *318*, 426.
- [359] J. Zhang, W. D. Zhang, N. C. Zhou, Y. Y. Weng, Z. J. Hu, *RSC Adv.* **2014**, *4*, 24973.
- [360] D. J. Miller, D. R. Paul, B. D. Freeman, *Polymer* **2014**, *55*, 1375.
- [361] Y. Baek, B. D. Freeman, A. L. Zydney, J. Yoon, *Ind. Eng. Chem. Res.* **2017**, *56*, 5756.
- [362] S. J. Gao, Z. Shi, W. B. Zhang, F. Zhang, J. Jin, *ACS Nano* **2014**, *8*, 6344.
- [363] Y. B. Peng, Z. G. Guo, *J. Mater. Chem. A* **2016**, *4*, 15749.
- [364] Z. Wang, D. Hou, S. Lin, *Environ. Sci. Technol.* **2016**, *50*, 3866.
- [365] L. Hu, S. Gao, X. Ding, D. Wang, J. Jiang, J. Jin, L. Jiang, *ACS Nano* **2015**, *9*, 4835.
- [366] S. Sommer, A. Ekin, D. C. Webster, S. J. Stafslie, J. Daniels, L. J. VanderWal, S. E. Thompson, M. E. Callow, J. A. Callow, *Biofouling* **2010**, *26*, 961.
- [367] S. Krishnan, N. Wang, C. K. Ober, J. A. Finlay, M. E. Callow, J. A. Callow, A. Hexemer, K. E. Sohn, E. J. Kramer, D. A. Fischer, *Biomacromolecules* **2006**, *7*, 1449.
- [368] S. Colak, G. N. Tew, *Biomacromolecules* **2012**, *13*, 1233.
- [369] H. Kitano, A. Kawasaki, H. Kawasaki, S. Morokoshi, *J. Colloid Interface Sci.* **2005**, *282*, 340.
- [370] R. Rosario, D. Gust, A. A. Garcia, M. Hayes, J. L. Taraci, T. Clement, J. W. Dailey, S. T. Picraux, *J. Phys. Chem. B* **2004**, *108*, 12640.
- [371] M. Natali, S. Giordani, *Org. Biomol. Chem.* **2012**, *10*, 1162.
- [372] L. Florea, G. M. Guirk, F. Benito-Lopez, D. Diamond, *18th Int. Conf. on Miniaturized Systems for Chemistry and Life Sciences (MicroTAS 2014)*, Curran Associates, Inc., San Antonio, TX, USA **2014**, p. 1891.
- [373] S. Scarmagnani, Z. Walsh, C. Slater, F. Benito-Lopez, M. Macka, B. Paull, D. Diamond, *Int. J. Nanomanuf.* **2010**, *5*, 38.

- [374] A. Dunne, C. Delaney, A. McKeon, P. Nesterenko, B. Paull, F. Benito-Lopez, D. Diamond, L. Florea, *Sensors* **2018**, *18*, 1083.
- [375] S. Chen, F. J. Jiang, Z. Q. Cao, G. J. Wang, Z. M. Dang, *Chem. Commun.* **2015**, *51*, 12633.
- [376] F. J. Jiang, S. Chen, Z. Q. Cao, G. J. Wang, *Polymer* **2016**, *83*, 85.
- [377] E. Aznar, M. Oroval, L. Pascual, J. R. Murguia, R. Martinez-Manez, F. Sancenon, *Chem. Rev.* **2016**, *116*, 561.
- [378] W. B. Shi, J. Deng, H. Qin, D. S. Wang, C. S. Zhao, *J. Membr. Sci.* **2014**, *455*, 357.

CHAPTER 2

2. POLYMER MEMBRANES DISPERSED LIQUID CRYSTAL (PMDLC): A NEW ELECTRO-OPTICAL DEVICE

Published as: G. De Filpo, K. Armentano, E. Pantuso, A.I. Mashin, G. Chidichimo, F.P. Nicoletta, Polymer Membranes Dispersed Liquid Crystal (PMDLC): a new electro-optical device, *Liquid Crystals* **2019**, *46*, 986. <https://doi.org/10.1080/02678292.2019.1566506>

2.1 SUMMARY

Polymer Dispersed Liquid Crystals (PDLCs) are liquid crystal dispersions in a polymer matrix, which look like opaque in their OFF state, when no electric field is applied, and transparent in their ON state. They are generally obtained by a phase separation process, such as Thermal, Solvent- and Polymerization-Induced Phase Separation (TIPS, SIPS and PIPS, respectively), between two transparent conductive glass substrates. In this paper, a new electro-optical device, formed by a porous polymer membrane imbided with liquid crystal by capillary suction, is presented (Polymer Membranes Dispersed Liquid Crystals, PMDLC). Polymer membrane surfaces were made conductive before liquid crystal loading by magnetron sputtering of a thin layer of conductive indium tin oxide. The morphology and the electro-optical response of these devices were investigated and the observed transmittances and relaxation times were found to be similar to those of conventional PDLCs. In addition, PMDLCs showed interesting flexibility as no solid conductive substrate is required and economic convenience as there is no loss of liquid crystal in the polymer matrix.

2.2 INTRODUCTION

Several types of materials have been proposed as smart windows, i.e. large area devices able to control the transmittance of light and heat in buildings. Photochromic, thermochromic, electrochromic, photoelectrochromic and liquid crystalline materials¹⁻⁵ can change their optical properties upon application of an external stimulus such as light, heat and electric field allowing the variation of the amount of incident light and/or heat and maintenance of outwards vision. In particular, Polymer Dispersed Liquid Crystals (PDLCs) are dispersions of a liquid crystal in a polymer matrix widely used as optical materials because they allow the transmitted light modulation by an electric change of the orientation of the LC domains⁵. In Swiss cheese PDLCs the LC domains consist of about spherical LC droplets dispersed in a solid polymer matrix. On the contrary polymer ball, PDLCs are characterised by a morphology where the LC molecules fill the voids and the crevices of a small polymer ball network⁶. In both cases, the random average orientation of LC domains causes the scattering of the light impinging on devices and their milky appearance in the OFF state. The application of an electric field (ON state) allows the re-orientation of the liquid-crystalline domains along the field direction and the modulation of light transmittance till a full transparent device, if the match condition between the ordinary refractive index of LC and that of the polymer matrix is fulfilled⁷. PDLCs were patented

in 1987 by Doane et al.⁵. They are generally obtained by a phase separation process, such as Thermal-, Solvent- and Polymerization-Induced Phase Separation (TIPS, SIPS and PIPS, respectively), between two transparent conductive glass substrates. In TIPS and SIPS processes, starting from a homogeneous mixture of liquid crystal and polymer, phase separation is induced by either cooling the mixture or allowing the solvent evaporation from the mixture at a controlled rate. In PIPS processes, the initial homogeneous mixture is generally formed by liquid crystal, monomers, cross-linkers and a thermal- or photo-initiator. The phase separation is induced by the growth and cross-link of monomer/oligomer molecular chains, which at the end result less miscible with liquid crystal than the initial short chain length monomers⁶.

For the sake of completeness, in 1982, some years before Doane's patent, Craighead et al.⁸ proposed a new display based on electrically induced index matching in an inhomogeneous medium by filling a filter, composed of mixed esters of cellulose (Millipore type MF, nominal pore size of 5 μm and refractive index $n = 1.495$) with ZLI-1083 liquid crystal, whose ordinary refractive index matched that of the filter. The liquid crystal-filled matrix was placed between two transparent ITO-coated conductive glasses. Despite the refractive index matching, the liquid crystal domains size distribution did not allow an adequate transmittance value in the ON state (maximum value $\sim 30\%$, saturation field $\sim 1 \text{ V } \mu\text{m}^{-1}$, response times \sim some tens of ms). In addition, the presence of conductive glasses did not give flexibility to the device. The authors did not claim the economic convenience of their device as PDLCs were not yet invented and Drzaic used the term of imbibing porous structure with liquid crystal to define such devices in his book⁶.

Despite the great technological advances in the fabrication of PDLCs with the above described methods, one important drawback of PDLCs is the liquid crystal lost within the polymer matrix^{6,9} due to its solubility, giving rise to unpredictable final electro-optical properties and increased costs. Several research groups have investigated polymerization parameters and PDLC components chemical nature and composition in order to minimise the above-mentioned drawback and maximise the PDLC performance¹⁰⁻¹⁵. In particular, any parameter, able to increase the LC domain size, will reduce the driving fields and rise times, but increase the decay times and costs. An attempt to improve the device performance and minimise costs recently included the use of nanoparticles^{16,17}. In addition to their well-known applications in many different fields such as adsorption, photocatalysis, disinfection, electrical conductivity, reaction rates, drug delivery, topological defects of liquid crystals and enhancement of the performance of liquid crystal devices¹⁸⁻²⁴, Aerosil® NPs were interconnected by free radical polymerisation to form a network^{25,26}, whose voids were filled by nematic mixtures. In such way, it was possible to obtain electro-optical devices working both in direct- and reverse-mode (being this last device characterised by a transparent OFF state and an opaque ON state) with no liquid crystal lost in the surrounding network and, consequently, reduced costs and excellent electro-optical performance. In this paper, a new electro-optical device, formed by a porous polymer membrane imbibed with liquid crystal by capillary suction, is presented (Polymer Membranes Dispersed Liquid Crystals, PMDLC). Polymer membrane surfaces were made conductive before liquid crystal loading by magnetron sputtering of a thin layer of conductive indium tin oxide. The morphology and the electrooptical response of these devices were investigated and the observed transmittances and relaxation times were found to be similar to those

conventional PDLCs. In addition, PMDLCs showed interesting flexibility as no solid conductive substrate is required and economic convenience as there is no loss of liquid crystal dispersed in the polymer matrix.

2.3 EXPERIMENTAL

The nematic liquid crystals used in this work was E49 (Merck, Darmstadt, Germany), a nematic eutectic mixture whose main chemical-physical properties are reported in Table 1.

Porous membrane rectangles ($40 \times 20 \text{ mm}^2$) were cut from commercially available polypropylene membrane sheets (Accurel PP2EHF, Membrana GmbH, Wuppertal, Germany, refractive index 1.490, porosity 70%, mean pore diameter $0.4 \mu\text{m}$, thickness $\sim 170 \mu\text{m}$) and washed in methanol (Sigma-Aldrich, Milan, Italy) by an ultrasonic bath (model M1800H-E, Branson, Danbury, CT, USA) and overnight dried at 40°C .

Table 1. Some chemical-physical properties of E49. From the left: nematic-isotropic temperature, T_{NI} ; ordinary refractive index, n_o ; birefringence, Δn ; dielectric anisotropy, $\Delta\epsilon$; parallel dielectric permittivity, $\epsilon_{||}$; splay constant, K_{11} ; bend constant, K_{33} ; rotational viscosity, γ .

$T_{NI}/^\circ\text{C}$	n_o	Δn	$\Delta\epsilon$	$\epsilon_{ }$	$K_{11}/10^{-12} \text{ N}$	$K_{33}/10^{-12} \text{ N}$	γ/cSt
100	1.5270	0.2610	16.6	23.9	15.80	28.20	47

The deposition of indium tin oxide on polypropylene membranes was obtained by sputtering of an ITO target (purity 99.99%, Goodfellow Cambridge Ltd., Huntingdon, England) for different times (20, 40, 60 and 90 min) by process inert gas ions (Argon, purity 99.999%) in a Edwards AUTO-306 sputtering system (Edwards, Burgess Hill, United Kingdom). ITO-sputtered surface resistance of PP membranes was measured by 4-point probes method as a function of sputtering time. The sputtered ITO layer acts as a conductive substrate for PMDLCs. A copper tape with conductive adhesive was applied to each of the two opposite surfaces of PP membranes in order to insure optimal electric contacts between ITO layers and wires. Finally, an acrylic protective lacquer (APLSP from Electrolube, Ashby de la Zouch, United Kingdom) was sprayed on samples to protect electric circuitry and avoid LC leakage without losing flexibility. The complete PMDLC preparation is schematised in Figure 1. Membrane and layer morphology was investigated by scanning electron microscopy, SEM. Observations were performed both on membrane top surfaces and cross-sections by a Leica LEO 420 (Leica Microsystems, Cambridge, England) scanning electron microscope. Before SEM analysis, samples were left under vacuum for several hours in order to extract LC and, then, coated with a thin gold film.

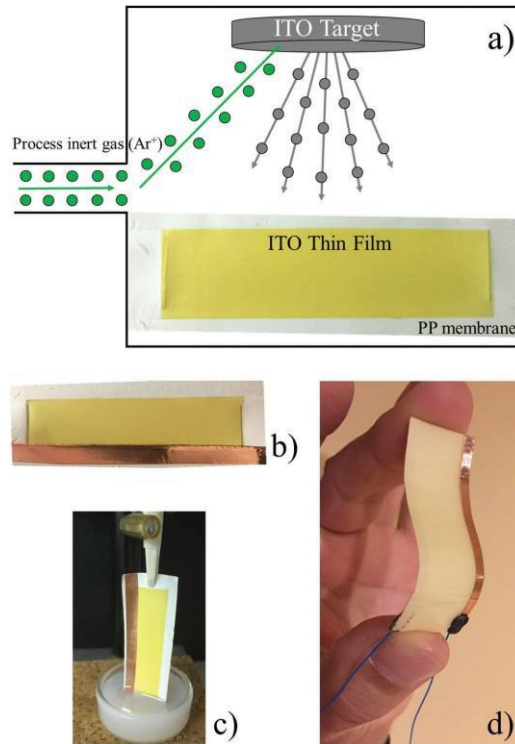


Figure 1. Scheme of the preparation of a PMDLC: a) after cleaning, PP membranes were sputtered on both surfaces with a conductive ITO layer in a Edwards AUTO-306 sputtering system; b) two copper strips with conductive adhesive were placed on one side of both membrane surfaces; c) membrane pores were filled with liquid crystal by capillary suction; d) after external ring trimming and sealing with an acrylic protective lacquer, electric wires were glued on copper strips with an electrically conductive paste.

Transmission Electron Microscope, TEM, images were collected with a JEM 1400 Plus transmission electron microscope operating at 100 kV (Jeol, Akishima, Tokyo, Japan). The size of ITO nanoparticles was obtained by software analysis of TEM pictures. The number of measured nanoparticles, taken from different pictures of the same sample, was at least 100 and their size was evaluated with an image software (Motic Images Plus 2.0). The electro-optical properties of PMDLCs were investigated with the experimental setup described in a previous work [1] by applying electric fields, whose strength ranged from 0 to $5 \text{ V}\mu\text{m}^{-1}$ at a driving frequency of 1 kHz. The light intensity transmitted through air was assumed as full-scale intensity. The rise time, τ_{ON} , and decay time, τ_{OFF} , of a PMDLC are, respectively, defined as the time required to reach 90% of its maximum transmittance and return to 10% of the optical response after the external field switching off.

2.4 RESULTS AND DISCUSSION

PMDLCs were prepared with different sputtering times according to the procedure outlined in the experimental part and schematised in Figure 1. As shown in Figure 1(d) PMDLC has a yellowish opaque appearance in its OFF state due to the deposition of the ITO layer. The longer the sputtering time, the more yellowish the film appearance. Figure 2 shows the SEM pictures from the top surfaces and cross-sections of virgin and ITO sputtered PP membranes after different sputtering times ($t = 0, 20, 40, 60 \text{ min}$). It is evident from the observation of top surfaces that the higher the sputtering time, the denser the morphology. At the same time,

from the observation of cross sections, it is clear that the higher the sputtering time, the thicker the ITO layer. An almost complete ITO coverage on surfaces is gained with a 60 min sputtering time.

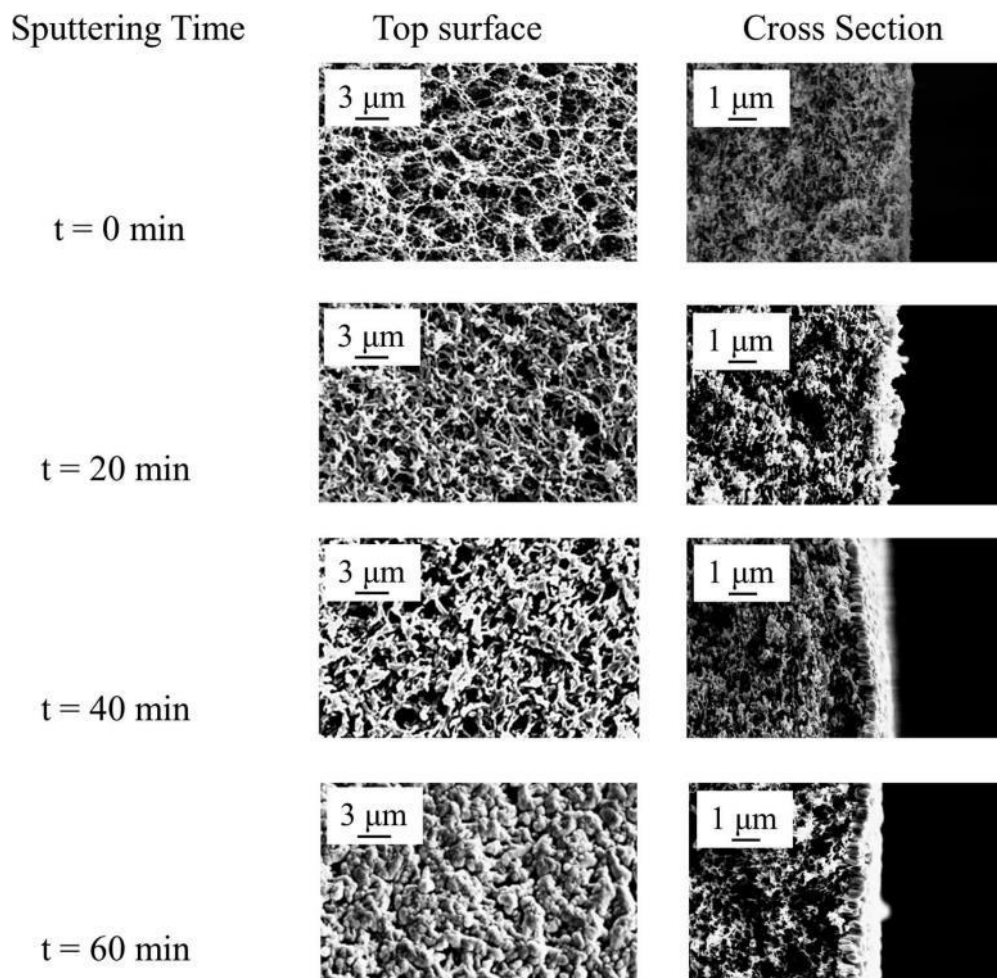


Figure 2. Top surface and cross-section of virgin and ITO sputtered PP membranes after different sputtering times: t = 0 (virgin PP membrane), t = 20 min, t = 40 min, and t = 60 min. The higher the sputtering time, the closer the morphology. almost complete ITO coverage on surfaces is gained with a 60 min sputtering time.

Figure 3 reports a TEM picture of the morphology of ITO layer grown on PP membranes after few minutes of sputtering time. The layer is composed by aggregates of primary ITO nanoparticles, which are rather spherical in shape with an average diameter of 15 nm. These nanoparticles agglomerate into larger aggregates. It is expected that the increase of sputtering time and consequent increase in surface coverage and thickness of ITO layer gives a decrease in the surface resistivity of ITO sputtered PP membranes.

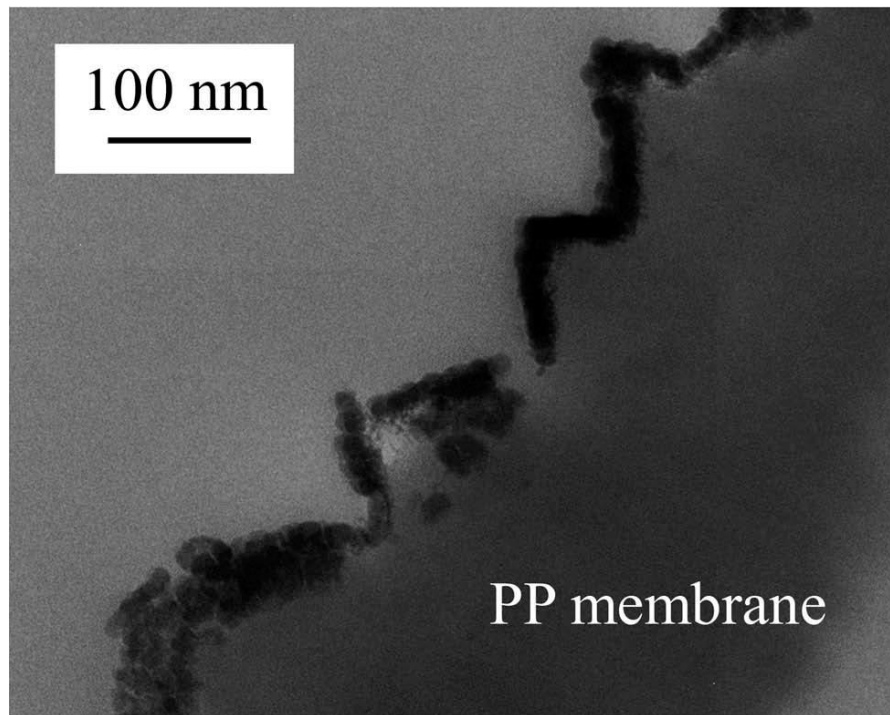


Figure 3. Morphology of ITO layer grown on PP membranes. The layer is composed by aggregates of primary nanoparticles, which are rather spherical in shape with an average diameter of 15 nm.

Figure 4 shows the dependence of the surface resistivity of ITO layer on PP membranes as a function of the sputtering time. The surface resistivity of ITO layers decreases according to a single exponential decay curve (full line in Figure 4, $R^2 = 0.994$) and reaches a plateau of about $35 \Omega \text{ sq}^{-1}$ after 60 min with a decay time of about 15 min. As a consequence, the time of 60 min was assumed to be the best sputtering time to prepare PMDLCs as it guarantees an optimal surface resistivity (few tens of $\Omega \text{ sq}^{-1}$ as ITO covered glasses used in conventional PDLCs) and the minimum yellowish of devices. Figure 3 reports the electric field-dependent transmittance of a PMDLC. After LC capillary suction samples were characterised by an opaque yellowish appearance with very low transmittances in the OFF state ($T_{\text{OFF}} = 0.5\%$, left inset in Figure 5) thanks to the high scattering arising from the random distribution of LC directors in the PP membrane pores. By applying an electric field of increasing strength (up to $3 \text{ V } \mu\text{m}^{-1}$) the transmittance values gradually increase leading to a highly transparent yellowish device due to the re-orientation of LC directors along the electric field direction because of their positive dielectric anisotropy ($T_{\text{ON}} = 65\%$, right inset in Figure 5). Even if the refractive indices of E49 (1.527, ordinary one) and PP (1.490) are very close; nevertheless, the maximum transmittance achieved was only 65%, due probably to both the presence of the two ITO layers and the membrane thickness ($170 \mu\text{m}$). As reported in Table 2 the contrast ratio, CR defined as the ratio between the transmittance value in the ON and OFF states, is 130, while the switching and saturation electric fields, $E_{10\%}$ and $E_{90\%}$ defined as the field strength able to gain 10% and 90% of the maximum transmittance, are 0.6 and $1.8 \text{ V } \mu\text{m}^{-1}$, respectively.

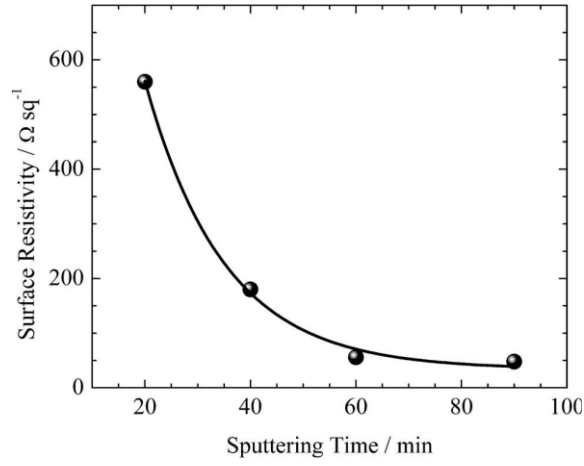


Figure 4. Dependence of the surface resistivity of ITO layer on PP membranes as a function of the sputtering time. The line is the exponential single decay fit of experimental points ($R^2 = 0.994$).

The values of the rise slope of T vs E curve and $E_{90\%}$ are slightly larger than those generally found in conventional PDLCs. This could be due to the size dispersion of membrane pores larger than the size dispersion of LC domains achievable in PDLCs. In fact, the switching field is reached as the smallest LC crystal domains, able to influence the transmittance, are reoriented by the applied electric field. These results are in rather good agreement with the following theoretical Equation (1) for switching fields in PDLCs with a droplet radius R ⁶:

$$E_{90\%} \sim \frac{1}{R} \sqrt{\frac{K}{\epsilon_0 \Delta \epsilon}} \quad (1)$$

where $\Delta\epsilon$ is the LC dielectric anisotropy, ϵ_0 the vacuum permittivity constant and K the LC elastic constant in the one constant approximation. Equation (1) predicts that smaller LC droplets will be characterised by a larger switching field.

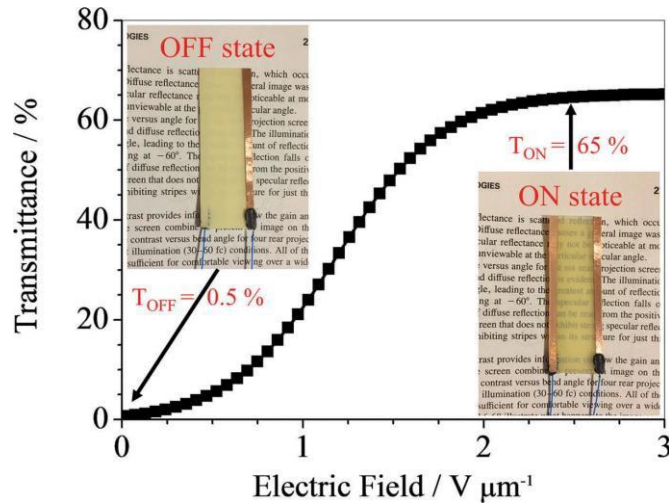


Figure 5. Electric field-dependent transmittance of a PMDLC. In the insets: the device as it looks in its OFF ($T_{OFF} = 0.5\%$) and ON state ($T_{ON} = 65\%$).

Table 2. Electro-optical properties of PMDLCs: transmittance in the OFF and ON state, T_{OFF} and T_{ON} ; contrast ratio, CR; switching and saturation electric fields, $E_{10\%}$ and $E_{90\%}$; rise and decay time, τ_{rise} and τ_{decay} .

$T_{OFF}/\%$	$T_{ON}/\%$	CR	$E_{10\%}/V \mu m^{-1}$	$E_{90\%}/V \mu m^{-1}$	τ_{rise}/ms	τ_{decay}/ms
0.5	65	130	0.6	1.8	4	40

Consequently, by inserting in Equation (1) the following values $\Delta\epsilon = 16.6$, $\epsilon_0 = 8.85 \times 10^{-12} NV^{-2}$, $K \sim 2.2 \times 10^{-11} N$ and assuming the minimum pore size affecting transmittance is $R \sim 2 \times 10^{-7} m$ the estimation for the required switching field in a PMDLC is around $2 V \mu m^{-1}$ in quite good agreement with the experimental results. After the electric field switching off, the restoring forces acting at PP pores causes the recovery of the initial random alignment of LC directors and opaque OFF state. The electro-optical response of PMDLCs was characterised by a τ_{ON} value less than 4 ms and a τ_{OFF} of about 40 ms, which are comparable with those measured in conventional PDLCs [6]. In fact, from a theoretical point of view the rise times are essentially dependent from the driving field strength, as reported in the following Equation (2):

$$\tau_{ON} \sim \frac{\gamma}{\epsilon_0 \Delta \epsilon (E_{applied}^2 - E_{thr}^2)} \quad (2)$$

where $E_{applied}$ and E_{thr} are the applied and threshold electric fields, and γ the rotational viscosity coefficient, while the decay times are dependent from R , γ and K as reported in the following Equation (3) ⁶:

$$\tau_{OFF} \sim \frac{R^2 \gamma}{K} \quad (3)$$

i.e. larger LC domains are expected to be characterized by a longer OFF time. In the case of PMDLCs, the average pore size was 0.4 μm , so assuming that the maximum droplet radius involved in the reorientation was 2 μm (see Figure 2), Equations (2) and (3) give a τ_{ON} value less than 1 ms and a τ_{OFF} value of around 10 ms. These values are lower than the experimental ones (4 and 40 ms, respectively), due probably to the assumption of strong anchoring of liquid crystal molecules to the polymer walls made for Equations (2) and (3), which could not hold for PP, being an apolar polymer.

Therefore, PMDLCs can be designed with enhanced electro-optical properties similar to or better than those of conventional PDLCs by choosing a polymer matrix with an adequate pore size and refractive index (matching the LC ordinary refractive index n_o) and a liquid crystal with optimal electro-optical and visco-elastic properties (i.e. Δn , $\Delta \epsilon$, γ and K). It is important to note that PMDLC can be obtained with a LC amount lower than that generally required in conventional PDLC (from 40 to 85 wt%) ⁶ and no LC is dispersed inside the dense fibres of polymer matrix, on the contrary of what happens in conventional PDLCs, where polymer matrix and liquid crystal keep a mutual solubility after phase separation. These two characteristics represent a liquid crystal saving and so a relevant reduction in the device costs.

2.5 CONCLUSIONS

In this paper polymer membrane dispersed liquid crystals were successfully prepared and their electro-optical properties were investigated as a function of the applied electric field. Polymer membranes were sputtered with a thin layer of conductive ITO in order to play the role of a polymer network, hosting LC after capillary suction, with conductive substrates for the electric modulation of scattering properties. The required amount of liquid crystal is dependent on the membrane porosity and the electro-optical properties of the devices can be predicted in advance thank to the use of a polymer network with well-defined optical and visco-elastic characteristics, which do not change after LC filling (on the contrary to what happens in procedures requiring phase separation processes). PMDLCs were characterised by an opaque OFF state with a $T_{OFF} = 0.5\%$, thanks to the LC director random orientation, and a transparent ON state with a $T_{ON} = 65\%$, due to the re-orientation of LC directors under the action of a saturation electric field $E_{90\%} = 1.8 \text{ V } \mu\text{m}^{-1}$. Response times were fast and similar to those found in conventional PDLCs. Results indicated that the electro-optical properties of devices were essentially determined (and, consequently, could be easily enhanced) by polymer membrane average pore size and refractive index values and by LC visco-elastic parameters (γ/K ratio) and refractive indices.

Therefore, PMDLC could be proposed both as alternative, cheap and flexible PDLC devices, thanks to the reduced amount of used LC and the absence of rigid conductive supports. In addition, they could find application for theoretical investigation of LC in special and restricted geometries.

REFERENCES

- [1] M.L. Macchione, G. De Filpo, F.P. Nicoletta, *Liq Cryst.* **2005**, *32*, 315.
- [2] A. Seeboth, D. Löttsch, *Thermochromic and thermotropic materials*, Singapore: Pan Stanford Publishing Pte. Ltd, **2014**.
- [3] G. De Filpo, F.P. Nicoletta, L. Ciliberti, P. Formoso, G. Chidichimo, *J. Power Sources* **2015**, *274*, 274.
- [4] M. Macchione, G. De Filpo, A. Mashin, F.P. Nicoletta, G. Chidichimo, *Adv. Mater.* **2003**, *15*, 327.
- [5] J.W. Doane, G. Chidichimo, N.A.P. Vaz, Light modulating material comprising a liquid crystal dispersion in a plastic matrix. US Patent 4,688,900. **1987**.
- [6] P.S. Drzaic. *Liquid crystal dispersions*. Singapore: World Scientific, **1995**.
- [7] S. Zumer, J.W. Doane, *Phys. Rev. A.* **1986**, *34*, 3373.
- [8] H.G. Craighead, J. Cheng, S. Hackwood, *Appl Phys Lett.* **1982**, *40*, 22.
- [9] G.W. Smith. *Phys. Rev. Lett.* **1993**, *70*, 198.
- [10] C. Zhang, D. Wang, H. Cao, P. Song, C. Yang, H. Yang, G-H. Hu, *Polym Adv Tech.* **2013**, *24*, 453.
- [11] S-M. Guo, X. Liang, C-H. Zhang, M. Chen, C. Shen, L-Y. Zhang, X. Yuan, B-F. He, H. Ynag, *Appl. Mater. Interfaces.* **2017**, *9*, 2942.
- [12] X. Liang, S. Guo, M. Chen, C. Li, Q. Wang, C. Zou, C. Zhang, L. Zhang, S. Guo, H. Yang, *Mater Horizons.* **2017**, *4*, 878.
- [13] Y. Zhang, L. Zhou, J. Yang, J. Zhang, M. Hai, L. Zhang, F. Lim, C. Zhang, Z. Yang, H. Yang, S. Zhu, *Liq. Cryst.* **2018**, *45*, 728.
- [14] Y. Wu, H. Cao, M. Duan, E. Li, H. Wang, Z. Yang, D. Wang, W. He, *Liq. Cryst.* **2018**, *45*, 1023.
- [15] L. Wenbo, H. Cao, M. Kashima, F. Liu, Z. Cheng, Z. Yang, S. Zhu, H. Yang, *J. Polym. Sci. B Polym. Phys.* **2008**, *46*, 2090.
- [16] Y. Zhang, J. Yang, L. Zhou, Y. Gao, M. Hai, L. Zhang, *Liq. Cryst.* **2018**, *45*, 1068.
- [17] W. Zhang, X. Liang, C. Li, F. Li, L. Zhang, H. Yang, *Liq Cryst.* **2018**, *45*, 1111.
- [18] D.F. Ollis, E. Pelizzetti, N. Serpone, *Photo-catalysis. Fundamentals and applications*. New York (NY): John Wiley & Sons Inc, **1989**.
- [19] G. De Filpo, A.M. Palermo, R. Munno, L. Molinaro, P. Formoso, F.P. Nicoletta, *Int. Biodeterior Biodegrad.* **2015**, *103*, 51.
- [20] M.A. Kudryashov, A.I. Mashin, A.S. Tyurin, G. Chidichimo, G. De Filpo. *J Surf Investig-X-RA.* **2010**, *4*, 437.
- [21] M.A. Kudryashov, A.I. Mashin, A.A. Logunov, G. Chidichimo, G. DE Filpo, **2012**, *57*, 965.
- [22] P. Formoso, R. Muzzalupo, L. Tavano, G. De Filpo, F.P. Nicoletta. *Mini-Rev Med Chem.* **2016**, *16*, 668.
- [23] I. Dierking, G. Scalia, P. Morales, D. LeClere, *Adv Mater.* **2004**, *16*, 865.

- [24] P. Poulin, H. Stark, T.C. Lubensky, D.A. Weitz, *Science*. **1997**, 275, 1770.
- [25] S. Mormile, G. De Filpo, G. Chidichimo, F.P. Nicoletta, *Liq. Cryst.* **2008**, 35, 1095.
- [26] G. De Filpo, P. Formoso, A.I. Mashin, A. Nezhdanov, L. Mochalov, F.P. Nicoletta, *Liq. Cryst.* **2018**, 45, 721.

PART II

CHAPTER 3

3. CHEMICAL VAPOR DEPOSITION OF PHOTOCATALYST NANOPARTICLES ON PVDF MEMBRANES FOR ADVANCED OXIDATION PROCESSES

Published as: G. De Filpo, E. Pantuso, K. Armentano, P. Formoso, G. Di Profio, T. Poerio, E. Fontananova, C. Meringolo, A.I. Mashin, F.P. Nicoletta, Chemical Vapor Deposition of Photocatalyst Nanoparticles on PVDF Membranes for Advanced Oxidation Processes, *Membranes*, **2018**, *8*, 35. <https://doi:10.3390/membranes8030035>

3.1 SUMMARY

The chemical binding of photocatalytic materials, such as TiO₂ and ZnO nanoparticles, onto porous polymer membranes requires a series of chemical reactions and long purification processes, which often result in small amounts of trapped nanoparticles with reduced photocatalytic activity. In this work, a chemical vapor deposition technique was investigated in order to allow the nucleation and growth of ZnO and TiO₂ nanoparticles onto polyvinylidene difluoride (PVDF) porous membranes for application in advanced oxidation processes. The thickness of obtained surface coatings by sputtered nanoparticles was found to depend on process conditions. The photocatalytic efficiency of sputtered membranes was tested against both a model drug and a model organic pollutant in a small continuous flow reactor.

3.2 INTRODUCTION

Thin films are material layers that have thicknesses varying from tens of nanometers to a few micrometers¹. They are generally obtained by deposition processes on the surface of given substrates. The thin film growth is generally a two-step process where an initial random nucleation step is followed by an ordered growth. Nucleation and growth—and consequently the film structure—depend on the substrate chemistry (surface composition and structure), the method used², and deposition conditions³.

Thin film deposition methods are classified in solid, liquid, and gas phase deposition methods according to the physical state of the deposited material. A further classification of gas deposition methods distinguishes chemical vapor deposition (CVD) and physical vapor deposition (PVD) processes. Both methods involve the deposition of atoms or molecules carried in their vapor phase industries. Efficient separation and purification are also important for food and pharmaceutical

plants in order to guarantee high-quality water after removal of toxic components from industrial wastewater. Pharmaceutical active compounds can be considered as hazardous substances because of their potential threat to health and the environment. They are also considered an emerging pollutant due to the failure of classical treatments (such as filtration, adsorption, bio-oxidation, sedimentation, coagulation, chlorination, and UV-irradiation) to effectively remove them⁵⁻⁷. In addition to common chemical pollutants, over 80 pharmaceutical

active compounds have been detected in wastewater effluents and surface water across the world⁸, with concentration ranging from few ng L^{-1} to several g L^{-1} . The most important sources of pharmaceutical active compound are incorrect disposal of unused drugs and effluents of wastewater treatment plants (including pharmaceutical industries, hospital wastewater, aqua-farming, and cattle-breeding)^{9–11}. While the measured concentrations can result in water that is low or below drinking water guidelines and health criteria¹², their continuous accumulation in aquatic environment can also represent a real hazard.

More recently, polymer membranes have been used as innovative separation materials¹³. A membrane can be defined as “a barrier that separates and/or contacts two different regions and controls the exchange of matter and energy between the regions”¹⁴. Today, membranes are efficiently used for water desalinization, wastewater purification, recovery of valuable constituents from production waste, gas separation in petrochemical processes, concentration and purification in food and drug applications, artificial organs and therapeutic systems, energy conversion, and storage systems^{15–17}. In addition to their technical simplicity and energy efficiency, membrane processes can be easily upscaled from batchwise treatment of small quantities to large-scale continuous operations.

An advanced oxidation process (AOP) is a simple technique that allows an efficient degradation of organic pollutants generally found in wastewater. In an AOP, organic pollutants are mineralized by the generation of highly reactive hydroxyl radicals¹⁸. Among the advanced treatment technologies, UV photocatalysis by nanoparticles (e.g., ZnO and TiO_2), has attracted great interest in recent years¹⁹. In a photooxidation process (Figure 1), electrons are promoted from valence band to conduction band—resulting in the formation of electron-hole pairs—when the catalyst nanoparticle (CNp) is irradiated by UV light with energy intensity larger than the characteristic band gap (3.37 eV for ZnO and 3.2 for TiO_2 , respectively)^{20,21}.

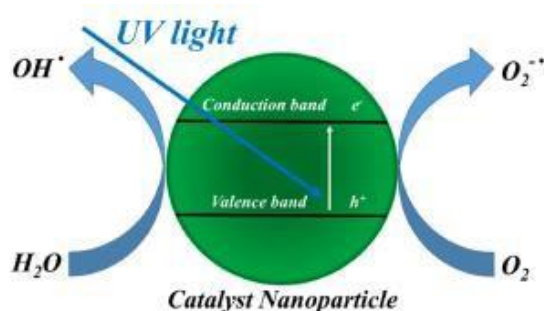
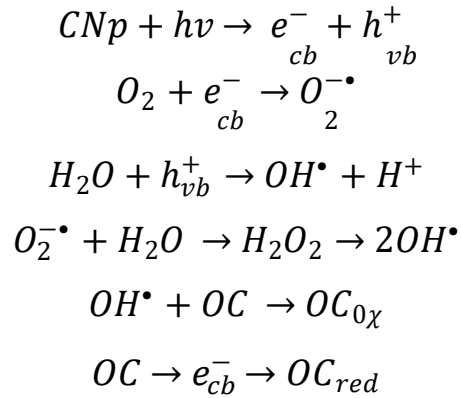


Figure 1. Schematization of the photoactivity of a catalyst nanoparticle (CNp).

Both electrons and holes can move to the semiconductor surface and produce radicals, which can oxidize organic compounds (OC), whereas electrons can reduce them, according to the reactions Both electrons and holes can move to the semiconductor surface and produce radicals, which can oxidize organic compounds (OC), whereas electrons can reduce them, according to the reactions reported^{19,22}. The degradation of organic compounds (OC) by photocatalyst nanoparticles (CNp) is shown below.



ZnO and TiO₂ are the most commonly used photocatalysts due to their redox ability, chemical stability, reduced toxicity towards the environment and health, and low cost²³. In addition to the mineralization of organic compounds, the reactive redox species—such as hydroxyl radicals (OH[•]), superoxide anions (O₂^{•-}), and hydrogen peroxide molecules (H₂O₂) generated by UV irradiation—can damage the cell membrane of microorganisms²⁴ and kill bacteria, viruses, fungi, and algae²⁵, thus conferring long-term antibacterial and antifungal properties^{26–28} to photocatalysts. More recently, submerged membranes have been integrated by semiconductor photocatalysts in order to photomineralize membrane fouling^{29,30}, thereby reducing cleaning and maintenance costs. In particular, Ho et al. obtained an enhancement in the filtration flux of a submerged membrane reactor by integration of photooxidation process and membrane filtration³¹, while Mendez-Arriaga et al.³² studied the TiO₂ photocatalytic degradation of pharmaceutical compounds such as diclofenac, naproxen, and ibuprofen.

The combination of membrane separation and advanced oxidation processes is an emerging technology for the complete removal of pollutants because each technique complements the advantages of the other. In particular, the AOP eliminates membrane fouling and allows the remediation of the concentrate while, at the same time, the membrane process filters the feed and concentrates pollutants to an optimal level for AOP^{33–35}.

Nevertheless, the chemical binding of photocatalysts onto porous polymer membranes requires a series of chemical reactions and long cleaning processes, which often result in small amounts of trapped nanoparticles with reduced photocatalytic activity. In addition, some polymers, such as polytetrafluoroethylene and polyvinylidene fluoride, are hardly functionalizable in order to trap photocatalyst molecules.

In this work, a chemical vapor deposition process was investigated in order to allow the nucleation and growth of ZnO and TiO₂ photocatalytic nanoparticles onto polyvinylidene difluoride (PVDF) porous membranes for applications in AOP. The purpose of this work was the coupling of filtration properties of polymer membranes with the photocatalytic activity of ZnO and TiO₂ nanoparticles nucleated and grown on PVDF porous membranes using the CVD technique. The substrates used were membrane disks in PVDF, which is a thermoplastic material characterized by high strength and nontoxicity and, consequently, widely used in membrane processes and food applications. Moreover, PVDF is characterized by high chemical and UV stability, which renders this material particularly interesting for photocatalytic applications. CVD is a well-known chemical process for the production of high-purity, high-performance solid thin films. In a typical CVD

process, the substrate is exposed to one or more volatile precursors, which react on the substrate surface to produce the desired layer (Figure 2).

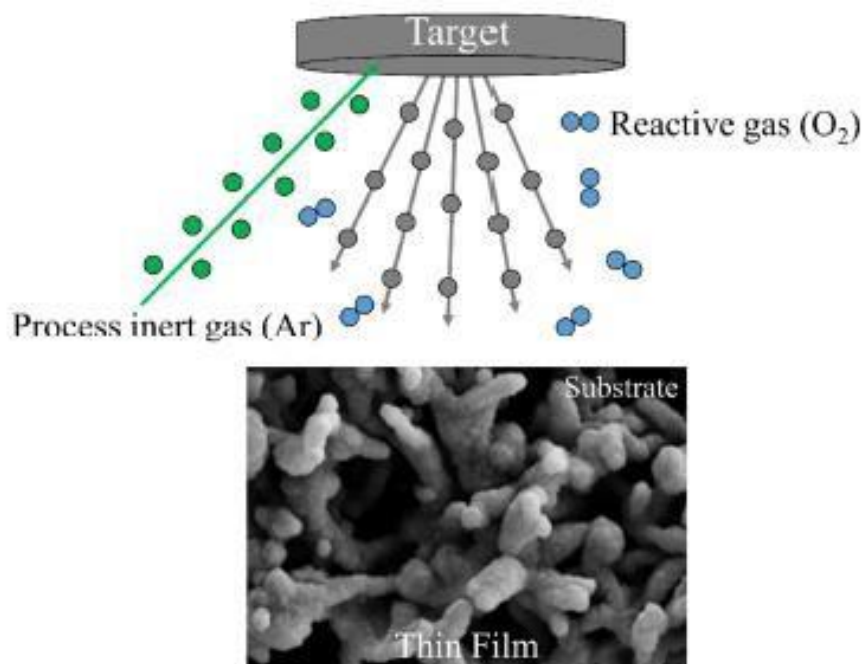


Figure 2. Schematization of the chemical vapor deposition (CVD) technique. The substrate is exposed to one or more volatile precursors, which react on the substrate surface to produce the desired thin film.

The photocatalytic efficiency of sputtered membranes was tested against a model drug (diclofenac sodium) and a model pollutant (methylene blue) in a small continuous flow reactor.

3.3 MATERIALS AND METHODS

The substrates used were PVDF membrane disks with a diameter of 47 mm, a porosity of 70%, and a mean pore size of 0.10 μm (Durapore ©, Merck KGaA, Darmstadt, Germany). Prior to use, membranes were washed in methanol (Sigma-Aldrich, Milan, Italy) by an ultrasonic bath (model M1800H-E, Branson, Danbury, CT, USA). The deposition of nanostructured photocatalysts on PVDF membranes was obtained by sputtering of appropriate targets by process inert gas ions (argon) in a Edwards AUTO-306 sputtering system (Edwards, Burgess Hill, UK).

ZnO was deposited on PVDF membranes by Argon (purity 99.999%) sputtering of a ZnO target (purity 99.99%, Goodfellow Cambridge Ltd., Huntingdon, England). The deposition of nanostructured TiO_2 was obtained by reactive sputtering using a Ti target (purity 99.999%, Goodfellow Cambridge Ltd., Huntingdon, England) in presence of a gaseous mixture of argon and oxygen (purity 99.999%, pressure of gas mixture: $p(\text{Ar}) = 2.8 \times 10^{-3}$ mbar and $p(\text{O}_2) = 1.2 \times 10^{-3}$ mbar, $p(\text{Ar})/p(\text{O}_2) = 2.3$). The reactive gas mixture reacts with the substrate and sputtered atoms, forming a thin film of desired compound onto the substrate. The particular pressure ratio between Ar and O_2 was chosen in order to form the anatase polymorph of TiO_2 ³⁶, which is more photoactive than rutile polymorph³⁷.

A microRaman spectrometer (Labram, Horiba Jobin Yvon) equipped with an Olympus microscope and

interfaced to a color camera was used to confirm the presence of TiO₂ anatase thin layers. The Raman spectra were collected through a 100× objective using a He–Ne laser (emission wavelength at 632.8 nm, power 5 mW). Membrane and nanoparticle morphology was investigated by scanning electron microscopy (SEM). Observations were performed on membrane top surfaces coated with a thin gold or graphite film by a Leica LEO 420 (Leica Microsystems, Cambridge, England) or a Quanta 200 (FEI/Philips, Eindhoven, Netherlands) scanning electron microscope equipped with a backscatter electron detector. Energy-dispersive X-ray (EDX) maps were obtained with a Phenom ProX SEM (Phenom-World, Eindhoven, The Netherlands). Transmission electron microscope (TEM) image were collected with a JEM 1400 Plus transmission electron microscope operating at 100 kV (Jeol, Akishima, Tokyo, Japan). The shape and size of nanoparticles was obtained by software analysis of TEM pictures. The number of measured nanoparticles—taken from different pictures of the same sample—was at least 100, and their size was evaluated with an image software (Motic Images Plus 2.0, MoticEurope S.L.U., Barcelona, Spain).

Static contact angles to pure water were measured with a CAM 200 contact angle meter (KSV Instruments LTD, Helsinki, Finland) at 25 °C. A drop (2 μL) of water was put onto the sample surface by a microsyringe, and measurements were carried out by setting the tangents on both visible edges of the droplet on five different positions of each sample and calculating the average value of the measurements.

The permeation tests were carried out with distilled water using a tangential flow filtration cell having an active area of 14.5 cm². The feed solution (at 25 ± 1 °C) was pumped parallel to the membrane surface by a gear pump at the transmembrane pressure of 0.4 bar. The feed flow rate was 250 mL min⁻¹. Permeate samples were collected every 5 min in order to determine the transmembrane flux, *J*, defined as:

$$J = \frac{V_p}{A \Delta t} \quad (1)$$

where *V_p* is the permeate volume passed through the membrane in the fixed time interval *Dt* and *A* is the effective membrane area. The photoactivity of ZnO and TiO₂ layers was tested in a small continuous plant where either a diclofenac sodium (9.3 × 10⁻⁵ M, Sigma Aldrich, Milan, Italy) or methylene blue (1.3 × 10⁻⁵ M, Sigma Aldrich, Milan, Italy) water solution was recirculated by a peristaltic system through a round cell, which was equipped with a quartz window to allow UV irradiation and divided into two compartments by membrane³⁸. The sputtered side of membranes was exposed to the UV light from a medium-high pressure mercury vapor lamp (ZS lamp, Helios Italquartz, Italy) with an irradiance of 6W m⁻². At the cell exit, the solution passed through a quartz flow cuvette placed inside a spectrophotometer able to read the absorbance value at either 275 nm or 665 nm, which are the wavelength of maximum absorption of diclofenac sodium and methylene blue, respectively. The absorbance was measured at regular intervals of 5 or 15 min.

3.4 RESULTS AND DISCUSSION

The quality of the obtained thin film is strongly dependent on the process parameters. In particular, the sputtering yield (*Y*) is defined as the number of sputtered atoms per impinging ion. Consequently, a higher

yield results in a higher sputtering deposition rate. The sputtering yield depends on several parameters³⁹, including the energy of the incident ions, the masses of the ions and target atoms, the binding energy of atoms in the solid, and the incident angle of ions. The sputtering yield can be expressed as:

$$Y = \alpha \frac{Mm E_m}{(M + m)^2 U_M} \quad (2)$$

where m and M are the mass of the bombing ion and target atom, respectively, E_m is the kinetic energy of bombing ion, and U_m is the bonding energy of target metal. α takes into account the incident angle of ions. It is important to recall that magnetic field strength, CVD chamber volume, power density, gas composition and pressure are other factors that can affect yield values⁴⁰. In addition, the film deposition rate decreases for increasing target-substrate distances. Therefore, under the chosen sputtering process parameters (obtained starting from values based on the previous works^{41,42} using the same sputtering source), an optimal deposition rate for ZnO and TiO₂ of about 2 and 1 nm min⁻¹, respectively, was gained. The sputtering time used for the ZnO target was twice that of the Ti one in order to have similar layer thicknesses. The different sputtering conditions (sputtering power and time, target distance, and gas pressure) were tested in order to find the optimal set of parameters able to give a homogeneous membrane coverage with no polymer substrate damage and very small photocatalyst nanoparticles. This last condition ensures a high photoactivity, with catalysis being a surface process. Due to inadequate sputtering conditions, typical sample drawbacks were inhomogeneous coverage, pore occlusion, and presence of cracks (damage of thin film), as shown in Figure 3. The best results—in terms of both coverage quality and nanoparticle size—were obtained with the sputtering conditions (sputtering power, target distance, gas pressure, sputtering time) shown in Table 1.

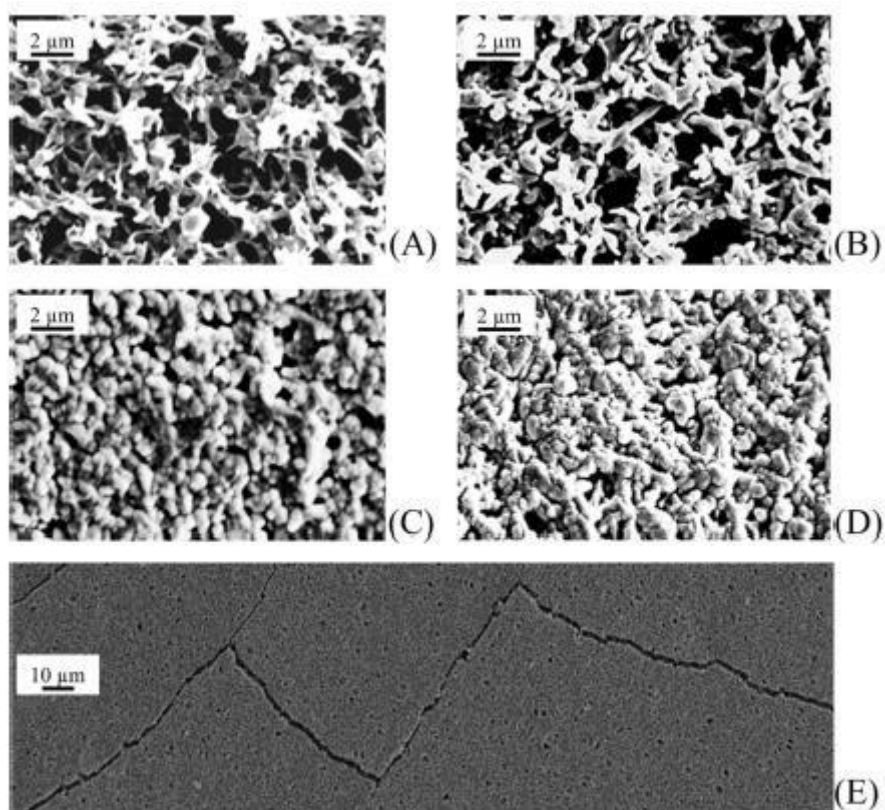


Figure 3. Morphology of virgin and TiO₂ sputtered polyvinylidene difluoride (PVDF) membranes after different sputtering times (t): (A) virgin PVDF membrane; t = 0, (B) t = 1 h; (C) t = 2 h; (D) t = 3 h; (E) t = 4 h.

Table 1. Optimal sputtering parameters able to give a homogeneous coverage with no substrate damage and small nanoparticles.

Target	Photocatalyst Layer	Sputtering Power/W	Target Distance/10 ⁻² m	Pressure/10 ⁻⁶ bar	Sputtering Time/min
ZnO	ZnO	35	8	P(Ar) = 4.5	30
Ti	TiO ₂	65	7	P(Ar) = 2.8 ¹	60

¹ P(O₂) = 1.2 × 10⁻⁶ bar.

Figure 4 shows the morphology of the top surface in virgin and sputtered PVDF membranes under the experimental conditions reported in Table 1. Both photocatalyst coatings (Figure 4B,C for ZnO and TiO₂, respectively) were homogeneous with no evident alteration/damage of the virgin PVDF membrane (Figure 4A). In addition, no occlusion of membrane pores was present. Coatings had a cauliflower structure with aggregate diameters of around 100 nm and formed by agglomeration of smaller primary nanoparticles (see later).

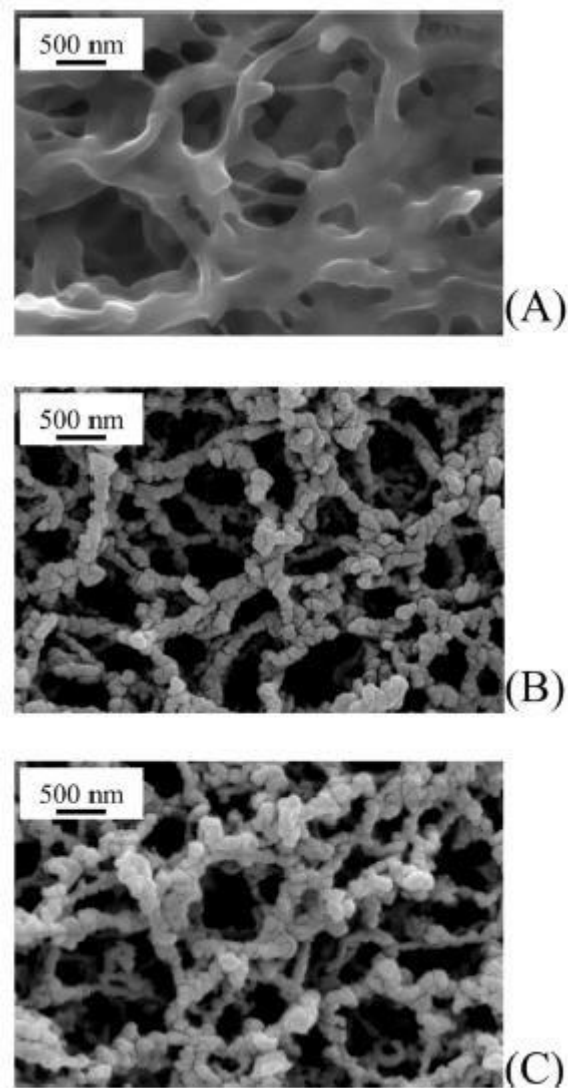


Figure 4. Morphology of virgin and sputtered PVDF membranes under the experimental conditions reported in Table 1: (A) virgin PVDF membrane; (B) ZnO sputtered PVDF membrane; and (C) TiO₂ sputtered PVDF membrane.

In order to further confirm that PVDF membranes were homogeneously covered with photocatalysts, SEM backscattering electron micrographs and spot EDX analysis on sputtered PVDF membranes were performed. Figure 5 shows SEM backscattering electron micrographs and EDX maps for ZnO and TiO₂ sputtered membranes.

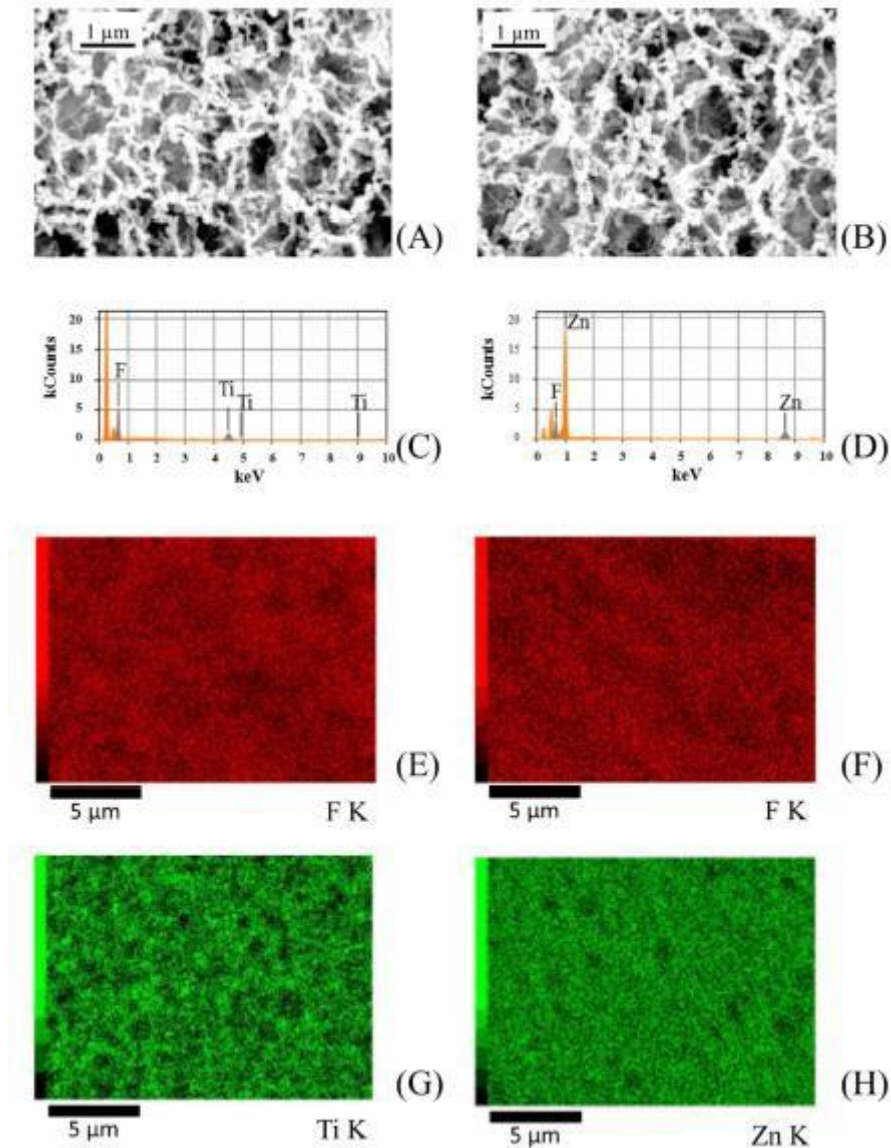


Figure 5. (A,B) Scanning electron microscopy (SEM) backscattering electron micrographs, (C,D) elemental mapping, and (E–H) energy-dispersive X-ray (EDX) analysis performed on TiO₂ (on the **left**) and ZnO (on the **right**) sputtered PVDF membranes.

At larger magnifications, TEM analysis allows characterizing the morphology of primary nanoparticles grown on PVDF membranes. As shown in Figure 6A,B, both ZnO and TiO₂ primary nanoparticles were rather spherical in shape with similar average diameters of 11.6 ± 4.2 and 12.1 ± 3.4 nm, respectively (Figure 7). Primary nanoparticles agglomerated into larger aggregates.

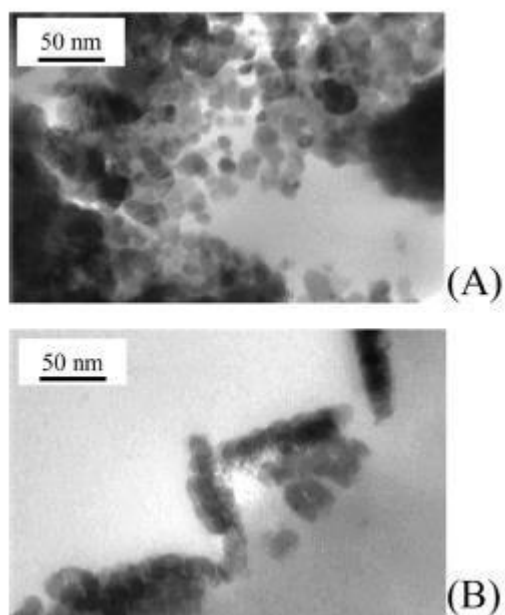


Figure 6. Morphology of catalyst nanoparticles grown on PVDF membranes under the experimental conditions reported in Table 1: (A) ZnO sputtered PVDF membrane; and (B) TiO₂ sputtered PVDF membrane.

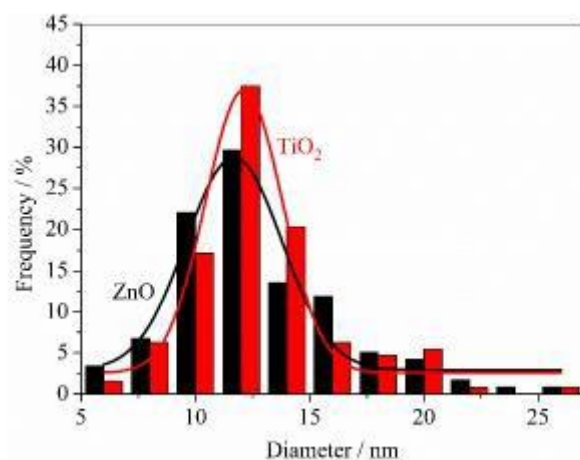


Figure 7. Distribution of diameters shown by primary nanoparticles present on ZnO and TiO₂ sputtered PVDF membranes.

MicroRaman spectrum of PVDF membrane obtained by reactive sputtering using a Ti target is reported in Figure 8.

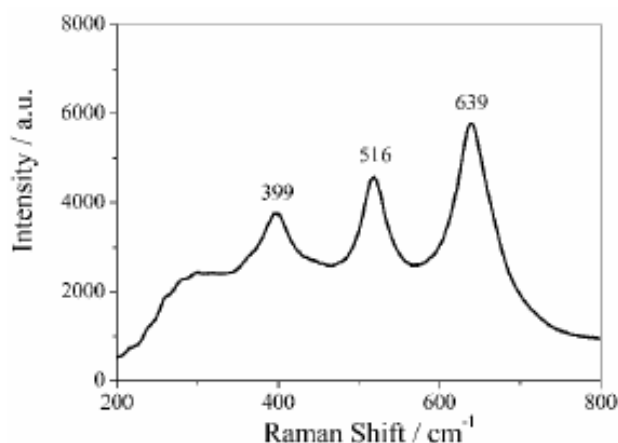


Figure 8. Raman spectrum of TiO₂ nanoparticles sputtered on PVDF membrane. The peaks at 399, 516, and 639 cm⁻¹ are associated to the Raman active modes B1g, A1g, and Eg, respectively, confirming the anatase structure of TiO₂.

The Raman spectrum of TiO₂ nanoparticles consisted of three peaks with strong intensities at 399, 516, and 639 cm⁻¹, which can be associated to the Raman active modes B1g, A1g, and Eg of anatase structure of TiO₂ thin layers. These values are in good agreement with the Raman bands reported in literature⁴³. The fourth active Raman mode of anatase structure of TiO₂, which is generally placed at 196 cm⁻¹ (Eg mode), was out of the instrument range. It is expected that the deposition of ZnO and TiO₂ thin films could change the hydrophilicity of virgin PVDF membranes. Table 2 shows the static contact angles to pure water measured for virgin and sputtered membranes. Both ZnO and TiO₂ thin films drastically reduced the contact angle, i.e., increased the hydrophilicity of virgin PVDF membrane from 61° to 27° and 26°, respectively, with a consequent decrease in fouling. It is important to recall that the photoactivity of ZnO and TiO₂ layers is able to further overcome this drawback. Moreover, the increase in hydrophilicity is expected to have a positive effect in the membrane permeation properties. Table 2 also shows the transmembrane fluxes of virgin and sputtered membranes. The performant effect of catalyst thin film increased the transmembrane flux of virgin PVDF from a value of 200 to 760 and 710 L m⁻²h⁻¹ for ZnO and TiO₂ thin films, respectively, as a result of the increased hydrophilicity. These results also confirm that the sputtered thin layer did not occlude the membrane pores.

Table 2. Contact angle and transmembrane flux of virgin and sputtered PVDF membranes under the experimental conditions reported in Table 1.

Photocatalyst	Contact Angle/deg	Transmembrane Flux/L m ⁻² h ⁻¹
Virgin PVDF	61 ± 1	200 ± 15
ZnO	27 ± 2	760 ± 15
TiO ₂	26 ± 2	710 ± 15

In order to test their photocatalytic activity against pharmaceutical active compounds and organic pollutants, sputtered membranes were placed in a small continuous flow reactor where a water solution of either diclofenac sodium—a well-known anti-inflammatory drug—or methylene blue—a well-known organic dye— was circulated. Figure 9 shows the activity of ZnO and TiO₂ sputtered membranes in the diclofenac sodium salt photodegradation. The drug photodegradation by PVDF membranes with sputtered ZnO and TiO₂

nanoparticles followed a first order kinetics with similar rate constants of $6.8 \times 10^{-3} \text{ min}^{-1}$ and $8.3 \times 10^{-3} \text{ min}^{-1}$ respectively. An almost complete photodegradation of diclofenac sodium salt was obtained within 6 h in both cases. Similarly, Figure 10 shows the activity of ZnO and TiO₂ sputtered membranes in the methylene blue photodegradation. Also in this case, the photodegradation kinetics of the organic pollutant by PVDF membranes with sputtered ZnO and TiO₂ nanoparticles was a first order kinetics but with larger rate constants of $2.2 \times 10^{-2} \text{ min}^{-1}$ and $2.8 \times 10^{-2} \text{ min}^{-1}$, respectively. Nevertheless, the methylene blue photodegradation stopped after 4 h with a plateau of 33% and 8% for PVDF membranes with sputtered ZnO and TiO₂ nanoparticles, respectively. The behavior of virgin PVDF membrane reported in Figures 9 and 10 takes into account the UV photolysis of diclofenac sodium and methylene blue, respectively. Several parameters can affect the degradation efficiency of photocatalysts including the particular dye/drug, the pH of the solution, the presence of oxygen, the addition of hydrogen peroxide, the nanoparticle average size, and the amount and type of catalyst⁴⁴. In particular, several experimental investigations have found that TiO₂ nanoparticles show a photocatalytic efficiency higher than ZnO nanoparticles due to their band gap values^{45,46}. Indeed, ZnO samples have a larger band gap, which leads to the production of less radicals and, consequently, to a lower dye photodegradation. On the contrary, TiO₂ has a higher quantum yield engendered by a relatively slower electron-hole pair recombination, faster electron-hole pair migration to the surface, fewer defects, and exciton traps in the crystal lattice⁴⁷.

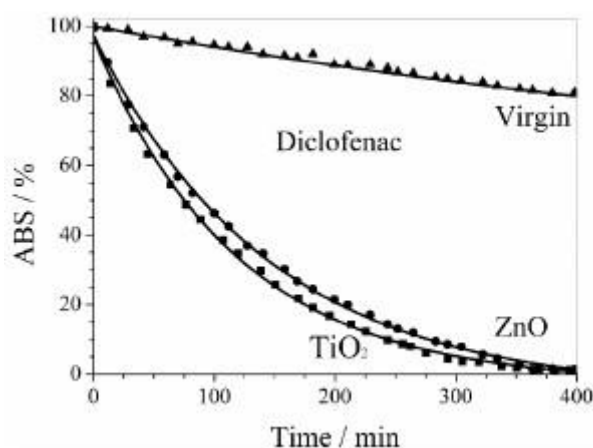


Figure 9. Photodegradation diclofenac sodium by PVDF membranes with sputtered ZnO and TiO₂ nanoparticles. The behavior of virgin PVDF membrane takes into account the UV photolysis of diclofenac.

Even if kinetic rate constants are strongly dependent on membrane composition, investigated pollutants and the UV lamp power used⁴⁸, it is important to note that the obtained values of kinetic rate constants are the same order of magnitude as those found in other literature works where the photoactive nanomaterial was either directly synthesized or immobilized on polymer substrates⁴⁹⁻⁵¹. These rate values make the CVD of photocatalyst nanoparticles on porous polymer membranes a suitable technique for applications in the field of advanced oxidation processes. In fact, the CVD of photocatalysts is a fast process that avoids expensive and time-consuming syntheses and cleaning post-treatments, as it is possible to directly sputter photocatalysts onto commercially available membranes while keeping good photocatalytic activities at the same time. Recycling

of a catalyst is a very important property in practical applications. In order to assess the recycling properties of photocatalysts, ten photodegradation cycles were performed using the same film and fresh methylene blue. Both ZnO and TiO₂ sputtered membranes were reused in successive runs without performing any cleaning procedure and gave percentages of degraded methylene blue similar to those obtained after the first run. These results demonstrated the ability of the ZnO and TiO₂ sputtered membranes to fully preserve/restore their initial photocatalytic efficiency. In addition, the long-term stability of photocatalyst deposit onto polymer substrates was checked after ten cycles of successive photocatalysis processes. No evident damage was revealed in the nanoparticles layer morphology, confirming the main advantage of an easy reuse of membranes with sputtered catalysts over the homogeneous and heterogeneous catalysis processes, which suffer the drawbacks of catalyst recovery and damage of polymers used to functionalize membranes or bind catalysts⁵². Further work is in progress in order to control the primary particle size in a finer way.

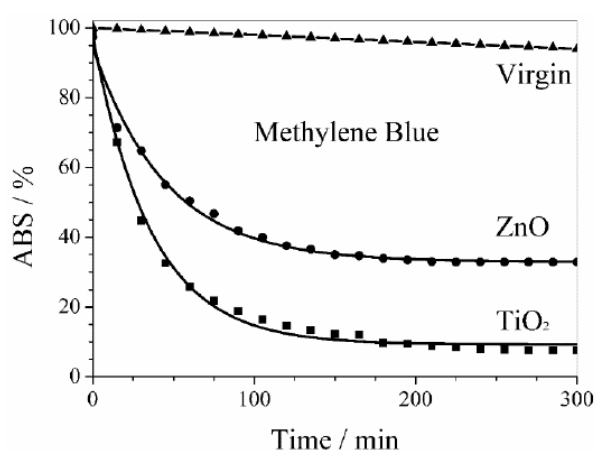


Figure 10. Photodegradation of methylene blue by PVDF membranes with sputtered ZnO and TiO₂ nanoparticles. The behavior of virgin PVDF membrane takes into account the UV photolysis of methylene blue.

3.5 CONCLUSIONS

In this work, the results of a CVD functionalization of polymer porous membranes with photocatalytic nanoparticles, and an application of their use in AOP were shown. The overall sputtering process took less than 1 h, which is lower than conventional times employed in organic synthesis processes of similar materials. The thickness of obtained surface coating by sputtered nanoparticles was found to depend on process conditions. The membranes functionalized with ZnO and TiO₂ nanoparticles were characterized by contact angles lower than that shown by virgin membrane, making these composite membranes suitable for the filtration of aqueous solutions. The deposition of a thin layer of nanoparticles increased the transmembrane fluxes as hydrophilicity increased, and no pore occlusion occurred. In addition to its long-term stability and solvent-free features, the proposed process of membrane functionalization can be easily upscaled to manufacture membrane modules for the efficient degradation of organic pollutants generally found in wastewater.

REFERENCES

- [1] G. Chidichimo, D. Cupelli, G. De Filpo, P. Formoso, F.P. Nicoletta, in *Sustainable Development in Chemical Engineering, Innovative Technologies*; (Eds. V. Piemonte, M. De Falco, A. Basile) Wiley, Chichester, UK **2013**.
- [2] M.A. Kudryashov, A.I. Mashin, A.A. Logunov, G. Chidichimo, G. De Filpo, *Tech. Phys.* **2012**, 57, 965.
- [3] P. Löbl, M. Huppertz, D. Mergel, *Thin Solid Films* **1994**, 251, 72.
- [4] C.B. Carter, M.G. Norton, In *Ceramic Materials*; (Eds. Carter, C.B., Norton, M.G.) Springer, NY, USA, **2007**.
- [5] E. Drioli, A. Ali, F. Macedonio, *Desalination* **2015**, 356, 56.
- [6] D. Bhattacharyya, *Clean Technol. Environ.* **2007**, 9, 81.
- [7] G. Di Profio, M. Polino, F.P. Nicoletta, B.D. Belviso, R. Caliandro, E. Fontananova, G. De Filpo, E. Curcio, E. Drioli, *Adv. Funct. Mater.* **2014**, 24, 1582.
- [8] T. Heberer, *Toxicol. Lett.* **2002**, 131, 5.
- [9] O.A.H. Jones, N. Voulvoulis, J.N. Lester, *Environ. Technol.* **2001**, 22, 1383.
- [10] J.L. Santos, I. Aparicio, E. Alonso, *Environ. Int.* **2007**, 33, 596.
- [11] A. Ziyilan, N.H. Ince, *J. Hazard. Mater.* **2011**, 187, 24.
- [12] D.W. Kolpin, E.T. Furlong, M.T. Meyer, E.M. Thurman, S.D. Zaugg, L.B. Barber, H.T. Buxton, *Environ. Sci. Technol.* **2002**, 36, 1202.
- [13] S.M. Salehi, G. Di Profio, E. Fontananova, F.P. Nicoletta, E. Curcio, G. De Filpo, *J. Membr. Sci.* **2016**, 504, 220.
- [14] H. Strathmann, in *Introduction to Membrane Science and Technology*, Wiley-VCH, Weinheim, Germany **2011**.
- [15] E. Drioli, L. Giorno, in *Encyclopedia of Membranes*, Springer, Heidelberg, Berlin, Germany, **2016**.
- [16] F.P. Nicoletta, D. Cupelli, P. Formoso, G. De Filpo, V. Colella, A. Gugliuzza, *Membranes* **2012**, 134, 134.
- [17] P. Formoso, E. Pantuso, G. De Filpo, F.P. Nicoletta, *Membranes* **2017**, 7, 39.
- [18] E. Pelizzetti, N. Serpone, in *Photo-Catalysis Fundamentals and Applications*, Wiley, NY, USA, **1989**.
- [19] J. Arana, J.A.H. Melian, J.M.D. Rodriguez, P.P. Pena, *Catal. Today* **2002**, 76, 279.
- [20] M.R. Hoffmann, S.T. Martin, W.Y. Choi, D.W. Bahnemann, *Chem. Rev.* **1995**, 95, 69.
- [21] C.A. Minero, *Sol. Energy Mater. Sol. Cells* **1995**, 38, 42.
- [22] N.M. Mahmoodi, M. Arami, N.Y. Limaee, N.S. Tabrizi, *J. Colloid Interface Sci.* **2006**, 295, 159.
- [23] D.S. Bhatkhande, V.G. Pangarkar, A. Beenackers, *J. Chem. Technol. Biotechnol.* **2002**, 77, 102.

- [24] M. Cho, Chung, H.; W. Choi, J. Yoon, *Water Res.* **2004**, *38*, 1069.
- [25] Z. Huang, P.C. Maness, D. Blake, A.J. William, *J. Photochem. Photobiol. A* **2000**, *130*, 163.
- [26] G. De Filpo, A.M. Palermo, R. Tolmino, P. Formoso, F.P. Nicoletta, *Cellulose* **2016**, *23*, 3265.
- [27] G. De Filpo, A.M. Palermo, F. Rachiele, F.P. Nicoletta, *Int. Biodeterior. Biodegrad.* **2013**, *85*, 217.
- [28] G. De Filpo, A.M. Palermo, R. Munno, L. Molinaro, P. Formoso, F.P. Nicoletta, *Int. Biodeterior. Biodegrad.* **2015**, *103*, 51.
- [29] H.K. Shon, S. Vigneswaran, H.H. Ngo, J.H. Kim, *Water Res.* **2005**, *39*, 2549.
- [30] S. Mozia, A.W. Morawski, *Catal. Today* **2006**, *118*, 181.
- [31] D.P. Ho, S. Vigneswaran, H.H. Ngo, *Sep. Sci. Technol.* **2010**, *45*, 155.
- [32] F. Mendez-Arriaga, S. Esplugas, J. Gimenez, *Water Res.* **2008**, *42*, 585.
- [33] S.O. Ganiyu, E.D. Van Hullebusch, M. Cretin, G. Esposito, *Sep. Purif. Technol.* **2015**, *156*, 891.
- [34] R. Molinari, A. Caruso, P. Argurio, T. Poerio, *J. Membr. Sci.* **2008**, *319*, 54.
- [35] V.C. Sarasidis, K.V. Plakas, S.I. Patsios, A.J. Karabelas, *Chem. Eng. J.* **2014**, *239*, 299.
- [36] P. Zeman, S. Takabayashi, *Surf. Coat. Technol.* **2002**, *153*, 93.
- [37] T. Luttrell, S. Halpegamage, J. Tao, A. Kramer, E. Sutter, M. Batzill, *Sci. Rep.* **2014**, *4*, 4043.
- [38] T.F. Mastropietro, C. Meringolo, T. Poerio, F. Scarpelli, N. Godbert, G. Di Profio, E. Fontananova, *Ind. Eng. Chem. Res.* **2017**, *56*, 11049.
- [39] J.D. Plummer, M. Deal, P.D. Griffin, in *Silicon VLSI Technology*, Prentice Hall Press: Upper Saddle River, NJ, USA, **2008**.
- [40] M. Tavakolmoghadam, T. Mohammadi, M. Hemmati, F. Naeimpour, *Desalin. Water Treat.* **2014**, *57*, 3328.
- [41] S.M. Marques, C.J. Tavares, S. Lanceros-Mendez, Z. Denchev, *J. Appl. Polym. Sci.* **2011**, *119*, 726.
- [42] C.J. Tavares, S.M. Marques, S. Lanceros-Mendez, L. Robouta, E. Alves, N.P. Barradas, F. Munnik, T. Girardeau, J.P. Riviere, *J. Nanosci. Nanotechnol.* **2010**, *10*, 1072.
- [43] T. Ohsaka, F. Izumi, Y. Fujiki, *J. Raman Spectrosc.* **1978**, *7*, 321.
- [44] M. Qamar, M.A. Muneer, *Desalination* **2009**, *249*, 535.
- [45] E. Colombo, W. Li, S.K. Bhangu, M. Ashokkumar, *RSC Adv.* **2017**, *7*, 19373.
- [46] R.J. Barnes, R. Molina, J. Xu, P.J. Dobson, I.P. Thompson, I.P. *J. Nanopart. Res.* **2013**, *15*, 1432.
- [47] S.W. Bennett, A.A. Keller, *Appl. Catal. B Environ.* **2011**, *102*, 600.
- [48] P.M. Martins, R. Miranda, J. Marques, C.J. Tavares, G. Botelho, S. Lanceros-Mendez, S. Leong, A. Razmijou, K. Wang, K. Hapgood, *J. Membr. Sci.* **2014**, *472*, 167.

- [49] P.M. Martins, R. Miranda, J. Marques, C.J. Tavares, G. Botelho, S. Lanceros-Mendez, *RSC Adv.* **2016**, *6*, 12708.
- [50] K. Fischer, M. Grimm, J. Meyers, C. Dietrich, R. Gläser, A. Schulze, *J. Membr. Sci.* **2015**, *478*, 49.
- [51] B.J. Starr, V.V. Tarabara, M. Herrera-Robledo, M. Zhou, S. Roualdès, A. Ayrál, *J. Membr. Sci.* **2016**, *514*, 340.
- [52] H. Song, J. Shao, Y. He, B. Liu, X. Zhong, *J. Membr. Sci.* **2012**, *405*, 48.

CHAPTER 4

4. WO₃/BUCKYPAPER MEMBRANES FOR ADVANCED OXIDATION PROCESSES

Published as: G. De Filpo, E. Pantuso, A.I. Mashin, M. Baratta, F.P. Nicoletta, WO₃/buckypaper membranes for advanced oxidation processes, *Membranes*, 10, 157 (2020). [https:// doi:10.3390/membranes10070157](https://doi.org/10.3390/membranes10070157).

4.1 SUMMARY

Photocatalytic materials, such as WO₃, TiO₂, and ZnO nanoparticles, are commonly linked onto porous polymer membranes for wastewater treatment, fouling mitigation and permeation enhancement. Buckypapers (BPs) are entanglements of carbon nanotubes, which have been recently proposed as innovative filtration systems thanks to their mechanical, electronic, and thermal properties. In this work, flexible membranes of single wall carbon nanotubes are prepared and characterized as efficient substrates to deposit by chemical vapor deposition thin layers of WO₃ and obtain, in such a way, WO₃/BP composite membranes for application in advanced oxidation processes. The photocatalytic efficiency of WO₃/BP composite membranes is tested against model pollutants in a small continuous flow reactor and compared with the performance of an equivalent homogeneous WO₃-based reactor.

4.2 INTRODUCTION

Advanced oxidation processes, AOPs, allow the mineralization of organic pollutants by the generation of highly reactive hydroxyl radicals¹. Photocatalytic reactions are particular AOPs, which are carried out when a catalyst is irradiated by a radiation of suitable wavelength². Photocatalysis finds several interesting applications including selective organic reactions, pollutant degradation, photocatalytic surfaces (e.g., tiles, cements, paints, and asphalts), filters for air purification, water splitting in H₂ and O₂, water purification plants, CO₂ reduction to energy fuels and bacterial disinfection³⁻⁸. Semiconductors are the most common used materials used in photocatalytic processes. Upon irradiation, electrons are promoted from the valence band to the conduction band, generating electron-hole pairs. Electrons and holes can move to the semiconductor surface and generate oxidizing species such as hydroxyl radicals (OH[•]), superoxide anions (O₂^{-•}) and hydrogen peroxide molecules (H₂O₂), which are able to react with the present chemical species (dyes, pollutants, and other undesired molecules) and degrade them⁹. Several materials have photocatalytic properties (GaP, GaAs, CdSe, CdS, Fe₂O₃, TiO₂, WO₃, ZnO, SnO₂, and CdS, just to mention a few), however not all of them are sufficiently efficient and stable over time to be used. In fact, GaP, GaAs, CdSe, CdS, or Fe₂O₃ are less stable in the air and degrade more easily. ZnO forms a passivating layer of Zn(OH)₂ on its surface, which seriously compromises its photocatalytic properties⁹. Another important factor determining the choice of a semiconductor is its band-gap value, which must be as small as possible in order to allow the use of electromagnetic radiation with larger

wavelengths. Titanium dioxide, TiO_2 , and tungsten trioxide, WO_3 , are low-cost semiconductor materials characterized by reduced toxicity towards environment and health and relatively low energy band-gaps (3.2 eV and 2.6 eV, respectively), which allow their activation with UV-Vis light (387 nm and 476 nm, respectively)¹⁰. Further problems for the use of semiconductors in the photocatalytic processes are:

1. The need of high surface area, which can be overcome by using nanometer sized materials; and
2. The semiconductor recovery after their use, which can be solved, for example, by nano-semiconductors with a magnetic core, by chemically cross-linked semiconductor nanoparticles onto polymer or ceramic membranes and, more recently, by vapor deposition of thin semiconductor films onto suitable substrates¹¹.

Thin film deposition methods can be distinguished in physical vapor deposition, PVD, and chemical vapor deposition, CVD, processes. In both methods, atoms or molecules in their vapor phase are carried onto the substrate surface and settle to form a thin layer¹¹. Food, pharmaceutical, and, more in general, chemical plants need efficient separation and purification processes in order to guarantee an efficient treatment of their wastewaters. The removal of toxic pollutants from industrial wastewaters is a challenge due to the facts that they could not be effectively removed by filtration, adsorption, sedimentation, bio-oxidation, chlorination, coagulation, UV, and other classical treatments^{12,13} and could represent potential threats to environment and health even at low concentrations (few ng L^{-1}) as a consequence of their bio-accumulation^{14,15}. Recently, polymer membranes have been suggested as simple and efficient materials to be used in water treatments including separation, purification, desalinization, recovery of critical raw materials and AOPs¹⁶⁻¹⁹. In fact, photocatalytic membranes, i.e., membranes with embedded or supported semiconductors by chemical binding, physical blending and vapor deposition, have been prepared in order to reduce/mitigate membrane fouling^{20,21}, enhance filtration fluxes²², degrade wastewater pollutants, and remediate the concentrate²³. Nevertheless, the binding of photocatalysts and polymer functionalization could need several chemical reactions and long cleaning processes, while the physical blending generally alters the mechanical properties of membranes and reduce the photocatalytic performance, as only the catalysts onto the membrane surface can play their photocatalytic activity. In addition to their potential applications as TV screens, fire protection systems, heat dispersion in microelectronics, electrical-conductive tissue engineering, electromagnetic interferences shielding, electrodes for batteries and supercapacitors, buckypapers (BPs) have been proposed as innovative, high-temperature resistant and lightweight filtration systems. They consist of an entangled assembly of carbon nanotubes (CNTs) obtained by filtration of CNT dispersions through a polymer membrane^{24,25}. According to such simple procedure, it is possible to get large-scale BP membranes that merge the mechanical, electronic, and thermal properties of CNTs with the flexibility, porosity, and transport properties of polymer membranes²⁶. At a microscopic level, BPs show a highly disordered porous morphology due to π - π and van der Waals interactions between and within bundles of carbon nanotubes^{27,28}. Consequently, BPs can result brittle. Such a problem and the risk of nanotubes release can be overcome enhancing the mechanical properties of BPs by polymer intercalation^{29,30}. In this work, flexible membranes of single wall carbon nanotubes, SWNT, (or buckypaper, BP) were prepared and characterized as efficient substrates to deposit by CVD thin layers of WO_3

and obtain, in such a way, WO₃/BP composite membranes for application in advanced oxidation processes. The photocatalytic efficiency of WO₃/BP composite membranes was tested against model pollutants (Methylene Blue, Indigo Carmine, and Diclofenac Sodium) in a small continuous flow reactor and compared with the performance of an equivalent homogeneous WO₃-based reactor.

4.3 MATERIALS AND METHODS

4.3.1 PREPARATION OF BP MEMBRANES

Buckypaper membranes were obtained by filtration of SWNT dispersions through PTFE disks (diameter = 47 mm, average pore size = 5 μm, Durapore®, Merck KGaA, Darmstadt, Germany). The average diameter of SWNTs was 1.4 ± 0.1 nm and their length was longer than 5 μm as reported in the datasheet from Sigma-Aldrich, Milan, Italy. Thirty milligrams of SWNTs were dispersed in 200 mL of a 0.4% TRITON X100 water solution by an ultrasonic bath (model M1800H-E, Branson, Danbury, CT, USA) for 30 min. Then, solutions were filtered through the PTFE disks with a vacuum pump (pressure = -0.04 bar), washed with 20 mL of methanol and, finally, dried at room temperature. All chemicals were purchased from Sigma-Aldrich, Milan, Italy.

4.3.2 DEPOSITION OF WO₃ ONTO BP MEMBRANES

The deposition of nanostructured tungsten trioxide onto BP membranes was obtained by reactive RF sputtering using of a tungsten target (purity 99.999%, Goodfellow Cambridge Ltd., Huntingdon, England) in the presence of oxygen (purity 99.999%) as process and reactive gas under different conditions of oxygen flow, sample-target distance, sputtering time, and applied RF process power. The optimal process conditions in term of layer homogeneity and catalyst droplet size were found to be: Oxygen flow 35 mL min⁻¹, sample-target distance 8 cm, sputtering time 30 min, applied RF process power 50W.

The amorphous WO₃ thin films deposited on BP membranes were converted in monoclinic WO₃ thin films, which are characterized by a larger catalytic activity, by heat treatment at 350 °C for 30 min.

4.3.3 CHARACTERIZATION OF BP AND WO₃/BP MEMBRANES

The porosity, P, of BP and WO₃/BP membranes was determined by gravimetric method at 25 °C, measuring the weight of a wetting liquid (3M-FC-40, 3M Italia Srl, Pioltello, Milan, Italy), contained in the membrane pores. The porosity was calculated according to the following Equation (1):

$$P = \frac{\frac{w_w - w_d}{d_w}}{\frac{w_w - w_d}{d_w} + \frac{w_d}{d_m}} \quad (1)$$

where w_w is the weight of the wet samples, w_d the weight of dry samples, d_w the wetting liquid density (1.855 g·cm⁻³), and d_m is the average membrane density (0.60 ± 0.03 g·cm⁻³ as calculated from measurements of buckypaper weight, thickness, and surface area).

Pore size distribution was evaluated by a capillary flow porometer (CFP-1500 AEXL, PMI Porous Materials Inc., Ithaca, NY, USA). Membranes were fully wetted by keeping them in Porewick® (Sigma-Aldrich, Milan, Italy) for 24 h. Then, nitrogen was gradually allowed to flow into the membrane by increasing its pressure and the registration of gas pressure and permeation flow rate allowed the calculation of the pore size distribution. The electrical conductivity of membranes was determined from the BP electrical resistance in I–V (current–voltage) measurements by a waveform generator (33220A Agilent, Santa Clara, CA, USA) and a digital multimeter (34410A Agilent, Santa Clara, CA, USA) on BP rectangular strips (width 5 mm and length 3 cm). The mechanical properties were measured with a Sauter TVO-S tensile tester equipped with a Sauter FH-1k digital dynamometer and AFH FAST software (Sauter GmbH, Balingen, Germany).

The rectangular strips (width 5 mm and length 3 cm) were tested at a strain rate of 0.1 mm·min⁻¹. The tests allowed the determination of the tensile strength as the maximum stress, the fracture strain as the percentage of elongation at the breaking point, and the Young's modulus. Thermogravimetric analysis (TGA, STA 2500 Regulus simultaneous thermal analyzer, Netzsch, Selb, Germany) was employed to assess the BP membrane thermal stability. TGA was carried out from room temperature to 750 °C with a heating rate of 5 °C/min in a flowing gas mixture consisting of 1% O₂ and 99% Ar at a flow rate of 100 sccm. The average roughness of WO₃/BP surfaces was evaluated by atomic force microscopy (Nanoscope III, Digital Instruments, Santa Barbara, CA, USA).

Static contact angle measurements of BP and WO₃/BP membranes were measured with a goniometer (Nordtest, Serravalle Scrivia AL, Italy) at 25 °C. A drop (2 µL) of water was put onto the sample surface by a micro-syringe and measurements were carried out by setting the tangents on both visible edges of the droplet on five different positions of each sample and calculating the average value of the measurements.

The permeation tests were carried out with distilled water using a filtration cell having an active area of 5 cm². The feed solution at 25 ± 1 °C was pumped by a gear pump at a transmembrane pressure of 1 bar. The feed flow rate was 250 mL·min⁻¹. Permeate samples were collected every 5 min in order to determine the transmembrane flux, *J*, defined as:

$$J = \frac{V_p}{A\Delta t} \quad (2)$$

where *V_p* was the permeate volume passed through the membrane in the fixed time interval, Δ*t*, and *A* was the effective membrane area.

4.3.4 PHOTODEGRADATION EXPERIMENTS

The photoactivity of WO₃/BP membranes was investigated in a small continuous plant with model pollutant water solutions (250 mL) of a cationic dye (Methylene Blue, MB, 5, 10, and 20 ppm), an anionic dye (Indigo Carmine, IC, 20 ppm) and a drug (Diclofenac Sodium, DS, 20 ppm), which were recirculated by a peristaltic system (flow rate 16.6 mL·min⁻¹, Masterflex® L/S®, Cole-Parmer Srl, Cernusco sul Naviglio, MI, Italy) through a round cell. All model pollutants were purchased from Sigma-Aldrich, Milan, Italy. The experiment temperature was 25 ± 1 °C being the becker with the pollutant solutions placed in a thermostatic bath (model

1225, VWR, Milan, Italy), which kept constant the flowing solution temperature and avoided the pollutant thermolysis. All model pollutants were purchased from Sigma Aldrich, Milan, Italy. The WO₃/BP membranes divided the cell volume in two compartments: The upper one (thickness 5 mm, photocatalytic area 8 cm², irradiated volume 4 cm³) was equipped with a N-BK7 optical glass window to allow UV-Vis irradiation from a Suntest CPS+sun simulator (1.5 kW Xenon arc lamp, with an average irradiance of 500W·m⁻² in the wavelength range 300 nm–800 nm, see Figure S1 of SI, Atlas, Linsengericht-Altenhaßlau, Germany). The light power of sun simulator was calibrated by a FieldMaxII-TO digital power/energy meter (Coherent Italia S.r.l., Monza, Italy) equipped with a PM10 thermopile. The WO₃ sputtered surface of membranes was exposed to UV light. After irradiation, the solution passed through a quartz flow cuvette placed inside a spectrophotometer able to read at regular intervals (5 min) the absorbance value at the maximum absorption wavelength of MB (665 nm), IC (610 nm), and DS (275 nm). Similarly, the photoactivity of 0.2 mg of monoclinic WO₃ nano-powder (which was the same amount of WO₃ sputtered onto BP membranes) was measured. As each experiment generally lasted 150 min and the recirculation time was around 15 min, the average contact time of solutions with the active photocatalysis region was estimated in 10 min.

The photodegradation of pollutants³¹ is generally described by the first-order kinetics

$$\frac{dC}{dt} = -kC \quad (3)$$

where C is the pollutant concentration, k is the rate constant and t is the reaction time. After integration, the following equation is obtained:

$$\ln \frac{C(t)}{C_0} = -kt \quad (4)$$

where C₀ and C(t) are the initial concentration and the concentration at time t of the pollutants. The rate constant can be obtained from the slope of the plot of $\ln \frac{C(t)}{C_0}$ as a function of t.

Experimental data were corrected by taking into account the effective photon fluence impinging on WO₃ layer (see SI).

The percentage of pollutant removal, %R, was calculated as:

$$\%R = \frac{C_0 - C(t)}{C_0} \times 100 \quad (5)$$

4.4 RESULTS AND DISCUSSION

Several factors influence the BP membrane properties including sonication time of the SWNT solution, the magnitude of the vacuum depression used to filter the SWNT solution, the porosity and material of the filtration membranes. After several trials, which gave unacceptable results, including un-detachable BP from polymer membranes (due to small pore size filtration membrane), and brittle and broken BP (due to fast solvent evaporation), Figure 1a, intact BP were obtained under the optimal conditions reported in the Materials and Methods, Figure 1b. Such BPs are easily detachable from the filtration membranes, Figure 1c, and look like free-standing and flexible disks (average thickness $45 \pm 2\mu\text{m}$) as shown in Figure 1d.

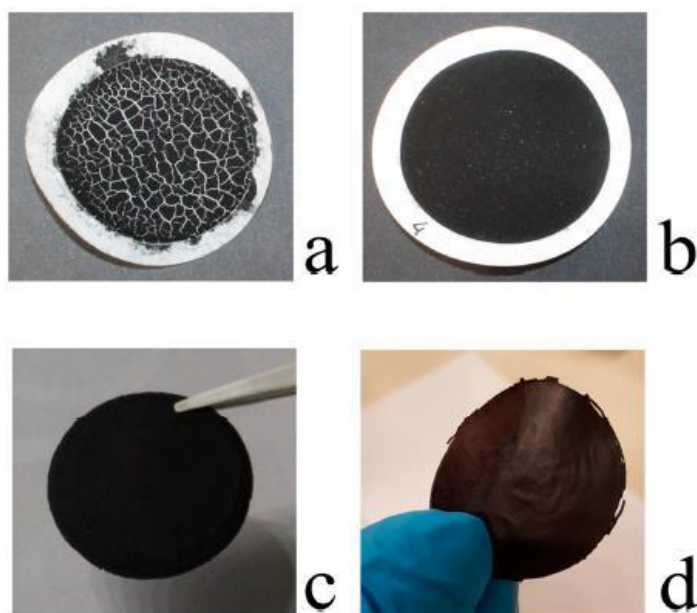


Figure 1. Appearance of buckypaper (BP) membranes under different experimental preparation procedures: (a) Brittle and un-detachable BP membrane filtered through a poly (vinylidene fluoride) (PVDF) membrane with reduced pore size; (b) whole and detachable; (c) free-standing and (d) flexible BP membrane obtained under the optimal conditions reported in the Experimental section.

At a microscopic level, BP membranes showed a highly disordered porous morphology due to π - π and van der Waals interactions between and within bundles and clusters of carbon nanotubes, Figure 2a,b.

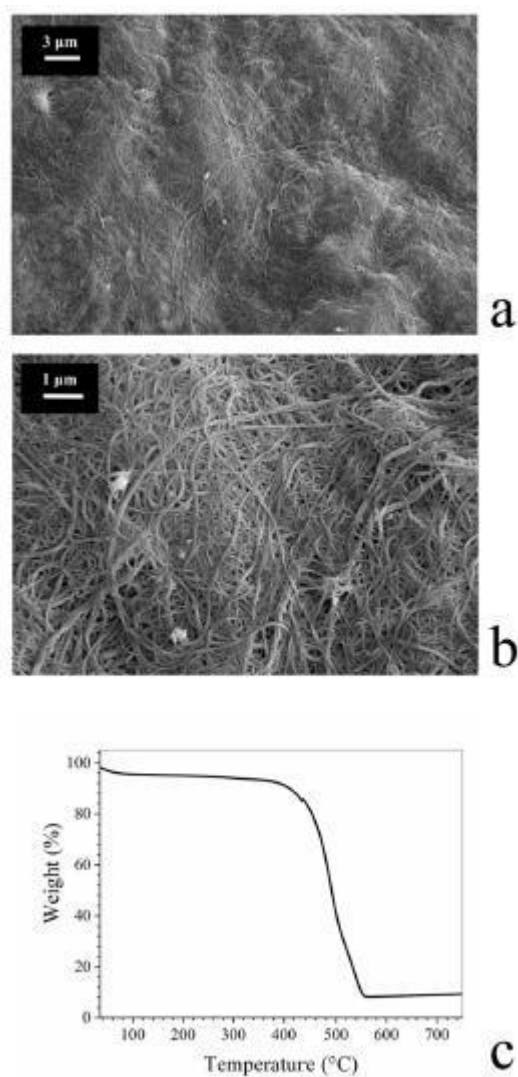


Figure 2. (a,b) Morphology of BP membranes at two different magnification; (c) Thermal stability of BP membranes. The initial weight loss is due to solvent evaporation, while the second one, which starts at around 400 °C, is due to the thermal degradation of single wall carbon nanotubes (SWNTs).

The thermal stability of BP membranes was assessed by TGA. As reported in Figure 2c, after an initial weight loss of about 5% due to water evaporation, BP membranes were found to be stable up to 400 °C. For larger temperatures, the degradation of SWNTs is observed. Table 1 reports some geometrical data and properties for BP membranes. In particular, density, porosity, and water flow rate values of BPs ($0.60 \pm 0.03 \text{ g} \cdot \text{cm}^{-3}$, $70 \pm 5\%$, and $12,500 \pm 100 \text{ L} \cdot \text{m}^{-2} \cdot \text{h}^{-1} \cdot \text{bar}^{-1}$ respectively) fall in the range of values shown by porous polymer membranes, generally used for filtration processes³². In addition, the electrical conductivity and the mechanical properties, namely tensile strength, fracture strain and Young's modulus, reported in Table 1, allow to consider BPs as strong and conductive membranes³³.

Table 1. Physical-chemical properties of BPs.

Property	Value
Thickness	$45 \pm 2 \mu\text{m}$
Diameter	$37.0 \pm 0.1 \text{ mm}$
Density	$0.60 \pm 0.03 \text{ g}\cdot\text{cm}^{-3}$
Porosity	$70 \pm 5\%$
Electrical Conductivity	$83 \pm 4 \text{ S cm}^{-1}$
Tensile strength	$11.8 \pm 2.2 \text{ MPa}$
Fracture Strain	$2.6 \pm 0.1\%$
Young's Modulus	$0.9 \pm 0.1 \text{ GPa}$
Water Flow Rate	$12,500 \pm 100 \text{ L m}^{-2}\cdot\text{h}^{-1}\cdot\text{bar}^{-1}$

In order to give photocatalytic properties to BP membranes, they were covered with thin layers of WO_3 by RF magnetron chemical vapor deposition. CVD is a well-known chemical process for the deposition of desired thin films onto substrate surfaces by chemical reactions among one or more volatile precursors. Nevertheless, the film quality is strongly dependent on the CVD process parameters. Consequently, in this work different sputtering conditions (oxygen flow, sample-target distance, sputtering time, and power) were tested in order to find the optimal set of parameters able to give a homogeneous BP coverage without cracks and small WO_3 nanoparticles to avoid BP membrane occlusion and increase photoactivity.

The best results, in terms of both coverage quality and nanoparticle size, were obtained with the following conditions: $\text{Flow}(\text{O}_2) = 35 \text{ mL}\cdot\text{min}^{-1}$, $d = 8 \text{ cm}$, $t = 30 \text{ min}$, $\text{power} = 50 \text{ W}$. The WO_3/BP membranes looked like flexible, greenish/yellowish disks as shown in Figure 3a.

Figure 3b shows the morphology of the top surface of a WO_3/BP membrane sputtered under the experimental conditions previously reported. A homogeneous layer of small nanoparticles, with a rather spherical shape and an average diameter of around 50 nm, constitutes the WO_3 coating without cracks and pore occlusion. It is important to remind the presence of BP membrane under the WO_3 layer. Figure 3c shows the picture of a particular faulty WO_3/BP membrane with a small crack, where it is possible to see inside the crack the texture of SWNT bundles, which form the BP substrate.

Figure 4a,b report the pore size distribution of both a pristine BP and a WO_3/BP photocatalytic membrane and the SEM cross section picture of a WO_3/BP membrane, respectively. As shown in Figure 4a both membranes show similar pore size distribution (within experimental errors) with two size populations placed at around $0.160 \mu\text{m}$ ($0.163 \pm 0.016 \mu\text{m}$ and $0.155 \pm 0.018 \mu\text{m}$, respectively) and at around $0.035 \mu\text{m}$ ($0.037 \pm 0.003 \mu\text{m}$ and $0.035 \pm 0.003 \mu\text{m}$, respectively) accounting for the presence of a major macroporous structure and a

mesoporous structure (inter-tube pores with a size between 2 and 50 nm) formed between SWNT criss-crossings in the sample³⁴.

It is evident from the cross section of WO₃/BP membrane, that the WO₃ layer is a few tens of nanometers thick, but WO₃ nanoparticles penetrate the BP membrane for $\approx 2 \mu\text{m}$, accounting, most likely, for the reduction in the mesopore average size. However, all the membranes prepared are characterized by a porosity of $70 \pm 5\%$, which is expected to favour the water permeability through them.

The homogeneous covering of BP membranes WO₃ was further assessed by EDX spectroscopy. Figure 5 shows the EDX color mapping images of the border area between a WO₃/BP membrane (lower area) and a BP membrane (i.e., the part of sputtered BP membrane, which was covered by a locking mask, upper area). BP membrane area looks like a red homogeneous region due to the presence of carbon and chemical impurities from SWNT, on the contrary WO₃/BP membrane area looks like a red background covered by yellow and green spots, deriving by the covering of SWNT with WO₃ nanoparticles.

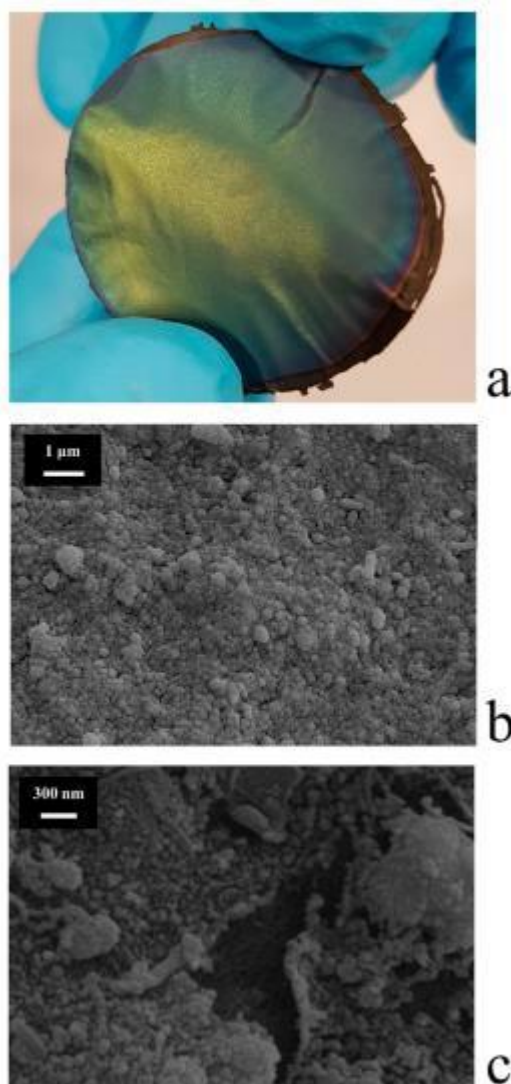


Figure 3. (a) Flexible, greenish/yellowish WO₃/BP membranes; (b) Morphology of the top surface of a WO₃/BP. The WO₃ coating is a homogeneous layer of small nanoparticles, without cracks and pore occlusion; (c) Crack of a faulty WO₃/BP membrane, inside which it is possible to see the texture of BP substrate.

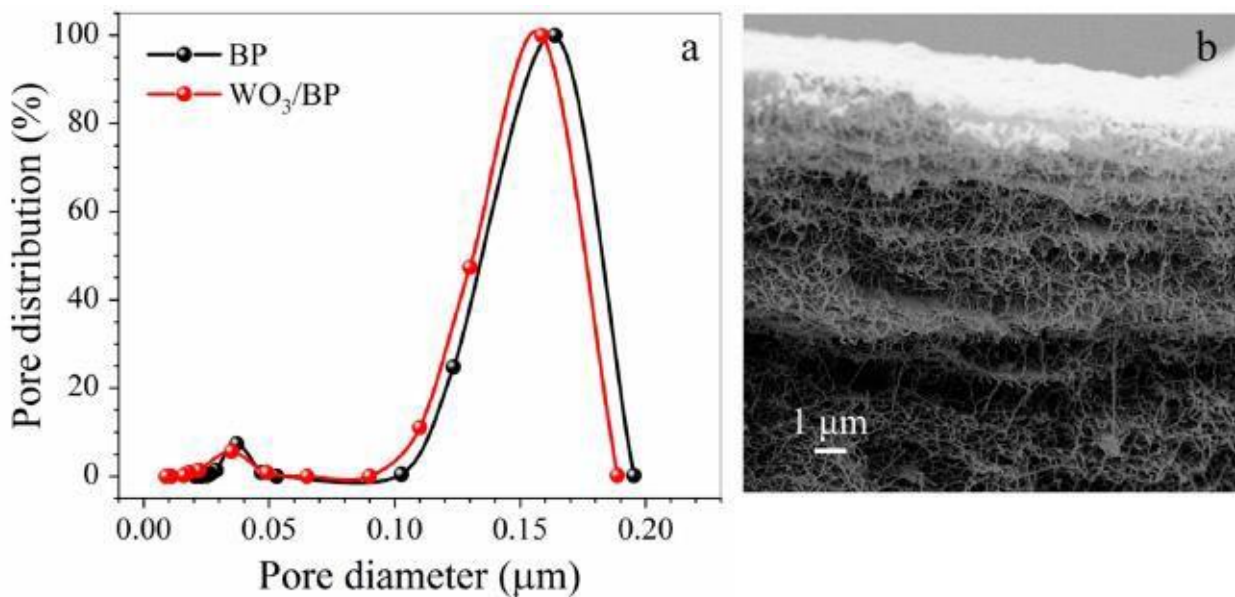


Figure 4. (a) Pore size distribution of both a BP membrane (black dots) and a WO₃/BP photocatalytic membrane (red dots); (b) SEM cross section picture of a WO₃/BP membrane.

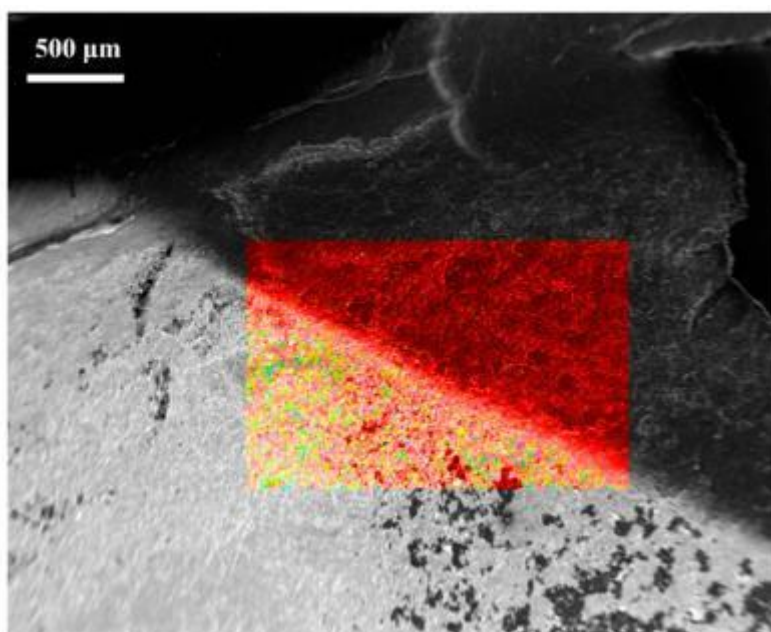


Figure 5. EDX color mapping image and EDX spectra of the border area between a WO₃/BP membrane (lower area) and a BP membrane (upper area).

The WO₃ layer showed an average rms roughness of 0.268 μm as determined by AFM measurements, Figure 6a. Such roughness gives a hydrophilic character to the top surface of WO₃/BP membranes, as confirmed by contact-angle measurements. In fact, the average contact-angle value of WO₃/BP membranes was found to be equal to 57.0° ± 0.5°, which is significantly smaller than the average contact-angle value (119.0° ± 0.5°) shown by a BP, Figure 6b,c. The contact angle values of the WO₃/BP membranes did not change after 3 h continuous irradiation by solar simulator, confirming the stability of WO₃ layer under UV-Vis light. The hydrophilicity of

WO₃/BP membranes could result in a possible increase of membrane fouling, i.e., the deposition of organic cakes onto the surfaces, but such possible drawback is overcome by fouling mitigation deriving from the photoactivity of WO₃ layers. Moreover, the increase in hydrophilicity is expected to have a positive effect in the membrane permeation properties and makes such membranes suitable for the filtration of aqueous solutions.

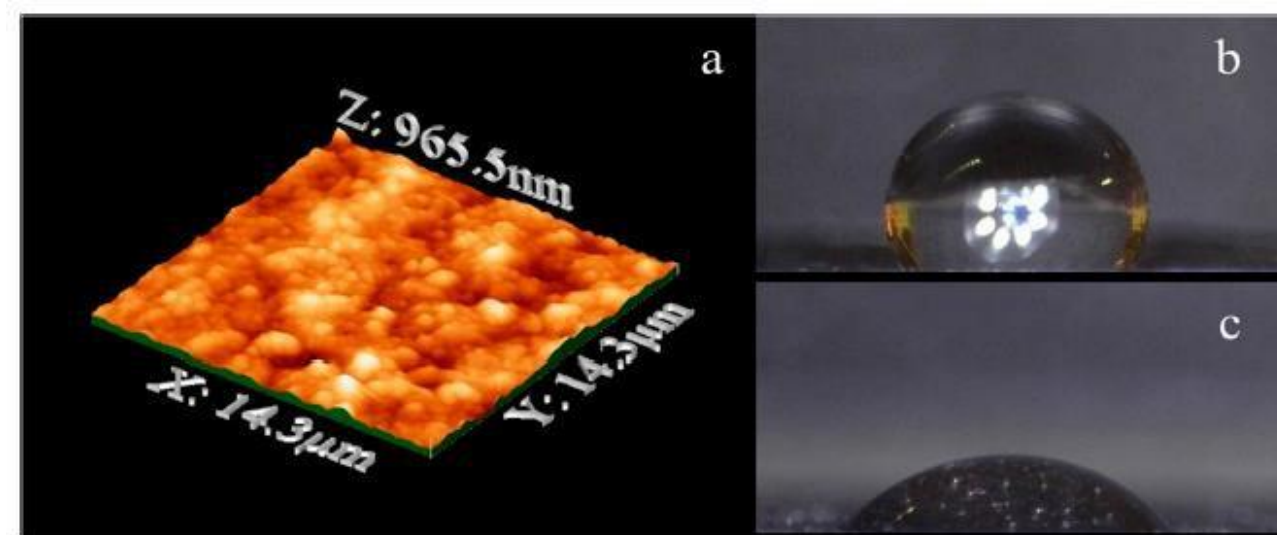


Figure 6. (a) AFM topology image of a WO₃/BP membrane. The average rms roughness is 0.268 μm; (b) Average contact-angle value of a BP membrane; (c) Average contact-angle value of a WO₃/BP membrane.

It is well known that CVD deposition of tungsten trioxide onto substrates gives amorphous WO₃, which is about ten times less photoactive than monoclinic WO₃³⁵. Consequently, WO₃/BP membranes were thermal treated at 350 °C in order to convert the amorphous WO₃ layer into the more photoactive monoclinic one. Obviously, such treatment was possible thanks to the enhanced thermal properties of BP compared to polymer membranes. Figure 7a shows the thermal evolution of micro-Raman spectrum of WO₃/BP membranes. The Raman spectrum of as-deposited WO₃ layer shows three main vibrational bands in the range of 200–1000 cm⁻¹ observed at 265, 781, and 969 cm⁻¹. The first peak increases in height as a function of the temperature, while the second splits into two intense peaks at around 700 and 800 cm⁻¹. These peaks are the typical Raman peaks of monoclinic crystalline WO₃, which correspond to the stretching vibrations of the bridging oxygen^{36,37}, and are assigned to WO stretching (ν), WO bending (δ) and OWO deformation (γ) modes, respectively^{38,39}.

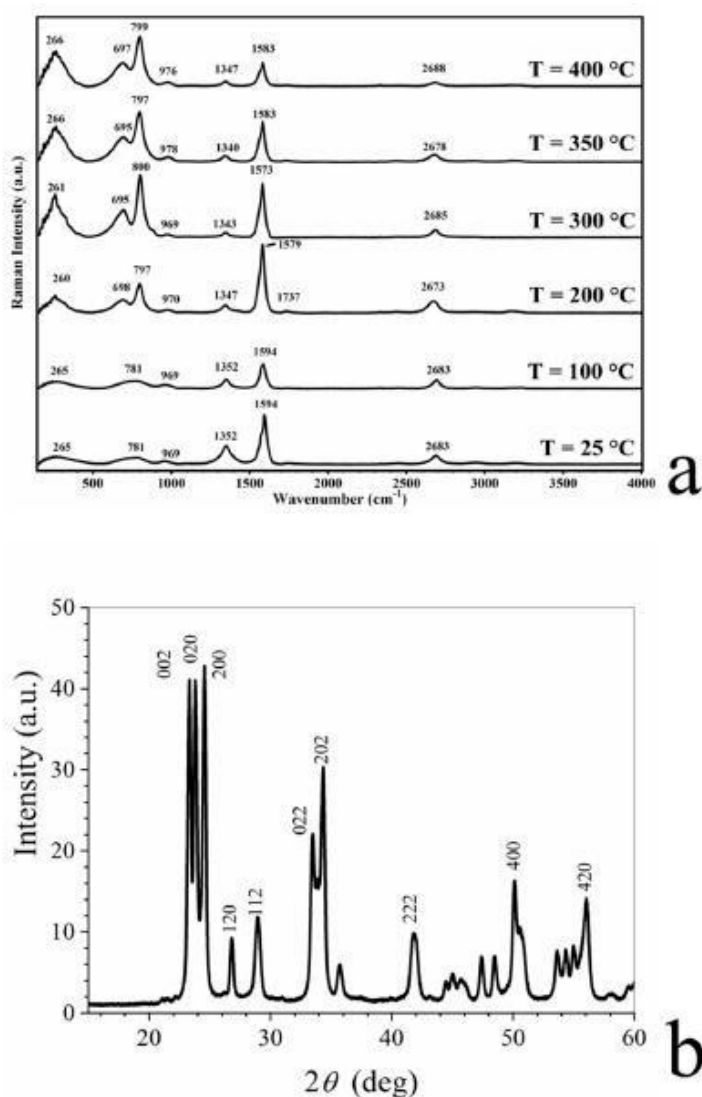


Figure 7. (a) Thermal evolution of Raman spectrum of WO₃ deposited onto BP membranes. The peaks at around 700 and 800 cm⁻¹ are assigned to WO stretching (ν), WO bending (δ), and OWO deformation (γ) modes, respectively, confirming the monoclinic structure of WO₃; (b) X-ray diffraction patterns of WO₃ layer sputtered onto BP membranes. Peaks are related to the reflection planes of the monoclinic phase of WO₃.

The transmembrane flux WO₃/BP membranes was evaluated in a small continuous plant and found to be $9.4 \times 10^3 \text{ L m}^{-2} \cdot \text{h}^{-1} \cdot \text{bar}^{-1}$, a value which is slightly lower (-25%) than pristine BP membrane as a consequence of the deposition of WO₃ layer.

The photoactivity of WO₃/BP membranes was tested with model pollutant water solutions (250 mL) of a cationic dye (Methylene Blue, MB, 5, 10, and 20 ppm), an anionic dye (Indigo Carmine, IC, 20 ppm) and a drug (Diclofenac Sodium, DS, 20 ppm), which were recirculated by a peristaltic system through a round cell. The effect of initial concentrations of Methylene Blue (5, 10, and 20 ppm) on the reaction rate is shown in Figure 8. It is evident that the kinetic constant values decrease with increasing initial concentration (k values

were 0.122 ± 0.003 , 0.113 ± 0.003 , and $0.085 \pm 0.002 \text{ min}^{-1}$, respectively). The higher values for the kinetic constant obtained at lower MB concentrations are explained as a consequence of^{31,40}:

- The increase of the number of photons available per BM molecule;
- the higher amount of available catalytically active sites per BM molecule; and
- an easier penetration of photons through the less concentrated solutions.

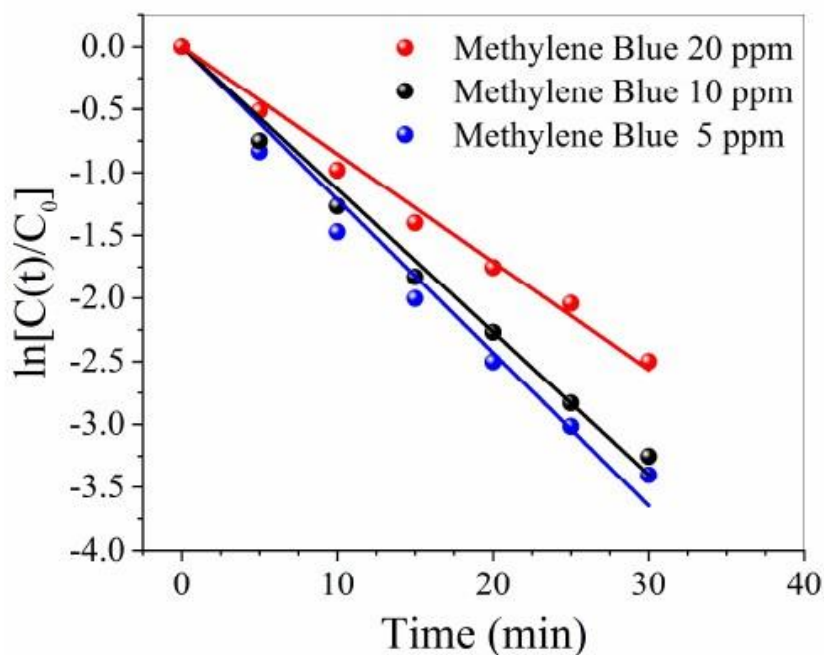


Figure 8. Effect of initial concentrations of Methylene Blue (5, 10, 20 ppm) on the reaction rate.

Nevertheless, the reported rate constants were corrected for the different photon fluence and their values do not differ so much from the uncorrected ones (0.118 ± 0.003 , 0.110 ± 0.002 and $0.082 \pm 0.002 \text{ min}^{-1}$, respectively, see SI). Accordingly, the different photon absorption from Methylene Blue solutions at different concentrations is not the major cause for the observed differences in the rate constants for Methylene Blue degradation. Most probably, such differences could arise from the competition of MB molecules towards active surface sites and reactive oxygen species⁴¹.

In all cases the percentage of MB removal within 35 min was larger than 90%. The residual concentration of MB was respectively 0.3, 0.7, and 1.5 ppm, values in agreement with other data present in literature⁴⁰. Removal experiments with no irradiation found very low pollutant adsorption by WO_3/BP membranes. After a 3 h run a WO_3/BP membrane was able to adsorb about 0.003 mg of MB, which was not a significant quantity compared to the weight amount of MB present in the used solutions.

Figure 9 reports the photocatalytical properties of WO_3/BP membranes against water solutions of a cationic dye (Methylene Blue 20 ppm), an anionic dye (Indigo Carmine 20 ppm) and a drug (Diclofenac Sodium 20 ppm), generally used as model pollutants. In all cases WO_3/BP membranes are able to efficiently degrade the water contaminants with a kinetic constant value of 0.085 ± 0.002 , 0.064 ± 0.001 , and $0.019 \pm 0.001 \text{ min}^{-1}$, respectively. Such values are of the same order of magnitude or lower than the kinetic constants against the

same pollutants, found with WO_3 , TiO_2 , or other catalyst nanoparticles dispersed either in the solutions or casted on carbon nanotubes, flakes of graphene oxide or porous polymer membranes⁴²⁻⁵⁰, as no BP bearing photocatalysts, to the knowledge of authors, was ever proposed in literature.

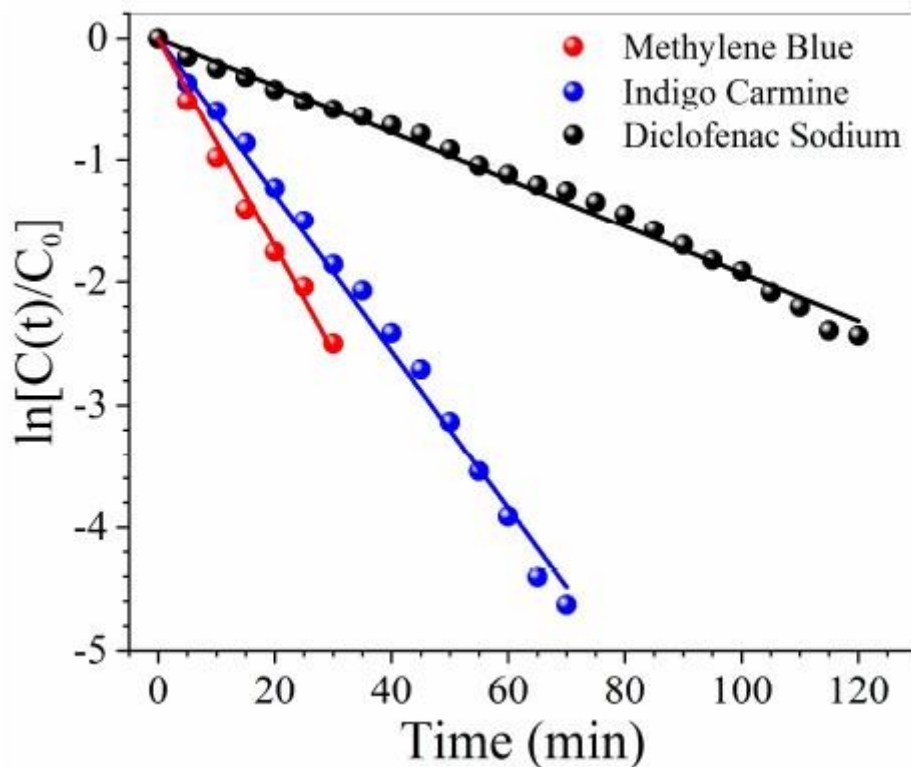


Figure 9. Photoactivity of WO_3/BP membranes against water solutions of a cationic dye (Methylene Blue 20 ppm), an anionic dye (Indigo Carmine 20 ppm) and a drug (Diclofenac Sodium 20 ppm).

Dark changes in absorbance were less than 1%, while UV controls for all three pollutant solutions found that after three hours of irradiation the absorbance changes due to the photolysis through a BP membrane were less than 2%. Such results can be explained by the particular spectrum of solar simulators (see Figure S1), which have only UV-A and UV-B emissions, and by the particular transmittance of N-BK7 optical glass cover, which cuts UV-B emissions with wavelengths lower than 300 nm. The absence of UV-C and lower UV-B wavelengths remarkably reduces the molecular degradation of pollutants by photolysis. The performance of WO_3/BP membranes was also compared with the photoactivity of 0.2 mg of monoclinic WO_3 nano-powder (the same amount of WO_3 sputtered onto BP membranes). As shown in Figure 10, the photodegradation of Methylene Blue by both systems (WO_3/BP membrane and monoclinic WO_3 nano-powder) follows a first order kinetics with a rate constant of $0.085 \pm 0.002 \text{ min}^{-1}$ and $0.029 \pm 0.001 \text{ min}^{-1}$, respectively. The enhancement of the photoactivity in WO_3/BP membranes can be due to the presence of BP, as the SWNT substrate prevents the electron/hole pair recombination during photocatalysis and increases the kinetic rate constant⁵¹. An almost complete photodegradation of Methylene Blue was obtained within ≈ 50 min and ≈ 140 min by using WO_3/BP membranes and WO_3 nano-powder, respectively. Such relatively short degradation times make the WO_3/BP

membranes suitable for applications in advanced oxidation processes. In addition, the long-term stability of WO_3/BP membranes was checked by ten cycles of successive photocatalysis processes. Figure 10 shows the morphology and the photocatalytic efficiency of a WO_3/BP membrane after the tenth photocatalytic cycle of a 20 ppm BM solution, revealing no evident damage in the morphology of WO_3/BP membranes and no important change in the degradation efficiency, being the rate constant value equal to the pristine one within experimental errors ($0.081 \pm 0.002 \text{ min}^{-1}$).

In addition, the morphology of the WO_3/BP membrane, after the tenth photocatalytic cycle, reveals the absence of any cakes on the surface and a morphology similar to that shown in the pristine WO_3/BP membrane (Figure 3b), thanks to its photoactivity and different surface chemistry preventing and destroying any deposition. Further investigations are in progress to test the antifouling activity of WO_3/BP membranes on real industrial wastes rather than on model dye and drug water solutions.

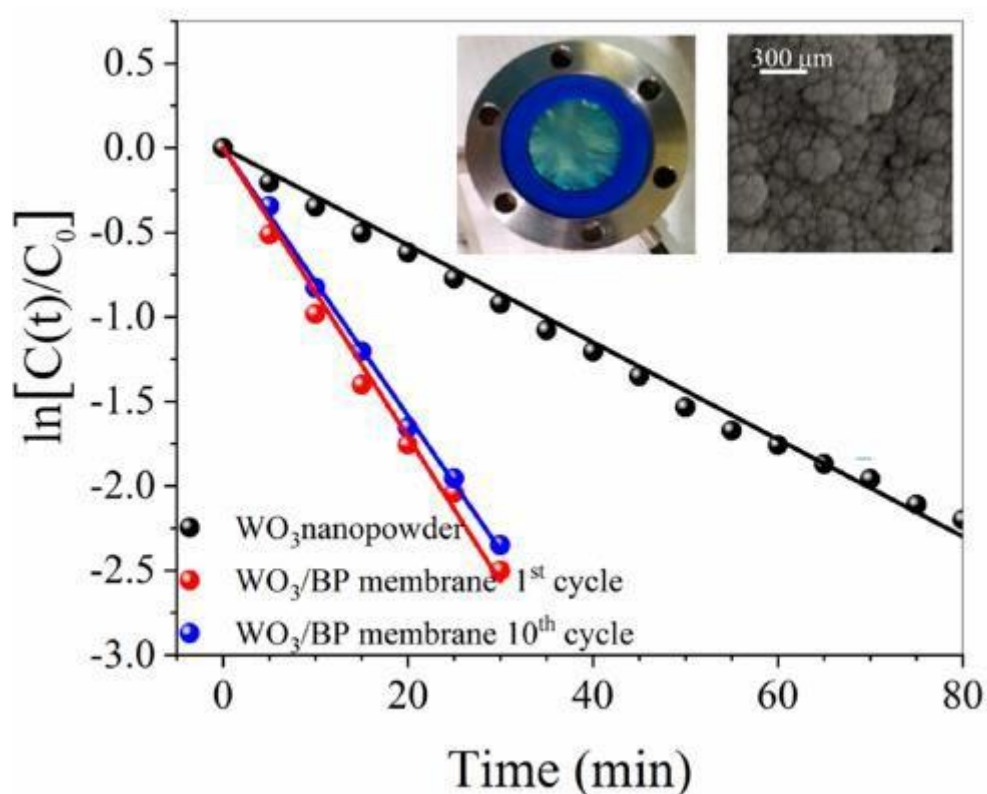


Figure 10. Photodegradation of Methylene Blue by a WO_3/BP membrane (red dots) and by monoclinic WO_3 nanopowder (black dots) in the same amount of WO_3 present on WO_3/BP membrane.

4.5 CONCLUSIONS

A new flexible membrane, based on SWNT and with improved thermal and catalytic properties, was obtained by RF magnetron sputtering of a nanostructured thin layer of tungsten trioxide and successive conversion in the more photoactive monoclinic phase. The WO_3/BP membrane was characterized by SEM, TGA, porosimetry, XRD, EDX, AFM, Raman, contact angle and permeation measurements. The photocatalytic

activity of WO₃/BP membranes was tested following the degradation of three different pollutant water solutions in a small continuous plant confirming the beneficial contribution of the hydrophilic WO₃ layer. The degradation kinetics rate of the Methylene Blue by WO₃/BP membranes was about three times that found by an equivalent amount of WO₃ nano-powder. The main advantages of the proposed WO₃/BP membranes can be summarized in:

1. The possibility to make heterogeneous photocatalytical processes with an easier catalyst recovery and reuse;
2. their application in continuous flow plants;
3. a simpler and cleaner synthetic approach. Chemical vapor deposition processes do not require long and expensive purification procedures, which are necessary in other chemical syntheses, such as solvo-thermal processes. In addition, CVD allows the catalyst amount saving, avoiding its dispersion in the substrate bulk;
4. a higher photocatalytical efficiency, due to the facilitated electron-transfer between carbon nanostructures and catalyst nanoparticles, a reduced recombination between electrons and holes⁵¹, and the presence of catalyst nanoparticles with small size just only on the top surface of substrates rather than in the polymer bulk (where they cannot play any catalytic action);
5. the possibility to change the photocatalyst crystal structure in a more photoactive one by thermal annealing processes at temperatures higher than the melting point of commonly used polymer substrate. PTFE, polytetrafluoroethylene, which has one of the highest melting points, melts at 327°C, a temperature lower than the WO₃ amorphous-monoclinic phase transition temperature.

On the contrary, BP membranes result thermally stable up to 400°C;

6. BPs have both light weight and strong mechanical resistance, and, consequently, are easy to handle. In addition, BPs are resistant to all organic solvents and acid and base solutions, while porous polymer membranes can be damaged; and
7. a green chemistry approach with an almost zero environmental footprint, as the BP preparation is based on rather simple and clean experimental set-ups, which allow the recovery and reuse of solvents, CNT processing waste, end of life BPs and photocatalysts for the preparation of new catalyst/BP membranes.

The improved photoactivity, long-term stability, solvent-free features, fast catalyst recovery and re-use, and the possibility of an easy up-scale make WO₃/BP membranes efficient devices for the pollutant degradation by advanced oxidation processes.

Supplementary Materials: The following are available online at <http://www.mdpi.com/2077-0375/10/7/157/s1>, Figure S1: Spectrum of Suntest CPS+ sun simulator for three different irradiance values. Reprinted from [S1], with permission from Royal Society of Chemistry, Figure S2: Normalized fluence across solutions of Methylene Blue, Indigo Carmine, and Diclofenac Sodium, Table S1: Fluence uncorrected and fluence corrected rate constants.

REFERENCES

- [1] D.F. Ollis, E. Pelizzetti, N. Serpone, in *Photo-Catalysis Fundamentals and Applications*, Wiley: Hoboken, NJ, USA, **1989**.
- [2] J. Araña, J.A. Herrera Melián, J.M. Doña Rodríguez, O. González Díaz, A. Viera, J. Pérez Peña, P.M. Marrero Sosa, P.M.; Jiménez, V.E. *Catal. Today* **2002**, *76*, 279.
- [3] M.L. Di Gioia, A. Leggio, A. Le Pera, A. Liguori, C. Siciliano, *J. Org. Chem.* **2005**, *70*, 10494.
- [4] M. Cho, H. Chung, W. Choi, J. Yoon, *Water Res.* **2004**, *38*, 1069–1077.
- [5] G. De Filpo, A.M. Palermo, R. Tolmino, P. Formoso, F.P. Nicoletta, *Cellulose* **2016**, *23*, 3265.
- [6] Z. Huang, P.C. Maness, D. Blake, E.J. Wolfrum, S.L. Smolinski, W.A. Jacoby, *J. Photochem. Photobiol. A* **2000**, *130*, 163.
- [7] G. De Filpo, A.M. Palermo, R. Munno, L. Molinaro, P. Formoso, F.P. Nicoletta, *Int. Biodeterior. Biodegrad.* **2015**, *103*, 51.
- [8] G. De Filpo, A.M. Palermo, ; F. Rachiele, F.P. Nicoletta, *Int Biodeter Biodegr* **2013**, *85*, 217.
- [9] M.R. Ho_mann, S.T. Martin, W.Y. Choi, D.W. Bahnemann, *Chem. Rev.* **1995**, *95*, 69.
- [10] D.S. Bhatkhande, V.G. Pangarkar, A. Beenackers, *J. Chem. Technol. Biot.* **2002**, *77*, 102.
- [11] G. De Filpo, E. Pantuso, K. Armentano, P. Formoso, G. Di Profio, T. Poerio, E. Fontananova, C. Meringolo, A.I. Mashin, A.I., F.P. Nicoletta, *Membranes* **2018**, *8*, 35.
- [12] D. Bhattacharyya, *Clean Technol. Envir.* **2007**, *9*, 81.
- [13] E. Drioli, A. Ali, F. Macedonio, *Desalination* **2015**, *356*, 56.
- [14] O.A.H. Jones, N. Voulvoulis, J.N. Lester, *Environ. Technol.* **2001**, *22*, 1383.
- [15] A. Ziyilan, N.H. Ince, *J. Hazard. Mater.* **2011**, *187*, 24.
- [16] P. Formoso, E. Pantuso, G. De Filpo, F.P. Nicoletta, *Membranes* **2017**, *7*, 39.
- [17] F.P. Nicoletta, D. Cupelli, P. Formoso, G. De Filpo, V. Colella, A. Gugliuzza,, *Membranes* **2012**, *2*, 134.
- [18] S.M. Salehi, G. Di Profio, E. Fontananova, F.P. Nicoletta, E. Curcio, G. De Filpo, *J. Membr. Sci.* **2016**, *504*, 220.
- [19] J. Salminen, J. E. Garbarino, G. Orveillon, G. H. Saveyn, V. Mateos Aquilino, T. Llorens González, F. García Polonio, L. Horekmans, P. D'Hugues, E. Balomenos, G. Dino, M. de la Feld, F. Madai, J. Foldessy, G. Mucsi, I. Gombkoto, I. Calleja, Recovery of Critical and Other Raw Materials from Mining Waste and Landfills: State of Play on Existing Practices; (Eds. G.A. Blengini, F. Mathieux, L. Mancini, M. Nyberg, H.M. Viegas) Publications Office of the European Union: Luxembourg, **2019**.
- [20] H.K. Shon, S. Vigneswaran, S. H.H. Ngo, J.H. Kim, *Water Res.* **2005**, *39*, 2549.
- [21] S. Mozia, A.W. Morawski, *Catal. Today* **2006**, *118*, 181.
- [22] D.P. Ho, S. Vigneswaran, H.H. Ngo, *Sep. Sci. Technol.* **2010**, *45*, 155.

- [23] F. Mendez-Arriaga, S. Esplugas, J. Gimenez, *Water Res.* **2008**, *42*, 585.
- [24] Y.A. Kim, H. Muramatsu, T. Hayashi, M. Endo, M. Terrones, M.S. Dresselhaus, *Chem. Vapor. Depos.* **2006**, *12*, 327.
- [25] M. Endo, H. Muramatsu, T. Hayashi, Y.A. Kim, M. Terrones, M.S. Dresselhaus, *Nature* **2005**, *433*, 476.
- [26] M.H.O. Rashid, S.F. Ralph, *Nanomaterials* **2017**, *7*, 99.
- [27] C.J. Frizzell, D.H. Coutinho, K.J. Balkus, A.I. Minett, W.J. Blau, J.N. Coleman, *Phys. Rev. B* **2005**, *72*, 245420.
- [28] U. Vohrer, I. Kolaric, M.H. Haque, S. Roth, U. Detla-Weglikowska, *Carbon* **2004**, *42*, 1159.
- [29] J.N. Coleman, W.J. Blau, A.B. Dalton, E. Muñoz, S. Collins, B.G. Kim, J. Razal, M. Selvidge, G. Vieiro, R.H. Baughman, *Appl. Phys. Lett.* **2003**, *82*, 1682.
- [30] J. Boge, L.J. Sweetman, S.F. Ralph, *J. Mater. Chem. A* **2009**, *19*, 9131.
- [31] N. Zhang, J.M. Li, G.G. Liu, X.L. Chen, K. Jiang, *Water. Sci. Technol.* **2017**, *75*, 2163.
- [32] F. Russo, C. Ursino, E. Avruscio, G. Desiderio, A. Perrone, S. Santoro, F. Galiano, A. Figoli, A., *Membranes* **2020**, *10*, 36.
- [33] B. Ashrafi, B. J. Guan, V. Mirjalili, P. Hubert, B. Simard, A. Johnston, *Compos. Part A-Appl S* **2010**, *41*, 1184.
- [34] R.L.D. Whitby, T. Fukuda, T. Maekawa, S.L. James, S.V. Mikhailovsk, *Carbon* **2008**, *46*, 946.
- [35] A.B.D. Nandiyanto, R. Oktiani, R. Ragadhita, A. Sukmafritri, R. Zaen, *Arab. J. Chem.* **2020**, *13*, 2912.
- [36] G.A. de Wijs, R.A. de Groot, *Electrochim Acta* **2001**, *46*, 1989.
- [37] P. Tagtstrom, U. Jansson, *Thin Solid Film* **1999**, *352*, 107.
- [38] M.F. Daniel, B. Desbat, J.C. Lassegues, B. Gerand, B. M. Figlarz, *J. Solid. State Chem.* **1987**, *67*, 235.
- [39] J. Díaz-Reyes, R. Castillo-Ojeda, M. Galván-Arellano, O. Zaca-Moran, *Adv. Cond. Matter Phys.* **2013**, *2013*.
- [40] M. Srinivasan, T. White, *Environ. Sci. Technol.* **2007**, *41*, 4405.
- [41] W.Y. Wang, Y. Ku, *Water Res.* **2006**, *40*, 2249.
- [42] T.F. Mastropietro, C. Meringolo, T. Poerio, F. Scarpelli, N. Godbert, N., G. Di Profio, E. Fontananova, *Ind. Eng. Chem. Res.* **2017**, *56*, 11049.
- [43] C. Gómez-Solís, I. Juárez-Ramírez, E. Moctezuma, L.M. Torres-Martínez, *J. Hazard. Mater.* **2012**, *194*, 217.
- [44] K. Devarahosahalli Veeranna, M. Theeta Lakshamaiah, R. Thimmasandra Naraya, *Int. J. Photochem.* **2014**, *2014*.
- [45] M.J. Sampaio, C.G. Silva, R.R.N. Marques, A.M.T. Silva, J.L. Faria, *Catal. Today* **2011**, *161*, 91.
- [46] J. Singh, Y.Y. Chang, J.R. Koduru, J.K. Yang, *Environ. Eng. Res.* **2018**, *23*, 1.

- [47] M.J. Sampaio, R.R.N. Marques, P.B. Tavares, J.L. Faria, A.M.T. Silva, C.G., *J. Environ. Chem. Eng.* **2013**, *1*, 945.
- [48] X. Zhou, T. Shia, H. Zhou, *Appl. Surf. Sci.* **2012**, *258*, 6204.
- [49] L. Tian, L. Ye, K. Deng, L. Zan, *J. Solid State Chem.* **2011**, *184*, 1465.
- [50] M. Bojarska, B. Nowak, J. Skowron' ski, W. Pia, tkiewicz, L. Gradon, *Appl. Surf. Sci.* **2017**, *391*, 457.
- [51] G. Jeevitha, R. Abhinayaa, D. Mangalaraj, N. Ponpandian, *J. Phys. Chem. Solids* **2018**, *116*, 137.

CHAPTER 5

5. ELETTROCOAGULATION AND ELECTRORESPONSIVE MEMBRANES

5.1 SUMMARY

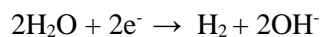
Electrocoagulation (EC) is an electrochemical process used for wastewater treatment with the aim of removing various types of pollutants. Since the beginning of the 21st century it has become one of the most studied methods in the environmental field, thanks to its energy efficiency, environmental compatibility, versatility, safety use and its low costs.¹ Electrocoagulation in large-scale industrial processes represents a preliminary or intermediate step for the treatment of wastewater, which is generally followed by separation and filtration processes². One of the most used and innovative separation and filtration techniques is the membrane separation process, in which a porous membrane is used to separate the components present in a feed solution rejecting unwanted substances, but allowing the others to pass through the membrane. In this work an integrated system is proposed in which the EC and filtration processes can proceed simultaneously within the same system, using as electrodes for the EC process polymer porous membranes made conductive by sputtering a thin layer of aluminum. The integration of the two processes can lead to greater efficiency of the electrocoagulation system in industrial purification processes due to a greater removal of pollutant and a reduction of membrane fouling.

5.2 INTRODUCTION

Electrocoagulation is an electrochemical process based on the dissolution of a metal from a sacrificial anode to obtain an active metal hydroxide as a strong coagulant that destabilizes and aggregates the particles and then removes them by precipitation or adsorption. The theoretical principles of this process are similar to those of traditional coagulation but presents greater advantages in terms of efficiency, less use of additional reagents and, consequently, advantages in economic terms.³ This technique finds its main application in wastewater treatment, but it has potential applications in the delivery of drugs, proteins and polymers.⁴

During electrocoagulation performed using aluminum electrodes, the reaction occurring are:

- The generation of aluminum ions on the anode: $\text{Al} \rightarrow \text{Al}^{3+} + 3\text{e}^-$
- The reduction of water to gaseous hydrogen and hydroxide anion on the cathode:⁵



The hydrolyzed aluminum forms several monomeric species such as $\text{Al}(\text{OH})^{2+}$, $\text{Al}(\text{OH})^{2-}$ and also large insoluble polymeric species, $\text{Al}_6(\text{OH})_{15}^{3+}$, $\text{Al}_7(\text{OH})_{17}^{4+}$, $\text{Al}(\text{OH})_{15}^{3+}$, $\text{Al}_7(\text{OH})_{17}^{4+}$ e $\text{Al}_8(\text{OH})_{20}^{4+}$. These monomeric and polymeric species turns into large and insoluble amorphous $\text{Al}(\text{OH})_3$ able to chemically adsorb the desired substances and remains in solution in the form of gelatinous suspension. Pollutants of different chemical-physical nature (suspended solids, solutions, emulsions or colloidal systems) can be involved in electrocoagulation process. In particular, colloidal particles finely dispersed in solution (of the order of dimensions between 1nm and 10 μm) present removal difficulties with traditional separation methods⁶.

Flocculated contaminants can be removed by physical methods or *in situ*, by sedimentation or electroflotation. In the latter case, H_2 , developed from the cathode in the form of bubbles, drags floccules to the surface.

The greater efficiency and the lower use of chemical additives compared to traditional clarification techniques led the research to investigate on the influence of different parameters on the efficiency of the electrocoagulation process.

In this work, a multi-factorial analysis was carried out on three of the most influential parameters on the electrocoagulation process including initial pollutant concentration, current density and pH with the aim of identifying optimal values for the removal of methylene blue dye from an aqueous solution. These values were crossed according to the experimental model of Taguchi to understand the interaction between them and how they contribute to the entire process of electrocoagulation. Other important parameters such as electrode material, distance between electrodes, volume of solution, reaction time, previously optimized, were kept constant during the tests. The concentration of H^+ ions greatly influences the electrocoagulation process, as it determines which chemical species are prevalent in solution⁷. The prevailing concentration of one species is deduced from the pH of the solution: soluble cationic species prevail at pH lower than 4, the presence of aluminates (anions) prevails when the pH is greater than 10, while the insoluble form $Al(OH)_3$ is the predominant in the pH range between 4 and 10. The aluminic cationic species counterbalance the negative charge of the hydroxyl ions generated at the cathode, with a *buffer* effect that brings the final pH to a value between 7 and 8. As a result, the prevalent formation of $Al(OH)_3$, in the form of amorphous floccules with a large surface area, optimal for rapid adsorption of soluble organic compounds and for trapping colloidal particles.³ The current density is the key operating parameter of electrocoagulation, on it depends the amount of ions released from the anode and the amount of bubbles generated by the cathode responsible, respectively, of coagulation and flotation of the substance to be removed⁸. The amount of metal released by the oxidation of the anode is defined by the law of Faraday. However, the higher applicable current density is not the ideal value for achieving the higher efficiency of the system⁸, in fact excessive electrical stimulation of the anode may result in the formation of a layer of stable oxides on its surface, promoting corrosion phenomena and generating passive effects⁷. Electrocoagulation in large-scale industrial processes represents a preliminary or intermediate step for wastewater treatment, generally followed by separation and filtration processes. The most used and innovative separation and filtration techniques is the membrane separation process, where a porous membrane is used to separate the components present in a feed solution by rejecting unwanted substances allowing others to cross the membrane itself. The second goal of this work was to propose electroresponsive membranes produced with the aim of coupling to electrocoagulation a membrane separation process, in a *one-pot* system. For this purpose, PVDF membranes were sputtered superficially with an aluminum layer and used as electrodes.

5.3 MATERIALS AND METHODS

5.3.1 MATERIALS

The methylene hydrochloride blue used was from Sigma-Aldrich and the sodium chloride and sodium hydroxide were from Carlo Erba. The conductivity and the pH of solutions were measured using a conductivity meter (WTW-Profiline Cond 3310) a pH meter (VWR-pHenomenal® pH 1100L), respectively.

The substrates used as electrodes in the various tests were:

- plates of aluminum,
- strip of aluminum,
- PVDF membrane disks sputtered with a thin layer of aluminum.

The membranes used were PVDF disks with a diameter of 47 mm, a porosity of 70%, and a mean pore size of 0.10 μm (Durapore ©, Merck KGaA, Darmstadt, Germany). The deposition of the thin layer of aluminum on PVDF membranes was obtained by sputtering of appropriate targets by process inert gas ions (argon) in a Edwards AUTO-306 sputtering system (Edwards, Burgess Hill, UK).

The electrodes were connected to the two poles of an electric current generator (Aim Tti-CPX400S).

Samples of solution analysed by spectrophotometer (Thermo Scientific™ Evolution™ 201 UV-Visible) to determine the residual methylene blue concentration.

5.3.2 ELECTROCOAGULATION PROTOCOL

5.3.2.1 TEST 1. DOE TAGUCHI

A Design Of Experiments (DOE) is a method of approach to the design and organization of experiments, by which it is possible to analyze in a systematic way the nature, the objectives, the significant elements of the experiments and the processes on which they operate, and thus finalize the experimental tests in order to obtain the maximum efficiency. In particular, through the adoption of orthogonal matrices and the Taguchi method, it was possible to investigate a large number of parameters with a minimum number of experimental tests.⁹ Taguchi's strategy is to minimise the influence of uncontrollable parameters optimising the levels of controllable factors. The optimized design is achieved not choosing the best performance in ideal conditions, but rather searching an acceptable performance condition even when the system is exposed to the influence of uncontrollable factors.¹⁰

In this work for three parameters, initial methylene blue concentration $[BM]$, current density J and pH, three values have been defined (minimum, maximum and intermediate) and DOE-Taguchi method reduced the number of the experimental tests from 27 to 9 in order to assess the influence of these parameters on the process simultaneously. Table 2 lists the tests with the respective values of J , pH and $[BM]$ required by DOE-Taguchi model.

The electrocoagulation setup consisted of a 500 ml reactor containing 300 ml of methylene blue aqueous solution. Two aluminum plates were placed in the reactor, immersed vertically in the solution for a total immersed area of 33.6 cm^2 . The plates, acting as electrodes, were connected to the two poles of an electric current generator and spaced of 5 cm each other. At the bottom of the beaker, a magnetic stirrer was placed to ensure a slow but constant stirring. Samples of solution were taken every 5 minutes and analysed by spectrophotometer to determine the residual methylene blue concentration. After each sampling 5 ml of

distilled water were introduced, to avoid the alteration of values caused by the loss of volume and to maintain the *sink* conditions. The duration of the test was 100 min.

The percentage removal of methylene blue is calculated using the following equation:

$$R = \frac{C_0 - C_t}{C_0} \times 100 \quad (1)$$

Where C_0 is the initial concentration (mg/L) and C_t is the concentration at time t (min).

The experimental parameters of preliminary tests are summarized in Table 1. While the value of analyzed parameters, [BM], J and pH are reported in the Table 2.

Table 1. Experimental parameters of DOE-Taguchi tests.

Volume	300 ml
Electrodes	Plates of Aluminium
Total immersed area of electrodes	33.6 cm ²
Distance between electrodes	5 cm
Test time	100 min
Sampling	5 ml / 5 min

Table 2. Values of current density (J), initial concentration [BM] and pH for DOE-Taguchi tests.

Test	[BM] [mg/L]	J [mA/cm ²]	σ [μ S/cm]	Current Intensity [A]	pH
#1	7.16	5	670	0.17	6.0
#2	7.16	10	1340	0.34	7.5
#3	7.16	15	2010	0.51	9.0
#4	18.00	10	1340	0.34	6.0
#5	18.00	15	2010	0.51	7.5
#6	18.00	5	670	0.17	9.0
#7	25.83	15	2010	0.51	6.0
#8	25.83	5	670	0.17	7.5
#9	25.83	10	1340	0.34	9.0

To act on the J it was necessary to vary the values of current intensity I and electrical conductivity σ , keeping the submerged surface area constant.

5.3.2.2 TEST 2. EC SYSTEM OF SMALL SIZE

In order to replace the aluminum plates used in the preliminary tests with polymeric porous membranes sputtered with a thin layer of aluminum, a smaller EC system has been developed. In fact the sputtered PVDF samples were disks of small size having a diameter of 47 mm due to the geometry of the vacuum chamber of the sputtering system. To this purpose EC system was first tested with two aluminum electrodes (7.5 cm x 1 cm) consisting of two pieces of Aluminum strip, attached to a glass support. The reduced electrocoagulation system consisted of a 50 ml beaker containing the MB solution. The electrodes were vertically immersed in the solution, placed at 1.1 cm from each other and 1 cm from the bottom of the beaker, to allow magnetic stirring, as shown in Figure 1. The electroconductive surfaces of the two electrodes were directed towards each other and the total submerged surface area was 4 cm².

The parameters used in these tests are summarized in the Table 3.

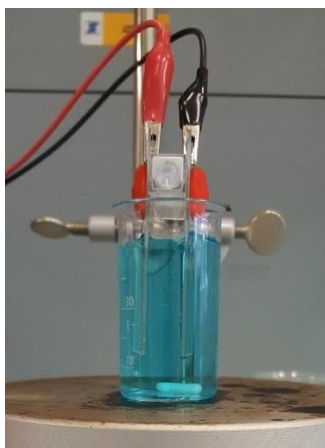


Figure 1. Small EC system.

Table 3. Parameters for small-scale EC.

Test	[MB] mg/ml	Volume	σ mS/cm	pH
S1	50	25	40.8	9
S2	50	25	$26.5 \cdot 10^{-3}$	5.6
S3	25	25	22.7	7.3

5.3.2.3 TEST 3. EC TEST WITH SPUTTERED MEMBRANES AS ELECTRODES

The electrocoagulation system consisted of a 25 ml beaker containing 25 ml MB blue solution, two electrodes consisting of sputtered PVDF membranes, each attached to an aluminum strip and to a plastic support. The distance between the two electrodes was 1 cm and both are distant 2 cm from the bottom to facilitate magnetic stirring. The total immersed area of the two electrodes was 2 cm². The electrodes are connected to a DC power supply 12V-0.5 A.

Table 4. Parameters for EC process with spattered membranes

Volume	25 mL
Electrodes	Sputtered aluminum membranes
Distance between electrodes	1 cm
Submerged area	2 cm ²
Reaction time	450 min

5.4 RESULTS AND DISCUSSION

5.4.1 TEST 1. DOE TAGUCHI

The objective of the DOE-Taguchi electrocoagulation tests was to identify the optimal values of three key parameters (initial dye concentration, current density and pH) of the solution for the removal of methylene blue from an aqueous solution. Variable parameter values and percentages of dye removal achieved at the end of each test were reported in the Table 5:

Table 5. Values of current density (J), initial concentration [BM] and pH for DOE-Taguchi tests.

Test	[BM] [mg/L]	J [mA/cm ²]	o [μS/cm]	Current Intensity [A]	pH	Dye Removal [%]
#1	7.16	5	670	0.17	6.0	16.2
#2	7.16	10	1340	0.34	7.5	21.0
#3	7.16	15	2010	0.51	9.0	10.9
#4	18.00	10	1340	0.34	6.0	12.8
#5	18.00	15	2010	0.51	7.5	25.4
#6	18.00	5	670	0.17	9.0	16.1
#7	25.83	15	2010	0.51	6.0	37.5
#8	25.83	5	670	0.17	7.5	8.0
#9	25.83	10	1340	0.34	9.0	46.9

5.4.1.1 ANALYSIS OF THE RESULTS AS FUNCTION AGAINST BM CONCENTRATION

In the graph in Figure 1a. the three tests at the lowest initial concentration of BM (tests #1, #2 and #3) are reported: test #2, with intermediate pH and J values, was not only the one with the highest percentage of removal achieved, but also the test with more regular removal as a function of time, as shown by the value of $R^2 \approx 1$ in the trend of the graph shown in Figure 2b., which shows the trend of the percentage of removal of the BM during the reaction.

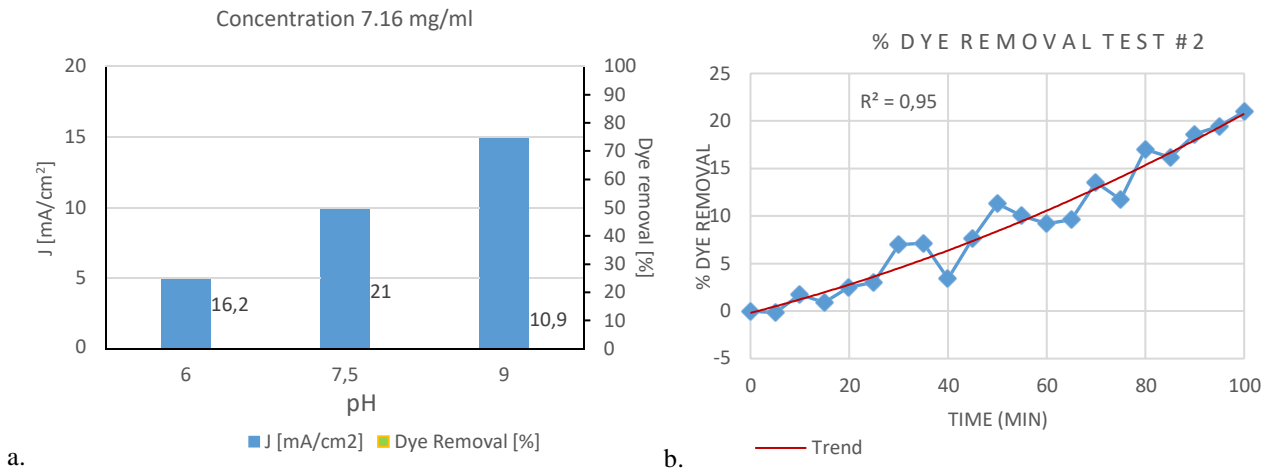


Figure 2. a. Percentage of dye removal in three tests at low concentration of BM (7.16 mg/L); b. trend of percentage of removal of BM during the test 2.

From these results, it was assumed that for limited concentrations of BM, particularly "aggressive" reaction conditions, such as those adopted in test #3, are not preferable. In fact, as shown in Figure 3, during the test #3, the solution assumed a grey-opaque coloration, symptom of the excessive liberation of Al^{3+} ions, and presented an unstable flocculate tending to disintegrate.

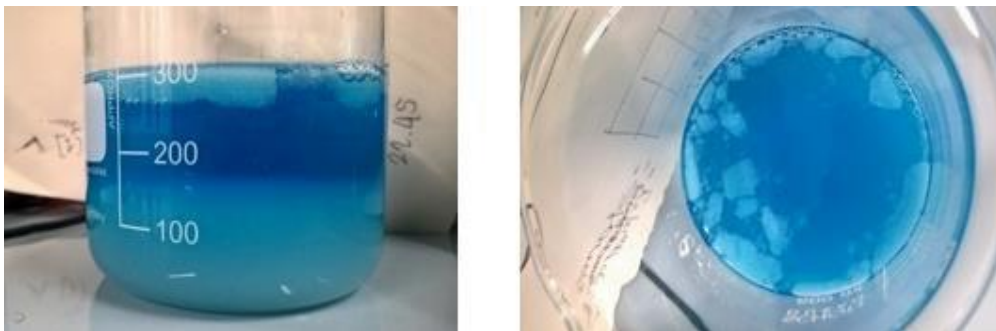


Figure 3. Flocculate disintegration and precipitate formation at the bottom in the EC solution during test #3.

Flocculated disintegration led to the release of the previously trapped dye as confirmed by the trend of the percentage of removal during the test #3 shown in Figure 3, which began to decline after having reached a maximum point.

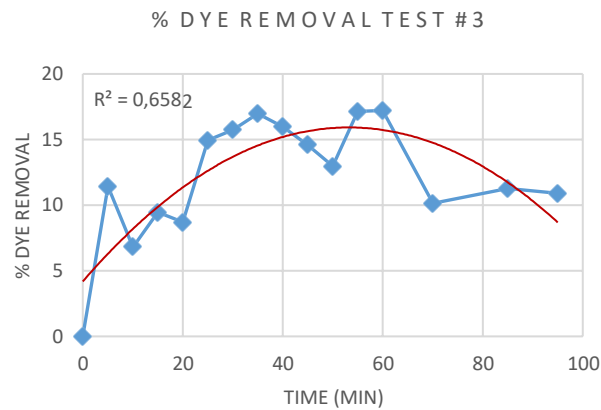


Figure 4. Trend of percentage of removal of the BM during the test 3.

The graph in Figure 5a. shows the results of the three tests (#4, #5 and #6) at intermediate initial BM concentration (18.00 mg/L). The highest percentage of dye removal at medium concentration of BM was found in #5, with intermediate pH (7.5) and maximum pH J (15 mA/cm²). Similarly, to test #3, even in test #5 the removal rate began to decrease over a certain reaction time (as reported in the graph in Figure 5b.), due to excessive current density applied. However, in this case the negative effects of high J are balanced by a neutral pH and for this reason the maximum point of the curve is reached at a higher reaction time.

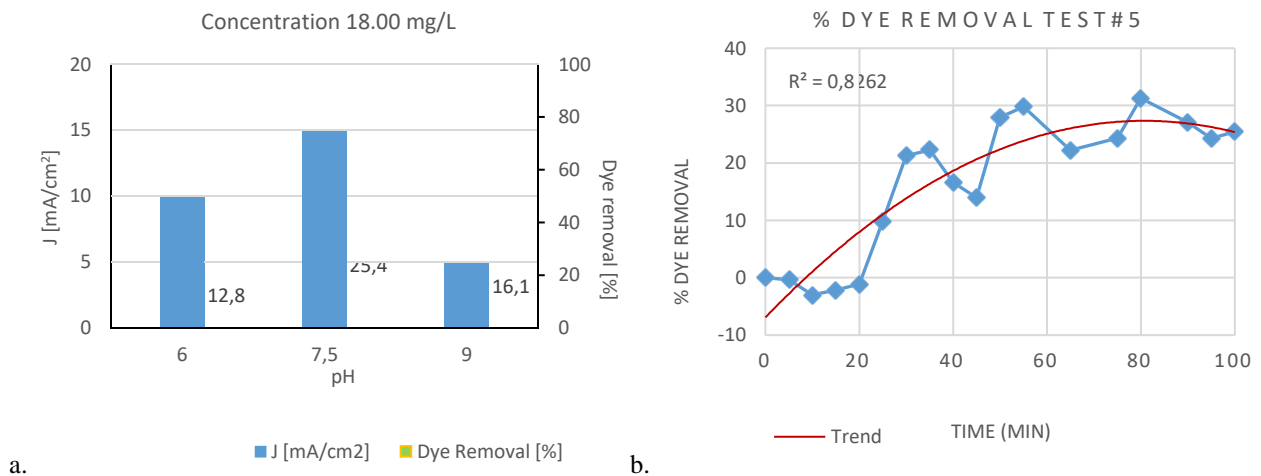


Figure 5. a. Percentage of dye removal in three tests at intermediate concentration of BM (18 mg/L); b. trend of percentage of removal of BM during the test 5.

The graph in Figure 6a. and b. shows the results of the three tests (#7, #8 and #9) at higher initial BM concentration (25.83 mg/L) and the trend of percentage of removal of BM of the test #9, respectively. The highest percentage of dye removal achieved was obtained in #9 (pH = 9; J= 10 mA/cm²).

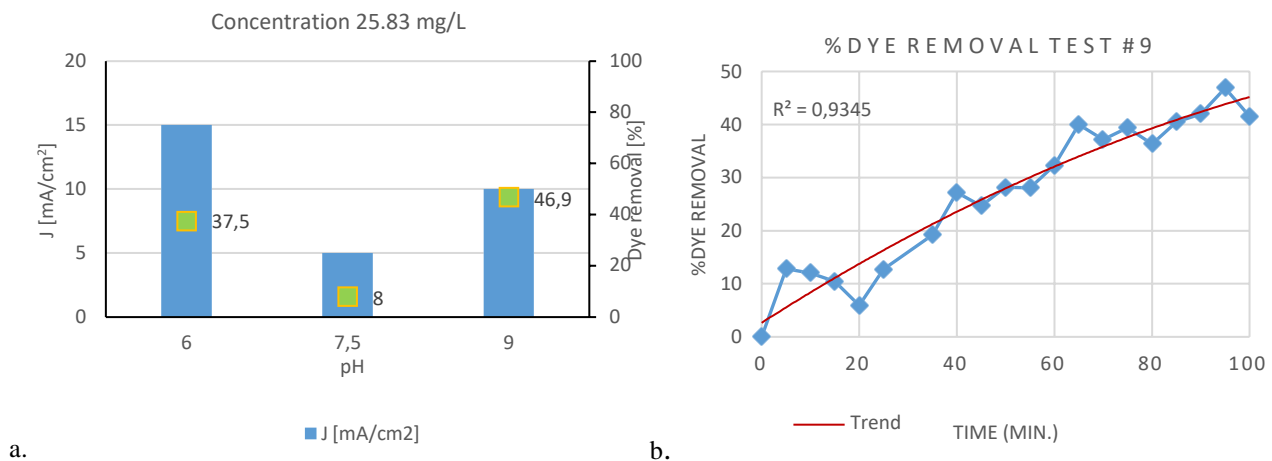


Figure 6. a. Percentage of dye removal in three tests at high concentration of BM (25.83 mg/L); b. trend of percentage of removal of BM during the test 9.

The graphs in Figures 2a., 5a. and 6a. show how higher BM removal rates can be achieved from more concentrated solutions. In particular, as can be seen in the graph in Figure 5 it is necessary that there is at least a "forced" reaction condition (J or pH) to treat a more concentrated solution obtaining satisfactory results (as in test #8, which has an intermediate pH and a low J value).

5.4.1.2 ANALYSIS OF THE RESULTS AS FUNCTION OF pH

The graph in Figure 7 analyses the tests at different values of pH. Under slightly acidic pH conditions, MB solution requires high J values to obtain a satisfactory percentage of dye removal in 100 minutes.

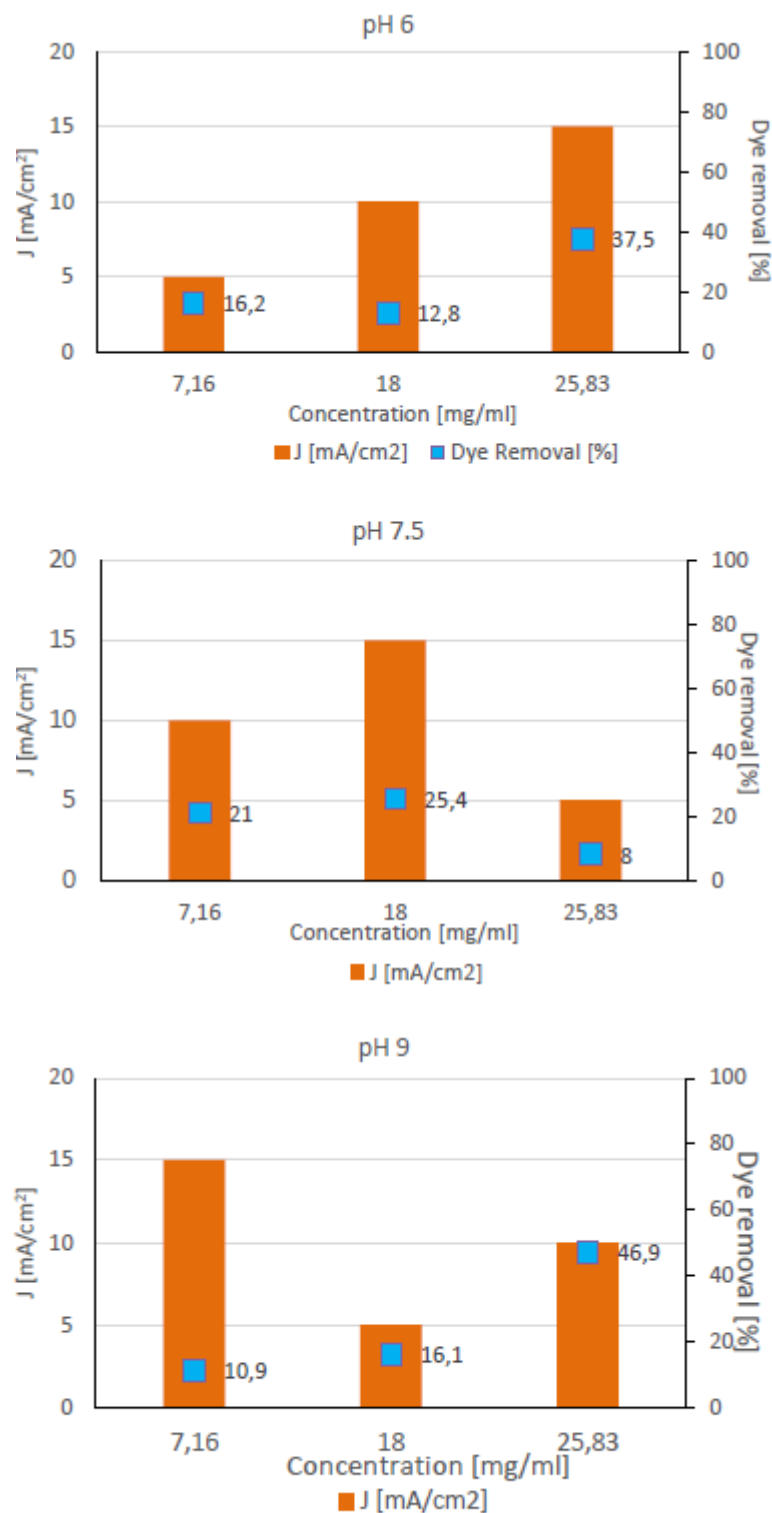


Figure 7. Percentage of dye removal at a. pH 6, b. pH 7.5 and c. pH 9.

At the pH value of 7.5, the removal percentage depended mainly on the applied J value; under neutral conditions, in fact, it was possible to increase the applied current intensity without incurring the side effects occurred during test #3 (at pH=9). A basic value of pH (pH=9) allowed to treat more concentrated solutions, obtaining high removal percentages and stable systems over time, with intermediate J values (see test #9).

Using the Taguchi method, it was possible to make the graph in Figure 8 which allows to analyze how the three factors in analysis affected the percentage of average removal of the dye. In particular:

1. The percentage of BM removal increased as the initial concentration of the solution increased. Specifically, a significant increase was observed between 18 mg/L and 25.83 mg/L;
2. A moderately alkaline pH value (9) was the best condition for the removal of MB, while a neutral pH did not provide a good yield of EC treatment;
3. By increasing the current density value J from 5 to 10 mA/cm², the percentage of dye removal could be greatly increased. A further increase of up to 15 mA/cm² led to a decrease in the process yield.

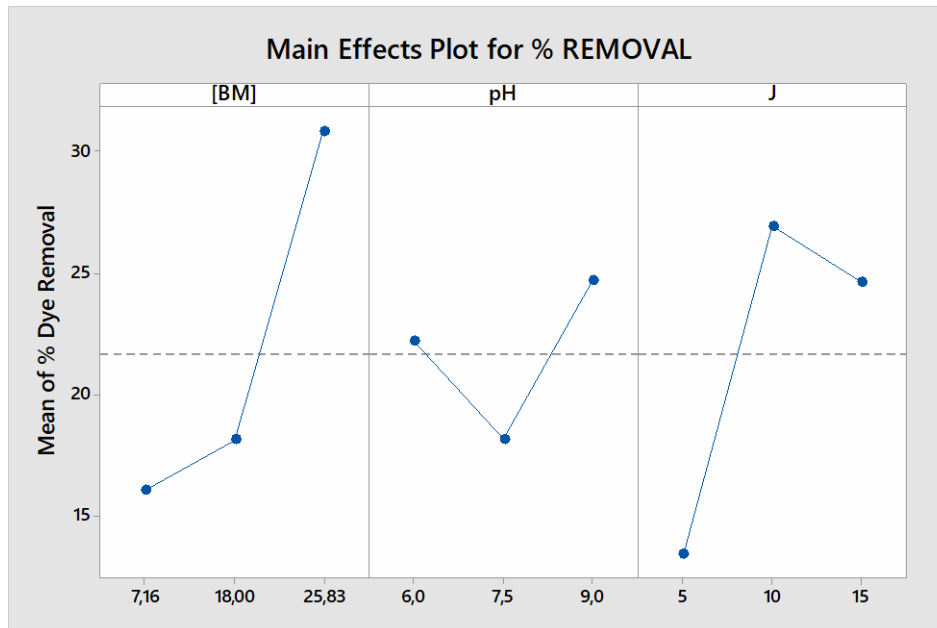


Figure 8. Graph of the main effects on the average percentage of dye removal.

As a result of the results and experimental observations obtained from tests carried out with the DOE-Taguchi model, it was possible to define optimal values for the treatment of aqueous MB solution with electrocoagulation system. In particular, it has been observed how it was possible to remove 47% of the dye in 100 minutes of treatment for solutions with concentrations of MB of 25.83 mg/L. For this purpose, it was necessary to have some basic pH conditions (pH=9) and use a current density at intermediate values (J=10 mA/cm²). An excessively high J value may present several problems:

- Excessive electrical stimulation of the anode can cause the formation of a layer of stable oxides on its surface promoting corrosion phenomena and generating passivation effects⁸. This may result in the shutdown of the operation of the EC system;
- the increase in the electrode dissolution rate may lead to changes in pH; in particular, an excessive increase in the concentration of OH⁻ ions may alter the relative concentrations of the chemical species present in solution and, consequently, alter the stability of flocculate;
- the excessive release of aluminum from the electrodes leads to the formation of a proportion of Al³⁺ ions that does not participate in the phenomena of coagulation and flocculation and, therefore, remains free in solution. This would lead to the formation of a new pollutant in a system which has as its objective the recovery of waste water.

5.4.2 EC TESTS OF SMALL SIZE

Electrocoagulation tests with a small system were carried out in order to obtain a system compatible with the use of sputtered membranes as electrodes. These tests have highlighted that a "fragile" system represented by electrodes having reduced thickness, if subjected to excessive pH and conductivity conditions, may suffer corrosion phenomena and excessive consumption of aluminum that cause the failure of the process.

In the test S1, after 30 minutes, the solution was clearer than the initial one and the anode is completely consumed due to its reduced thickness and the dispersion of aluminum in the solution.

The cathode connected to the black clamp remained almost intact, while the anode was completely consumed as shown in the Figure 9. The aluminum strip at the anode was replaced twice in one hour.

In addition, the increased turbidity of the solution gave a UV spectrum characterized by multiple peaks which had not made it possible to determine the concentration of MB. After an hour the test was stopped.



Figure 9. The intact cathode (connected to the black caliper) and the consumed anode.

At the end of the test S2, the solution had a much lighter color, as shown in Figure 10, while at the flocculate between the two electrodes appeared an aggregate of dark blue color.



Figure 10. Appearance of solutions at the end of the test S2

After 12 hours the solution appeared completely discoloured, but had small fragments of flocculate finely dispersed. From the spectrophotometric analysis of an aliquot of the solution it was possible to determinate the residual concentration of MB equal to 2.37 mg/L and calculate the percentage of dye removal equal to 95.26%. In the test S3, Figure 11 shows that after 30 minutes the solution concentrates methylene blue on the surface, while the rest of the solution has a light-grey appearance. This is due to the release of aluminum from the anode, almost completely consumed. After one hour the test has been suspended because the aluminum released in solution made this so opaque that it could not be analyzed at the spectrophotometer.



Figure 11. Solution after a. 30 minutes and b. 1 hour of EC treatment.

The reduced system test which led to more satisfactory results was the EC test with initial concentration solution [BM]=50 mg/L and unchanged conductivity conditions. While in previous tests the high conductivity of the solution had led to a rapid consumption of aluminum electrodes, in this test it was possible to obtain an almost complete removal of the dye ($R=95.26\%$), even if in long times ($\approx 12\text{h}$).

5.4.3 TEST 3. EC TEST WITH SPUTTERED MEMBRANES AS ELECTRODES

After 330 minutes of treatment the test was interrupted because the membrane acting as the anode was worn in the part in contact with the aluminum strips and it was no longer conductive (Figure 12). The cathode (Figure 12) showed traces of corrosion but maintains conductive spots. In figure 13 the trend of the percentage of removal of dye is shown.



Figure 12. Anode (up) and cathode (down) after 330 of EC test.

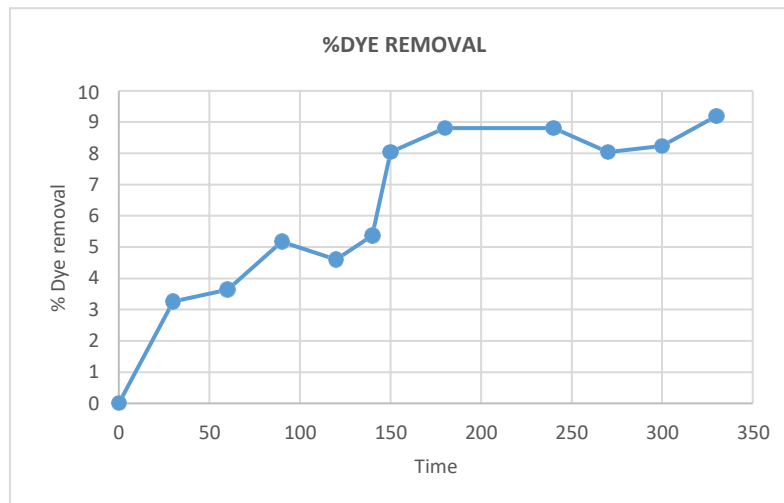


Figure 13. Percentage of removal during EC treatment with sputtered Al membranes.

The removal rate obtained at the end of the test was 9.2%. It was demonstrated that the use of electro responsive sputtered membranes within an EC system is possible, highlighting that the main problems to overcome is the excessive consumption of aluminum resulting in loss of membrane functionality as electrode.

5.5 CONCLUSION

Electrocoagulation and membrane separation processes are currently two of the most studied and used technologies for wastewater treatment. Both systems have great advantages and some limits, for which research is looking for new solutions: electrocoagulation requires reaction conditions that make it more biocompatible (lower use of electricity, lower release of residual metals in the reaction environment), while the membranes have the limit of fouling, which involves its replacement when this phenomenon irreparably compromises their functionality.

The creation of an integrated system, which includes both technologies, could give the opportunity to improve the performance of the entire process and to overcome the problems of individual treatments. The possibility

of developing electro responsive composite membranes, in order that they can be inserted in an electrocoagulation system, can lead both to a decrease of the phenomenon of fouling of the membranes themselves, an increase in the energy efficiency of the electrocoagulation system.

REFERENCES

- [1] M.Y.A. Mollah, P. Morkovsky, J.A.G. Gomes, M. Kesmez, J. Parga, D.L. Cocke, in *Fundamentals, present and future perspectives of electrocoagulation*, Elsevier B.V, **2004**.
- [2] K. Rajeshwar, J.G.Ibanez, G.M. Swain, *J. App. Electrochem.* **1994**, 24, 1077.
- [3] J.N. Hakizimana, B. Gourich, M. Chafi, *Desalination* **2016**, 404, 1.
- [4] G. Robic, E.A. Miranda, *Biotechnol. Prog.* **2010**, 26, 1.
- [5] G. Chen, *Sep Purif Technol.* **2004**, 38, 11.
- [6] S.S. Borchate, G.S. Kulkarni, V.S. Kore, S.V. Kore, *Inter. J. Inn. Eng. Technol.* **2014**.
- [7] M. Kobya, M. Bayramoglu, M. Eyvaz, *J.Hazard. Mater.*, **2007**, 148, 311.
- [8] O. Sahu, B. Mazumdar, P.K. Chaudhari, *Environ. Sci. Pollut. Res. Int.* **2014**, 21, 2397.
- [9] A.K. Panda, R.K. Singh R. K, *Int. J. Multidiscip. Curr.* **2013**, 1, 50.
- [10] A. Prakash, G. Sarkhel, K. Kumar, *Mater Today-Proc*, **2015**, 2, 2380.

PART III

INTRODUCTION

In an ideal situation, defined *homogeneous nucleation*, molecules crystallize in a solution extremely pure without inhomogeneities or impurity. The formation of a crystalline bond occurs when molecules brought together by translational diffusion inside the solution and a successful collision between them happens. This delicate step requires a close approach and a strict constraint on the spatial orientation of the species. To increase the chance for finding the correct physical patches leading to aggregation, a subsequent rotational diffusion movement of molecules is necessary. However, the chances of molecular interaction are reduced in large systems where the random rotation of molecules slow down rapidly. This concerns in particular complex biomacromolecules such proteins, that require highly selective and precise directional interaction for the aggregation to take place.

In homogeneous nucleation, the formation of nuclei depends by the product of two factors:

- (a) the number of nucleation sites and
- (b) the probability that a nucleus of critical size has grown around it.

The rate of nucleation (R) is given by the Equation (1):

$$R = N_S Z j \exp \left(\frac{-\Delta G^\ddagger}{k_B T} \right) \quad (1)$$

where N_S is the number of nucleation sites, Z is a proportionality constant, the Zeldovich factor (term that refers to the probability of the critical nuclei at the top of the activation energy barrier to grow into stable crystal), j is the rate of attachment of molecules to one another in the nucleus, ΔG^\ddagger is the free energy barrier for forming a nucleus, k_B is the Boltzmann constant, and T is absolute temperature.

The size of the free-energy barrier to homogeneous nucleation is relatively high (of the order of $100k_B T$ or more). Consequently, in many crystallization experiments, supersaturation is not reached and nucleation does not occur.

The surface of a foreign material is able to lower the activation energy barrier for nucleation facilitating the aggregation under conditions which would not be adequate for spontaneous homogeneous nucleation. This process is defined *heterogeneous nucleation*.

Heterogeneous nucleants reduce the change in free energy required to induce nucleation and hence obtain crystals at low solute concentration. The request for a lower amount of starting material and the possibility to increase the nucleation rate shortening protein crystallization times are interesting aspects that led the research to investigate on different surfaces able to create an environment that favors the nucleation process.

Several studies highlighted the contribution of surface properties in heterogeneous nucleation. These studies demonstrated the effects of protein-surface interactions on nucleation and crystal growth. Different surface-based approaches for promoting the crystal nucleation have been studied with a focus on surface chemistry and topography.

Some important examples of surface used as heterogeneous nucleants for the promotion of nucleation include disordered porous surfaces having wide pore size distribution, surfaces with charged functional groups able to

interact with the charged molecule to crystallize. Biopolymers and biominerals are also reported to induce protein crystallization at relatively low protein concentrations.

Furthermore, there are many studies on surfaces with different functional groups that suggest that functionalized surfaces could promote nucleation.

An innovative crystallization concept based on the use of membranes was proposed in 2001, when the concept of membrane distillation (MD) was applied to the crystallization of sodium chloride.¹ Since then, the use of porous hydrophobic membranes were extended to the crystallization of biomolecules.² The working principle of a membrane crystallization process is based on the evaporation of a volatile solvent through a microporous hydrophobic membranes in order to concentrate feed solution above its saturation limit thus attaining a supersaturated environment where crystals can nucleate and grow. During the membrane crystallization process, the membrane surface put in direct contact with the solution containing the molecule to crystallize acts as heterogeneous nucleants. For this reason, the structural and the chemical properties of the membrane surface play an important role in controlling nucleation and growth of crystals.³ Different functionalization strategies were investigated with the aim of creating an ideal environment for the nucleation process, promoting the chemical and physical interactions between the crystallizing molecules and the membrane surface. Functionalized porous polymer surfaces are able to promote biomolecular heterogeneous nucleation in a variety of experimental conditions, which could be not fruitful in batch methods.

Since the crystallization is the result of attractive interaction between protein and surface, the control of porosity and surface chemistry of heterogeneous nucleants are key considerations for successful application of membranes in protein crystallization process.

Different methods of functionalization were investigated in order to improve approaches to protein crystallization. Among the many materials, hydrogels have attracted special attention as heterogeneous supports. Composite polymeric membranes supporting a homogeneous thin hydrogel layer characterized by tailored chemical composition, nano-architecture and selected morphologies were used as crystallization platform. These materials offered the possibility to increase the efficiency of the crystallization process enhancing the diffraction properties of crystals produced at lower protein concentration.⁴

Specific physical-chemical properties of hydrogel composite membrane surfaces such topography and wettability have been found to influence the heterogeneous nucleation of protein crystals of lysozyme and thermolysin.⁵

In the past years, several studies have been carried out on the realization of cross-linked soft polymer able to act as a heterogeneous crystallization platform [polino] in which protein and additives were easily delivered to the gel network, the supersaturation was generated by gradual solvent removal in vapor phase through the porous structure of both support membrane and hydrogel layer, and crystals appeared at lower protein concentration and in experimental conditions which are not conventionally fruitful.⁶⁻⁹

It was demonstrated that cross-linked soft polymers are unique in their ability to concentrate solute molecules thanks to the favorable interactions between polymer and molecules of solute. Despite that, the main problem related to the use of hydrogels as crystallization platforms is represented by their poor stability and handling.

At this purpose, the research on hydrogels and in particular on composed porous membranes highlighted the necessity to improve the mechanical stability of these materials.

During the PhD work several functionalized hydrogel surfaces were used as crystallization support in order to investigate the effect of the gel sub-microstructure and different additives on the nucleation process of the model protein lysozyme. Among the many surfaces studied special attention was paid to the realization of polypropylene membrane completely transparent realized matching the refractive index of its constituents, Polypropilene (PP) (RI =1.49) and hydrophobic compounds dissolved in the hydrogel solution Darocur®1173 (RI =1,53) and PEGDMA (RI =1,46) and the monomer Acrylamide. The PP was pretreated in a solution of benzophenone in heptane and grafted by a photo-polymerization process induced by UV light, with a solution containing Poly(acrylic acid) (PAA) to promote the adhesion of the hydrophilic components to the matrix of the hydrophobic membrane. This functionalization strategy offered the possibility of interpenetrating the gel within the pore structure of the polymeric membrane, in order to improve the mechanical stability of the hydrogel obtaining an innovative material. The PP membranes characterized by transparency, stability in aqueous environment, mechanical strength and storage capacity over time, were used as crystallization support in a traditional vapour diffusion hanging drop process using a low concentration of the protein (10 mg/mL). The achievement of over-saturation in the macromolecular solution allows the nucleation and growth of crystals. The observation by optical microscope allowed to characterize a higher number of crystals appeared after 48 h on the functionalized membrane having smaller dimensions crystals than those growth on the reference sample (glass). The ability of transparent functionalized membranes to promote the growth of numerous smaller crystals was attributable to the filling of the pores of the polymer support with a layer of hydrogel and the size of the three-dimensional network of the hydrogel itself; the compartmentalization of the macromolecular solution within the 3D porous gel network limited the mobility of adsorbed molecules and provided a favorable environment for protein crystallization. In addition to being a good substrate for protein crystallization, transparent membrane presents an important advantage, that is to allow the observation of the crystals in an easy way to the conventional transmission optical microscope, unlike the opaque supports that require the reflective microscope to monitor the presence of crystals.

REFERENCES

- [1] E.Curcio, A.Criscuoli, E.Drioli, *Ind. Eng. Chem. Res.* **2001**, *40*, 2679.
- [2] E.Curcio, G.Di Profio, E.Drioli, *Desalination* **2002**,*145*, 173.
- [3] G.Di Profio, E.Curcio, A.Cassetta, D.Lamba, E.Drioli, *J. Cryst. Growth* **2003**,*257*,359.
- [4] G.Di Profio, M.Polino,F.P.Nicoletta, B.D.Belviso, R.Caliandro, E.Fontananova, G.De Filpo, E.Curcio, E.Drioli, *Adv. Funct. Mater.* **2014**,*24*, 1582.
- [5] S.M.Salehi, A.C.Manjua, B.D.Belviso, C.A.M.Portugal, I.M.Coelhoso, V.Mirabelli, E.Fontananova, R.Caliandro, J.G.Crespo, E.Curcio, G.Di Profio, *Cryst. Growth Des.* **2018**,*18*,3317.
- [6] N. E. Chayen , E. Saridakis , *Nat. Methods* **2008** , *5* , 147.
- [7] A. S. Myerson, in *Handbook of industrial crystallization 2nd ed.* , Butterworth-Heinemann , Woburn, MA , **2002** .
- [8] N. E. Chayen , E. Saridakis , *Trends Biotechnol.* **2008** , *27* , 99.
- [9] M. Polino, C. A. M. Portugal, G. Di Profio, I. M. Coelhoso, J. G. Crespo, *Cryst. Growth Des.* **2019** *19*, 4871.

CHAPTER 6

6. SILICA SPUTTERED PVDF MEMBRANE FOR THE CRYSTALLIZATION OF LYSOZYME

6.1. SUMMARY

In this work PVDF membranes were surface functionalized by physical vapor deposition (PVD), a well-known process for the production of high-purity, high-performance solid thin films, in order to create a thin layer of hydrophilic silica. The functionalization of the membrane surface used as substrate of crystallization, promotes the creation of sites for the heterogeneous nucleation of crystals combining the effect of specific surface porosity at nano- and micro-meter length-scale and surface chemistry on the heterogeneous nucleation process of lysozyme used as protein model at lower supersaturation conditions.

6.2. INTRODUCTION

During the crystallization process, the surface properties of the material in direct contact with the molecule to crystallize, play a fundamental role. The roughness and porosity of membrane surface may physically block protein molecules into the concaves so that they are forced to be packed into compact aggregates resulting in a relatively higher local supersaturation, which could increase the possibility of nucleation. A recent study examined the combined effect of specific surface porosity at nanometer length-scale and surface chemistry on crystallization of proteins at lower supersaturation.¹ This study demonstrated that nanoporous silica particles with controlled pore diameter, narrow pore size distribution, and surface chemistry having specific functional end groups are able to significantly lower the critical protein concentrations required to induce controlled heterogeneous nucleation and crystallization of five model protein systems: lysozyme, thaumatin, human serum albumin (HSA), concanavalin A and catalase. Nanoporous silica offers heterogeneous nucleation sites having a fixed diameter size range in which the protein can reach the supersaturation conditions required for the nucleation process. Despite this significant achievement, it is important to note that protein molecules having different dimensions require pore of different size to access them inside. Nanoporous silica is able to promote the crystallization of proteins but provided that there is an optimal ratio of protein size and pore diameters. Here, a novel method of surface functionalization based on the physical vapor deposition (PVD) of a thin layer of silica nanoparticles was investigated. This technique allowed to obtain a high-purity, high-performance solid thin films of the desired material leaving its physical and mechanical properties unchanged. The surface functionalization offers the possibility to combine silica nanoparticles which favor interactions protein-surface, and porous structure of polymeric membranes generally used in crystallization processes. The porous distribution of the polymeric membrane is preserved and molecules, depending on their size, can choose the required range of pore size in which they can concentrate and nucleate (Figure 1).

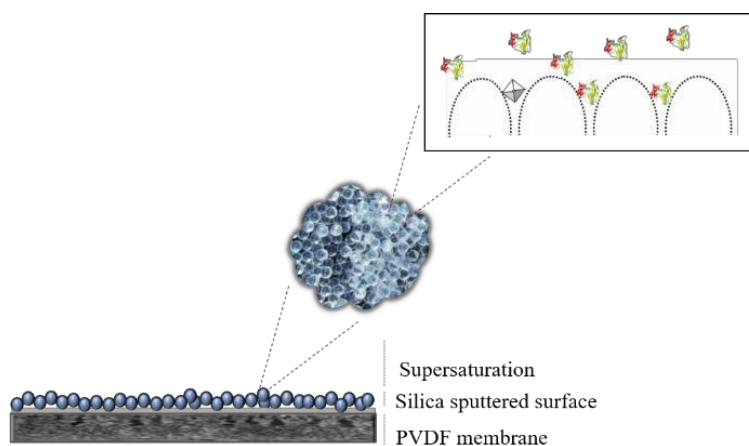


Figure 1. Schematic representation of a porous polymeric membrane covered by a thin layer of silica nanoparticles used as heterogeneous nucleants.

6.3. MATERIALS AND METHODS

Hydrophobic PVDF membrane disks with a diameter of 47 mm, a porosity of 70%, and an average pore size of 0.10 μm (Durapore©, Merck KGaA, Darmstadt, Germany) were used as substrate for the crystallization tests. PVDF membranes were covered with silica inorganic layers of different thickness by physical vapor deposition (PVD). The substrate is exposed to one or more volatile precursors, which react on the substrate surface to produce the desired layer. The deposition of silica nanoparticles on PVDF membranes was obtained by sputtering of appropriate targets by process inert gas ions (argon) in an Edwards AUTO-306 sputtering system (Edwards, Burgess Hill, UK), shown in the Figure 2. The reactive gas mixture reacts with the substrate and sputtered atoms, forming a thin film of the desired compound onto the substrate.

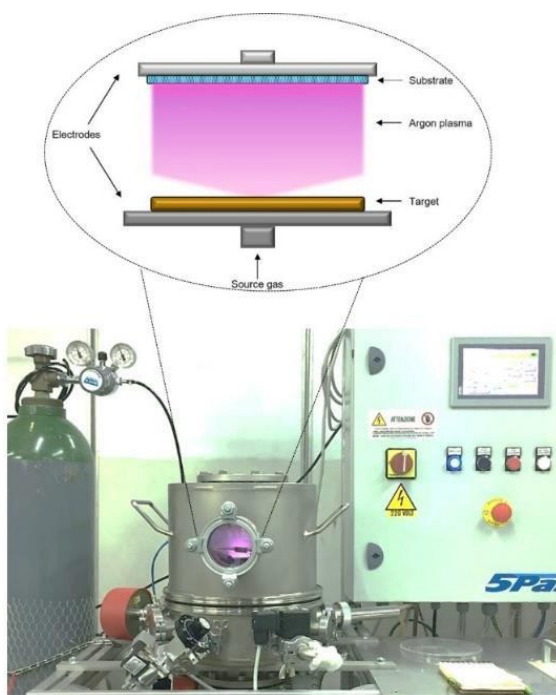


Figure 2. Edwards AUTO-306 sputtering system and a schematic representation of sputtering process.

The presence of nanoparticles on membrane surface could also reduce membrane hydrophobicity, resulting in a

potential mitigation of fouling, while keeping its non-wetting aptitude.

The optimal sputtering conditions shown in Table 1 were found after several trial in which different setting parameters were changed including power, target distance, pressure and sputtering time in order to find the optimal conditions able to give homogeneous coverage avoiding pore occlusion or substrate damage.

Table 1. Parameters of sputtering process.

TARGET	PHOTOCATALYST LAYER	SPUTTERING POWER/W	TARGET DISTANCE/10 ² M	PRESSURE/10 ⁵ BAR	SPUTTERING TIME/MIN	DEPOSITION RATE NM/MIN
SiO ₂	SiO ₂	35	8	P(Ar)= 3.5	30	2
SiO ₂	SiO ₂	35	8	P(Ar)= 3.5	40	2

Crystallization trials were carried out using the hanging drop vapor diffusion method, in which a drop of protein solution was deposited on the membrane surface and added with an equal volume of precipitant solution. Sodium chloride solution 7 wt. % was used as precipitant agent.

The system was then incubated at 20 ± 0.1 °C before optical microscopy inspection of the droplets. The used crystallization parameters are reported in Table 2.

Table 2. Crystallization parameters

[LYSOZYME]	10 mg/ml
Buffer solution (solvent water)	0.1 M sodium acetate, pH 4.6
Precipitant solution (solvent buffer)	NaCl 7%
Volume of protein solution and precipitant solution in the drop 1:1	5 µl
Reservoir volume	6 ml
Temperature of incubation	20°C

During the crystallization process schematized in the Figure 3, protein concentration in the drop increases by solvent removal in vapor phase, while, the film of silica sputtered on porous surface of PVDF membrane, put in contact with the drop, favors the crystallization of protein because it acts as heterogeneous template nucleant thanks to its large pore size distribution and controlled surface chemistry.

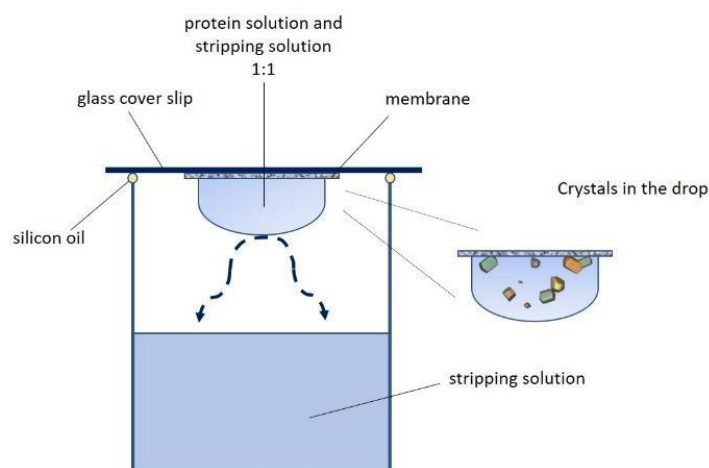


Figure 3. Hanging drop with a membrane used as crystallization support.

Protein crystals were observed under an optical microscope equipped with a video-camera.

6.4. RESULTS AND DISCUSSION

In the SEM pictures shown in Figure 4 are shown sputtered silica membrane surface with a large range of pore size.

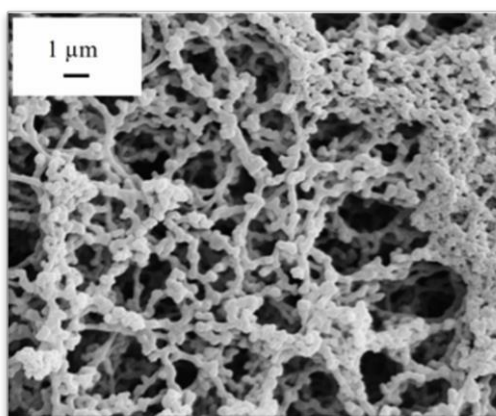
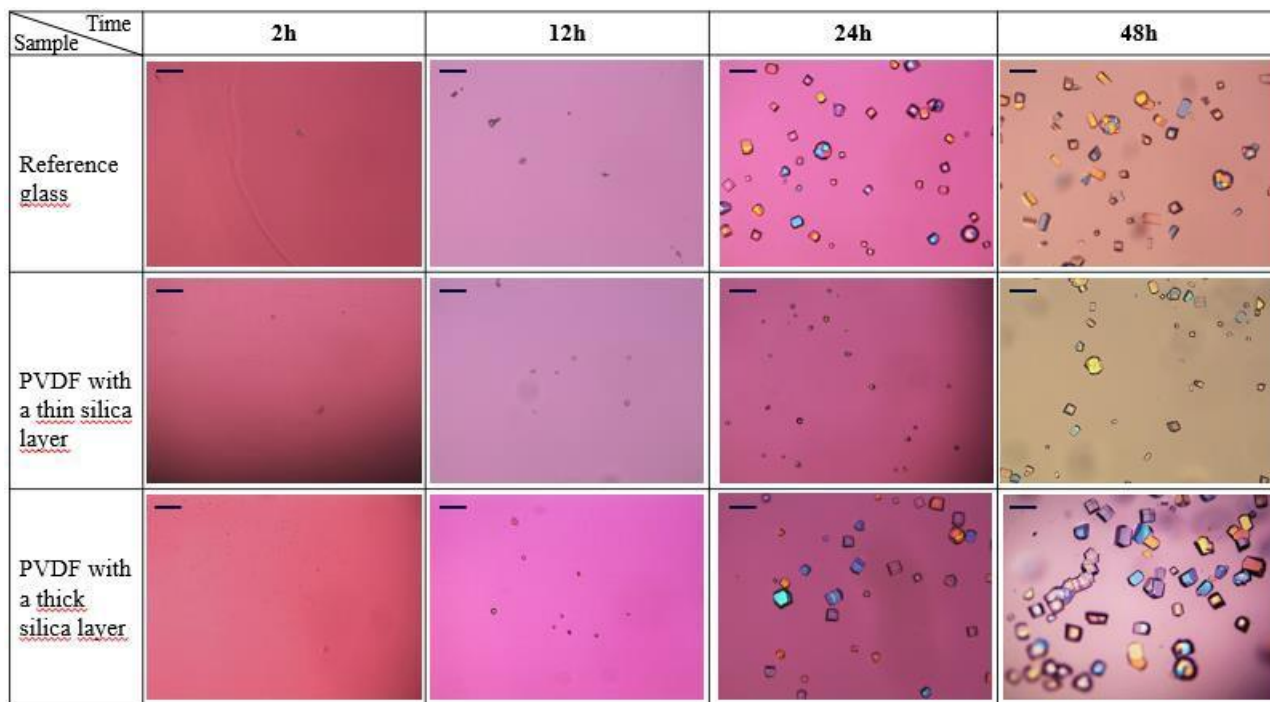


Figure 4. SEM picture of sputtered silica PVDF membrane.

Preliminary results showed that layers were able to confer hydrophilic properties to membrane surfaces as confirmed by contact angle measurements and favor lysozyme crystallization.

As it can be seen in the scheme the size of lysozyme crystals on glass cover slip used as reference are similar to crystals growth on PVDF membrane sputtered with a thick layer of hydrophilic silica.



Scheme 1: Size of lysozyme crystals grown on different substrates

This silica layer reproduces the ideal hydrophilic condition of glass surface, keeping the porosity of membrane, while the surface roughness offers different heterogeneous nucleation sites in which the protein can reach the supersaturation conditions required for the nucleation process.

6.5. CONCLUSIONS

The functionalized membranes were able to favor lysozyme crystallization. The enhancement of crystallization process can be attributed to the combined effect of surface chemistry and surface porosity.

The preliminary crystallization batch trials demonstrate that silica sputtered PVDF membranes allow an accurate control of supersaturation by solvent removal in vapor phase.

REFERENCES

- [1] U.V. Shah, M.C.Allenby, D.R.Williams, J.Y.Y.Heng, *Cryst. Growth Des.* **2012**,12, 1772.

CHAPTER 7

7. HYBRID HYDROGELS FOR THE CRYSTALLIZATION AND THE CONTROLLED RELEASE OF LYSOZYME

7.1. SUMMARY

This work is focused on the synthesis and the analysis of chemical-physical parameters of specific hybrid alginate hydrogels (H_{AL}), made in the form of thin polymeric films in order to demonstrate their versatility in two distinct fields of application related to the world of proteins: crystallization and controlled release. In the field of crystallization, a possible damage mitigation strategy based on the use of hydrogel functionalized with a phenolic compound with antioxidant activity, Caffeic Acid (CA) as crystallization support was investigated. While, in the field of controlled release of proteins of pharmaceutical interest, the possibility of creating an electrosensitive release device adding graphene oxide (GO) to the starting polymer system was evaluated.

7.2. INTRODUCTION

Protein crystallization represents the preliminary step in X-ray crystallography studies since this technique is based on the diffraction of the three-dimensional ordered structure of the crystalline lattice. Over the years, X-ray crystallography provided unprecedented opportunities to promote the development of biological research and drug design.¹ The exact knowledge of the structure of a specific macromolecule with biological activity, for example, allows the design of a drug (lead-compound) that could act on a specific binding site and block a pathological pathway. Data on the gene sequence of biological systems derived from recent advances in DNA-recombinant technology, together with the information on the three-dimensional structure of proteins, allow to investigate on the basic biochemical mechanisms of a living organism essential in the development of targeted therapies.

X-ray crystallography is certainly the method of choice to determinate the structure of a protein. When a monochromatic x-ray beam strikes the crystal, the light scatters and a diffraction pattern is generated. The resulting diffraction patterns made of dispersed black spots can be processed to obtain the electron density map of the unit molecule used to finally determinate the molecular structure of the analyzed protein.² However, the incident x-rays contain so much energy that could damage the crystal. Radiation damage of crystals inflicted during diffraction data collection in macromolecular crystallography represents a challenge and affects the interpretation of the correct structure of the protein. This damage is caused by heating and the generation of radical species that are responsible for the damage of the protein, but also determine the unwanted appearance of artifacts that make difficult the interpretation of the biological-structural properties of the crystal.^{3,4} In addition, structural changes induced radiation-damage could affect the biological properties of macromolecules, for example changing the oxidation state of metal ions in structural/active sites and causing decarboxylation of glutamate and aspartate residues.⁵ The number of studies on the radiation damage in

macromolecular crystallography is constantly growing. The first attempt to mitigate radiation damage highlighted the importance of temperature in the damage process.⁶ In cryo-crystallography the diffraction data are collected with the sample held at low temperature (around 100 K), reducing the secondary radiation damage arising from the formation of low-energy secondary electrons able to diffuse and induce further ionization and excitation events.⁷

However, even at cryo-temperatures was observed the degradation of data quality and specific structural damage to particular aminoacids due to radiation damage. Besides, certain macromolecular crystals (e.g. of viruses) suffer large increases in mosaicity upon flash cooling.⁸ A valid alternative to cryocooling for prolonging crystal lifetime is the use of radioprotectants, compounds able to scavenge the free radical species formed upon X-ray irradiation.⁹

The aim of this work was to realize and analyze the chemical-physical characteristics of a polymeric system, a hydrogel based on Alginate, demonstrating its remarkable versatility in two specific fields of application: protein crystallization and controlled drug release, using Lysozyme as the model protein.

The work focused primarily on the realization of Alginate hydrogels, starting from monomers such as 2-hydroxyethyl acrylate (HEA) and polyethylene glycol dimethacrylate (PEGDMA), exploiting a synthetic biocompatible strategy and interesting for a real biotechnological application.

Caffeic acid (CA) and graphene oxide (GO) have been introduced in the chemical composition of the hydrogel, as functional additives in order to improve the performance of the system, depending on the specific purpose. The hydrogel was designed for the application in the field of protein crystallization. In this context, an efficient strategy to mitigate one of the unresolved problems that occurs during the collection of RX diffraction data, the radiation-induced damage was investigated. Therefore, the idea of introducing into the hydrogel a specific protective function for crystals led to its derivatization with a molecule with known antioxidant properties.

Specifically, the synthetic strategy concerned the functionalization of Alginate (ALG) with CA, a phenolic compound with antioxidant activity to obtain a sodium alginate-caffeic acid bioconjugate (ALGC).

CA is a phenolic compound that, as reported in the literature, has demonstrated *in vivo* significant beneficial effects, such as anti-inflammatory, anti-mutagenic, anti-bacterial and anti-carcinogenic properties related to its known anti-oxidant activity.¹⁰ CA is produced, both in free and in esterified form from the secondary metabolism of plant substances, such as coffee grains, olives, potatoes, carrots, propolis and various fruits. At the level of the cell walls, of these substances CA is abundant and intervenes in the defense mechanisms of plants by inhibiting the growth of bacteria, fungi and insects and protecting them from ultraviolet radiation B; it also represents the main hydroxyinnamic acid in the human diet. From a chemical-structural point of view, CA (3,4-dihydroxyinnamic acid) belongs to the phenolic acid family and has a phenylpropanoid structure (C6-C3) with an aromatic ring 3,4-dihydroxylate bonded to carboxylic acid by a transethylene component.¹¹ As the existing literature suggests, the antioxidant action and the role of "scavengers" of free radicals responsible for damaging oxidative processes against oxidizable substrates of phenolic compounds, is closely related to the chemical structure of the compound in question: the number and location of hydroxyl groups (-

OH) present in the structure, and also related to the concentration of the same compound in the reaction environment.¹²

At the same time, the possibility of making hydrogel applicable in the field of drug delivery of proteins-peptides was evaluated. Specifically, the possibility of making the polymer system "intelligent" electrosensitive, able to modulate the release profile as a function of the application of an external electric field was studied. For this purpose, GO was introduced in the chemical composition of the hydrogel, exploiting its known electrical conduction properties. GO which is a derivative of graphene is the oxidized form of graphene with hydroxyls, epoxides, diols, ketones and carboxyls functional groups. Thanks to the specific properties as electrical conductor, GO gave the hydrogel sensitivity to an electric field applied, with the consequent possibility of modulation of chemical properties-physical system and release of charged drug molecules.

The comparison of Lysozyme release profiles from the hybrid polymer system with those recorded using the control hydrogel without GO, both in the absence and in the presence of external electric field, allowed to highlight the potential applicability of the proposed system for the release of protein molecules of pharmaceutical interest.

The research work also focused on the characterization of the final composite polymer system, carried out through instrumental and functional analysis. Through the differential scanning calorimetry (DSC) analysis, information on the chemical-physical stability of the polymer system were obtained, while, by means of optical microscopy observation the growth of the Lysozyme crystals over time was observed.

7.3 MATERIALS AND METHODS

7.3.1 SYNTHESIS OF THE SODIUM ALGINATE-CAFFEIC ACID CONJUGATE

The synthesis of the bioconjugate (ALGC) was performed in heterogeneous phase using as biocatalyst the polymeric membrane containing the enzyme Lipase. The Lipase was immobilized on a thin polymeric support prepared using the monomer Acrylamide (Aam) and the crosslinking agent Polyethyleneglycol dimethacrylate (PEGDMA 750) in the presence of the solubilized enzyme.^{13,14} Briefly, 100 mg of ALG and 20 mg of CA were dissolved in a mixture (3.5 mL) of DMSO (5%) in water, then the catalyst Lipase (20 mg) was added.

After incubation, the mixture was purified of unreacted CA by dialysis (membranes Spectra/Por, Medicell International LTD, MWCO: 12.000-14.000 Da) against reaction medium (mixture of DMSO/H₂O) and then distilled water at room temperature for 7 days, changing the solution twice a day. At suitable time intervals, the amount of CA in the wash water was determined by UV-vis at 325 nm. The dialyzed solution was freeze-dried to obtain a white vaporous solid. All chemicals were obtained from Merck/Sigma Aldrich, Germany.

7.3.2 SYNTHESIS OF POLYMERIC MATRIX

The copolymers containing GO (H_{AL-GO}, H_{ALCA-GO}), were synthesized according to the following procedure: a given amount of GO was dispersed by sonication in an aqueous solution of ALG or ALGC. Then the monomer 2-hydroxyethyl acrylate (HEA) and the crosslinker polyethylene glycol dimethacrylate (PEGDMA) were added. The resulting solution was stirred to obtain a homogeneous mixture of GO. Then the polymerization initiator potassium persulfate (K₂S₂O₈) was added (8 wt.% respect to the monomer). The hydrogels were thermo-polymerized at 37 °C in an oven for 24 h in two different ways:

- a. Single glass plate (2.5 x 2.5 cm²) on which, a circular Teflon spacer (thickness of 2mm) was fixed by binder clips. The glass support was previously dipped in a 50% nitric acid solution for 30 min, in order to increase the roughness of the glass surface improving the adhesion of the hydrogel thin film, a process called “etching”;
- b. Two glass plates separated with Teflon spacers (thickness 0.8 mm) and brought together by binder clips.

The obtained hydrogels were extensively washed with distilled water and ethanol/water mixtures of increasing concentrations for 6 h and then dried at room temperature under reduced pressure. Blank hydrogels without GO (H_{AL} e H_{ALCA}) were prepared following the same procedure. The used composition was reported in the Table 1. All chemicals were obtained from Merck/Sigma Aldrich, Germany.

Table 1. Hydrogel composition.

Reagent	H _{AL}	H _{ALCA}	H _{AL-GO}	H _{ALCA-GO}
Graphene Oxide (mg)	-	-	5.0	5.0
Distilled H ₂ O (mL)	2.5	2.5	2.5	2.5
ALG (mg)	100	-	100	-
ALGC (mg)	-	100	-	100
HEA (mg)	184	184	184	184
PEGDMA (mg)	196	196	196	196
KPS (mg)	30	30	30	30

ALG: Sodium Alginate; ALGC: Sodium Alginate- Caffeic Acid conjugate; GO: Graphene Oxide; HEA: 2-hydroxyethyl acrylate; KPS: Potassium persulfate; PEGDMA: polyethylene glycol dimethacrylate.

7.3.3 CHARACTERIZATION OF CONJUGATE HYDROGELS

The calorimetric analysis of the hydrogels was carried out using a differential scanning calorimeter Netzsch DSC200 PC, heating the sample from 25°C to 300 C° under nitrogen with a flow rate of 25 ml min⁻¹ and a speed of 15 C min⁻¹. Spectrophotometric analysis was performed using an Evolution 201 spectrophotometer (Thermofisher Scientific, Hillsboro, OR, USA).

7.3.4 DETERMINATION OF SWELLING PROFILES

The swelling degree (S%) of prepared hydrogels was determined in water at room temperature using a known amount of hydrogel (30 mg). The swelling percentage (WR) was measured either in the absence or in the presence of an electric field (12, 24 and 48 V). After 24 h, excess water was removed and samples were weighed. The water content percentage (WR) was expressed by the following equation (1):

$$WR = \frac{w_s - w_d}{w_d} \times 100 \quad (1)$$

where W_d and W_s are the weight of dried and swollen sample, respectively.

7.3.5 CRYSTALLIZATION EXPERIMENTS

The crystallization tests were performed by conventional hanging drop vapor diffusion method using the prepared thin films of hydrogel as crystallization supports. Lysozyme (Merck/Sigma Aldrich, Germany) was dissolved in sodium acetate buffer (0.1 M, pH 4.6) at the initial concentration 10 mg mL^{-1} . The precipitant and stripping solution were composed of Sodium Chloride, NaCl (purchased from Panreac) (7.0 wt.%), dissolved in the same buffer. A drop of protein solution (5 μL) pipetted on the surface of the hydrogel membrane and added with the equal volume of precipitant solution was left equilibrating with 6 mL of stripping solution in the well.

The final crystallization solution after mixing the protein and precipitant solutions, was 5 mg mL^{-1} .

To assure the result reproducibility 5 replica experiments for each tested condition were carried out by introducing samples in the crystallization system. The crystallization system was then incubated at $20 \pm 0.1^\circ\text{C}$ before optical microscopy inspection of the droplets after time intervals of 24, 48 and 72 h. Protein crystals were observed under an optical microscope (Zeiss-Axiovert 25) equipped with a video-camera. To analyze the antioxidant performance of the hydrogel conjugate, the same experimental conditions were used adding H_2O_2 as oxidative stress. H_2O_2 solution at the concentration of 15% was added to the hanged drop and the reservoir solution.

7.3.6 LYSOZYME LOADING AND RELEASE EXPERIMENTS

Lysozyme was loaded by the impregnation technique consisting of the introduction of the polymer into the solution containing the protein. For the impregnation process, a known amount of polymeric matrix (150 mg) was dipped in a solution of lysozyme (0.75 ml) having a known concentration of 1.0 mg/mL in PBS 0.4 M, pH 4.6. The loading was performed at room temperature away from light and heat for 3 days. The loaded hydrogels were dried at reduced pressure.

The release profiles of lysozyme were determined inserting the sample (10 mg) in the release media (5 mL) consisting of phosphate buffered saline 0.1 M at pH 8.0 and acetate buffer 0.4 M at pH 4.6. The analysis of release profiles were performed in the presence of an electric field of 12, 24 and 48 V and in the absence of electric field (0 V) in a thermostatically-controlled water bath (TRM 750) at the temperature of 37°C . At suitable time intervals, the amount of lysozyme in the release media was determined by UV-vis at 325 nm.

7.4 RESULTS AND DISCUSSION

H_{AL} was prepared via a thermal free radical polymerization at a temperature of 37°C , using potassium persulfate as a catalyst (Figure 1).

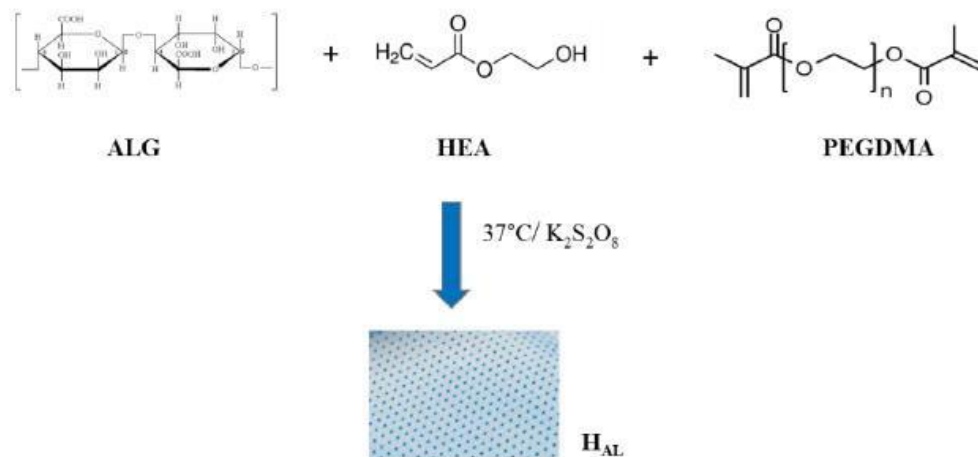


Figure 1. schematic representation of H_{AL} preparation.

The general mechanism of the reaction consisted in a radical grafting: ALG was grafted on the growing network HEA-PEGDMA. As reported in the literature, natural polysaccharides such as Alginate have the ability to take part in a process of radical polymerization thanks to the reactivity of the heteroatoms present in the side chains of such polymers, which react with the growing radicals leading to the formation of a "macroradical" that can participate in the propagation reaction of the polymeric chain.¹⁵

Different polymeric compositions were investigated by varying the ratio of ALG respect to the total amount of monomers (10, 30, 40, 50%). The best chemical composition of the reaction mixture that provided an ALG ratio of 40% was the best in terms of mechanical properties given the considerable self-consistency and the best adhesion to the glass slide on which the polymerization was carried out, an essential point for a potential application in the process of protein crystallization using the Hanging-drop method. The hydrogel is also macroscopically homogeneous and the adhesiveness is maintained even after repeated treatments of the polymer system with water/ethanol mixtures used as washing solutions.

7.4.1 CHARACTERIZATION OF COMPOSITE HYDROGELS

The ALGC conjugate was characterized by determination of the phenolic groups available by Folin-Ciocalteu assay and Differential Scanning Calorimetry (DSC). The results of the Folin-Ciocalteu test gave a degree of functionalization, expressed as mg of CA per gram of conjugate, equal to 120 ± 3 mg/g.

The DSC analysis of ALG and ALGC (Figure 2) shown that the conjugation of the antioxidant molecule to the polysaccharide chain resulted in an increase in the thermal stability of the conjugate. In fact, The ALG thermogram was characterized by an endothermic transition around 100 °C due to the loss of water molecules, while the exothermic transition around 241 °C corresponds to the decomposition of the polymeric chain. In the case of ALGC, the exothermic transition relative to decomposition was shifted to 252 °C, indicating the stabilizing effect of CA residues on the polymer chains.

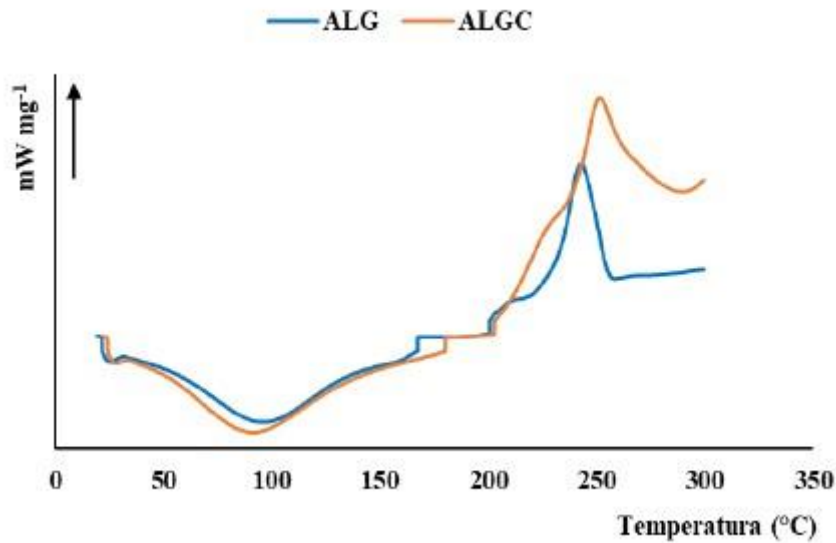


Figure 2. DSC thermogram of ALG and ALGC.

For the preparation of the electrosensitive hybrid hydrogel, Graphene Oxide was added to the polymerization mixture. The functional groups in the structure of GO, such as carboxylic groups (-COOH), hydroxyl groups (-OH), epoxy groups (-O-) may establish interactions with the polymeric matrix of Alginate hydrogel.¹⁶ The chemical-physical characterization of hydrogels H_{AL} e H_{AL-GO} was carried out by differential scanning calorimetry (DSC) and determination of the degree of swelling in water (S%). The analysis of the thermograms of the H_{AL} and H_{AL-GO} hydrogels shown in Figure 3, shown that the introduction of the GO in the chemical structure of the hydrogel resulted in a significant increase in chemical stability of the system. In fact H_{AL} had a transition to 250 °C, while in the same area there was no effect on the hydrogel H_{AL-GO}, confirming the increase in rigidity given to the system by the interconnection between the polymer lattice and the graphene sheets. Besides, from the analysis of the thermograms it is possible to observe that there was no difference between hydrogels synthesized using the conjugate ALGC those synthesized using native Alginate, because of the low amount of CA present in the polymer lattice.

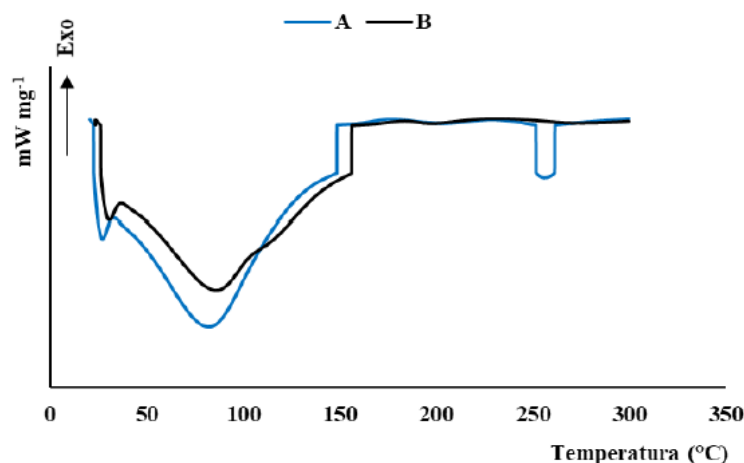


Figure 3. DSC thermogram of (A) H_{AL} and (B) H_{AL-GO}.

The determination of the degree of swelling ($S\%$) is crucial in obtaining information useful for evaluating the release of a drug from a polymeric system. The swelling study was carried out in aqueous medium both in the absence and in the presence of electric field (at voltage values of 12, 24 and 48 V), and the behaviour of the hybrid HAL-GO system was compared with that of the H_{AL} control system (Table2).

Table 2. Swelling values ($S\%$) of H_{AL} e H_{AL-GO} after 24h in aqueous medium without (0V) and in the presence of electric field (12, 24, 48V).

S (%)	0V	12V	24V	48V
HAL	605 ± 9	599 ± 10	591 ± 15	597 ± 12
HAL-GO	696 ± 12	540 ± 8	564 ± 11	598 ± 10

The application of an electric field (12, 24, 48 V) did not involve a significant variation in the degree of swelling of the H_{AL} hydrogel compared to the conditions of absence of electrical stimulation.

The addition of GO in the polymer system H_{AL-GO} gave a certain degree of mechanical rigidity, greater hydrophobicity and considerable electro-responsibility. In particular, the electrosensitive behavior could be explained on the basis of the change in osmotic pressure, which occurs within a hydrogel due to the different concentration of ions between the inside and the outside of the polymeric network (Figure 4).

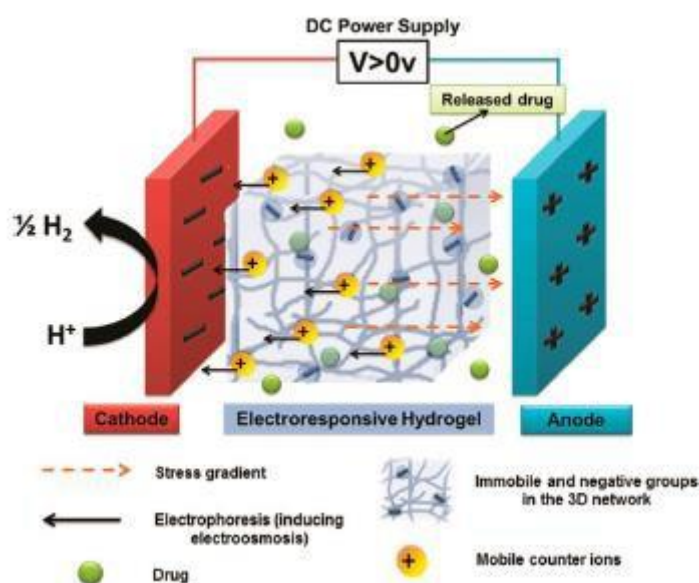


Figure 4. Schematic representation of the contraction mechanism of an electrosensitive hydrogel.

When a charged gel strip was placed in parallel to a pair of electrodes and an electric field was applied to the system, a migration of the ions present inside the gel, as well as free ions in solution, towards the electrode of

opposite sign occurred. As a result of this movement of charges, there was the formation of an ionic gradient within the polymer matrix which underwent a contraction. At the same time, ionization of the ionizable residues present in the lateral chain of the hydrogel, consisting of the carboxylated groups of the Alginate, led to the formation of negative charges that tend to repel counteracting the contraction force due to the ionic gradient. From the summation of these effects, the result was a contraction of the hydrogel which was more marked at 12 V, a value at which the ionization of carboxylated groups was not able to counteract the osmotic flow. As voltage increases, the osmotic force lost its effectiveness with respect to electrostatic repulsion forces between negative charges in the polymeric lattice, and swelling values tend to rise progressively without reaching the values recorded in the absence of electric field.

7.4.2 CRYSTALLIZATION TESTS

The conventional Hanging-drop crystallization technique allowed to investigate the best conditions for obtaining good results in terms of the quality of the Lysozyme crystals and their protection against radical species. In general, in a crystallization process the best result in terms of crystal quality was obtained when the crystals displayed on the drop at the end of the process are few and large. However, several parameters could influence the phases of nucleation and growth of the crystals. Nucleation takes shape when the protein solution reaches an optimal level of oversaturation. In an ideal condition, key parameters related to the solution such as pH, temperature, precipitating agent, lead the protein solution to the labile area of over-saturation, at which the protein may encounter a spontaneous nucleation. When the crystalline nuclei are formed and, therefore, the level of over-saturation is reduced, the metastable zone is reached, where the growth of the crystal is favored.⁹ As a general rule, the condition of over-saturation can be favored by the addition to the protein solution of suitable precipitating agents, such as PEG, organic solvents, or even inorganic salts such as sodium chloride. These contribute to the achievement of the state of over-saturation of the solution by varying the chemical-physical characteristics (temperature, ionic force, pH). In detail, inorganic salts act for this purpose by influencing the ionic strength of the protein solution. In addition, to achieve the state of over-saturation the amount of precipitating agent must be balanced at the concentration of the protein in solution.

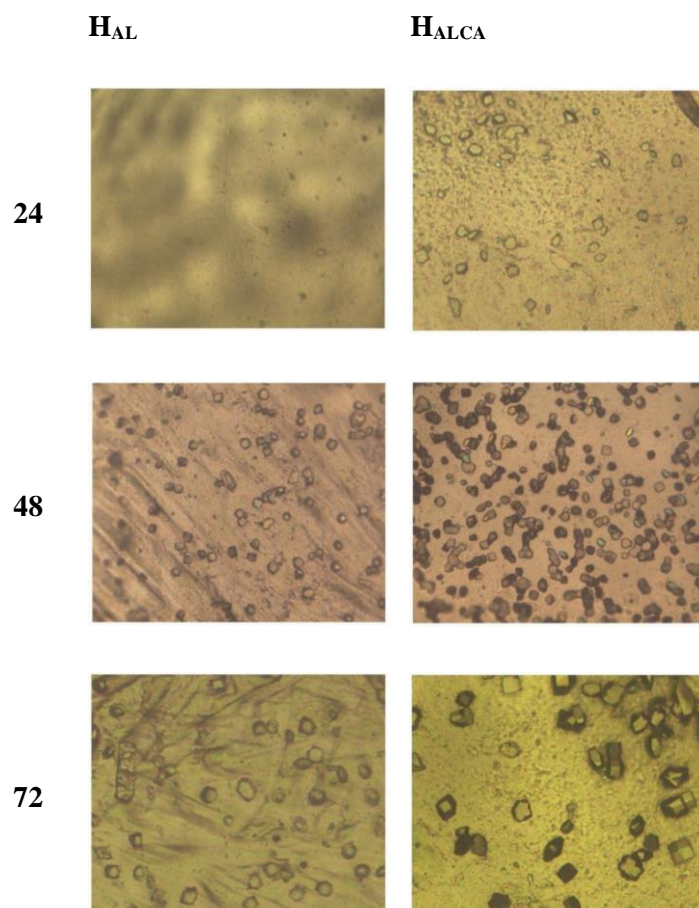
In this work, crystallization tests were performed using the polymeric systems H_{AL} and H_{ALCA} as support of the crystallizing drop to promote the growth of crystals. Specifically, in a process of crystallization in vapour phase, the polymeric hydrogel film used as support, thanks to its porosity, promoted the establishment of a condition of balance between the protein drop and the stripping solution in the well, through the migration and subsequent evaporation of the solvent in vapor phase from the drop to the stripping solution. At these conditions, the state of over-saturation at which the nucleation can take place was more easily reached.

The best conditions, among the various analyzed in this work, were:

- Lysozyme protein solution concentration of 10 mg/ml in Acetate Buffer 0.1M, pH4.6;
- 7% w/v of precipitating agent (NaCl) diluted in the same Buffer Acetate, in the drop and in the well.

In the Table 3 are reported the images of Lysozyme crystals at optical microscope obtained at certain intervals of time (24, 48 and 72h) using the polymeric system H_{AL} and H_{ALCA} .

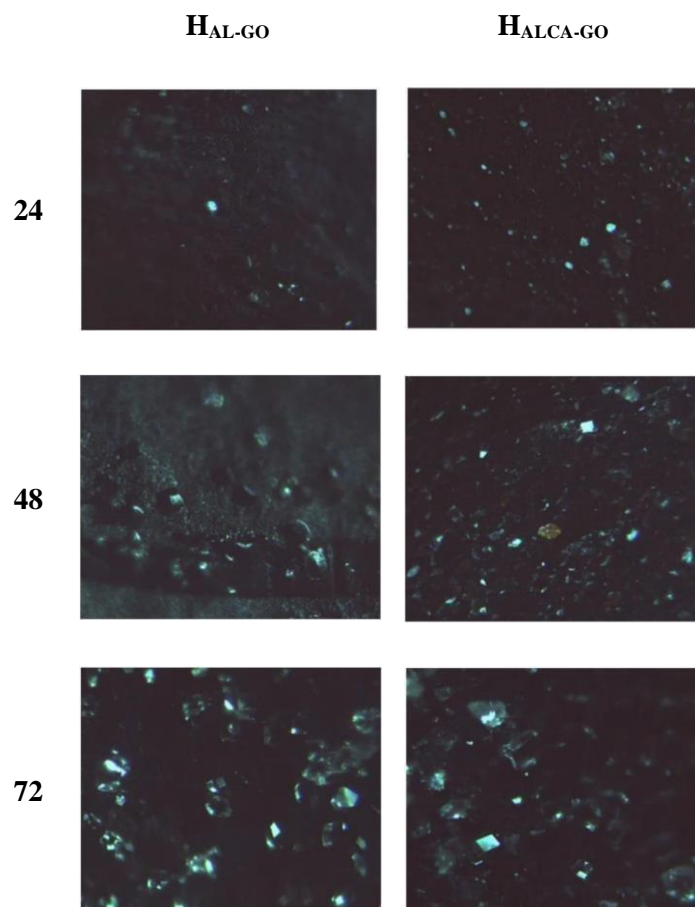
Table 3. Lysozyme crystals on H_{AL} and H_{ALCA} at 24, 48 e 72h.



The predominantly morphological shape of observed lysozyme crystals was the tetragonal form.

The crystallization test was also performed on hybrid polymer H_{AL-GO} and $H_{ALCA-GO}$, and the crystals obtained are shown in the Table 4.

Table 4. Lysozyme crystals on H_{AL-GO} and H_{ALCA-GO} at 24, 48 e 72h.

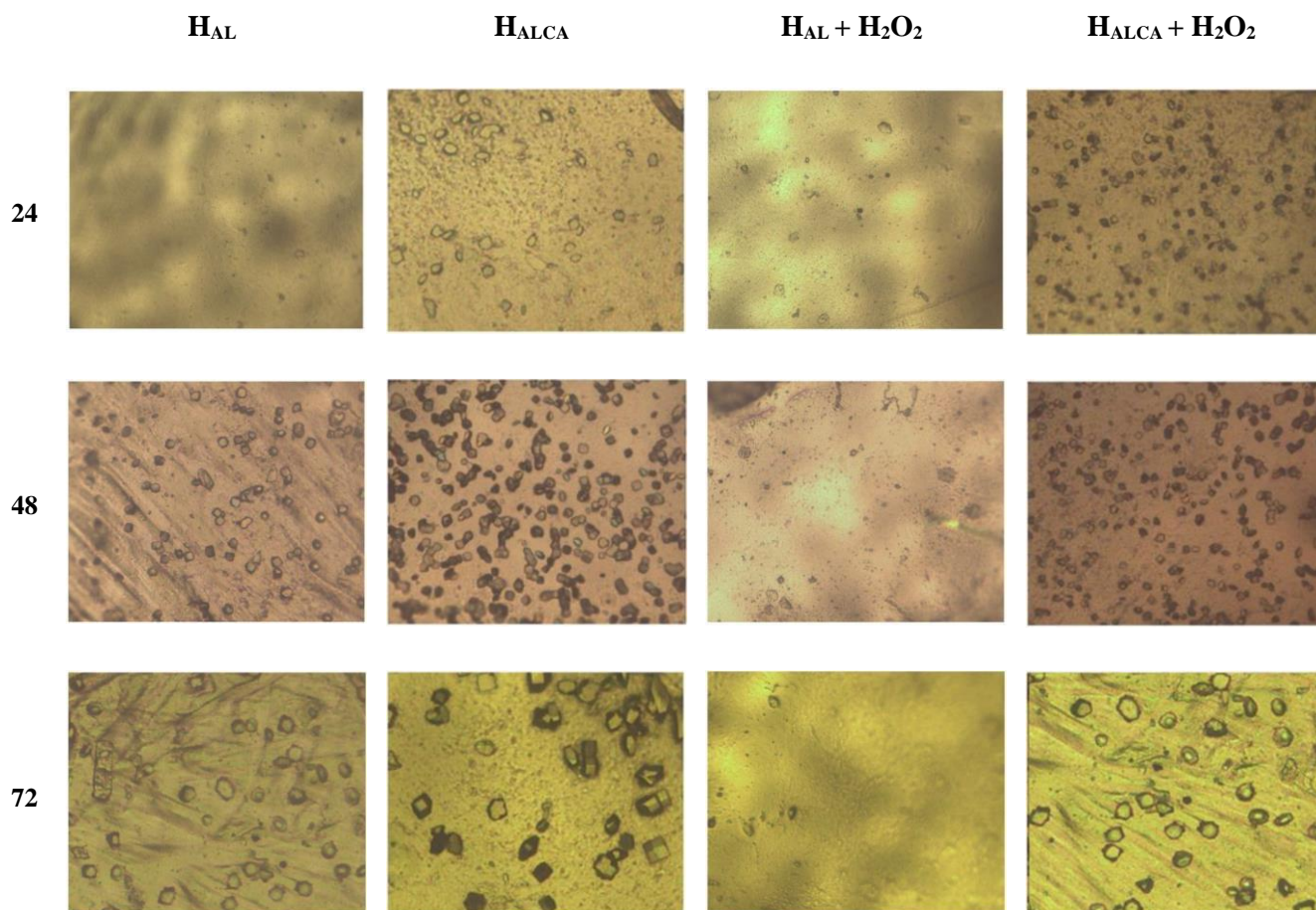


7.4.3 CRYSTALLIZATION STUDIES IN THE PRESENCE OF OXIDATIVE STRESS

In order to demonstrate the efficiency of the polymer support containing the antioxidant CA in the mitigation of radiation damage, a crystallization test was performed on the prepared hydrogel H_{ALCA}.

Radiation damage usually occurs on the protein crystal during X-ray crystallography analysis inevitably affects the structural interpretation of the studied protein. For this purpose, to investigate the effect of CA against the development of free radical species Hydrogen Peroxide (H₂O₂) 30% was added to the crystallization drop. The results are shown in the Table 5 for H_{AL} and H_{ALCA}, respectively.

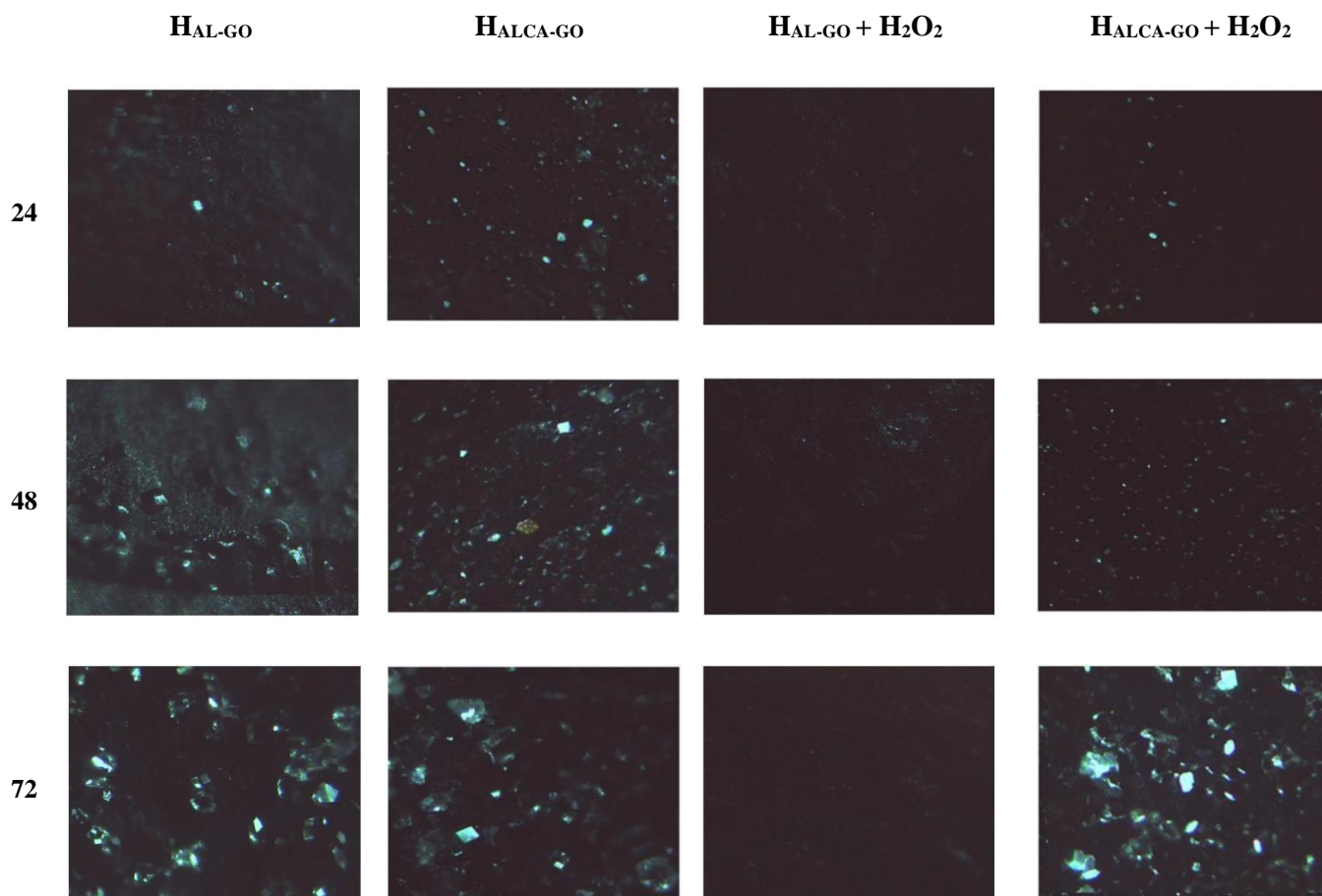
Table 5. Lysozyme crystals on HAL and HALCA both without and in the presence of H₂O₂ at 24, 48 e 72h.



From the comparison of the results obtained it is possible to highlight the antioxidant properties of the H_{ALCA} support in terms of the number and size of the Lysozyme crystals. In fact, in the presence of H₂O₂ on the H_{AL} support without antioxidant functionality, there was no formation of real crystals, but rather structures comparable to "clusters", small molecular aggregates, probably due to oxidative damage to the protein and, thus, the denaturation of its tertiary structure. Instead, the antioxidant action exerted by the residuals of CA in H_{ALCA} contrasted the oxidative stress induced from H₂O₂. Compared to the conditions of absence of oxidative stress, a greater number of small crystals with their characteristic shape was obtained.

The similar results obtained on H_{AL-GO} and H_{ALCA-GO} supports confirmed the validity of the synthetic strategy (Table 6).

Table 6. Lysozyme crystals on HAL-GO and HALCA-GO both without and in the presence of H₂O₂ at 24, 48 e 72h.



7.4.4 DRUG RELEASE EXPERIMENTS

The release profiles were recorded using H_{AL} and H_{AL-*GO*} under two different pH conditions: acid (PBS 0.4M, pH 4.6) and basic (PBS 0.4 M, pH 8.0), in the absence (0V) and in the presence (12, 24, 48 V) of an electric field applied according to Equation 2:

$$\text{Release}(\%) = \frac{M_t}{M_0} \times 100 \quad (2)$$

where M_t represents the proportion of drug released at a certain time t, M₀ represents the proportion of drug charged into the hydrogel.

In detail, the release profiles of Lysozyme H_{AL} in acidic (Figure 5 A) and basic environment (Figure 5 B), clearly proved that the release was faster in basic environment, probably due to the weakening of the hydrogen interactions between the matrix and the protein. At pH 4.6, the system employed about 70 h to complete the release, while at pH 8.0 it reached 100% of lysozyme released in 24 h. In addition, the application of the electric field did not significantly change the release profiles, which appeared comparable to all voltage values

tested. This is in full agreement with the data of S (%), which indicate no significant response to the application of the external electric field.

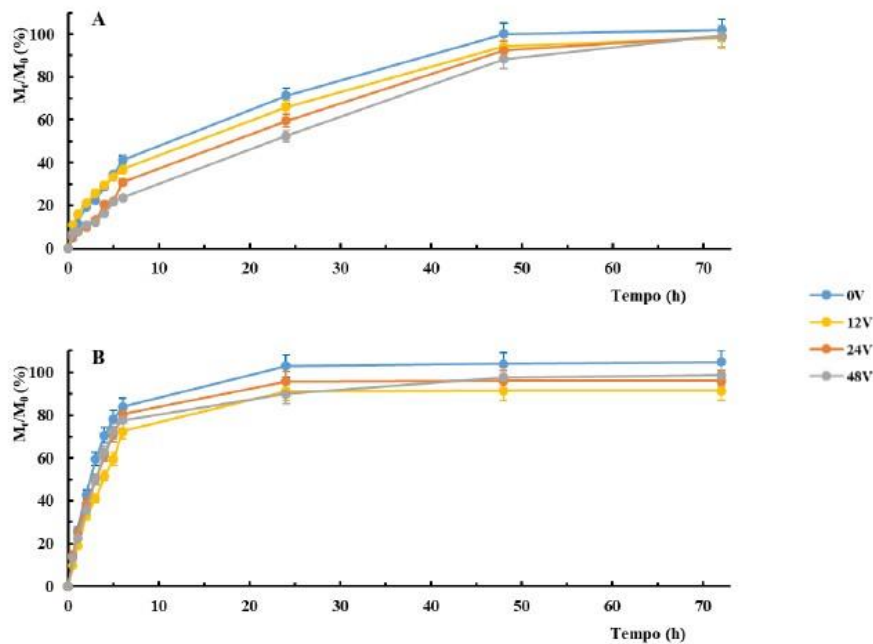


Figure 5. Release profile of HAL at pH 4.6 (A) and 8.0 (B).

Instead, the trend of the release profiles of H_{AL-GO} hydrogel (Figure 6), shown that the presence of the GO changed both the speed and the total amount of protein released, and made possible a modulation of the release as a function of the electric field applied. The predominantly hydrophobic character of the GO determined a lower amount of Lysozyme released, since in addition to the hydrogen bridge interactions also occurred hydrophobic interactions between protein and sp^2 carbons system on the GO surface. In this case the pH variation mainly changed the release rate, while it influenced in a lesser way the total amount of protein released after 72 h, which is equal to 45% at acidic pH and 54% at basic pH.

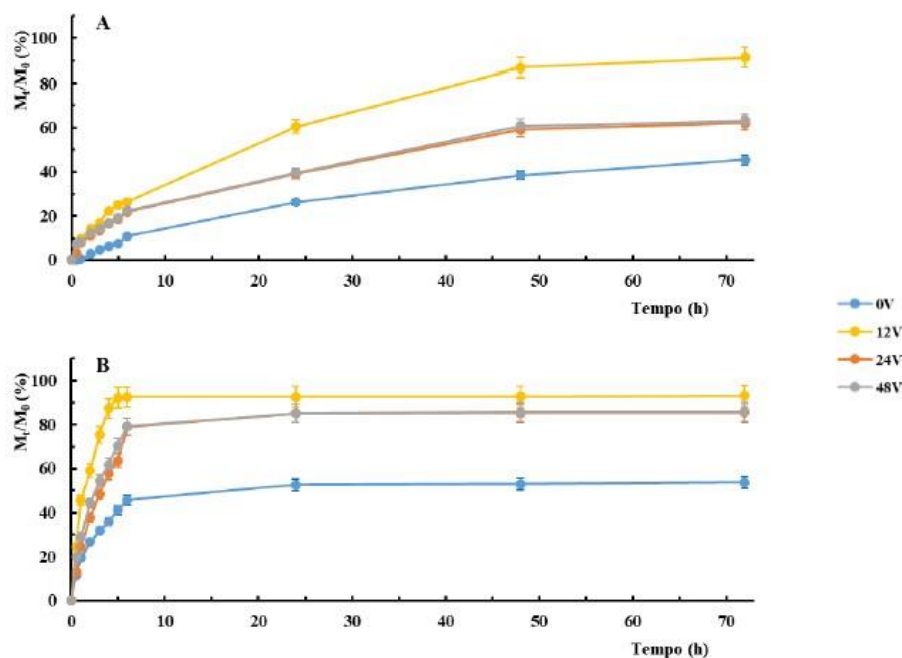


Figure 6. Release profile of HAL-GO at pH 4.6 (A) and 8.0 (B).

Regarding the release rate, after 24 h the amount of Lysozyme released at pH 8.0 is almost twice that released at acidic pH (53% against 25%), to underline that the interaction between the drug and the matrix occurred mainly for hydrophobic interactions and/or through H bonds. The application of an electric field of voltage equal to 12V and current intensity equal to 0.1 A, resulted in a significant change in the release profile at both pH values. At 12V a clear increase in the amount of Lysozyme released by the polymer matrix after 72 h became equal to 91% and 93% at both pH values.

The application of the electric field contributed to the generation of an osmotic pressure responsible for a consequent physical deformation of the hydrogel resulting in an increase in the amount of protein released. The application of higher voltage values resulted in a reduction in the quantity and release rate compared to 12V, although both parameters were higher than those obtained in the absence of electrical stimulation. In this case, in fact, the polarization phenomena of the system prevailed, the introduction of drug-matrix electrostatic interactions opposed the diffusion of lysozyme from the matrix to the release medium.

The results shown that the hybrid system could act as a versatile platform for modulating the release of a drug according to the voltage applied, with the possibility of obtaining three profiles clearly different depending on the intensity of the electric field. This characteristic made the system suitable to meet different therapeutic needs and represented a valid starting point for subsequent investigations to demonstrate its real potential application.

The functionalization of the Alginate hydrogel with the Graphene Oxide has also greatly improved its mechanical properties, in fact the control hydrogel without the functionalization with the GO shown less self-confidence and tends to flake off more easily inside the polymerization reactor.

7.5 CONCLUSION

In the present work a hydrogel based on Alginate in the form of a thin polymeric film was realized, in order to examine its characteristics and potential applications. Through specific modifications to the basic polymeric material, the functionalization with Caffeic Acid on the one hand and with Graphene Oxide on the other one, it was demonstrated the versatility of the proposed system in two potential fields of application related to the world of proteins: protein crystallization and electrosensitive controlled release.

In the protein crystallization process, the synthesized hydrogel was used as support for crystalline growth, appreciating the advantages that a process of crystallization in gel involves. The conjugation of Alginate with Caffeic Acid offered the possibility of creating a hydrogel with antioxidant and protective activity. The antioxidant property of the polymer system can be exploited for the protection of the protein crystal against the radiation damage that, inevitably, happens during the analysis of X-ray crystallography.

Since radiation damage inflicted on crystal during the execution of such analytical procedures results in a biological-structural misinterpretation of the protein, this research activity demonstrated the possibility of creating a polymeric system that could promote the crystallization process having a protective action against protein crystals.

In the field of the Drug-delivery, the introduction of Graphene Oxide in the reaction mixture of the polymer network allowed the realization of a hydrogel in the form of thin polymer film, able to control the release of the protein over time in response to the application of an external electric field.

The electroresponsive hydrogel was able to modulate the release of the loaded drug as a function of two effects due to the application of external voltage:

- i) the variation in the degree of swelling as a result of the establishment of an osmotic gradient within the hydrogel and electrostatic repulsion between the ionized lateral chains of the hydrogel and
- ii) the establishment of electrostatic interactions between the matrix and the drug.

Further experimental investigations will be aimed at demonstrating the possibility of applying the proposed system as a protection agent against oxidative damage induced by X-rays and to modulate the release of lysozyme as an antibacterial agent for biomedical applications, such as the treatment of skin wounds.

REFERENCES

- [1] S.Sugiyama, N.Shimizu, G.Sazaki, M.Hirose, Y.Takahashi, M.Maruyama, H.Matsumura, H.Adachi, K.Takano, S.Murakami, T.Inoue, Y.Mori, *Cryst. Growth Des.* **2013**, *13*, 1899.
- [2] M.S.Smyth, J.H.J. Martin, *Mol. Pathol.* **2000**, *53*, 8.
- [3] E.F.Garman, *Acta Crystallogr. D* **2010**, *66*, 339.
- [4] H.Taberman, *Crystals* **2018**, *8*, 157.
- [5] A.I.Barker, R.J.Southworth-Davies, K.S.Paithankar, I.Carmichael, E.F.Garman, *J. Synchrotron Radiat.* **2009**, *16*, 205.
- [6] M.V.King, *Nature* **1958**, *181*, 263.
- [7] E.F.Garman, T.R. Schneider, *J. Appl. Crystallogr.* **1997**, *30*, 211.
- [8] T.C.Genaro-Mattos, A.Q.Maurício, D.Rettori, A.Alonso, M.Hermes-Lima, *Plos One* **2015**, *10*.
- [9] K.M.M.Espíndola, R.G.Ferreira, L.E.M.Narvaez, A.C.R.S.Rosario, A.H. Machado da Silva, A.G.B.Silva, A.P.O.Vieira, M.C.Moteiro, *Frontiers in Oncology* **2019**, *9*.
- [10] A.Masek, *Int. J. Electrochem. Sc.* **2016**, *11*, 10644.
- [11] O.Vittorio, M.Cojoc, M.Curcio, U.G.Spizzirri, S.Hampel, F.P.Nicoletta, F.Iemma, A.Dubrovskaya, M.Kavallaris, G.Cirillo, *Macromol. Chem. Physic.* **2016**, *217*, 1488.
- [12] M.Curcio, G.Cirillo, P.Tucci, A.Farfalla, E.Bevacqua, O.Vittorio, F.Iemma, F.P.Nicoletta, *Pharmaceuticals* **2020**, *13*, 2.
- [13] G.Cirillo, U.G.Spizzirri, M.Curcio, T.Spataro, N.Picci, F.P.Nicoletta, F.Iemma, *Int. J. Polym. Mater. Po.* **2016**, *65*, 442.
- [14] D.Ege, A.R.Kamali, A.R.Boccaccini, *Adv. Mater. Res-Switz.* **2017**, *19*, 1700627.
- [15] J.R.Luft, J.R.Wolfley, E.H.Snell, *Cryst Growth Des* **2011**, *11*, 651.

CHAPTER 8

8. THE IMPACT OF POLYELECTROLYTES ON THE CRYSTALLIZATION OF LYSOZYME CRYSTALS

8.1. SUMMARY

In this work the impact of different polyelectrolytes on the crystallization of lysozyme, a positively charged protein, was investigated. The crystallization tests of the protein were carried out using coatings of polyelectrolytes and multilayer polyelectrolyte membranes. Two types of polyelectrolytes, poly(acrylic acid) (PAA) and polydiallyldimethyl ammonium chloride (PDADMAC) were used. The surface of polymeric membranes was modified by Layer-by-Layer deposition method. The protein molecules were put in contact with the polyelectrolytes able to promote the heterogeneous nucleation. It was found that the crystallization of lysozyme by the vapor diffusion technique was influenced by the presence of polyelectrolytes positively charged. The growth rate increased when the polyelectrolyte PDADMAC was used. Non-specific attractive and local interactions between the protein and the polyelectrolyte might promote molecular collisions for the formation of the protein crystal nuclei. The results of this preliminary study suggest that there is a proportionality between the amount of polyelectrolyte and crystal growth for which it may become possible to choose the amount of polyelectrolyte to be used to achieve the desired crystal size.

8.2. INTRODUCTION

Since all proteins contain charged amino acids, i.e., aspartate, glutamate, lysine, arginine, and histidine they are considered polyelectrolytes¹ and are charged either positively or negatively depending on the pH of the system. The charged areas on their surface are important for the interaction of the protein with other molecules. The interactions of proteins and charged polyelectrolytes had attracted the interest of scientists' attention in glycobiology, tissue engineering, biosensing, and pharmacology due to their potential applications in different fields such as separations, delivery and wound repair.² Besides, in many applications such as chromatographic separation of proteins, immobilization, biosensors, and design of biocompatible materials for medical applications the interactions of proteins with charged surfaces play a key role.³ Polyelectrolyte films realized by the alternated adsorption of cationic and anionic polyelectrolyte layers represents a simple and promising technique to modify surfaces in a controlled way.^{4,5}

In practice, the Layer-by-Layer (LbL) deposition method involves alternating sequential adsorption of polyelectrolytes, polycations and polyanions, on the surface, that self-organize on a charged surface, leading to the formation of polyelectrolyte multilayer (PEM) films.⁶

Polyelectrolyte multilayer assemblies on material surfaces found application in the field of biomaterials, tissue engineering and biophysics. The possibility to adsorb biomolecules such proteins on an oppositely charged thin layer^{7,8} or to immobilize anti-IgG's within multilayer films⁹⁻¹¹ opens new ways to design biomaterials with specific biological properties. In particular, PEMs have emerged as a powerful tool for the immobilization of biomolecules with preserved bioactivity⁶. PEM films are 2D materials and their surface composition is important because it can affect protein adsorption (depending on the pI of the protein and surface charge of the substrate) and ultimately cell adhesion. In

addition, PEMs may serve as new biomimetic matrices with controlled physical properties and controlled presentation of biochemical moieties, for investigating cell/material or cell/cell interactions.⁶

To date, this technique has allowed, by simple contact, to adsorb on the film a great variety of compounds such as proteins, antibodies,^{7,9,12} dyes,¹³ particles,^{14,15} clay microplates.¹⁶

However, PEMs have not been used before to crystallize macromolecules.

This work aims to investigate the impact of two different polyelectrolytes, poly(diallyldimethylammonium chloride) (PDADMAC) and poly(acrylic acid) PAA, on the crystallization of the model protein lysozyme.

Poly (diallyldimethylammonium chloride) (PDADMAC) is a cationic polyelectrolyte used as an electrolytic solution in a variety of applications such as water purification,¹⁷ drug administration,¹⁸ biomedical systems,¹⁹ and sensors, which include biosensors and chemical sensors.²⁰ Poly(acrylic acid) is an anionic polyelectrolyte which finds numerous application in the development of functional materials and systems²¹⁻²³.

Polyelectrolyte Multilayer Membranes (PEMMs) are prepared on top of a polymeric substrate by dip-coating method, which involves consecutive immersions of the polymeric membrane into oppositely charged polyelectrolytes (PE) solutions for a certain time, followed by a rinsing step to remove excess and weakly adsorbed PE, as depicted in Figure 1.²⁴

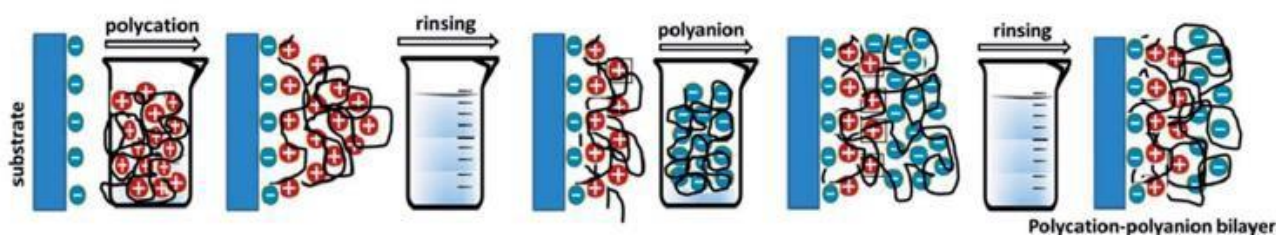


Figure 1. Preparation of PE multilayer membranes by Layer-by-Layer method (dip-coating)²⁴

The interfacial concentration of ions caused by attractive interactions, which promote the crystallization of biomacromolecules²⁵⁻²⁷, suggests that charged polymeric films should be considered as suitable surfaces for protein nucleation.²⁸ The goal of this work is to study the effect of different polyelectrolytes having opposite charge on the crystallization of lysozyme, a positively charged protein. The polyelectrolytes were deposited on polymeric surfaces by LbL deposition method or used as dried polymeric layer and tested as heterogeneous nucleant surfaces. In the latter way the polyelectrolyte molecules are free to interact with the protein molecules present in the crystallization drop.

8.3 MATERIALS AND METHODS

8.3.1 MEMBRANES AND POLYELECTROLYTES

Two types of polymeric membranes were used as support of layer-by-layer system in this work: hydrophobic Polyvinylidene difluoride (PVDF, disks with a diameter of 47 mm, a porosity of 70%, and a mean pore size of 0.10 μm) purchased from Durapore[®] and Hydrophilic Polyethersulfone (PESH, UH050P) purchased from Nadir. In Table 1 the isoelectric point (IEP) of used membranes, the pH at which the positive and negative charges exactly balance so that the membrane can be considered uncharged²⁹ are reported.

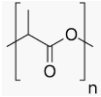
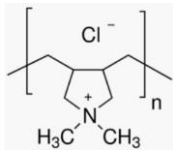
Table 1. Isoelectric point of membranes

Membrane	IEP	Ref
Hydrophilic Polyethersulfone	3 – 2.8 – 2.1	30,31

PESH		
Polyvinylidene fluoride	3 – 3.5	31-34
PVDF		

Poly(acrylic acid) (PAA, average Mw 1800, cod. 323667) and Poly(diallyldimethyl ammonium chloride) (PDADMAC solution having average Mw 200,000-350,000, 20 wt. % in H₂O, cod. 409014) were obtained from Sigma Aldrich. In Table 2 the molecular structures and the pKa value (which is the pH at which 50% of the polymer's functional groups are ionized) of used polyelectrolytes are reported.

Table 2. Polyelectrolytes chemical structure and pKa.

PE	PE type	Structure	pKa	Ref.
PAA Poly(acrylic acid)	polyanion		~4.5 PAA becomes ionized above its pKa value of 4.7. The PAA is fully ionized at high pH values (pH 9.5 or pH 10), and almost completely deionized at pH 4.	35,36 37
PDADMAC Polydiallyldimethylammonium chloride	polycation		PDADMAC, a poly(quaternary ammonium), is charged at all pH values.	38

PAA and PDADMAC were dissolved in TRIS buffer pH =7.5 at the concentration of 1 g L⁻¹. At this pH value the carboxylic groups in PAA are deprotonated and negatively charged³⁹, whereas PDADMAC is positively charged³⁸. The molarity of the buffer was 0.1 M for PAA and 1 mM for PDADMAC.

8.3.2 MONOLAYER AND MULTILAYER MEMBRANES PREPARATION

PESH membranes were initially soaked in deionized water for about 24 h, during which the water was replaced several times. The activation of hydrophobic PVDF is achieved by wetting the membrane with a short treatment in ethanol, which increases the hydrophilic degree of the membrane. PESH and PVDF membranes were soaked in the polyelectrolyte solutions for 1 h in a vertical position. Then, they were washed in a large amount of buffer.

For the preparation of bilayer multilayered membranes, PESH and PVDF were alternately immersed into 1 g/L PDADMAC and 1 g/L PAA for 30 min. After each deposition step, the membranes were taken out and rinsed for 3 min with the buffer solution of the corresponding polyelectrolyte. Rinsing should remove any loosely bound polyelectrolytes. Thus, one bilayer of self-assembly membrane was completed. The adsorption procedure was repeated 2 times for bilayer

membrane and 10 times for the multilayer one. A schematic representation of the preparation procedure of multilayer samples is reported in Figure 2.

Since PESH membranes are negatively charged (IEP= 2.1) at pH 7.5, the first layer adsorbed on its surface was a polycation. ⁴⁰⁻⁴²

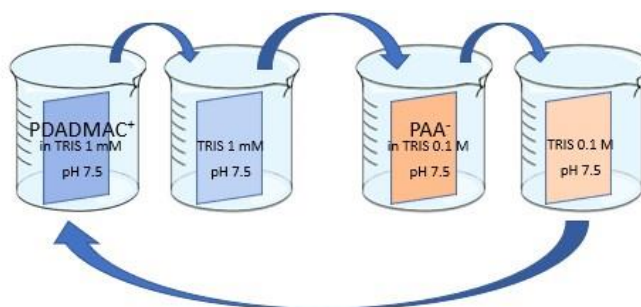


Figure 2. Preparation of PAA⁻/PDADMAC⁺ multilayer membrane.

8.3.3 PREPARATION OF POLYMERIC LAYERS

During the crystallization tests the protein drop was put in contact with the polyelectrolyte on the membrane surface and the heterogeneous nucleation may take place thanks to the contributions of the surface and the polyelectrolyte bound on it, Figure 3 a. However, if the bond of the polyelectrolyte with the membrane surface is not stable, it is possible that the protein interacts with the polyelectrolyte dissolved in the crystallization drop, Figure 3 b.

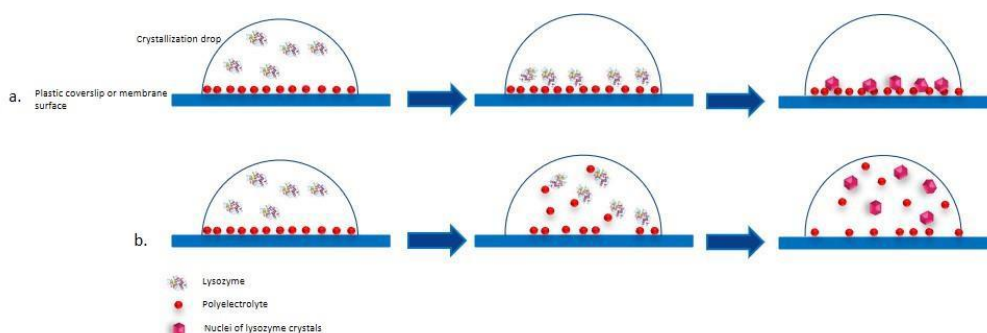


Figure 3. After the deposition of the drop on the cover slip or membrane surface, a. the protein interacts with the polyelectrolyte and binds on the surface. The heterogeneous nucleation takes place on the surface; b. the protein molecules interact with the polyelectrolyte dissolved in the drop.

In this regard, the effect of the polyelectrolytes in the crystallization drops was investigated preparing four different aqueous polymeric solutions of PDADMAC and PAA.

Polymeric layers were prepared using polymeric solutions of PAA and PDADMAC in water at 1%, 5%, 10% and 20% w/v concentration. For each polymer solution 10 μ l aliquots were manually pipetted onto the sample wells of the crystallization plate, in triplicate for reproducibility. The solvents of the polymer solution drops were left to evaporate completely at room temperature (20 °C) overnight. In the figure 4 is reported a schematic representation of the polymeric layer preparation. The polyelectrolyte was not bind on the surface and during the crystallization test it may dissolve in the drop interacting with the protein, reproducing the condition reported in the Figure 3 b.

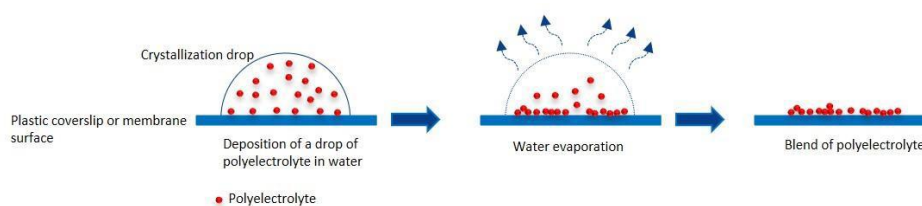


Figure 4. Preparation of polymeric layer.

This procedure was performed to prepare the bilayers PAA-PDADMAC and PDADMAC-PAA.

8.3.4 CRYSTALLIZATION EXPERIMENTS

Chicken hen egg white lysozyme (HEWL, cod. 62970) purchased from Sigma-Aldrich was used for the crystallization experiments. Sodium Chloride (NaCl, 7 wt%, cod. 131659.1211, from Panreac), dissolved in the same buffer, was used as stripping solution for HEWL. HEWL is a positively charged protein and its properties are resumed in the Table 3.

Table 3. Lysozyme properties.

Protein	Mw (kDa)	Isoelectric point	Net charge
Lysozyme	14.3	11.3	Positive at pH 7.4

Lysozyme solution at the initial concentration of 10 mg mL^{-1} prepared in sodium acetate buffer was mixed 1:1 volume ratio with the stripping solution. Crystallization tests were carried out by using 15-well plates (from Qiagen) conventionally used for the vapor diffusion technique and adapted for membrane-assisted crystallization experiments in hanging drop mode. The setup consisted of a $10 \mu\text{L}$ drop (equal volumes of protein and stripping solutions) placed on a membrane piece ($\sim 1 \text{ cm}^2$) fixed on the cap by double sided tape, and 1 mL of stripping solutions as reservoir. The crystallization tests were carried out at $20 \text{ }^\circ\text{C}$ with three replications for each condition to test the reproductively of the results. Crystallization trials were also carried out by using the untreated membrane and the conventional plastic coverslips as templates, for reference. Crystal growth was monitored at regular times through a stereomicroscope (Nokia AZ100) equipped with a video camera.

The final concentration of each crystallization drop was the following:

- Lysozyme 5 mg/ml
- Sodium chloride 3.5 wt %
- Sodium acetate buffer 0.1 M

The crystallization trials were performed on LbL membranes and on polymeric layers. The goal was to study the impact of polyelectrolyte on the growth rate of lysozyme crystals.

The hanging protein crystallization drop was deposited both on mono and multilayer LbL membranes and on the dry layer of polyelectrolyte prepared according to the method described in the Figure 4. Alternating layer of PAA and PDADMAC were deposited also on the inert plastic coverslip used as reference to evaluate the effect of the polyelectrolytes on the crystallization excluding the contribution of membrane surfaces.

8.4 RESULTS AND DISCUSSION

8.4.1 CRYSTALS ON LBL MEMBRANES

The crystallization tests were performed on monolayer and multilayer membranes prepared by LbL method. The crystal growth was followed over time by optical microscopy. It was not possible to observe and analyze crystals on monolayer

and multilayer PESH-PAA membranes because the crystallization drop dried a few minutes after the deposition on the membrane surface.

In the Figure 5, the number and length crystals after 24 h are compared. It is possible to observe that the polyelectrolyte PDADMAC monolayer had a slight positive effect on the growth of crystals compared to the unmodified PESH membrane, but not on their number (Figure 5a). The monolayer of PDADMAC had a positive effect on the general growth rate of the crystals, as shown in the Figure 5b. Crystals growth on PVDF membrane functionalized with the polyelectrolyte PDADMAC reached a larger size. In particular, the crystals on monolayer PVDF-PDADMAC and on multilayer PVDF-PDADMAC ending, after only 24 h of crystallization test were 43 μm and 66 μm , respectively. However, the presence of polyelectrolyte mono and multilayer had no effect on the growth rate of crystals.

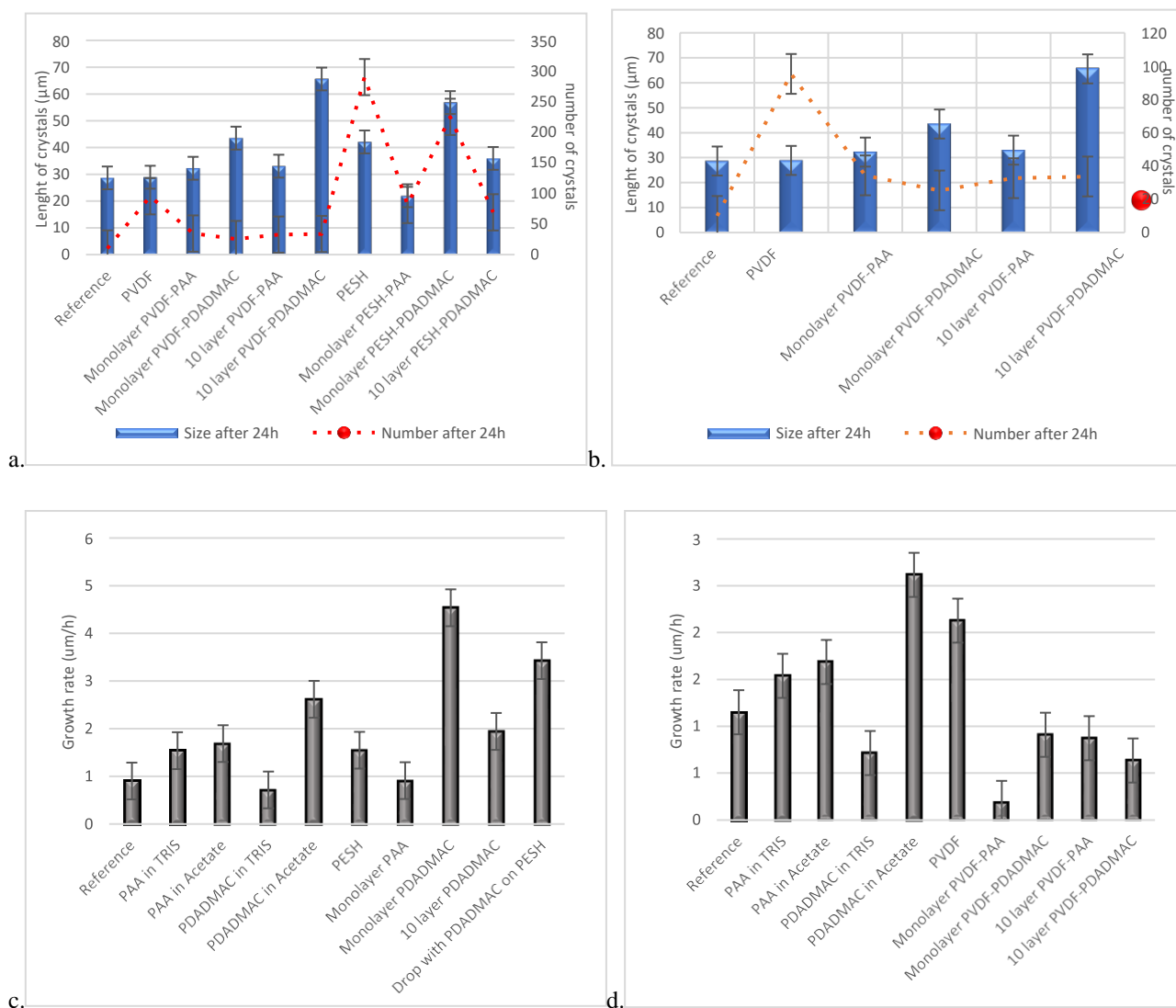


Figure 5. a. and b. Comparison between number and length crystals after 24h; b. and c. Growth rate of crystals on prepared PESH and PVDF membranes, respectively.

8.4.2 CRYSTALS ON POLYMERIC LAYERS OF PAA AND PDADMAC

The impact of polyelectrolyte coating on the crystallization of lysozyme was evaluated. The crystallization drops were deposited on the top of the dried polymeric coating and left equilibrating with the stripping solution in a closed system at 20°C. The experiments were performed in adapted crystallization well plates and followed over time by optical

microscopy. All sample wells containing PAA layers turned opaque when protein and buffer solutions were deposited onto them. No crystals appeared on PAA 20% and 10% layers. On PAA 1% and 5% layers crystals appeared after a longer time of 6 h and 20 h, respectively. Before then it was possible to observe a cloud made of thousands of little nuclei as shown in Figure 6.

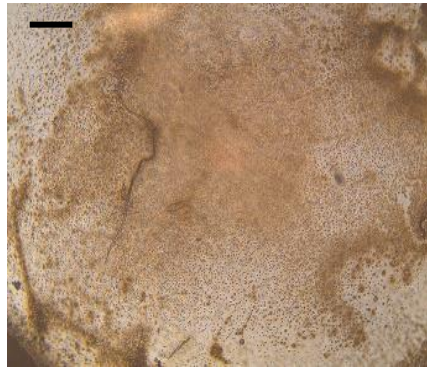


Figure 6. Crystals on PAA 5% before 20h, unit bar 200 μm .

Figure 7 shows the evolution of the length of crystals as a function of time for polymeric coatings of PAA and PDADMAC.

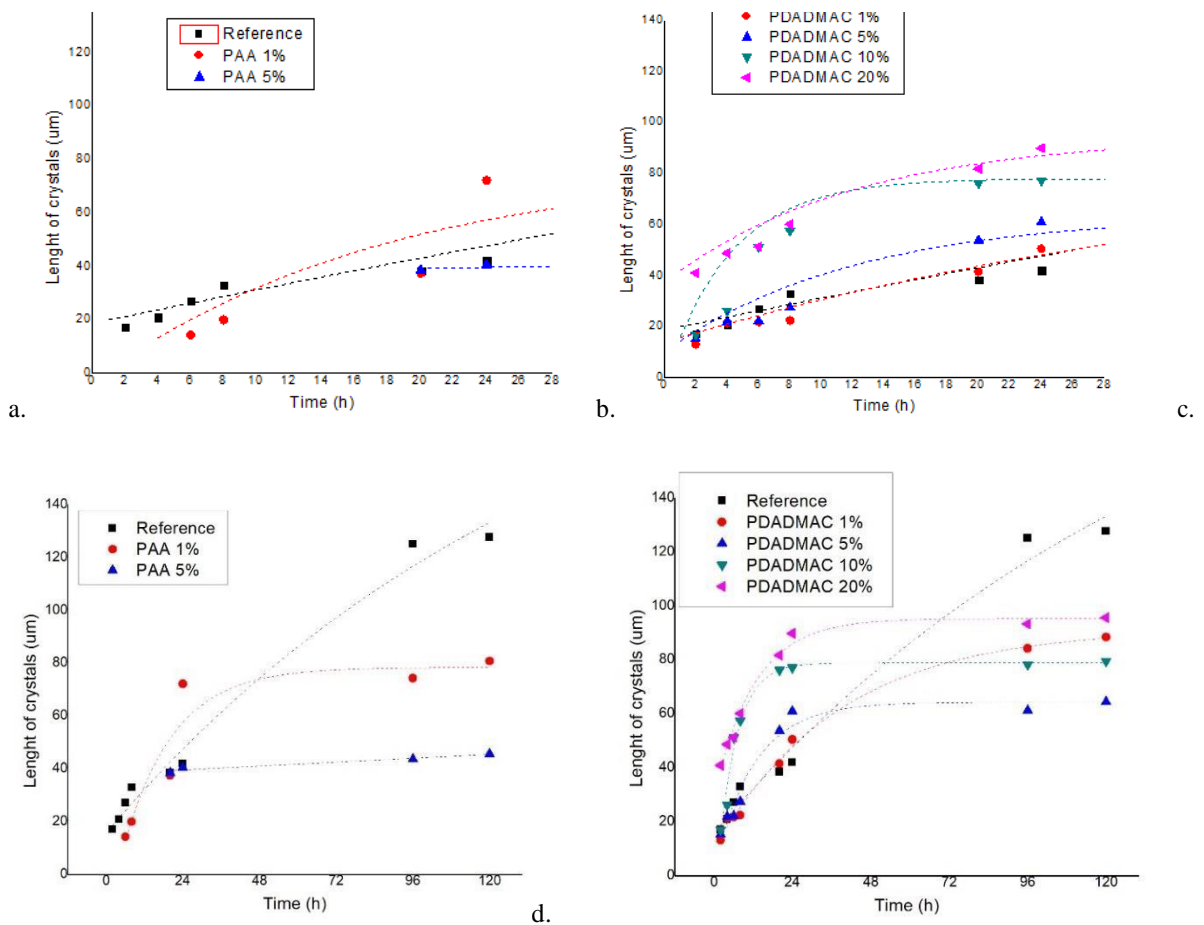


Figure 7. Length of crystals observed versus time for a., c. PAA and b., d. PDADMAC polymeric coating.

The presence of the electrolytes influenced the growth rates profiles leading to a faster growth rate in the initial 24 h followed by a stabilization of the crystal dimension in the following period, as shown in the Figure 7 c. and d. The position of the plateau was dependent on the concentration of used polyelectrolyte, i.e. bigger crystals were reached as the concentration of the polyelectrolyte increased.

In order to obtain a faster crystallization process the use of polyelectrolytes may be advantageous. In standard conditions, approximately 72 h was required to obtain the size of the crystals obtained in only 24 h in the presence of 20% of the polyelectrolyte PDADMAC. It is important to note that there is a difference of size crystals growth rate in the first 24 hours of the crystallization test, as shown in the Figure 8. In this time frame samples PDADMAC 20% and 10% shown an important growth rate respect to other samples and the reference.

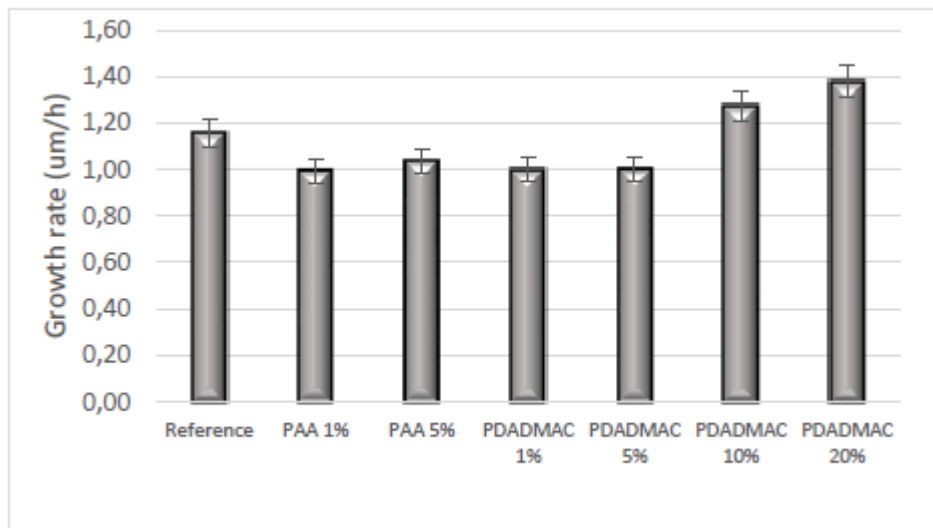


Figure 8. Growth rate of crystals on prepared polyelectrolyte layers.

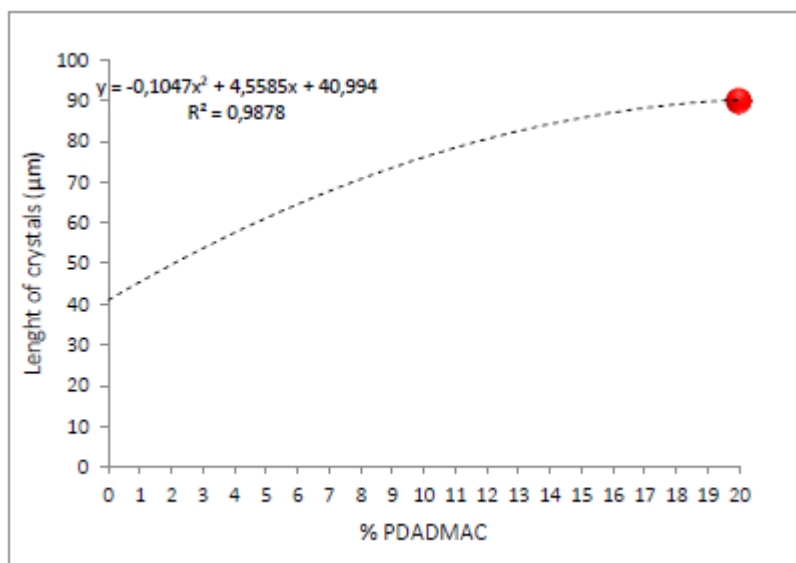


Figure 9. Length of crystals observed versus % PDADMAC.

The crystal size after 24 h versus the used percentage of PDADMAC is analyzed in Figure 9 with the aim of determining the dependence of the crystal dimension on the amount of PDADMAC and allowing to predict the final crystal size as function of the used amount of polyelectrolyte. In this way, it became possible the selection of the exact amount of the polyelectrolyte PDADMAC according to the desired crystal size.

8.5 CONCLUSION

It can be concluded that the use of cationic polyelectrolyte in the form of layer or deposited on polymeric layer by LbL method are suitable for protein crystallization. Crystals of different size can be obtained on these films at lower protein concentration and with shorter crystallization times than those required with the siliconized coverslips. However, the mechanism of proteins–polyelectrolyte interaction is still an open field of research in which much more experimental work is needed. The crystallization of lysozyme by the vapor diffusion technique was influenced by the presence of polyelectrolytes positively charged. The growth rate increased when the polyelectrolyte PDADMAC was used. Non- specific attractive and local interactions between the protein and the polyelectrolyte might promote molecular collisions for the formation of the protein crystal nuclei. The results of this preliminary study suggest that there is a proportionality between the amount of polyelectrolyte and crystal growth for which it may become possible to choose the amount of polyelectrolyte to be used to achieve the desired crystal size. The use of polyelectrolyte should be useful for crystallization of proteins from solutions at low concentration and for protein with very long crystallization times.

REFERENCE

- [1] P.J. Butterworth, *Lehninger: principles of biochemistry* (4th edn) (Eds. D. L. Nelson and M. C. Cox), W. H. Freeman & Co., New York, **2004**.
- [2] A.B. Kayitmazer, D. Seeman, B.B. Minsky, P.L. Dubin, Y. Xu, *Soft Matter* **2013**, *9*, 2553.
- [3] A. Steudle, J. Pleiss, *Biophys J* **2011**, *100*, 3016.
- [4] G. Decher, J.D., Hong, J. Schmitt, *Thin Solid Films* **1992**, *210*, 831.
- [5] G. Decher, *Science* **1997**, *277*, 1232.
- [6] V. Gribova, R. Auzely-Velty, C. Picart, *Chemistry of Materials* **2012**, *24*, 854.
- [7] Y. Lvov, K. Ariga, I. Ichinose, T. Kunitake, *Journal of the American Chemical Society* **1995**, *117*, 6117.
- [8] S. Guedidi, *Enzyme and Microbial Technology* **2012**, *51*, 325.
- [9] F. Caruso, K. Niikura, D.N. Furlong, Y. Okahata, *Langmuir* **1997**, *13*, 3427.
- [10] C.G. Kelly, *Nature biotechnology* **1999**, *17*, 42.
- [11] F. Caruso, D.N. Furlong, K. Ariga, I. Ichinose, T. Kunitake, *Langmuir* **1998**, *14*, 4559.
- [12] S.W. Keller, H.-N. Kim, T.E. Mallouk, *Journal of the American Chemical Society* **1994**, *116*, 8817.
- [13] I. Ichinose, K. Fujiyoshi, S. Mizuki, Y. Lvov, T. Kunitake, *Chemistry Letters* **1996**, *25*, 257.
- [14] T. Cassagneau, T.E. Mallouk, J.H. Fendler, *Journal of the American Chemical Society* **1998**, *120*, 7848.
- [15] Y. Lvov, K. Ariga, M. Onda, I. Ichinose, T. Kunitake, *Langmuir* **1997**, *13*, 6195.
- [16] K. Ariga, Y. Lvov, I. Ichinose, T. Kunitake, *Applied Clay Science* **1999**, *15*, 137.
- [18] Q. Yang, *Chemistry of Materials* **2005**, *17*, 5999.
- [19] Y. Qiu, *Biomaterials* **2010**, *31*, 7606.
- [20] X. Zhang, *Journal of the American Chemical Society* **2004**, *126*, 3064.
- [21] Y.-H. Chiao, *Polymers-Basel* **2020**, *12*.
- [22] X. Xu, *Colloids and Surfaces B: Biointerfaces* **2020**, *194*, 111206.
- [23] I. Merino-Garcia, F. Kotoka, C. Portugal, J. Crespo, S. Velizarov, S. *Membranes* **2020**, *10*, 134.
- [24] N. Joseph, P. Ahmadiannamini, R. Hoogenboom, I.F.J. Vankelecom, *Polym Chem-Uk* **2014**, *5*, 1817.
- [25] L. Addadi, J. Moradian, E. Shay, N.G. Maroudas, S.A. Weiner, *Proceedings of the National Academy of Sciences* **1987**, *84*, 2732.
- [26] G. Falini, S. Albeck, S. Weiner, L. Addadi, *Science* **1996**, *271*, 67.
- [27] G. Falini, S. Fermani, M. Gazzano, A. Ripamonti, *Chemistry – A European Journal* **1997**, *3*, 1807.

- [28] S. Fermani, G. Falini, M. Minnucci, A. Ripamonti, *Journal of Crystal Growth* **2001**, 224, 327.
- [29] A. Bandyopadhyay, in Book Review Water Quality Engineering: Physical/Chemical Treatment Processes (Eds. M.M. Benjamin, D.F. Lawler) Wiley, Hoboken, NJ, USA, **2013**.
- [30] S. Mozia, A. Grylewicz, M. Zgrzebnicki, D. Darowna, A. Czyzewski, *Polymers-Basel* **2019**, 11, 671.
- [31] A. Marszałek, J. Bohdziewicz, G. Kamińska, K. Wojciechowski, *Environment Protection Engineering* **2016**, 42, 197.
- [32] D. Breite, M. Went, A. Prager, A. Schulze, *Polymers-Basel* **2015**, 7, 2017.
- [33] A. Schulze, M. Went, A. Prager, *Materials* **2016**, 9, 706.
- [34] D.M. Davenport, M.H. Gui, L.R. Ormsbee, D. Bhattacharyya, *Polymers-Basel* **2016**, 8, 32.
- [35] J. Goicoechea, F.J. Arregui, J.M. Corres, I.R. Matias, *Journal of Sensors* **2008**, 7.
- [36] J. Choi, M.F. Rubner, *Macromolecules* **2005**, 38, 116.
- [37] M. Wiśniewska, T. Urban, E. Grządka, V.I. Zarko, V.M. Gun'ko, *Colloid Polym Sci* **2014**, 292, 699.
- [38] J.A. Jaber, J.B. Schlenoff, *Langmuir* **2007**, 23, 896.
- [39] D.S. Salloum, J.B. Schlenoff, *Biomacromolecules* **2004**, 5, 1089.
- [40] J. Kochan, T. Wintgens, J.E. Wong, T. Melin, *Desalination* **2010**, 250, 1008.
- [41] F.E. Jurin, *Colloid Surface A* **2015**, 486, 153.
- [42] R. Malaisamy, M.L. Bruening, *Langmuir* **2005**, 21, 10587.

PART IV

INTRODUCTION

The ever-expanding number of therapeutic proteins, including antibodies, cytokines, enzymes, hormones and growth factors, led the research to investigate on the possibility to formulate safe, stable and efficacious formulation that can be delivered in a patient-friendly manner.¹

Protein-based therapeutics, especially monoclonal antibodies (mAbs), have become a key driver in the pharmaceutical industry. They are a large growing class of drugs in a continuous development and represent an integrated part of treatment of life-threatening conditions including cancer, leukaemia, autoimmune disorders, inflammatory, cardiovascular, respiratory, and infectious diseases.

Generally, mAb-based therapies require high doses in the range of hundreds of milligrams to a gram per dose to reach the desired therapeutic concentration. As required by FDA, subcutaneous injections of mAbs are preferred over intravenous administrations from patient compliance. To administer such a high dose range in a small volume, typically less than 1.5 mL, by the subcutaneous route, mAb formulations need to be prepared at a concentration greater than 100 mg/mL.²

However, a highly concentrated mAb preparation could have adverse effects due to the increased viscosity, which can favor the formation of aggregates, the alteration of biological activity and the onset of immunogenic reactions. To overcome these formulation challenges, proteins can be developed in their crystallized forms. Crystalline suspensions guarantee highly concentrated formulations with low viscosity, small volume and increased stability. In fact, it has been demonstrated that highly concentrated crystalline suspensions do not show the large increase in viscosity observed in solution. In addition, biomolecules are usually more stable in crystal form than in solution, a feature that is crucial in the case of samples that easily degrade, such as protein molecules.³ Physical and chemical degradation may be significantly reduced for proteins in the crystalline form, thus the physical, chemical and biological integrity of the therapeutic agent in the lattice structure are protected during processing and storage and after delivery.⁴

Unfortunately, in the case of complex biomacromolecules such as mAbs, crystallization is not a trivial process and a thorough understanding of protein aggregation behavior in solution and an accurate study of optimal conditions are necessary.⁵ In fact, it is important to consider that protein structures are dynamic rather than static and the role of the solvent and the environmental conditions such as pH, ionic strength and temperature are essential since protein conformation and interactions depend on them.⁶ The state diagram of protein-solvent systems can provide indications about the phase behaviour of biomacromolecules and their stability in solution, but the intimate mechanism underlying protein nucleation and crystal growth remains elusive and needs to be investigated.

REFERENCES

- [1] S.K. Basu, C.P. Govardhan, C.W. Jung, A.L. Margolin, *Expert opinion on biological therapy* **2004**, *4*, 301.
- [2] B. Bittner, W. Richter, J. Schmidt, *BioDrugs* **2018**, *32*, 425.
- [3] H. Yang, B.D. Belviso, X. Li, W. Chen, T.F. Mastropietro, G. Di Profio, R. Caliandro, J.Y.Y. Heng, *Crystals* **2019**, *9*, 230.
- [4] B. Shenoy, Y. Wang, W. Shan, A.L. Margolin, *Biotechnol. Bioeng.* **2001**, *73*, 358.
- [5] H. Yang, W. Chen, P. Peczulis, J.Y.Y. Heng, *Cryst. Growth Des.* **2019**, *19*, 98.
- [6] Y.H. Kuo, Y.W. Chiang, *ACS Central Science* **2018**, *4*, 645.

CHAPTER 9

9. ON THE AGGREGATION AND NUCLEATION MECHANISM OF THE MONOCLONAL ANTIBODY ANTI-CD20 NEAR LIQUID-LIQUID PHASE SEPARATION (LLPS)

Published as: E. Pantuso, T.F. Mastropietro, M.L. Briuglia, *et al.* On the Aggregation and Nucleation Mechanism of the Monoclonal Antibody Anti-CD20 Near Liquid-Liquid Phase Separation (LLPS). *Scientific Report* 2020, 10, 8902. <https://doi.org/10.1038/s41598-020-65776-6>

9.1. SUMMARY

The crystallization of Anti-CD20, a full-length monoclonal antibody, has been studied in the PEG400/Na₂SO₄/Water system near Liquid-Liquid Phase Separation (LLPS) conditions by both sitting-drop vapour diffusion and batch methods. In order to understand the Anti-CD20 crystallization propensity in the solvent system of different compositions, we investigated some measurable parameters, normally used to assess protein conformational and colloidal stability in solution, with the aim to understand the aggregation mechanism of this complex biomacromolecule. We propose that under crystallization conditions a minor population of specifically aggregated protein molecules are present. While this minor species hardly contributes to the measured average solution behaviour, it induces and promotes crystal formation. The existence of this minor species is the result of the LLPS occurring concomitantly under crystallization conditions.

9.2. INTRODUCTION

A thorough understanding of protein aggregation behaviour in solution is crucial for the controlled manufacture and formulation of therapeutics and for the development of crystallization-based purification strategies for biological drugs¹⁻⁴. Unfortunately, while the state diagram of protein-solvent systems can provide indications about the phase behaviour of biomacromolecules and their stability in solution, the intimate mechanism underlying protein nucleation and crystal growth have not been fully understood yet and, in many cases, it remains elusive. Protein aggregation is directly related to protein-protein interactions and may be strongly related to protein crystallization behaviour⁵. Since different types of intermolecular forces are involved in protein interactions, such as electrostatic, van der Waals and hydrophobic⁶, environmental factors like pH, ionic strength and the presence of additives, can drastically alter the intermolecular interaction profile of proteins in solution^{7,8}.

Colloidal and conformational stabilities are the two main factors that govern the existence of a protein aggregate in a solution^{9,10}. Colloidal stability is a delicate balance between repulsive and attractive forces between proteins, while conformational stability is related to the free energy difference between two molecular

states, folded and partially or totally unfolded. Several investigations have found that the melting temperature (T_m) and the osmotic second virial coefficient (B_{22}) can respectively account for the protein conformational¹¹ and colloidal¹² stability. Both T_m and B_{22} can be experimentally determined by using correspondingly Dynamic Light Scattering (DLS) and Static Light Scattering (SLS) methods¹³. Aggregation induced by thermal unfolding can be monitored by measuring the average hydrodynamic diameter value as a function of temperature, while B_{22} describes the first deviation from ideal behaviour of dilute colloidal solutions¹⁴. A positive or negative value of B_{22} accounts for a net repulsive or attractive interaction balance, respectively, and could therefore be used to predict stable, crystallizing or precipitating protein solution conditions. According to the experimental crystallization slot of George and Wilson¹⁵, a protein solution would be: stable if $B_{22} > -0.8 \times 10^{-4} \text{ mL mol g}^{-2}$; crystallizing if $-8.4 \times 10^{-4} < B_{22} < -0.8 \times 10^{-4} \text{ mL mol g}^{-2}$; precipitating if $B_{22} < -8.4 \times 10^{-4} \text{ mL mol g}^{-2}$. Haas and Drenth¹⁶ postulated a modified crystallization slot, ranging from -0.9×10^{-4} to $-0.35 \times 10^{-4} \text{ mol mL g}^{-2}$ for protein with a molecular size as high as 140 kDa.

The Z-potential is another indicator of colloidal stability, which measures the magnitude of the electrostatic or charge repulsion/attraction between particles¹⁷. It is related to the surface charge of the molecules, the adsorbed layer at the interface and the nature and composition of the surrounding environment. A large Z-potential value ($|Z\text{-potential}| > 30 \text{ mV}$) can be considered an indicator of colloidal stability. Recently, the use of the interaction parameter k_d has been also suggested as a more high-throughput means to quantify protein-protein interactions^{18,19}.

In this work, we focus on the relationships between the crystallization propensity of Anti-CD20 in the $\text{Na}_2\text{SO}_4/\text{PEG400}$ solvent system of different compositions and its relation with some measurable parameters normally used to assess protein conformational and colloidal stability in solution, with the aim to understand the aggregation mechanism of this complex biomacromolecule. Anti-CD20 is a full-length monoclonal antibody (mAb) and it is a therapeutic protein extensively used for treatment of chronic lymphocytic leukaemia and non-Hodgkin's lymphoma, which is commercialized with the brand name of Rituxan or Mabthera. Here, the crystallization of this biomolecule has been observed in a $\text{PEG400}/\text{Na}_2\text{SO}_4/\text{Water}$ system near Liquid-Liquid Phase Separation (LLPS) conditions by both vapour diffusion and batch methods. LLPS is a very common phenomena for monoclonal antibodies²⁰ and is of great interest because the factors which induce the separation of protein solutions into coexisting protein-poor and protein-rich phases are observed to play a central role in protein interaction and crystallization²¹. For several protein/PEG or protein/salt systems both the LLPS and the aggregation propensity of proteins in solution have been shown to coincide with net attractive interactions between molecules²²⁻²⁴. Monte Carlo simulations performed on systems that undergo phase separation demonstrated that the interactions between the proteins fall into the short-range regime and are strongly anisotropic²⁵. Over time, the anisotropic interactions may be responsible for the evolution of the system from the phase separation to reversible aggregation conditions. In this situation, the LLPS has been speculated to behave as a metastable state towards nucleation²⁶⁻²⁸. In fact, the pathway for the formation of crystal nuclei drastically changes near the metastable low density-high density liquid region coexistence, with the free-energy barrier for crystal nucleation being strongly reduced. In this scenario, the crystal nucleation

rate increases by many orders of magnitude over that predicted from classical nucleation theory ²⁸, thus generating a fast and diffuse crystallization that often results in poor-quality crystals.

The results of this investigation allowed us to gain further insights into the mechanism governing the nucleation-crystallization of a complex system such as the Anti-CD20 mAb.

9.3. MATERIALS AND METHODS

Anti-CD20 crystallization experiments. Anti-CD20 monoclonal antibody (MW = 144.5 kDa) was kindly provided by FUJIFILM Diosynth Biotechnologies (Billingham, UK) at high level of purity (>98% HPLC, >95% SDS-PAGE) in 0.025 M sodium citrate buffer at pH 6.5 and 0.154 M sodium chloride solution. Sodium sulphate anhydrous (purity \geq 99.99%), PEG400, HEPES (purity \geq 9.5%), TRIS (purity \geq 99.5%), magnesium chloride hexahydrate (\geq 99%) and NaOH (purity \geq 98%), from Sigma-Aldrich (Italy), were used without further purification. MilliQ water was used to prepare all solutions. Anti-CD20 was thawed for 2–3 hours in an 8 °C water bath before buffer exchange with HEPES 0.1 M and concentration by Amicon Ultra centrifugal filter tube (Ultra-4, cutoff 10 kDa, from Merck) at 6,000 g and 8 °C. Finally, the protein solution was diluted to the desired concentration by adding HEPES buffer 0.1 M. NaOH 1 M was used to adjust the pH to the desired value. The Anti-CD20 concentration was determined by measuring protein absorbance at 280 nm by UV-Vis spectrophotometer (extinction coefficient at 280 nm 237,380 M⁻¹ cm⁻¹).

Protocols suitable for crystallizing Anti-CD20 reproducibly by vapour diffusion and batch methods were developed in previous works^{29,30}. Precipitant solutions were made by dissolving sodium sulphate in the HEPES buffer solution containing PEG400 at the proper concentration. All solutions were filtered through a 0.22 μ m Anotop 10 Filter Unit (Whatman). In sitting-drop vapour diffusion crystallization experiments, drops made of 10 μ L of precipitant solution and 10 μ L of protein solutions were equilibrated in a sealed well against 1 mL of a hypertonic solution of MgCl₂·6H₂O 30 wt.% used as reservoir. For the batch crystallization experiments, a volume of protein solutions having a certain initial concentration was mixed with the required volume of precipitant solution to obtain a supersaturated solution of known composition (final volume 1 mL). All crystallization experiments were performed in a vibration-free refrigerator at 20 °C.

Analysis of Anti-CD20 crystals. Crystals obtained from crystallization experiments were observed using an optical microscope (Eclipse LV 100ND, Nikon Instruments, Italy) equipped with a video camera, separated from the mother liquor by using a centrifuge (MiniSpin Plus Eppendorf model IVD) and centrifuge tubes (0.22 μ m pore size) and extensively washed. Washing solution was made by 0.1 M HEPES, Na₂SO₄ and PEG400 whose concentration was optimized to avoid crystal solubilisation according to standard procedures. Washed crystals were dissolved by using 0.01 M TRIS-HCl, NaCl 0.15 M, pH 8.0 and analysed by UV spectrophotometry

(Lambda EZ201, Perkin Elmer) to estimate protein concentration.

Circular dichroism (CD) measurements. The far-UV CD spectra of Anti-CD20 under initial conditions, after buffer exchange with HEPES 0.1 M, and after mixing with the precipitant solution, were recorded between 200 and 300 nm on a Chirascan CD spectrometer (Applied Photophysics, UK) at 20 °C with a 1 nm bandwidth resolution and current time-per-point of 3 s. 100 μ L of mAbs solution were added in a 0.1 mm path-length

quartz cuvette that was placed in the spectrophotometer. Typically, three scans were recorded and baseline spectra were subtracted from each spectrum. Data were processed using Applied Photophysics Chirascan Viewer.

9.3.2. MELTING POINT AND Z-POTENTIAL ASSESSMENT BY DLS

Thermal stability (melting temperature, T_m) of protein solutions was assessed by a Zetasizer Nano ZS instrument (Malvern) equipped with a 4 mW He–Ne laser at 632.8 nm and a detector placed at 173° in agreement to the proprietary NIBS (Non Invasive Back Scatter) technology.

Samples were placed in quartz cuvettes (1 cm path-length), heated by a Peltier module and the average hydrodynamic diameter was measured as a function of temperature from 20 °C to 90 °C (temperature increment 0.5 °C). DLS can monitor the thermal denaturation of proteins, which leads to irreversible loss of their structure and function as the protein unfolds. When the average protein size is observed by DLS versus temperature, one will observe a significant increase in the average protein size for temperatures larger than the aggregation point, which is generally assumed as the onset of protein melting point. For the Z-potential evaluations, the appropriate ratios of protein and buffer solutions were placed in disposable folded capillary cells (DTS 1070, Malvern), and then inserted into the Zetasizer instrument. The Z-potential was measured by laser Doppler micro-electrophoresis. Briefly, an electric field was applied to the protein solution and consequently each molecule moved with a velocity related to its Z-potential. The velocity was measured using a laser interferometric technique (M3-Phase analysis light scattering), which allowed the calculation of the electrophoretic mobility, and from this, the average Z-potential and Z-potential distribution.

9.3.3. LIGHT SCATTERING MEASUREMENTS

Static and dynamic light scattering measurements were performed on protein solution samples with a concentration between 0.1 and 5.0 mg mL⁻¹ in different crystallization cocktails.

The Anti-CD20 concentration in these solutions was checked by measurement of the absorbance at 280 nm. All the solutions were filtered on a 0.22 µm filter (Anotop 10, Whatman) before measurement. The samples were placed in quartz ultra-low volume cuvettes (ZEN 2112, optical path 3 mm, Malvern) to measure with the Zetasizer Nano ZS instrument (Malvern) in static mode for the second virial coefficient B_{22} or dynamic mode for the protein diffusion coefficient D_m . The light intensity and its time autocorrelation function were measured at 173° scattering angle. All measurements were performed at 20 °C after 2 min of equilibration using automatic time settings.

The Debye plots were generated by using Debye's light scattering equation:

$$\frac{KC}{R_\theta} = \frac{1}{M_w} + 2B_{22}C \quad (1)$$

where R_θ is the excess Rayleigh ratio of the protein in a solution with a protein concentration C and M_w is the average molecular weight of the protein. K is the optical constant and is defined as:

$$K = \frac{4\pi^2 n^2 \left(\frac{dn}{dc}\right)^2}{N_A \lambda^4} \quad (2)$$

where n is the solvent refractive index, dn/dc is the refractive index increment, λ is the wavelength of the incident light, and N_A is Avogadro's number. The second virial coefficient B_{22} [mL mol g⁻²] was obtained from the slope of the linear Debye plot of $KC/R\theta$ versus protein concentration C .

The static light scattering results for B_{22} were accepted if the following criteria were satisfied:

1. Signal to noise ratio >130%, where noise is solvent kcounts;
2. Increasing trend for signal kcounts vs. protein concentration.

The interaction parameter k_d [mL mg⁻¹] and the self-diffusion coefficient D_s [m² s⁻¹] were determined by using linear fitting of the protein diffusion coefficient D_m , determined from the dynamic light scattering measurements, plotted against the protein concentration C [mg mL⁻¹], using the following Eq. 3³¹:

$$D_m = D_s (1 + k_d C) \quad (3)$$

The determined interaction parameter k_d can be interpreted as the difference between a thermodynamic term related to the product $2B_{22} \cdot M_w$ and a hydrodynamic term ($\zeta_1 + \nu$):

$$k_d = 2B_{22} M_w - (\zeta_1 + \nu) \quad (4)$$

where ζ_1 is obtained from the virial expansion of the concentration-dependent frictional coefficient and ν is the solvent viscosity. Solutions that showed turbidity, indicating phase separation and crystallization/precipitation, were not used for measurements.

9.3.4. PROTEIN PARTITIONING MEASUREMENTS

Anti-CD20 repartition between aqueous and PEG phases has been estimated by the method described by Kress *et al.*³². A solution (5 mL) containing Na₂SO₄ 1.1 M (13.54 wt.%) and PEG400 10.46% V/V (10.22 wt.%) in HEPES 0.1 M at pH 7.4, was added with 200 μ L Anti-CD20 solution 10.3 mg mL⁻¹ in the same buffer. After vigorous stirring for 5 minutes by vortex, the mixture has been left to rest overnight. The concentration of the protein in the two separated phases visually detected and in presence of excess of precipitated protein, was then assessed by UV spectrophotometry at 280 nm.

Solution composition near the crystallization point: 20 mg mL⁻¹ Anti-CD20, 9.6% V/V PEG400, 0.86 M Na₂SO₄ in 0.1 M HEPES buffer at pH 7.4.

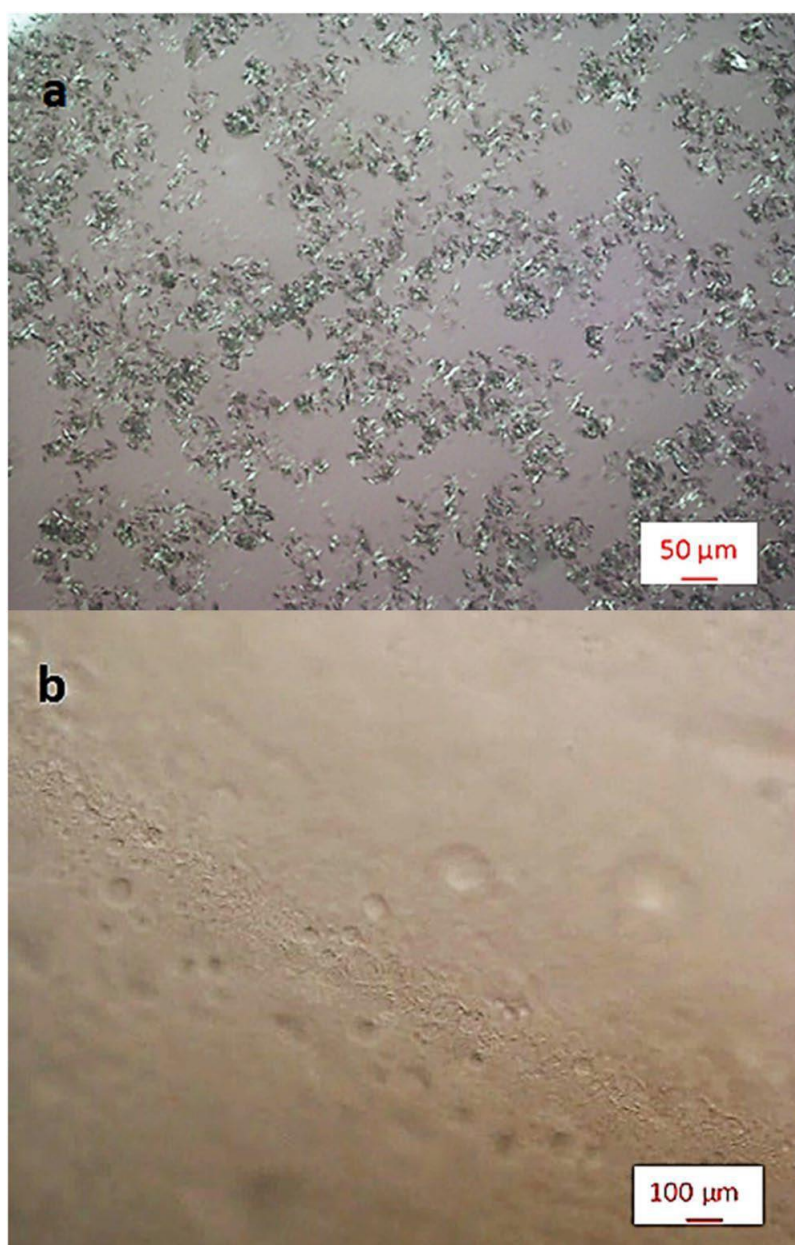


Figure 1. Optical microscope image of (a) crystalline Anti-CD20 monoclonal antibody obtained by sitting-drop vapour diffusion method and (b) Liquid- Liquid Phase Separation occurring just prior to crystallization.

9.4 RESULTS AND DISCUSSION

9.4.1 ANTI-CD20 CRYSTALLIZATION AND CRYSTALS ANALYSIS

Anti-CD20 needle-like crystals (Fig. 1a) appear by sitting-drop vapour diffusion crystallization experiments using a 1:1 volume ratio mixture of a 20 mg mL⁻¹ protein solution in HEPES buffer 0.1 M at pH 7.4 and a precipitant solution containing PEG400 9.6% V/V (9.4 wt.%) and Na₂SO₄ 0.86 M (10.6 wt.%) in the same buffer. Therefore, the initial composition of the drop in the vapour diffusion tests corresponds to 10 mg mL⁻¹ Anti-CD20, 4.8% V/V PEG400, 0.43 M Na₂SO₄ in 0.1 M HEPES at a pH of 7.4 and is shown by the diamond symbol in Fig. 2. The crystals appear when the volume of the drop is nearly halved with respect to its initial volume. Accordingly, the final concentration of the components in the crystallizing drops is almost doubled that compared

to the initial compositions and it is indicated by the pentagon symbol of Fig. 2.

Batch experiments in similar solution composition as that for crystallizing drops in the vapour diffusion tests (the term “similar” is used since the exact composition of the droplet at the crystallization point under equilibration with the reservoir solution it is not known), give also rise to crystals. Therefore, the batch working point coincides with the final conditions of the vapour diffusion tests. Since the batch composition does not vary with time, due to the absence of solvent evaporation, it is evident that the solution is supersaturated immediately upon mixing the protein and precipitant solutions, which results in a shorter crystallization time (12–18 h) than that observed with the sitting drop set up (36–48 h). The UV-Vis and DLS measurements of washed and dissolved crystals confirmed their protein nature. All the analysed samples showed an intense band centred at 280 nm, typical of proteins absorption. The size distribution analysis by intensities show a single peak near 12 nm, size expected for Anti-CD20 protein molecules³³, and a polydispersity <20%, indicating a high monodispersity. Liquid-Liquid Phase Separation (LLPS) is observed nearly simultaneously with, or just prior to, crystals appearance (Fig. 1b) both in the vapour diffusion and batch crystallization trials.

In accordance with other mAbs crystallization studies reported in literature^{20,34,35}, also here it appears that the LLPS is a key step in Anti-CD20 crystallization.

Crystallization trials, aiming to investigate the effect of precipitant solution composition on crystal quality have been also performed by changing the starting amount of PEG400 and/or Na₂SO₄. As expected, the shape, size and density of crystals (number of crystals per unity of volume) are found to depend on buffer composition, initial protein concentration and crystallization method (sitting drop or batch).

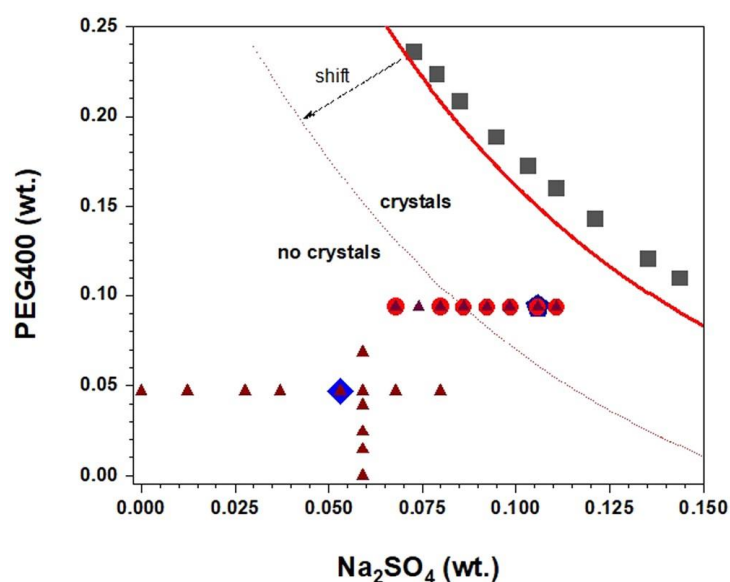


Figure 2. Experimental state diagram for the system PEG400/Na₂SO₄/H₂O at 293.15 K. Squares: experimental liquid-liquid equilibrium data from ref. 42; solid line: asymptotic fitting to tie-lines data from ref. 42; circles: batch crystallization conditions reported in Table 1; diamond: starting solution composition in vapour diffusion tests; pentagon: ending solution composition in vapour diffusion tests; triangles: measurements points for B22; dotted line: shifted binodal curve in the presence of Anti-CD20 protein. Solution composition is expressed as weight fraction (wt.).

Na ₂ SO ₄ [M]	Crystallization behaviour	Size [μm]	Shape
0.90	Opalescent solution, Instantaneous Precipitation	<1	gel beads
0.86	Precipitation/crystallization in 12–24 hours	<10	spherulite
0.80	Crystallization in 18–36 hours	<20	needle
0.75	Crystallization in 24–48 hours	20	needle
0.70	Crystallization in 24–48 hours	20	needle
0.65	Clear and stable solution	—	—
0.55	Clear and stable solution	—	—

Table 1. Mixed solution compositions, crystallization behaviour and crystal appearance in the batch crystallization experiments using an Anti-CD20 concentration 20 mg mL⁻¹, 9.6% V/V PEG400 and 100 mM HEPES buffer at a pH of 7.4.

All these parameters have also shown to impact on the time required to observe crystallization. Table 1 shows the effect of the salt concentration on the crystal appearance for the batch experiments. Needles with a size of nearly 20 μm are the largest crystals obtained for starting solutions with 9.6% V/V PEG400 and 0.70–0.80 M Na₂SO₄. A further increase in Na₂SO₄ concentration produces a faster and massive protein nucleation in less than 24 hours and crystals of smaller size (<10 μm) with a spherulite-like morphology appear. For a Na₂SO₄ concentration of 0.9 M or larger, upon mixing the solution immediately turns opalescent due to a macroscopic LLPS in the solution, followed by a rapid protein precipitation as gel beads. On the opposite side, for the lowest amount of salt (Na₂SO₄ ≤ 0.65 M), the solutions remain clear for months.

Figure 2 shows the experimental state diagram for the system PEG400/Na₂SO₄/H₂O at 20 °C indicating the loci of the points related to solution compositions used for batch crystallization tests (circles) of Table 1, together with the starting (diamond) and ending (pentagon) solution compositions in vapour diffusion tests. The figure also displays the experimental liquid-liquid equilibrium data and the asymptotic fitting to tie-lines data reported in ref. 36.

Buffer	T _m [°C]	Z-potential [mV]	Z _{avg} [nm]	PDI
HEPES ^a	68.5 ± 0.5	2.2 ± 0.7	11.3 ± 0.1	0.10 ± 0.03
Sodium Citrate ^b	68.5 ± 0.5	1.1 ± 0.2	12.2 ± 0.2	0.04 ± 0.03
TRIS ^c	69.0 ± 0.5	7.0 ± 1.0	12.63 ± 0.03	0.12 ± 0.01
Sodium Citrate/HEPES (1:1 Vol)	69.0 ± 0.5	0.19 ± 0.04	13.6 ± 0.2	0.15 ± 0.03
TRIS/HEPES (1:1 Vol)	69.0 ± 0.5	2.3 ± 1.0	12.13 ± 0.03	0.06 ± 0.01

Table 2. Results for melting point (T_m), Z-potential, intensity weighted mean hydrodynamic size (Z_{avg}), and polydispersion index (PDI) from formulation buffers screening (Anti-CD20 concentration 20 mg mL⁻¹; a HEPES buffer 0.1 M, pH 7.4; b Sodium Citrate buffer 0.

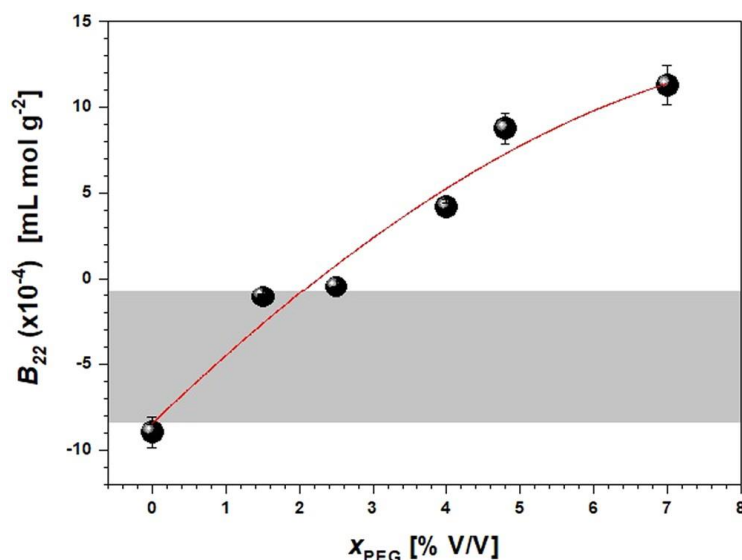


Figure 3. The second virial coefficient B_{22} as a function of PEG400 volume concentration (x_{PEG}) at a constant amount of 0.48 M Na_2SO_4 in HEPES 0.1 M buffer at pH 7.4. The crystallization slot according to ref. 15 is shown in light grey. The solid line is a guide for the eyes.

9.4.2 SLS/DLS ANALYSIS

The protein stability in several formulation buffers but without precipitating agents (PEG and/or Na_2SO_4), was assessed by DLS, resulting in values for the melting point and Z-potential. As reported in Table 2, all samples are characterized by similar values of melting point, Z-potential, intensity weighted mean hydrodynamic size Z_{avg} and polydispersion index (PDI). All protein samples show low positive values of the Z-potential, indicating a reduced colloidal stability in the various buffer solutions. Nevertheless, due to a PDI close to 0.1, all samples can be considered monodisperse. No significant variations were observed in the sample aggregation state over time in the range 12–24 h. Accordingly, further SLS/DLS studies were performed by using HEPES as formulation buffer since it was used in previously published crystallization protocols³⁰. To study the aggregation propensity on Anti-CD20 in HEPES buffer and in various PEG400/ Na_2SO_4 solution compositions, SLS and DLS measurements were performed on freshly prepared samples allowing to determine the second virial coefficient B_{22} and the interaction parameter k_d , respectively. The value of KC/R_θ was determined as a function of protein concentration, ranging from 0.1 to 5.0 mg mL^{-1} , by SLS. Results were used to evidence the combined effect of PEG400 and Na_2SO_4 on Anti-CD20 colloidal stability and to compare these results with effective crystallization outcomes.

It is well known that the addition of salts can cause an electrostatic double layer around the protein surface charges, which involves a shielding and the reduction of repulsive interactions among macromolecules. Furthermore, the salts ions compete with the protein for water molecules and dehydrate the protein (salting out effect³⁷), thus inducing aggregation by mainly electrostatic and hydrophobic interactions. On the other side, polymers such as PEG bring the protein molecules together due to preferential interactions and osmotic potential³⁸. Accordingly, the addition of PEG400 or Na_2SO_4 to Anti-CD20 solutions is expected to increase the aggregation aptitude of the protein and facilitate crystallization, as experimentally observed, e.g., in batch crystallization tests of Table 1. However, as displayed in Figs. 3 and 4, for increasing amounts of PEG or

Na_2SO_4 when both components are present in solution, the B_{22} moves towards larger positive values, theoretically indicative of an increase in repulsive interactions. Furthermore, effective Anti-CD20 crystallization conditions seems to lay outside the crystallization slot defined by George and Wilson ¹⁵.

Both Figs. 3 and 4 show that the combined effect of PEG400 and Na_2SO_4 has a noteworthy consequence on the B_{22} value. For instance, for the solution containing 0.48 M Na_2SO_4 in absence of PEG, a B_{22} value of $-8.9 \times 10^{-4} \text{ mL mol g}^{-2}$ is obtained (Fig. 3) that is slightly below the crystallization slot. However, when adding PEG400 to the solution while keeping salt concentration constant, B_{22} steeply increases through the crystallization window towards positive values already at 3% V/V of PEG.

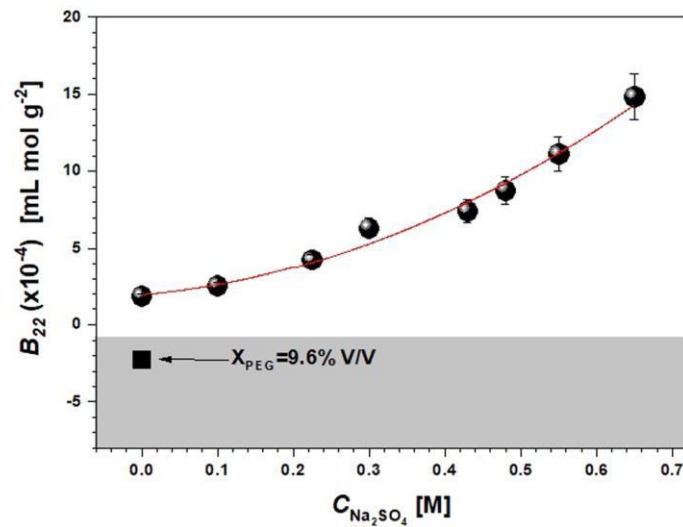


Figure 4. The second virial coefficient B_{22} as a function of Na_2SO_4 molar concentration ($C_{\text{Na}_2\text{SO}_4}$) for constant PEG400 volume concentration $X_{\text{PEG}} = 4.8\% \text{ V/V}$ in HEPES 0.1 M, pH 7.4. The solid square symbol indicates B_{22} for a PEG400 concentration of 9.6% V/V without NaCl. The crystallization slot according to ref. ¹⁵ is shown in light grey. The solid line is a guide for the eyes.

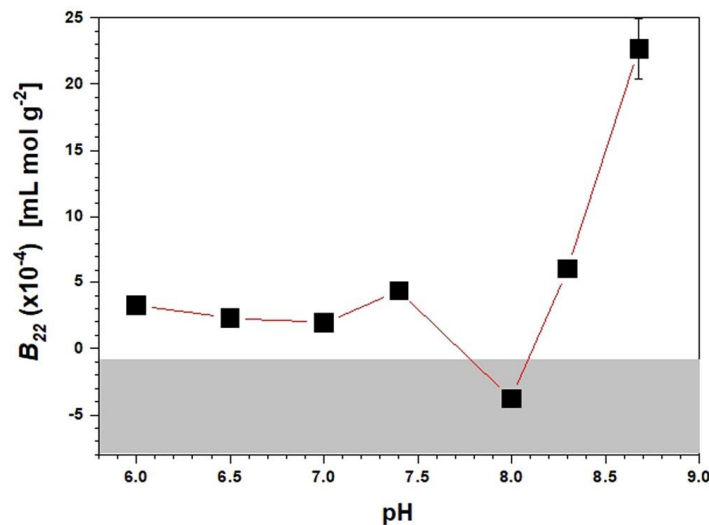


Figure 5. pH dependence of B_{22} for Anti-CD20 solutions with 4.8% V/V PEG400, 0.43 M Na_2SO_4 , and HEPES 0.1 M. The crystallization slot according to ref. ¹⁵ is shown in light grey. The solid line is a guide for the eyes.

The B_{22} value for the solution containing 4.8% V/V PEG400 in absence of Na_2SO_4 is found to be slightly positive ($B_{22} = 1.8 \times 10^{-4} \text{ mL mol g}^{-2}$), becoming negative ($B_{22} = -2.26 \times 10^{-4} \text{ mL mol g}^{-2}$) when increasing PEG400 up to $X_{\text{PEG}} = 9.6\%$ V/V without Na_2SO_4 (Fig. 4). This is in agreement with results from Ahamed *et al.*³⁹, who observed the reduction in solubility for a mAb for increasing amounts of PEG400. Nevertheless, when salt is added to the solution ($C_{\text{Na}_2\text{SO}_4} \neq 0$), the virial coefficient rises steeply with the salt concentration. These observations clearly indicate that a different effect on the measured value of B_{22} takes place when PEG400 and Na_2SO_4 are combined together, compared to the cases when they are used separately.

Figure 5 shows the effect of pH on B_{22} for solutions containing PEG400 and Na_2SO_4 . At $\text{pH} \leq 7.6$, the B_{22} remains roughly unchanged ($2.28 < B_{22} < 4.35 \times 10^{-4} \text{ mL mol g}^{-2}$). These positive values are indicative of repulsive protein–protein interactions. At a pH of 8.0, the B_{22} becomes negative ($-3.78 \times 10^{-4} \text{ mL mol g}^{-2}$) and then sharply increases approaching $\text{pH} = 8.8$, which is the theoretical isoelectric point of Anti-CD20 ($pI = 8.8$)⁴⁰. It is expected that protein-protein interactions at a pH substantially below or above the pI are repulsive, while at a pH near the pI they become increasingly attractive due to the overall neutral charge of the protein. However, the actual pI of biomolecules might change with ionic environment, and generally decreases at different extents with increasing ionic strength, depending on the nature of the counter-ion^{17,41}. It is speculated that in the presence of 0.43 M Na_2SO_4 , PEG400 4.8% V/V and 0.1 M HEPES, the effective pI of Anti-CD20 is around 8.0. Therefore, for $\text{pH} < 8.0$, the slightly positive B_{22} values are most likely due to partially screening of the net positive electrostatic charges of protein molecules, while at $\text{pH} = 8.0$, where the net charge becomes null, the net resultant interaction is attractive.

Above pH 8.0, the B_{22} values become strongly positive, indicating an ineffective screening of the net negative charge of molecules that results in repulsive interactions. Since solution composition strongly affects protein stability and aggregate formation, the Na_2SO_4 concentration dependence of B_{22} was also investigated at higher PEG and salt concentrations, thus reaching compositions close to that used for crystallization experiments of Table 1. Correlation between B_{22} and Na_2SO_4 concentration is shown in Fig. 6, confirming an increasing trend similar to that observed for lower concentrations of Fig. 4 also in this case.

In Fig. 6 it can be seen that the B_{22} values are negative (attractive interactions) for Na_2SO_4 concentration ranging from 0.55 to 0.6 M, corresponding to conditions in Table 1 that give clear solutions, while they become positive (repulsive interactions) when the salt concentration is further increased up to 0.9 M. Within the crystallization window, i.e. Na_2SO_4 ranging from 0.7 to 0.86 M, the B_{22} values range from 3.2×10^{-4} to $5.7 \times 10^{-4} \text{ mL mol g}^{-2}$. This would be theoretically indicative of the absence of attractive colloidal interactions, in opposition to the results of the crystallization tests.

DLS measurements were then used to determine the interaction parameter k_d . Generally, k_d and B_{22} display a qualitatively similar trend⁴². However, looking at the behaviour of the interaction parameter k_d in the crystallization range of Fig. 6, negative values are found for $X_{\text{PEG}} = 9.6\%$ V/V and sodium sulfate 0.55–0.80 M, with slight variations within this range. Generally, a negative value of k_d implies the existence of attractive interactions between protein molecules which slow down their diffusion in solution⁴³.

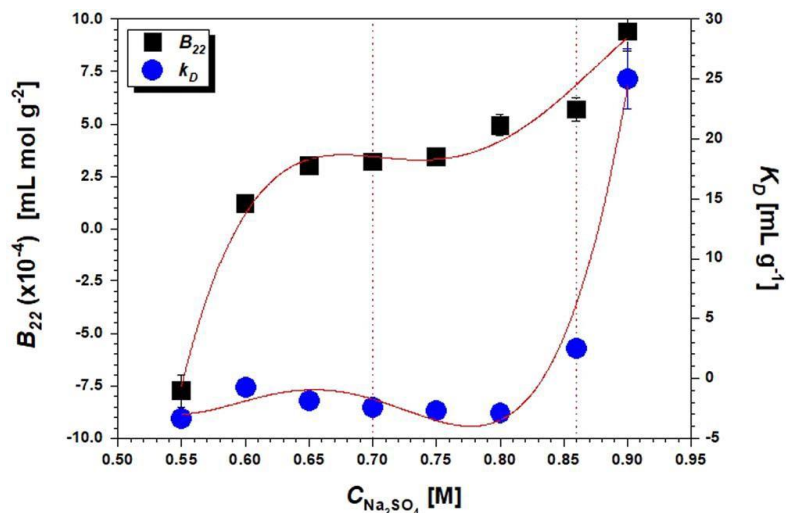


Figure 6. B_{22} and k_d as a function of Na_2SO_4 concentration for XPEG = 9.6% V/V and pH 7.4. The experimental crystallization window boundaries (see Table 1) are highlighted by the dotted vertical lines. The solid lines are guides for the eyes.

Since under the same conditions B_{22} is negative only for $\text{Na}_2\text{SO}_4 < 0.6$ M and then increases up to $1.23\text{--}4.94 \times 10^{-4}$ mL mol g $^{-2}$ in the salt concentration range 0.6–0.8 M, this indicates that underlying attractive interactions do not have a thermodynamic origin of colloidal nature. We can instead conclude that these interactions result from the hydrodynamic effects included in the second term of Eq. 4⁴⁴, most likely due to the increase of solution viscosity (from 1.949 cP in the PEG400 9.6% V/V solution without salt to 2.546 cP for PEG400 9.6% V/V and Na_2SO_4 0.9 M). Nevertheless, as for B_{22} , the increasing trend of k_d with the concentration of Na_2SO_4 does not comply with the outcome of crystallization tests. In fact, the increase of Na_2SO_4 concentration at values larger than 0.8 M gives rise to a theoretically significant increase of the strength in protein-protein repulsions, according to measured B_{22} , values that are exacerbated near the LLPS region, while crystals are obtained in such conditions. From the observed trends of B_{22} and k_d , we can conclude that neither PEG400 nor Na_2SO_4 act as conventional precipitants for Anti-CD20 when used together since, on average, Anti-CD20 monomers apparently repel one another. Nevertheless, this evidently contradicts the experimental outcomes of crystallization tests. The B_{22} values are negative (attractive interactions) in formulations that remain clears for months, whereas positive values, corresponding theoretically to net repulsive interactions, have been found for the best-performing crystallizing or either in precipitating conditions.

Considering the possible variations in their structure, morphology, size, surface charge and chemistry, proteins definitely represent one of the most complex colloidal systems. Several mechanisms could lead to molecular aggregation in solution and it is not excluded that more than one is active in certain conditions. Therefore, it is not surprising that B_{22} does not always reflect the aggregation propensities of proteins in a given formulation. Several papers can be found in literature reporting discrepancies between B_{22} and the susceptibility to aggregation of structurally complex macromolecules, like monoclonal antibodies^{42,45}. Crystallizing conditions with positive B_{22} values were found for a mAb molecule with PEG400 by Raket *et al.*³⁵. This behaviour has

been ascribed to the ambivalent character of PEG400 as precipitant and stabilizer^{35,46}. Kress *et al.*⁴⁷ observed the decrease in B_{22} of an immunoglobulin G (IgG) when increasing PEG2000, sodium citrate and NaCl solute concentration, if used separately. However, the mutual effect of PEG and salts resulted in a shift of B_{22} from negative to almost neutral values when increasing the NaCl amount if used together³². This behaviour has been explained by a solubilizing effect of IgG in PEG2000 induced by NaCl until a maximum salt concentration. Exceeding this NaCl value, a solid-liquid equilibrium, due to protein precipitation, was observed. Herhut *et al.*⁴⁸ measured B_{22} for an IgG and D-xylose ketol-isomerase (172.3 kDa) with ammonium sulphate and PEG12000 and PEG2000, respectively. They observed the initial decrease in B_{22} at low PEG concentration, passing through a minimum and then increasing for higher PEG concentrations. This behaviour has been explained by considering that polymer-induced interactions are not solely attractive over the whole polymer concentration range. Normally, polymer chains behave as coil-inducing attractive interactions between protein molecules at low-polymer concentration. However, at high polymer concentration, flexible coils elongate and enter space between the proteins, so that repulsive interactions are induced^{49,50}. This explanation has been also confirmed by molecular dynamic simulations at different polymer concentration by Cao *et al.*⁵¹.

It has also been reported that conformational stability plays an important role in aggregation propensity, with partially unfolded conformational intermediates being responsible of aggregate formation⁹. In this case, the B_{22} value is unlikely to correlate with long-term aggregation because the structurally perturbed state susceptible to aggregation could be present in a small fraction of molecules compared to the native species⁴⁵. Aiming to shed light on this aspect, protein structure in solution has been investigated in the present work.

9.4.3 PROTEIN STRUCTURE IN THE SOLUTION

On the bases of the results above, measurements of melting temperature (T_m) for several solution compositions, including $X_{\text{PEG}} = 9.6\%$ V/V and Na_2SO_4 at various concentrations, and Circular Dichroism (CD) in selected formulations, were performed aiming to investigate conformational stability of Anti-CD20. Results show slight variations of the melting points: $T_m = 67.0, 67.5, 68.0,$ and 67.5 ± 0.5 °C for 0.55, 0.65, 0.75, and 0.85 M Na_2SO_4 , respectively, confirming that samples, on average, share similar water activity according to the Wyman-Tanford equation⁵². Circular Dichroism spectra of protein solutions give information on the secondary structure, folding properties and conformational variation of the proteins⁵³. The general shape of the spectrum of the provided Anti-CD20 solution (Fig. 7, initial conditions) corresponds to the expected spectra for Anti-CD20, as it shows the typical shape of a monoclonal antibody with a minimum around 220 nm and a maximum around 200 nm, suggesting a secondary structure dominated by β -sheet motif⁵³. Moreover, these spectra correspond to the CD-spectra of Anti-CD20 from literature⁵⁴.

These spectra show that the protein is well folded in every buffer, i.e. the 3D-structure of Anti-CD20 is preserved under all conditions tested. However, the maximum ellipticity (around 200 nm) is much higher after the buffer exchange (red and green spectra in Fig. 7) than in the initial buffer (blue spectrum), while ellipticity at other wavelengths is similar in every buffer. This suggests that the β -sheet motifs of the mAbs are favoured

and stabilized in the new HEPES buffer, in comparison to the initial buffer (0.025 M sodium citrate at pH 6.5 and 0.154 M sodium chloride).

There is no significant difference in the far-UV CD spectra of Anti-CD20 before (Fig. 7, red spectrum) and after the addition of Na₂SO₄ and PEG400 as precipitating agents (Fig. 7, green spectrum), although a small shift can be observed, showing slight changes in the 3D-structure. The main difference between these spectra is around 230 nm, but the peak is quite narrow and this wavelength does not correspond to any typical feature of protein structure. Therefore, the difference could be due to Na₂SO₄ or PEG400 absorbance or might be due to some noise. It should be noted, though, that the crystallization solution had to be diluted in order to enable CD measurement. Since the spectra before and after the concentrated crystallization conditions are the same, it can be concluded that the concentrated crystallization conditions do not alter the secondary structure of the protein. The Anti-CD20 secondary structure is preserved after centrifugation and addition of the precipitating agents, as the typical β -sheet motif appears clearly in the spectrum (Fig. 7, green spectrum). Moreover, this secondary structure seems to be favoured in the crystallization buffer, meaning that the 0.1 M HEPES at pH 7.4 buffer promotes Anti-CD20 crystallization by making the secondary structure less flexible. However, no clear effect of Na₂SO₄ or PEG400 on the Anti-CD20 secondary structure is visible.

9.4.4 THE ROLE OF LLPS IN ANTI-CD20 CRYSTALLIZATION

A complementary scenario can be envisioned when considering LLPS phenomena observed concurrently or just prior of Anti-CD20 crystallization.

For simple protein/salts or protein/PEG systems, it has been often reported that the B_{22} value can be used as a predictor of LLPS formation, since weak protein-protein interactions, in general hydrophobic in nature or even limited to specific protein chain sequences, are at the origin of the phase separation²². However, our results seem to suggest that the LLPS (observed just prior or at the point of protein crystallization) proceeds without attractive interactions, since B_{22} is negative when a mono-phase system is observed while it turns positive as approaching the liquid phase separation and crystals formation. It could be argued that, in our complex mixture that includes several components, the B_{22} values fail to predict the experimentally observed crystallization since it may be rather related to the polymer-salt phase separation that can occur without protein. The liquid-liquid separation of PEG/salt aqueous solutions is a fundamentally different phenomenon from PEG/protein or salt/protein LLPS, which originate by a combination of hydrophobic and salting-out effects, whose origin has been attributed to the different conformations of the PEG polymer chain in aqueous solution and their respective hydration²⁴. Actually, the PEG400/Na₂SO₄/H₂O system is known to generate aqueous two-phase systems^{36,55,56}. Figure 2 displays the experimental binodal curve together with liquid-liquid equilibrium tie-lines data for PEG400 + Na₂SO₄ + H₂O system at 293.15 K (the temperature used in this work for crystallization experiments and SLS/DLS measurements)³⁶.

Concerning the specific system studied in this work, for a protein concentration of 20 mg mL⁻¹ and a PEG400 content of 9.6% V/V (9.4 wt.%), phase separation is observed for salt concentrations ≥ 0.7 M (≥ 8.6 wt.%) (crystallization points of Table 1 and dark circles in Fig. 2), that is quite far from both binodal curve. However,

the presence of the protein can reduce the amount of salt needed for observing LLPS in the multicomponent PEG/salt/protein/water systems²⁴. Consequently, it cannot be excluded that the effective binodal curve for PEG/salt LLPS is shifted down to conditions corresponding to the observed crystallization points, in a region of poor solvent conditions, thus giving a decisive contribute to the aggregation/crystallization behaviour of Anti-CD20.

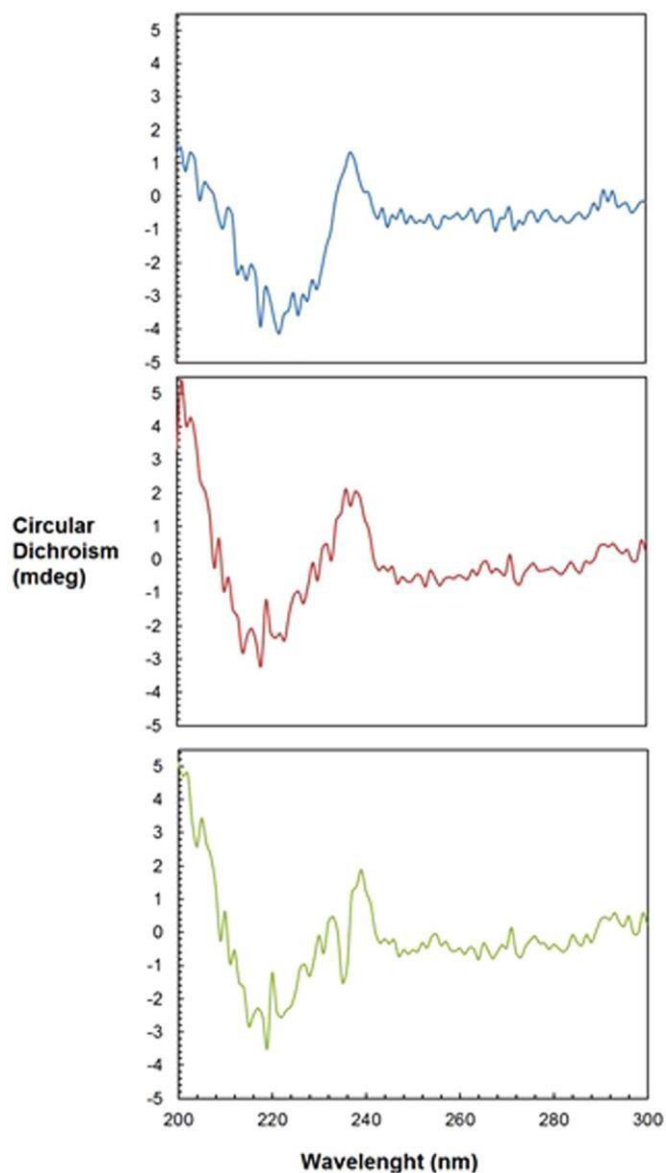


Figure 7. Far-UV CD spectra of Anti-CD20 under initial conditions (blue spectra, mAbs concentration 9.95 mg mL^{-1} in stock buffer), after buffer exchange with HEPES 0.1 M pH 7.4 (red spectra, mAb concentration 100 mg/mL in crystallization buffer) and after salt mixing (green spectra, mAb concentration 60 mg/mL in crystallization buffer and with 0.9 M Na_2SO_4 and 9.6% V/V PEG400).

Figure 8 shows the change in turbidity (Residual Intensity) for a solution containing PEG400 9.6% V/V in 0.1 M HEPES at pH 7.4 and increasing amount of Na_2SO_4 . It is observed that, in absence of the Anti-CD20, a sharp increase in solution turbidity is observed for salt concentration $>1.1 \text{ M}$ ($>13.5 \text{ wt.}\%$), that is very close

to the binodal curve reported in Fig. 2 for the PEG400 + Na₂SO₄ + H₂O system. Since in the presence of the protein turbidity due to liquid-liquid phase separation is observed for salt concentration larger than 0.65 M for the same amount of PEG, this proves the shift of LLPS region towards lower values of PEG and/or salt components when Anti-CD20 is present in the solution. It is worth noting that B_{22} measurements reported in Figs. 3 and 4 have been made in a region of Fig. 2 where LLPS (and crystallization) are not observed (triangles in the left-bottom side of the figure). This means that PEG/salt LLPS is not responsible for the contradiction between B_{22} measurements and the outcome of crystallization trials, but rather the intrinsic complexity of the system makes ineffective the measurement of the osmotic coefficient as predictor parameter for crystallization conditions.

According to our results, it can be proposed that PEG/salt LLPS causes the preferential partitioning of proteins in a specific salt- or PEG-rich phase. In general, the affinity of the protein for the polymeric component, due to hydrophobic interactions, favours the protein concentration in the PEG-rich phase^{39,57}. This is particularly true for PEG400, which is a low molecular weight polymer and, therefore, its size exclusion effects on proteins are negligible while the dominant factor in the separation is the salting out effect, produced by the sulphate, which causes the protein to migrate to the PEG-rich phase.

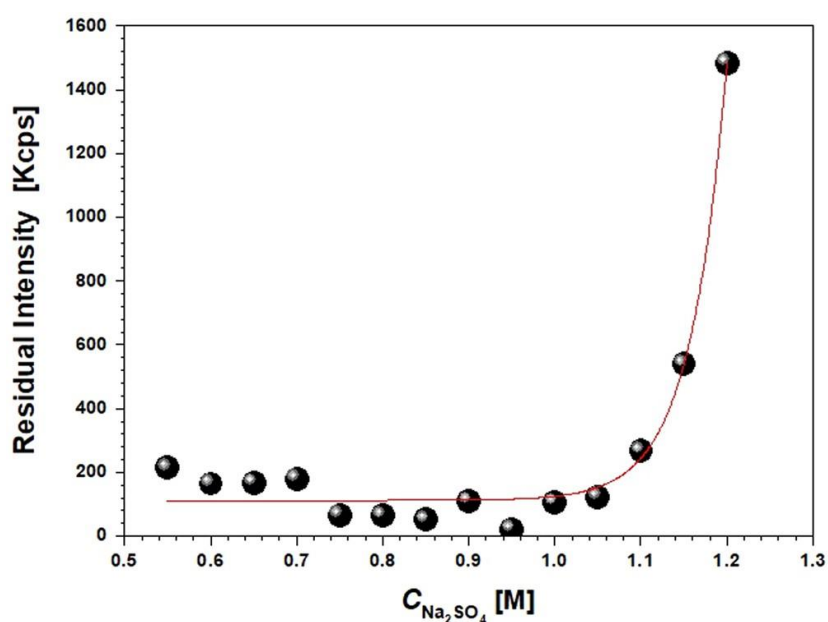


Figure 8. Residual Intensity measured by DLS at a fixed scattering angle of 173° for a solution containing PEG400 9.6% V/V in 0.1 M HEPES at pH 7.4 and increasing amount of Na₂SO₄, without protein. The solid line is a guide for the eyes.

This effect has been confirmed by measurements on Anti-CD20 partitioning, showing that more than 90% of the solution protein migrates in the PEG-rich phase in the protein-saturated Anti-CD20/PEG400/Na₂SO₄/HEPES/H₂O mixture displaying phase separation.

In such conditions, during LLPS, the Anti-CD20 concentrates in droplets that have a density higher than the average density of the whole system thus generating a much higher supersaturation. When the protein concentration exceeds a certain limit, precipitation at the interface is observed and the precipitated protein is

in equilibrium with the protein solubilised in each phase⁵⁸. For particularly high Anti-CD20 (>30 mg mL⁻¹ or PEG/salt concentrations (i.e. PEG400 9.4 wt.% and Na₂SO₄ ≥ 11.1 wt.%), these droplets look not to be as liquid, having instead the appearance of gel beads. Protein crystals initiate to nucleate and grow near the boundary of the most protein-concentrated droplets (Fig. 9), suggesting that the droplet interface participates in the nucleation mechanism⁵⁹.

Subsequently, crystals appear within the bulk of the droplets, which spread and coalesce. Many droplets disappear as crystal growth proceeds, suggesting that a continuous exchange exists between the droplets and the surrounding medium. Experimental observations clearly indicate the important role of LLPS and of the established liquid-liquid interface in inducing Anti-CD20 nucleation, even in absence of underlying net attractive interaction between proteins. It is likely that only protein molecules distributed at the droplets interface experience local short-range attractive interactions, due to the specific environment and/or conformational changes, not influencing the mean B_{22} value.

On the basis of our results, it could be hypothesized that the occurrence of LLPS in crystallizing/precipitating conditions results in a partially unfolded protein conformation or in a suitable variation of the secondary/tertiary protein structure, as already reported in other cases²⁷, which can be the species prone to aggregation through a mechanism driven by conformational change rather than colloidal interactions, and which initiate the crystallization process. The conformationally perturbed protein can be a minor species, which does not alter significantly the predominant native protein population and only slightly contributes to the net protein–protein interaction value measured by B_{22} . Indeed, SLS is an integrative technique, which provides only averaged information. If only specific short-range orientations or aggregation-prone structurally perturbed states can lead to attractive interactions, the remaining repulsive orientations or species dominate in the light scattering results. It is important to note that the measurements of intermolecular interactions were performed under low protein concentration conditions (≤ 5 mg mL⁻¹), while crystallization trials are generally conducted at higher concentrations (≥ 20 mg mL⁻¹). Both B_{22} and k_d determined in dilute conditions are considered generally predictive of high-concentration behaviour. Nonetheless, high concentration behaviour can differ from that observed at dilute conditions, since “crowding” effects, i.e. the increased chance of molecular interactions, deviation from thermodynamic ideality and higher-order interactions (e.g., B_{23} , B_{222}) can significantly alter the net inter-protein interactions^{54,60}. The contribution of these effects to aggregation propensity of structurally complex molecules such as mAbs, cannot be ruled out.

9.5 CONCLUSIONS

This work reports about the study of Anti-CD20 (a full-length monoclonal antibody) crystallization in a PEG400/Na₂SO₄/H₂O system occurring near LLPS conditions. The DLS/SLS studies performed to verify the correlation between the second virial coefficient and molecular diffusivity with the protein aggregation propensity in selected solution formulations indicates that B_{22} remains strongly positive (a sign of repulsive protein–protein interactions) for all conditions that have been instead ascertained to be effective for protein crystallization or precipitation. For all the crystallizing or precipitating conditions, the occurrence of LLPS phenomena was observed concomitantly or near the nucleation stage. Even in this case, the second virial

coefficient does not correlate with the LLPS, which mainly proceeds without attractive protein interactions, and that may be rather related to the polymer-salt phase separation that can occur without protein.

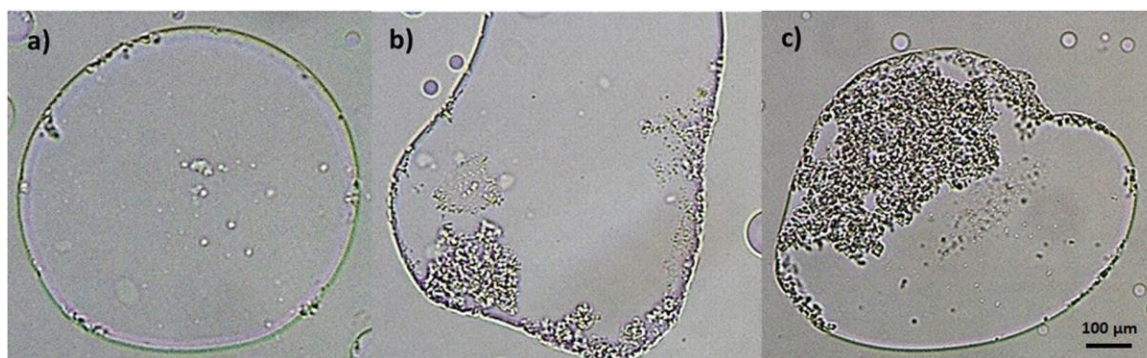


Figure 9. Protein crystals nucleating near the boundary of the droplets (a) and crystals forming within the bulk of the droplets (b,c).

The possible interplay between the salt/PEG and protein/PEG phase separation, which can affect the solvent quality, can have a role on the polymer mediated forces and finally on Anti-CD20 aggregation. On the basis of these measurements and the experimental observation of LLPS near the nucleation zone, it is proposed that a minor population of protein molecules can experience valuable protein-protein attractive interactions, induced by local environmental factor, slightly affecting the averaged B_{22} parameter.

FURTHER ACTIVITY

During my PhD experience I had the opportunity to collaborate on the research project AMECRYS, which is a research project funded by the European Commission under the Horizon 2020 program in the framework of Future and Emerging Technologies actions (FET-OPEN), supporting early-stages of the science and technology research and innovation around new ideas toward radically new future technologies.

AMECRYS project has as ambitious goal the realization of an innovative Continuous Template-Assisted Membrane Crystallization process for the recovery and purification of mAb Anti-CD20 directly from clarified fermentation broths ⁶¹.

For further information on AMECRYS project, please, visit <http://www.amecrys-project.eu/index.php>

REFERENCES

- [1] M.E.M. Cromwell, E. Hilario, F. Jacobson, *AAPS J* **2006**, 8, 572.
- [2] J. Thömmes, M. Etzel, *Biotechnology progress* **2007**, 23, 42.
- [3] D. Low, R. O'Leary, N.S. Pujar, *Journal of chromatography. B, Analytical technologies in the biomedical and life sciences* **2007**, 848, 48.
- [4] R. Dos Santos, A.L. Carvalho, A.C.A. Roque, *Biotechnology advances* **2017**, 35, 41.
- [5] H.Y. Chan, V. Lubchenko, *Nature Communications* **2019**, 10, 2381.
- [6] R. Chari, K. Jerath, A.V. Badkar, D.S. Kalonia, *Pharm Res* **2009**, 26, 2607.
- [7] K.R. Alford, *Journal of pharmaceutical sciences* **2008**, 97, 3035.
- [8] H.-C. Mahler, W. Friess, U. Grauschopf, S. Kiese, *Journal of pharmaceutical sciences* **2009**, 98, 2909.
- [9] E.Y. Chi, S. Krishnan, T.W. Randolph, J.F. Carpenter, *Pharmaceutical Research* **2003**, 20, 1325.
- [10] J. Wang, *Nature Communications* **2018**, 9, 5259.
- [11] S. Yadav, S.J. Shire, D.S. Kalonia, *Journal of pharmaceutical sciences* **2010**, 99, 4812.
- [12] C.J. Roberts, T.K. Das, E. Sahin, *International Journal of Pharmaceutics* **2011**, 418, 318.
- [13] O.D. Velev, E.W. Kaler, A.M. Lenhoff, *Biophys J* **1998**, 75, 2682.
- [14] B.L. Neal, D. Asthagiri, A.M. Lenhoff, *Biophys J* **1998**, 75, 2469.
- [15] A. George, W.W. Wilson, *Acta crystallographica. Section D, Biological crystallography* **1994**, 50, 361.
- [16] C. Haas, J. Drenth, *The Journal of Physical Chemistry B* **1998**, 102, 4226.
- [17] S. Salgin, U. Salgin, S. Bahadir, *International Journal of Electrochemical Science* **2012**, 7, 12404.
- [18] P.A. Hassan, S. Rana, G. Verma, *Langmuir* **2015**, 31, 3.
- [19] S.E. Harding, P. Johnson, *Biochem J* **1985**, 231, 543.
- [20] E. Trilisky, R. Gillespie, T.D. Osslund, S. Vunnum, *Biotechnology progress* **2011**, 27, 1054.
- [21] M. Muschol, F. Rosenberger, *The Journal of Chemical Physics* **1997**, 107, 1953.
- [22] M. Wolf, *Journal of Molecular Liquids* **2014**, 200, 20.
- [23] R.A. Lewus, P.A. Darcy, A.M. Lenhoff, S.I. Sandler, *Biotechnology progress* **2011**, 27, 280.

- [24] A.C. Dumetz, R.A. Lewus, A.M. Lenhoff, E.W. Kaler, *Langmuir* **2008**, *24*, 10345.
- [25] A. Lomakin, N. Asherie, G.B. Benedek, *The Journal of Chemical Physics* **1996**, *104*, 1646.
- [26] P. Wolde, D. Frenkel, P.R. Ten Wolde, D. Frenkel, *Science* **1997**, *277*, 1975.
- [27] Q. Chen, P.G. Vekilov, R.L. Nagel, R.E. Hirsch, *Biophys J* **2004**, *86*, 1702.
- [28] J. Wedekind, *Sci Rep-Uk* **2015**, *5*, 11260.
- [29] M.X. Yang, *Proceedings of the National Academy of Sciences* **2003**, *100*, 6934.
- [30] H. Yang, B. Belviso, X. Li, *Crystals* **2019**, *9*.
- [31] J. Zhang, X.Y. Liu, *The Journal of Chemical Physics* **2003**, *119*, 10972.
- [32] C. Kress, C. Brandebusch, *Journal of pharmaceutical sciences* **2015**, *104*, 3703.
- [33] AMECRYS Project, Deliverable D5.1 Simulation code for thermodynamics of coarse-grained model of mAbs in confined geometry, <<http://www.amecrys-project.eu/images/documents/AMECRYS-Deliverable-D5.1.pdf>> **2017**.
- [34] C. Hildebrandt, R. Mathaes, R. Saedler, G. Winter, *Journal of pharmaceutical sciences* **2016**, *105*, 1059.
- [35] N. Rakel, L. Galm, K.C. Bauer, J. Hubbuch, *Biotechnology progress* **2015**, *31*, 145.
- [36] D. de Araujo Sampaio, *The Journal of Chemical Thermodynamics* **2016**, *98*, 86.
- [37] D. Roberts, *Molecular Pharmaceutics* **2015**, *12*, 179.
- [38] T. Arakawa, S.N. Timasheff, *Biochemistry* **1985**, *24*, 6756.
- [39] T. Ahamed, T. *Biophys J* **2007**, *93*, 610.
- [40] AMECRYS Project, Deliverable D2.2 HEL4 domain fragment & Anti-CD20 mAb process specification report, <<http://www.amecrys-project.eu/images/documents/AMECRYS-Deliverable-D2.2.pdf>> **2017**.
- [41] A. Quigley, D.R. Williams, *Eur J Pharm Biopharm* **2015**, *96*, 282.
- [42] S. Saito, *Pharmaceutical Research* **2012**, *29*, 397.
- [43] G. Wu, *European Journal of Pharmaceutics and Biopharmaceutics* **2017**, *120*, 1.
- [44] L. Sorret, M.A. DeWinter, D.K. Schwartz, T.W. Randolph, *Biophys J* **2016**, *111*, 1831.
- [45] H. Bajaj, *Pharmaceutical Research* **2006**, *23*, 1382.
- [46] T. Peat, J. Christopher, J. Newman, *Acta crystallographica. Section D, Biological crystallography* **2006**, *61*, 1662.

- [47] C. Kress, G. Sadowski, C. Brandenbusch, *European Journal of Pharmaceutics and Biopharmaceutics* **2017**, *112*, 38.
- [48] M. Herhut, C. Brandenbusch, G. Sadowski, *Biotechnology journal* **2016**, *11*, 146.
- [49] D. Vivarès, L. Belloni, A. Tardieu, F. Bonneté, *The European physical journal. E, Soft matter* **2002**, *9*, 15.
- [50] N. Kozer, Y.Y. Kuttner, G. Haran, G. Schreiber, *Biophys J* **2007**, *92*, 2139.
- [51] X.-Z. Cao, H. Merlitz, C.-X. Wu, J.-U. Sommer, *Physical Review E* **2011**, *84*, 041802.
- [52] O. Miyawaki, M. Dozen, K. Nomura, *Biophysical Chemistry* **2014**, *185*, 19.
- [53] P. Manavalan, W.C. Johnson, *Nature* **1983**, *305*, 831.
- [54] K. H. Lee, J. Lee, J. S. Bae, Y. J. Kim, H.A. Kang, S.H. Kim, S.J. Lee, K.J. Lim, J.W. Lee, S.K. Jung, S.J. Chang, *mAbs* **2018**, *10*, 00.
- [55] J.P. Martins, *Journal of Chemical & Engineering Data* **2010**, *55*, 1247.
- [56] R.G. Nascimento, *Journal of Chemical & Engineering Data* **2018**, *63*, 1352.
- [57] J.A. Asenjo, B.A. Andrews, *Journal of Chromatography A* **2012**, *1238*, 1.
- [58] J.A. Asenjo, B.A. Andrews, *Journal of chromatography. A* **2011**, *1218*, 8826.
- [59] Y. Kuznetsov, A. Malkin, A. McPherson, *Journal of Crystal Growth* **2001**, *232*, 30.
- [60] M.A. Blanco, T. Perevozchikova, V. Martorana, M. Manno, C.J. Roberts, *The journal of physical chemistry. B* **2014**, *118*, 5817.
- [61] <http://www.amecrys-project.eu>